Title

Applications of High-Contrast Imaging Techniques and Polarimetry to (Exo-)Planetary Science

Author

Lewis, Briley Lynn

Publication Date

2024

Peer reviewed|Thesis/dissertation

UNIVERSITY OF CALIFORNIA

Los Angeles

Applications of High-Contrast Imaging Techniques and Polarimetry to (Exo-)Planetary Science

A dissertation submitted in partial satisfaction
of the requirements for the degree
Doctor of Philosophy in Astronomy and Astrophysics

by

Briley Lynn Lewis

2024

ABSTRACT OF THE DISSERTATION

Applications of High-Contrast Imaging
Techniques and Polarimetry to
(Exo-)Planetary Science

by

Briley Lynn Lewis
Doctor of Philosophy in Astronomy and Astrophysics
University of California, Los Angeles, 2024
Professor Michael P. Fitzgerald, Chair

The goal of this thesis is to characterize circumstellar disks and substellar objects, from moons to brown dwarfs, by improving and applying techniques from high-contrast imaging. To do so, I led four projects, two of which expand the range of targets accessible by high-contrast imaging. In Project 1, I develop an improved algorithm for high-contrast imaging data processing, enabling detection of fainter, smaller planets; this algorithm uses both spatial and temporal information on the speckle noise present in high-contrast images, and will be especially useful for next-generation photon-counting detectors such as Microwave Kinetic Inductance Detectors (MKIDs). In Project 2, I demonstrate a new technique to detect and monitor ejections of ice particles from subsurface oceans on outer solar system bodies, such as Jupiter's icy moon Europa, using ground-based polarimetric imaging. Such plumes have not been confirmed on Europa, but are of significant interest for astrobiology and planning for the upcoming Europa Clipper mission.

The remaining two projects use existing analysis techniques to investigate individual sys-

tems of interest that add to our understanding of planet formation. In Project 3, I characterize the atmosphere of a brown dwarf around HIP 93398, a recently discovered companion identified via the Hipparcos Gaia Catalog of Accelerations, using high-resolution spectra from SCExAO/CHARIS. With both a dynamical mass measurement and high-resolution spectroscopy, HIP 93398 B provides substantial constraints on models of brown dwarf evolution. In Project 4, I constrain the morphology and scattering properties of the debris disk around the bright star HD 155623, a unique "hybrid" debris disk that shows signs of youth despite it the system's older age, using polarimetric data from the Gemini Planet Imager. With the information from my investigation, the HD 156623 system can now serve as a benchmark for models aiming to explain how gas and dust interact during the later stages of planet formation.

These investigations both further innovation in exoplanet imaging techniques and, respectively, provide insight into detections of extrasolar planets, the nature of oceans beyond Earth, the mechanisms of planet formation, and the atmospheres of giant planets and brown dwarfs.

The dissertation of Briley Lynn Lewis is approved.

Tuan H. Do

David Clifford Jewitt

Erik A. Petigura

Michael P. Fitzgerald, Committee Chair

University of California, Los Angeles

2024

To my sweetest little buddy, Rocky,

for doing this degree with me

TABLE OF CONTENTS

LIST OF FIGURES

LIST OF TABLES

ACKNOWLEDGMENTS

This material is based upon work supported by the National Science Foundation Graduate Research Fellowship under Grant No. 2016-21 DGE-1650604 and 2021-25 DGE-2034835. Any opinions, findings, and conclusions or recommendations expressed in this material are those of the authors(s) and do not necessarily reflect the views of the National Science Foundation. This work was also supported in part by National Science Foundation award number 1710514 and by Heising-Simons Foundation award number 2020-1821.

This publication makes use of data from the following:

- the Wide-field Infrared Survey Explorer, which is a joint project of the University of California, Los Angeles, and the Jet Propulsion Laboratory/California Institute of Technology, and NEOWISE, which is a project of the Jet Propulsion Laboratory/California Institute of Technology. *WISE* and NEOWISE are funded by the National Aeronautics and Space Administration;

- the Two Micron All Sky Survey, which is a joint project of the University of Massachusetts and the Infrared Processing and Analysis Center/California Institute of Technology, funded by the National Aeronautics and Space Administration and the National Science Foundation;

- the European Space Agency (ESA) mission *Gaia* (https://www.cosmos.esa.int/gaia), processed by the *Gaia* Data Processing and Analysis Consortium (DPAC, https://www.cosmos.esa.int/web/gaia/dpac/consortium). Funding for the DPAC has been provided by national institutions, in particular the institutions participating in the *Gaia* Multilateral Agreement. This research is based on observations with *AKARI*, a JAXA project with the participation of ESA. The Infrared Astronomical Satellite (*IRAS*) was a joint project of the US, UK and the Netherlands;

- ADS/JAO.ALMA#2012.1.00688.S. ALMA is a partnership of ESO (representing its

member states), NSF (USA) and NINS (Japan), together with NRC (Canada), MOST and ASIAA (Taiwan), and KASI (Republic of Korea), in cooperation with the Republic of Chile. The Joint ALMA Observatory is operated by ESO, AUI/NRAO and NAOJ. The National Radio Astronomy Observatory is a facility of the National Science Foundation operated under cooperative agreement by Associated Universities, Inc.;

- the Subaru Telescope, which is operated by the National Astronomical Observatory of Japan. We are honored and grateful for the opportunity of observing the Universe from Maunakea, which has cultural, historical and natural significance in Hawai'i;

- the international Gemini Observatory, a program of NSF's NOIRLab, which is managed by the Association of Universities for Research in Astronomy (AURA) under a cooperative agreement with the National Science Foundation on behalf of the Gemini Observatory partnership: the National Science Foundation (United States), National Research Council (Canada), Agencia Nacional de Investigación y Desarrollo (Chile), Ministerio de Ciencia, Tecnología e Innovación (Argentina), Ministério da Ciência, Tecnologia, Inovações e Comunicações (Brazil), and Korea Astronomy and Space Science Institute (Republic of Korea);

- and Keck Observatory, which is a private 501(c)3 non-profit organization operated as a scientific partnership among the California Institute of Technology, the University of California, and the National Aeronautics and Space Administration. The Observatory was made possible by the generous financial support of the W. M. Keck Foundation. We recognize and acknowledge the very significant cultural role and reverence that the summit of Maunakea has always had within the Native Hawaiian community. We are most fortunate to have the opportunity to conduct observations from this mountain.

This research has made use of NASA's Astrophysics Data System Bibliographic Services, the VizieR catalogue access tool, CDS, Strasbourg, France, and, for the following data sets, the NASA/IPAC Infrared Science Archive, which is funded by the National Aeronautics

and Space Administration and operated by the California Institute of Technology. This work also made use of Astropy: a community-developed core Python package and an ecosystem of tools and resources for astronomy, the SpeX Prism Spectral Libraries, maintained by Adam Burgasser at http://www.browndwarfs.org/spexprism, and The UltracoolSheet at http://bit.ly/UltracoolSheet, maintained by Will Best, Trent Dupuy, Michael Liu, Aniket Sanghi, Rob Siverd, and Zhoujian Zhang, and developed from compilations by Dupuy and Liu [2012], Dupuy and Kraus [2013], Deacon et al. [2014], Liu et al. [2016], Best et al. [2017], Best et al. [2020], Sanghi et al. [2023], and Schneider et al. [2023]. Lastly, this research made use of computational and storage services associated with the Hoffman2 Shared Cluster provided by UCLA Institute for Digital Research and Education's Research Technology Group.

I acknowledge the results presented in this thesis are based upon published works with additional co-authors, and are reprinted here with permission when required. Chapter 2 is a version of B. Lewis et al. "Speckle Space-Time Covariance in High-Contrast Imaging." Astronomical Journal (2023): 165 59; arXiv:2301.01291 and is reprinted with permission from IOP Publishing. Thank you to co-authors Michael P. Fitzgerald, Rupert Dodkins, Kristina Davis, and Jonathan Lin. Thanks to Marcos M. Flores and Joseph Marcinik for helpful discussions on notation and LaTeX.

Chapter 3 is a version of a manuscript in preparation, preliminarily titled "Ground-Based Monitoring of Plumes on Europa with SCExAO/CHARIS Infrared Spectropolarimetry." Thank you to Proposal ID 2023A U010 PI Michael P. Fitzgerald, and Co-Is Eulrika Wu, Bruce Macintosh, Olivier Guyon, Julien Lozi, Tyler Groff, Timothy Brandt, and Motohide Tamura. Thanks to Jamie McCullough for useful correspondence about her prior work on using GPI to detect plumes on Europa, to Motohide Tamura for advice on using Subaru IRCS/NsIR, to Barnaby Norris for suggestions on polarization calibration standard stars, and to Thayne Currie and Kellen Lawson for resources on the CHARIS PDI pipeline.

Chapter 4 is a version of B. Lewis et al. "SCExAO/CHARIS Spectroscopic Characteriza-

tion of Cloudy L/T Transition Companion Brown Dwarf HIP 93398 B", recently submitted to the Astrophysical Journal. Thank you to co-authors Yiting Li, Aidan Gibbs, Michael P. Fitzgerald, Timothy Brandt, Daniella Bardalez Gagliuffi, Qier An, Minghan Chen, Rachel Bowens-Rubin, Maïssa Salama, Julien Lozi, Rebecca Jensen-Clem, and Ben Mazin. Thank you to Mark Popinchalk, Emily Calamari, and Genaro Suarez for providing helpful resources on brown dwarf atmospheres, and to Kellen Lawson and Thayne Currie for advice on up-to-date CHARIS calibrations.

Chapter 4 is a version of "Gemini Planet Imager Observations of a Resolved Low-Inclination Debris Disk Around HD 156623" Astronomical Journal (2024): 168 142; arXiv: 2407.15986 and is reprinted with permission from IOP Publishing. Thank you to co-authors Tom Esposito, Michael P. Fitzgerald, Pauline Arriaga, Ronald Lopez, Katie Crotts, Gaspard Duchene, Kate Follette, Justin Hom, Paul Kalas, Brenda Matthews, Max Millar-Blanchaer, David Wilner, Johan Mazoyer, and Bruce Macintosh, as well as the GPI collaboration as a whole. The authors would like to thank Dr. A. Meredith Hughes and Dr. John Carpenter for their helpful correspondence regarding the data used in Lieman-Sifry et al. 2016, and Carlos Quiroz and Fredrik Rantakyro for assistance in obtaining seeing monitor records from Gemini Observatory for our data from 2019.

On a more personal note – first and foremost, I want to thank Prof. Mike Fitzgerald for all the support over the course of my PhD. Thank you for having confidence in me that I could do this, for all that you've taught me, and for listening to all my worries over the years. I truly couldn't have asked for a better thesis advisor.

I've been lucky to have a series of wonderful mentors in my career so far, and want to say thank you to all of them who helped me get to this point. To BlueShift and the Columbia undergrads who helped me even get into grad school in the first place, especially Shreyas Vissapragada, Erin Flowers, Gabby Suissa, and Nick Luber. To my first research advisor, Rebecca Oppenheimer, for always believing in me and for taking the chance to hire me for my first research job in college. To the Project 1640 team, particularly Jonathan Aguilar and

Ricky Nilsson, who first taught me about high-contrast imaging. (Jonathan, I will *literally* never forget you teaching me the math behind KLIP in the middle of the night at Palomar!) To my STScI REU mentors, John Stansberry and Bryan Holler, for showing me how fun the outer solar system is and helping me finish my first scientific paper. And certainly to Emily Rice, who told me UCLA would be a great place to end up for grad school – you were definitely right.

I decided I wanted to be an astronomer all the way back in middle school, when my friend Mckenna gifted me a book about space and I thought it was the coolest thing ever. Thank you to my middle school Science Olympiad coach Mrs. Wong, for encouraging my interest back then, and to all the other teachers who helped empower me to pursue science. And thank you to my friends, who I'm so grateful to have grown up with, particularly Tori Buss, Deanna Johnson, Brooke Garrett, Blake Christie, and Miriam Keith. (Also to Tori Buss for being my partner in the solar system event way back in 8th grade – I still think of *tori borealis* anytime I read something about the aurora).

I'm so grateful that I have always had a community who believed in me and supported my goals in astronomy. Thank you to my mom and dad who, from my earliest days, encouraged me to do the best I could, and had absolute faith in me that I could succeed. To my grandma and grandpa for always making me feel so loved and taking such an interest in what I do, and to my nana for encouraging me so much when I was little. To my Aunt May May, for always checking in on me and also for having the coolest kid – and speaking of, thank you to Lola for letting me tell you all about cool space things! And to the rest of my family and family friends, especially my cousin Leaza, the Zarkades family, and Kay Davis and the whole AUMC community.

Thank you to my friends who got me through college, especially Hailey Winstead (we will always be a nightmare dressed like a nightmare, even if we don't have problem sets anymore), Ben Davidoff, and Serena Lewis. To my community outside of UCLA – namely my volleyball team (esp. Myco Weinstock, my personal hype man who just loves space

so much!) and book club – for helping me get through this final very tough year of grad school and reminding me that it's okay (encouraged even!) to take breaks. To Stephanie, for helping me grow so much during grad school and supporting me through it all. To the Astrobites community–especially Haley Wahl, Huei Sears, and Abby Waggoner but also so many more–for being such a great group of people to work with and for making me feel like I belong in astronomy. To Julia Zeh and Amy Bringhurst, for being the best friends a girl could ever hope for. From college through grad school, even from thousands of miles apart, I'm so glad we've gotten to do it together, Julia, and I'm always so proud of you. And Amy, even though we met about halfway through grad school, I feel like I've known you forever – and I am always grateful for your friendship, and absolutely in awe of how lucky I was to meet you at the market.

And of course, thank you so much to everyone at UCLA who has made grad school a positive experience for me. I feel so lucky that I get to say I enjoyed my PhD as much as I have, and it's because of all the wonderful people I get to work with. We say it all the time, but the UCLA astro grads are really what make this place so great. Thank you to Isabella Trierweiler, Rory Bentley, Evan Jones, and Mason MacDougall for going through this degree with me in our cohort, to Kelly O'Neil for helping me in the toughest times and for all your hugs, to Nick Ferraro for taking breaks with me to play tennis, to William Lake for getting me back into baseball (this was critical for the last year of grad school), to Graham Read for always being there. Thank you to everyone in the Fitzgerald group – I am so grateful for what a supportive environment our group is. Thank you to all my teaching mentors, who made the part of this degree you don't see in this document (all the hours spent in a classroom!) possible and helped me become the teacher that I am now, particularly Peggy Davis. I never would have guessed that writing and teaching writing would have been such a big part of my PhD, but I am so glad it was – thank you to Greg Rubinson for setting me on that path, to everyone in Writing Programs for encouraging me that I do belong in writing even as a scientist, and to Tony Friscia for getting me involved in the Clusters.

Perhaps most importantly in grad school, thank you to Ronald Lopez – just like you said, you're the first person I go to when astronomy gets hard. I couldn't be more excited to be following your path with NSF at UCSB next year. And thank you to my grad school besties – Joey Marcinik, Thomas Dellaert, Quinn Pratt, Marcos Flores, and Thea Faridani – who have taught me so much, answered so many questions, kept me company in the pandemic years on Minecraft, and just generally been there for everything in grad school. Taco Tuesday has been one of my favorite parts of the past six years. My other favorite part was probably listening to you talk in our office, Thea, while the glorious sound of Yoda screaming intermittently played in the background – I am so grateful for your friendship and the fact that I can spend all day with you at work and still want to hang out after.

And last but not least, thanks to my little buddy Rocky, who has been by my side nearly 24/7 while I work, whether in the office or at home. You've brought me so much joy and comfort, and I wish you could read this – I guess I'll just have to give you a carrot to show my appreciation instead.

VITA

2014 – 2018 B.A. in Astrophysics, Columbia University.

2018 – 2020 M.Sc. in Astronomy & Astrophysics, University of California, Los Angeles.

2018 – 2024 Ph.D. candidate in Astronomy & Astrophysics, University of California, Los Angeles.

Awards

2018 National Science Foundation Graduate Research Fellow.

2018 Graduate Dean's Fellowship, Graduate Division, UCLA.

2019 Outstanding Teaching Assistant, Physics & Astronomy, UCLA.

2022 Sonia Maasik Memorial Prize for Graduate Instructors of Writing, UCLA.

2024 National Science Foundation Astronomy and Astrophysics Postdoctoral Fellow, UCSB.

PUBLICATIONS

Briley L. Lewis, Yiting Li, Minghan Chen, Timothy D. Brandt, et al. "SCExAO/CHARIS Spectroscopic Characterization of Cloudy L/T Transition Companion Brown Dwarf HIP 93398 B." In review, submitted to the Astronomical Journal.

Briley L. Lewis, Michael P. Fitzgerald, Thomas Esposito, et al. "Gemini Planet Imager Observations of a Resolved Low-Inclination Debris Disk Around HD 156623." Astronomical Journal (2024): 168 142.

Briley L. Lewis, Astrobites Collaboration, et al. "Exploring the Effects of Astrobites Lesson Plans on Undergraduate Astronomy Students." In review, submitted to Physical Review PER; arXiv:2309.05822.

Briley L. Lewis, K. Supriya, et al. "Effects of Popular Science Writing Instruction on General Education Student Attitudes Towards Science: A Case Study in Astronomy." Astronomy Education Journal (AEJ) (2023); arXiv:2209.02852

Briley L. Lewis, Michael P. Fitzgerald, Rupert Dodkins, et al. "Speckle Space-Time Covariance in High-Contrast Imaging." Astronomical Journal (2023): 165 59; arXiv:2301.01291

Briley L. Lewis, John Stansberry, Bryan Holler, et al. and the New Horizons Science Team. "Distribution and Energy Balance of Pluto's Nitrogen Ice, as seen by New Horizons in 2015." Icarus Special Issue (2021): 113633.

CHAPTER 1

Introduction

The field of exoplanet science is still relatively young, especially in the context of the long history of astronomy. The first image of a circumstellar disk was taken in 1984, capturing the debris disk around β Pictoris [Smith and Terrile, 1984]. Nearly a decade later, the first exoplanet detection came in 1992, with two planets detected around the pulsar PSR1257+12 via pulsar timing measurements [Wolszczan and Frail, 1992]. The detection that many consider the true start of the field, however, is that of 51 Pegasi b, an exoplanet around a Sun-like star discovered in 1995 via the radial velocity method [Mayor and Queloz, 1995]. In the nearly 30 years since that discovery, over 5,600 exoplanets have been detected, many via the transit method as used by the *Kepler Space Telescope* and the more recent *Transiting Exoplanet Survey Satellite* (*TESS*) [NASA Exoplanet Science Institute, 2020, Borucki et al., 2010, Ricker et al., 2015].

The first direct detection of an exoplanet — that is, the first time we collected light from the object itself instead of its star — didn't come until 2004, with the famous imaging of the HR 8799 and beta Pictoris systems soon after in 2008 [Marois et al., 2008]. Although indirect methods such as transits and radial velocities have been indispensable for detecting large numbers of exoplanets, direct imaging of exoplanets is key for reaching the next big goal of exoplanet science, as set forth by the Astro2020 Decadal Survey: characterizing habitable worlds beyond our solar system [NASEM, 2021]. Direct imaging is often combined with spectroscopy, providing a clear look into an exoplanet's atmosphere, including deeper layers unable to be probed with transit spectroscopy [Madhusudhan, 2019].

Upcoming missions and facilities such as the Roman Space Telescope (launching late 2026 to early 2027), the Habitable Worlds Observatory (planned for the 2040s), and various 30-meter class telescopes aim to directly image planets closer in size to Earth, searching for signs of life [Kasdin et al., 2020, Tuchow et al., 2024]. However, that goal is quite the technical challenge. Current instruments are limited to planets that are young and still luminous from their formation, at wide separations from their host stars, and larger than Jupiter [Follette, 2023, Currie et al., 2022]. The contrast between planets and their host stars is incredibly large, on the order of 10^{10} difference in brightness for an Earth-like planet around a Sun-like star — thus why direct imaging is also often referred to as *high-contrast* imaging.

1.1 High-Contrast Imaging Instrumentation and Data Processing

To achieve the contrasts necessary for imaging exoplanets and circumstellar disks, the light of the host star must be suppressed as much as possible. This suppression is made more difficult by the image formation process, which is subject to dynamic and non-deterministic perturbations from sources of optical error leading to so-called speckle noise. Speckles arise from both the atmosphere, which distorts the light from the star leading to noise in the point spread function (PSF), and imperfections in the optical system [Racine et al., 1999]. The former are known as atmospheric speckles, while the latter are referred to as quasi-static speckles due to the fact that they evolve over longer timescales (minutes to hours as opposed to the milliseconds for atmospheric speckles). In high-contrast imaging instruments, starlight suppression is primarily accomplished by coronagraphy, wavefront control, and data processing techniques [Currie et al., 2022]. Coronagraphy is aimed at the static/deterministic portion of the wavefront, while wavefront sensing and control and post-processing deal with suppressing the stochastic speckle noise.

Coronagraphy was invented in the 1930s by Bernard Lyot, originally for use in observing

the faint solar corona [Lyot, 1939]. A coronagraph is simply an optical component that blocks out starlight. Traditional coronagraphs, such as the Lyot coronagraph, accomplish this by physically blocking the light with a coronagraphic spot [Soummer, 2004]; other modern coronagraphs, such as the vector vortex coronagraph, manipulate the phase of the light instead to achieve destructive interference [Mawet et al., 2009].

Wavefront control refers to the mitigation of optical aberrations caused by turbulence in Earth's atmosphere. This is accomplished using an adaptive optics system, which measures and corrects for these distortions in real-time, improving the angular resolution to near the diffraction limit [Babcock, 1953, Mendis and Rosenberg, 1994]. Adaptive optics systems generally function by using a wavefront sensor (WFS) to measure the aberrations of the incoming light, a deformable mirror (DM) to correct said aberrations, and a real-time control system to convert WFS measurements to DM commands. Although many telescopes now have adaptive optics systems, high-contrast imaging uses extreme adaptive optics, wherein the technology has been optimized for an higher fidelity level of wavefront correction over a relatively small field-of-view using a bright natural guide star [Guyon, 2018]. These systems include additional wavefront sensing to improve the wavefront correction.

Even after these measures, some speckle noise (mainly from quasi-static speckles) still remains in the images. This is commonly removed via post-processing methods, which often rely on some form of differential imaging. The goal with these methods is to find a way to differentiate between the real astrophysical signal and the speckle pattern, in order to create a model of the noise for PSF subtraction. Angular Differential Imaging (ADI) exploits the spatially quasi-static nature of the speckles by setting the instrument's derotator to stabilize the pupil for ground-based alt-azimuth telescopes or rolling a spacecraft such as *HST*; real astrophysical signals will move with the sky, whereas the speckle pattern will remain fixed, creating a distinction between the two [Marois et al., 2006]. Spectral Differential Imaging (SDI) exploits the fact that speckles are chromatic, as they are a result of diffraction within the telescope optics; with an integral field spectrograph (IFS), it is possible to observe this

chromaticity and use it to create a model of the noise for PSF subtraction [Marois et al., 2000, Follette, 2023]. Reference star Differential Imaging (RDI) is most often used in space, where the PSF is stable on longer timescales; this method uses separate observations of a reference star as the PSF model [Xuan et al., 2018, Currie et al., 2022]. Algorithms using these techniques — namely Karhunen-Loéve Image Processing, or KLIP — are discussed at length in Chapter 2.

Some high-contrast imaging instruments also have a polarimetric mode, in which the incoming light is split into two orthogonal polarization states and recorded as two simultaneous images of the target object, which — in conjunction with a half-wave plate for modulation — can be used to calculate the Stokes vector components I, Q, and U. (Note: With a different retardance you can also retrieve Stokes vector component V for circular polarization, but this component is less relevant for the scattered light processes though to be dominant in planets and disks.) This process is described in detail in Chapter 3, and is particularly useful for imaging circumstellar disks, whose scattered light is polarized (unlike the unpolarized starlight, creating a natural separation between the two), in a technique known as polarimetric differential imaging (PDI).

1.2 Current High-Contrast Imaging Instruments

A variety of high-contrast imaging instruments exist today, many of which were built for the explicit purpose of detecting and characterizing exoplanets. The W.M. Keck Observatory's NIRC2 infrared imager on Keck II in Hawai'i includes a coronagraph, which was used for the groundbreaking observations of the HR 8799 system in 2008 [Marois et al., 2008], and is still operational. In the years since that initial discovery, Keck's adaptive optics system has been upgraded to include cutting edge technologies such as a vector vortex coronagraph [Mawet et al., 2009, Xuan et al., 2018], an infrared pyramid wavefront sensor [Uyama et al., 2020, Bond et al., 2020], and a soon-to-be-completed polarimetric mode [Ragland et al., 2019].

NIRC2 was also used to discover the companion object characterized in Chapter 4 of this thesis.

Dedicated exoplanet-hunting instruments with extreme adaptive optics systems came online in the early 2010s: Project 1640 [Oppenheimer et al., 2012], the Gemini Planet Imager (GPI) [Macintosh et al., 2014b], and the European Spectro-Polarimetic High contrast imager for Exoplanets REsearch (SPHERE) [Beuzit et al., 2019]. These instruments had coronagraphic hyperspectral imagers — enabling the use of SDI in post-processing — and were located at Palomar Observatory in California, Gemini South in Chile, and teh Very Large Telescope in Chile, respectively. These projects revealed that giant planets are relatively rare at wide separations [Wang et al., 2017]. GPI additionally had a polarimetric mode, producing a survey of circumstellar disks [Esposito et al., 2020]. Although Project 1640 has been decommissioned, the Gemini Planet Imager is about to start its second life as GPI 2.0, coming soon to Gemini North [Chilcote et al., 2020]. GPI 2.0 plans to include a pyramid wavefront sensor and new Lyot coronagraph designs to improve its performance and reach higher contrasts. GPI, in its first iteration, is the source of the data analyzed in Chapter 5 of this thesis. SPHERE is also operational today, but does not play a role in this thesis, and accordingly will not be discussed in detail.

One more recent high-contrast imaging instruments is the Coronagraphic High Angular Resolution Imaging Spectrograph (CHARIS) on the Subaru Telescope in Hawai'i [Groff et al., 2015]. CHARIS is the source of the data analyzed in Chapters 3 and 4. CHARIS is an IFS with two modes: a lower-resolution "broadband" mode covering J, H, and K bands in the infrared simultaneously, and higher-resolution modes covering those bands individually. CHARIS is also capable of spectropolarimetry in both those spectral modes, and sits behind the Subaru Coronagraphic Extreme Adaptive Optics system (SCExAO) [Lozi et al., 2018], which is regularly used to develop and test new technologies in adaptive optics. High-contrast imaging has also been done with space-based observatories, namely the *Hubble Space Telescope* and the James Webb Space Telescope (*JWST*) [Krist, 2004, Krist et al.,

2005, Hinkley et al., 2022, Carter et al., 2023].

In addition to ongoing upgrades to existing facilities and adaptive optics systems, as well as the exciting high-contrast science happening with JWST, multiple instruments are in development for the upcoming 30-meter class telescopes. For example, the Narrow Field InfraRed Adaptive Optics System (NFIRAOS) and Infrared Imaging Spectrograph (IRIS) are planned as first-light instruments for the U.S. Thirty Meter Telescope [Herriot et al., 2012, Moore et al., 2014] and the Mid-infrared ELT Imager and Spectrograph (METIS) is a first-generation instrument for the European Extremely Large Telescope [Brandl et al., 2016]. Upcoming NASA space-based missions will also include high-contrast imaging capabilities; the Nancy Grace Roman Space Telescope will include a coronagraphic technology demonstration [Kasdin et al., 2020], and the eventual Habitable Worlds Observatory aims to include a high-contrast imager capable of detecting Earth-sized exoplanets to look for signs of life [Tuchow et al., 2024, NASEM, 2021].

1.3 Dissertation Summary

This thesis aims to illustrate both recent advances in high-contrast imaging techniques, and a handful of the various science cases that are made possible by those techniques. This work contributes to the larger goals in the field of maturing the technology necessary to characterize Earth-like planets in the coming decades and building our understanding of planetary systems, from formation to habitability.

In Chapter 2, I detail a new framework for point-spread function (PSF) subtraction based on the spatio-temporal variation of speckle noise in high-contrast imaging data where the sampling timescale is faster than the speckle evolution timescale. Removal of speckle noise is one of the main challenges in high-contrast imaging, and some of the most successful post-processing algorithms harness spatial variations in speckle noise to model and remove it. This work explores how the new generation of photon-counting detectors (e.g. Microwave Kinetic

Inductance Detectors, Infrared Avalanche Photodiodes) may allow us to harness both spatial *and* temporal information in these data processing algorithms, helping to improve the final contrast (and therefore to detect fainter planets) in high-contrast imaging data.

In Chapter 3, I present the first resolved infrared polarimetric imaging of Europa, obtained with the purpose-built high-contrast imaging instrument SCExAO/CHARIS on the Subaru Telescope. This spectropolarimetric data covers $J/H/K$ bands at R$\sim$18.4 and H band at R$\sim$65.2, providing a unique view into Europa's surface and geology. I propose such ground-based polarimetric observations as a possible avenue for long-term monitoring of plumes on Europa, which are still debated at present; an improved understanding of Europa's cryovolcanism will be crucial in the coming years for mission planning as *Europa Clipper* and *JUICE* reach the Jupiter system in the early 2030s.

In Chapter 4, I analyze new spectroscopic data of the recently discovered brown dwarf companion HIP 93398 B from Subaru SCExAO/CHARIS. HIP 93398 B was initially found using the Hipparcos-Gaia Catalog of Accelerations (HGCA), which predicted its position around its host star via astrometric measurements of HIP 93398's motion. Brown dwarfs discovered via the HGCA serve as excellent benchmarks for testing substellar atmosphere and evolution models, due to their model-independent dynamical mass measurements. The imaging discovery originally suggested that HIP 93398 B is an overmassive T dwarf, based on its L' band luminosity and dynamical mass; in this work, I revise HIP 93398 B's classification via comparison to spectral standards and atmospheric models, and explore the resulting implications for agreement with evolutionary cooling models.

In Chapter 5, I characterize the debris disk around the star HD 156623, a 16 Myr-old A0V star in the Scorpius–Centaurus association, as resolved in scattered light for the first time by the Gemini Planet Imager (GPI), a high-contrast imaging instrument previously located at Gemini South. I present new analysis of the GPI H-band polarimetric detection of the HD 156623 debris disk, with particular interest in its unique morphology. This debris disk lacks a visible inner clearing, unlike the majority of low-inclination disks in the GPI

sample and in Sco-Cen, and it is known to contain CO gas, positioning it as a candidate "hybrid" or "shielded" disk.

CHAPTER 2

Speckle Statistics in High-Contrast Imaging

2.1 Introduction

Direct imaging of exoplanets is a challenging endeavor, given the extreme contrasts that must be achieved to detect faint planets. Although significant starlight suppression can be achieved through optics and instrumentation, such as coronagraphs, adaptive optics (AO) systems, interferometers, and more, that alone is insufficient to detect analogs of planets in our solar system [Oppenheimer and Hinkley, 2009, Guyon, 2005]. Improving contrast expands the space of the types of planets that can be directly detected and characterized.

Existing instruments, such as the Gemini Planet Imager [Macintosh et al., 2008] and VLT's SPHERE [Beuzit et al., 2019] are able to image giant planets and brown dwarfs, reaching contrasts (in the astronomical sense, meaning the detectable planet-star flux ratio) of around 10^{-6}. This is enabled by a combination of wavefront sensing, control, and post-processing, which reduce the impact of noise by distinguishing between the planet signal and residual noise; this noise arises from uncorrected wavefront aberrations, resulting in quasi-static fluctuations in the focal plane known as "speckles." Generally, these algorithms use the data themselves to create a model of the speckle noise which can then be subtracted from the data to recover the target planet signal in a process known as point-spread function (PSF) subtraction. Previously developed algorithms include LOCI (Locally Optimized Combination of Images; [Lafreniere et al., 2007]), KLIP (Karhunen Loéve Image Processing; [Soummer et al., 2012]), and more [Gebhard et al., 2022]. Many directly imaged planet dis-

coveries to date have relied on such algorithms, such as the famous HR 8799 planets [Marois et al., 2008].

Improvements to data processing pipelines and methods are one way in which we can push forward and improve contrast for future high-contrast imaging instruments. Other approaches to improving high-contrast imaging methods focus on wavefront sensing and control, such as predictive control techniques, which aim to improve adaptive optics corrections [Guyon and Males, 2017, Guyon et al., 2018, Males and Guyon, 2018], and sensor fusion, both currently in development at multiple facilities, including Subaru's SCExAO facility [Guyon et al., 2017] and Keck Observatory van Kooten et al. [2021], Wizinowich et al. [2020], Jensen-Clem et al. [2019], Calvin et al. [2022]. Other recent work such as [Guyon and Males, 2017] focuses on using on Empirical Orthogonal Functions (EOFs), a similar mathematical framework, to analyze spatio-temporal correlations; their work is in the context of predictive control, whereas our work applies to image processing. New advances in detector technology also affect both wavefront sensing and post-processing. High-speed, low-noise detectors will provide multiple opportunities for improvements, including focal-plane wavefront sensing, which eliminates non-common-path wavefront errors [Vievard et al., 2020]. Of particular interest are arrayed photon-counting devices, such as Microwave Kinetic Inductance Detectors (MKIDs) [Schlaerth et al., 2008, Mazin et al., 2012, Meeker et al., 2018, Walter et al., 2020] and Infrared Avalanche Photodiodes (IR APDs) [Goebel, 2018, Wu et al., 2021]. Electron Multiplying CCDs (EMCCDs) are a functional equivalent in the optical [Lake et al., 2020]. Photon arrival times have already been used to distinguish speckles from incoherent signals, such as planets [Walter et al., 2019, Steiger et al., 2021], and MKIDs have been used for high contrast imaging with the DARKNESS instrument at Palomar [Meeker et al., 2018] and with MEC, the MKID Exoplanet Camera for high contrast astronomy at Subaru [Walter et al., 2018].

This new regime of photon-counting detectors and more advanced adaptive optics presents many opportunities. With the improved temporal resolution of next-generation detectors,

we will be able to resolve the spatial and temporal evolution of atmospheric speckles. Some prior work has investigated use of spatio-temporal correlations on longer timescales, such as [Mullen et al., 2019] and [Gebhard et al., 2022], but this work focuses the shorter timescale changes of atmospheric speckles.

There is a rich history of theory and measurements of space-time atmospheric speckle behavior in the past decades, which this work builds off of. Since the 1970s–1980s, speckle patterns and intensity distributions have been measured [Dainty et al., 1981, Scaddan and Walker, 1978, Goebel, 2018, Odonnell et al., 1982], demonstrating agreement with models based in Rician statistics [Cagigal and Canales, 2001, Canales and Cagigal, 1999] and the importance of speckles as the limiting noise source in the high-contrast regime [Racine et al., 1999]. The space-time covariance was even directly measured in [Dainty et al., 1981], indicating that speckle boiling has a directionality related to turbulence. Speckle intensity patterns have been modeled as a modified Rician distribution [Aime and Soummer, 2004, Gladysz et al., 2010], and speckle lifetimes have been constrained through models and direct measurements [Aime et al., 1986, Vernin et al., 1991, Glindemann et al., 1993]. In fact, models of speckle boiling directly relate the lifetime of speckles to atmospheric parameters related to wind and turbulence, as in [Roddier et al., 1982], estimating speckle lifetimes on the order of tens of milliseconds.

This work is a new addition to the variety of time-domain algorithms that have been developed in recent years. For example, the PACO algorithm uses temporal information from the background fluctuations of Angular Differential Imaging data [Flasseur et al., 2018], and the TRAP algorithm uses temporal information of the speckle pattern to improve contrast specifically at close separations [Samland et al., 2021]. Another algorithm, from [Gebhard et al., 2022], uses half-sibling regression on time-series data. These are all examples of the possibilities for temporal information in post-processing, in addition to the AO control improvements described earlier.

In this work, we aim for a second-order characterization of the statistical behavior of

atmospheric speckles in the high-contrast regime, described by the space-time covariance, which we then leverage for improving contrast in post-processing with the eventual goal of improving exoplanet detection capabilities. As previously mentioned, this goal is not without its challenges — with kHz readouts, these detectors can produce large datasets and lead to computationally intensive post-processing methods. While developing this new technique, we must also contend with data storage and computational limitations.

In this paper, we first provide an analytical justification for the existence of these covariances in the high-contrast regime, observe their occurrence in test simulations focusing on millisecond time sampling, and then present an initial algorithm to exploit these covariances for PSF subtraction. Specifically, we are testing this algorithm in a regime dominated by atmospheric speckles at short exposures (where the timescale of our exposures is short compared to that of changes in atmospheric residual wavefront error, so atmosphere is essentially frozen).

Here in Section 2.2, we describe the process of baseline Karhunen-Loéve Image Processing (KLIP), the origins of space-time speckle covariances, and the extension of KLIP to space-time covariances. Following, in Section 2.3, we describe the models used to create datasets for initial testing of this processing framework. Section 2.4 presents results of this new algorithm implemented on simulated data. Finally, in Sections 2.5 and 2.6, we discuss the promise of this new technique, as well as its current challenges/limitations and future work.

2.2 Space-Time Covariance Theory

Speckles can limit contrast, but can also be subtracted to some extent to improve contrast. One of the most successful post-processing algorithms has been KLIP, described in Section 2.2.1, which exploits spatial correlations in long-exposure images. We motivate our extension of this technique to include space-time correlations on shorter timescales in Section 2.2.2 by describing how these correlations arise in imaging through the atmosphere. This extension of

KLIP, referred to as space-time KLIP or stKLIP, is demonstrated in Section 2.2.3, exploiting spatio-temporal correlations between short-exposure images.

2.2.1 Karhunen-Loéve Image Processing

Karhunen-Loéve Image Processing is a data processing technique that uses principle component analysis (PCA), where data are represented by a linear combination of orthogonal functions. In high-contrast imaging, KLIP is used to build a model, used for PSF subtraction, that accounts for spatial correlations between speckles and other PSF features, first described in [Soummer et al., 2012]. This technique takes advantage of spatial covariances of the speckles in the image, because strong correlations exist in high eigenvalue modes and can be suppressed. This is a data-driven approach, which uses available information from the data itself to provide an approximation of the noise, by using a subset of the data as "reference images" from which to build the model of the noise while using another subset of the data as the "target image" for PSF subtraction.

To increase readability, all variables for the following mathematics are described in Notation Glossary A. As described in [Soummer et al., 2012], we assume we observe a point spread function $T(k)$, where k is the pixel index, that contains the stellar point spread function $I_\psi(k)$ and may also contain some faint astronomical signal of interest $A(k)$. Therefore, our target image can be described as

$$T(k) = I_\psi(k) + \epsilon A(k), \tag{2.1}$$

where ϵ is 0 when there is no astronomical signal of interest, or 1 if there is. The goal of PSF subtraction is therefore to recreate $I_\psi(k)$ in order to isolate $A(k)$. Without an infinite number of references, though, we cannot exactly infer $I_\psi(k)$; instead, we approximate the PSF $\hat{I_\psi}(k)$. For consistency in our notation, herein we represent $T(k)$, $A(k)$, and $\hat{I_\psi}(k)$ as vectors $\vec{t}$, $\vec{a}$ and $\vec{\hat{\psi}}$ respectively.

In order to approximate $\vec{\hat{\psi}}$, KLIP computes a Karhunen-Loéve Transform based on the

covariance matrix of the mean-subtracted reference images.

A sequence of reference images are first unraveled into one-dimensional vectors, each as $\vec{r}$. Note: henceforth vectors are denoted as bold, matrices with uppercase variables and subscript matrix elements. These image vectors $\vec{r}$ are then stacked into an $n_p \times n_i$ matrix R, where $n_p = n_x \times n_y$ and n_i is the number of images, as follows:

$$R = \begin{bmatrix} R_{1,1} & R_{1,2} & \dots & R_{1,n_i} \\ R_{2,1} & R_{2,2} & \dots & R_{2,n_i} \\ \vdots & \vdots & \ddots & \vdots \\ R_{n_p,1} & R_{n_p,2} & \dots & R_{n_p,n_i} \end{bmatrix} \tag{2.2}$$

We then subtract the mean image of the set (summing over the matrix columns) from the reference set R, in order to produce a set of mean-subtracted images M to use throughout the process of KLIP:

$$\vec{x_i} = \frac{1}{n_i} \sum_{j=1}^{n_i} R_{i,j} \tag{2.3}$$

$$M_{i,j} = R_{i,j} - \vec{x_i} \tag{2.4}$$

The resulting covariance matrix (2.5) C has size $n_p \times n_p$.

$$C = MM^T = \begin{bmatrix} C_{1,1} & C_{1,2} & \dots & C_{1,n_p} \\ C_{2,1} & C_{2,2} & \dots & C_{2,n_p} \\ \vdots & \vdots & \ddots & \vdots \\ C_{n_p,0} & C_{n_p,1} & \dots & C_{n_p,n_p} \end{bmatrix} \tag{2.5}$$

Note: in practice, this implementation is computationally expensive, so the covariance is instead often computed in image space on n_i by n_i images and then re-projected into pixel space, as is done in the [Soummer et al., 2012] implementation. The ideal implementation depends on which dimension is larger / more computationally expensive, e.g. [Long and

Males, 2021]. In this work, the mathematics for KLIP and stKLIP, as written here, will be in pixel space.

An eigendecomposition of the covariance matrix C, mathematically described as solutions to the equation

$$C\vec{v}_j = \lambda_j \vec{v}_j, \tag{2.6}$$

with

$$\lambda_1 > \lambda_2 > \lambda_3 > \ldots \lambda_{n_p}, \tag{2.7}$$

produces a length n_p vector of eigenvalues ($\vec{\lambda}$) and size $n_p \times n_p$ (or $n_m \times n_p$ if fewer than n_p eigenvectors/modes are used) matrix of eigenvectors/eigenimages (V) containing n_m rows of individual eigenvectors $\vec{v}$ each of length n_p, such that $V_{i,j} = (\vec{v}_j)_i$.

$$V = \begin{bmatrix} V_{1,1} & V_{1,2} & \ldots & V_{1,n_p} \\ V_{2,1} & V_{2,2} & \ldots & V_{2,n_p} \\ \vdots & \vdots & \ddots & \vdots \\ V_{n_m,1} & V_{n_m,2} & \ldots & V_{n_m,n_p} \end{bmatrix} \tag{2.8}$$

The eigenvalues order the eigenimages by their importance to rebuilding the original image and are used to construct the basis of the new subspace of greatest variation onto which we project our images. Assuming the vectors are sorted by decreasing eigenvalue, the first coordinate corresponds to the direction of greatest variation. The lowest-order (first coordinate) eigenimages are selected to represent $\vec{\hat{\psi}}$, while leaving the high-order terms to hopefully contain our astrophysical signal.

We select a given number n_m of the eigenimages as our number of modes of variation. The inner product of the matrix of eigenvectors V with the one-dimensional vector of the target image $\vec{t}$ (which has length n_p), is described mathematically as

$$\vec{t} = \begin{bmatrix} t_1 \\ t_2 \\ \vdots \\ t_{n_p} \end{bmatrix} \tag{2.9}$$

$$\vec{q} = V \cdot \vec{t} = \begin{bmatrix} q_1 \\ q_2 \\ \vdots \\ q_{n_m} \end{bmatrix} \tag{2.10}$$

and creates a vector of coefficients $\vec{q}$ of length n_{m} — each of these can be thought of as how much of each mode (or each eigenvector, v_j) is in the image, or equivalently, the coordinates in the new rotated principle axis space.

Lastly, we can project back into our original pixel space by taking the product of this vector of coefficients with the chosen eigenvectors, recovering a vector of length n_{p}, the same as our target image:

$$\vec{\hat{\psi}} = \vec{q}^{T} \cdot V \tag{2.11}$$

The resulting array is our image projected into the subspace of greatest variation, an estimation of the original PSF $\vec{\hat{\psi}}$, and what we will subtract from our target image for PSF subtraction. Note that the tuneable parameter here is the number of eigenvectors used in the basis (the number of "modes").

The planet signal is also projected onto a distribution of these modes, and it is assumed that the planet signal is primarily projected onto modes with lower eigenvalue. However, as we subtract more modes, the projection of the planet onto these modes is also subtracted. Therefore, a larger number of modes might lead to oversubtraction of a planet signal, but too few may not sufficiently subtract out the speckle noise. As a result, we must correct for this throughput effect and optimize the number of modes to attain the largest possible contrast gain.

2.2.2 Space-Time Covariances

Whereas KLIP harnesses spatial covariances of speckle noise, we propose to expand the scope of such projection methods to take advantage of space-time covariances in speckle noise. For bulk flow in a turbulent atmosphere, phase errors in the pupil, from atmospheric disturbances, translate across the telescope with wind motion, resulting in changes in phase and amplitude in the image plane. Atmospheric perturbations evolve across a broad set of spatial frequencies. Since the perturbations at these different spatial frequencies are correlated, we will illustrate that the speckles at the locations that correspond to those spatial frequencies in the image plane will be correlated as well. Similarly to the above section, all variables for the following mathematics are described in Notation Glossary B.

The covariance of intensity in the image plane for points separated in space and time is characterized through the second moment $\langle I(\vec{x}_1, t) I(\vec{x}_2, t-\tau)\rangle$, where I is the intensity in the image. Angle brackets ($\langle\rangle$) denote averaging over a statistical ensemble. Suppose we have a perfect coronagraph and only phase aberrations are present, ignoring polarization as well as static phase errors, and treating electric field as a scalar. Also, we presume the phase aberrations are small, a reasonable assumption for the high-contrast imaging limit. In this case, the pupil amplitude is

$$\Psi_{\text{pup}}(\vec{u}, t) = P(\vec{u}) e^{i\phi(\vec{u},t)}, \tag{2.12}$$

approximated as

$$\Psi_{\text{pup}}(\vec{u}, t) \approx [1 + i\phi(\vec{u}, t)] P(\vec{u}), \tag{2.13}$$

where $P(\vec{u})$ is the pupil function, ϕ is the phase, and $\vec{u}$ is the coordinate in the pupil plane ($\vec{x}$ is the coordinate in the focal plane, related by a Fourier transform). It is worth noting that departure from this assumption of linearity may affect results. The amplitude in the focal plane is

$$\begin{aligned} \Psi_{\text{foc}}(\vec{x}, t) &= \mathcal{F}\left\{P(\vec{u})\right\} + i\mathcal{F}\left\{\phi(\vec{u}, t) P(\vec{u})\right\}, & (2.14) \\ &= C(\vec{x}) + S_\phi(\vec{x}, t). & (2.15) \end{aligned}$$

$C(\vec{x})$ is the spatially coherent part of the wavefront, and $S_\phi(\vec{x},t)$ comes from phase aberrations – $S_\phi(\vec{x},t)$ corresponds to the "speckles" we want to remove [Aime and Soummer, 2004, Roddier et al., 1982]. In the case of a perfect coronagraph, $C(\vec{x}) = 0$ and the intensity in the image is only due to phase aberrations, and can be expressed as

$$\begin{aligned} I(\vec{x},t) &= |\Psi_{\text{foc}}(\vec{x},t)|^2, & (2.16)\\ &= |S_\phi(\vec{x},t)|^2, & (2.17)\\ &= |\mathcal{F}\{\phi(\vec{u},t)P(\vec{u})\}|^2. & (2.18) \end{aligned}$$

The covariance of the intensity is

$$\langle I(\vec{x}_1,t)I(\vec{x}_2,t-\tau)\rangle = \langle |S_\phi(\vec{x}_1,t)S_\phi(\vec{x}_2,t-\tau)|^2\rangle. \quad (2.19)$$

If we assume (complex) Gaussian statistics for S_ϕ [Soummer et al., 2007], then by Wick's theorem [e.g. Fassino et al., 2019] we have,

$$\langle I(\vec{x}_1,t)I(\vec{x}_2,t-\tau)\rangle = \langle I(\vec{x}_1,t)\rangle\langle I(\vec{x}_2,t)\rangle + |\langle S_\phi(\vec{x}_1,t)S_\phi^*(\vec{x}_2,t-\tau)\rangle|^2. \quad (2.20)$$

Therefore to compute this covariance, we need the quantity $\langle S_\phi(\vec{x}_1,t)S_\phi^*(\vec{x}_2,t-\tau)\rangle$, which is the covariance of the phase-induced aberration in the focal plane. Accounting for the Fourier relationship between the focal plane aberration S_ϕ and the pupil plane phase ϕ as in Equations 2.14 and 2.15, we find

$$\langle S_\phi(\vec{x}_1,t)S_\phi^*(\vec{x}_2,t-\tau)\rangle = \int d\vec{u}\int d\vec{\xi}\exp[2\pi i\vec{\xi}\cdot\vec{x}_2 - 2\pi i\vec{u}\cdot(\vec{x}_1-\vec{x}_2)]\times \langle\phi(\vec{u},t)\phi(\vec{u}+\vec{\xi},t-\tau)\rangle P(\vec{u})P(\vec{u}+\vec{\xi}) \quad (2.21)$$

where $\vec{\xi}$ is the coordinate of the displacement in the pupil plane. If $\phi(\vec{u},t)$ is statistically stationary in the pupil plane position $\vec{u}$ (and time), then we can define the phase covariance function as

$$B_\phi(\vec{\xi},\tau) = \langle\phi(\vec{u},t)\phi(\vec{u}+\vec{\xi},t-\tau)\rangle, \quad (2.22)$$

independent of $\vec{u}$ and t. Equation 2.22 for B_ϕ relates space-time covariance in the pupil to space-time covariance in the image, and can be simplified into the Kolmogorov phase covariance function for turbulence with an assumption about time.

Kolmogorov's theory of turbulence describes a cascade of large scale turbulent motions that dissipate energy onto smaller scales, following a power spectrum described by $\Phi_n(\vec{k}) \propto |\vec{k}|^{-11/3}$, where Φ_n is the variation in index of refraction and $|\vec{k}|$ is the magnitude of the turbulence [Kolmogorov, 1941, Hickson, 2008]. Fluctuations in density correspond to fluctuations in the index of refraction. These variations in index of refraction lead to differences in path length for the incoming light, creating some of the phase and amplitude error that we observe. However, we assume the timescale of change for this turbulence is generally slow when compared to wind speeds, an assumption known as Taylor frozen flow [Taylor, 1938]. This assumption is valid so long as the turbulent intensity is low compared to the wind speed, generally accepted to be true for astronomical contexts with the possible exception of boundary layer turbulence [Bharmal, 2015]. The turbulence can be thought of then as a "phase screen" propagating horizontally across the telescope with the wind. This phenomenon is described mathematically as

$$\phi(\vec{u}, t) = \phi(\vec{u} - \vec{v}_{\text{wind}}\tau, t - \tau) \tag{2.23}$$

which states that the phase structure at one time is related to the phase structure at a different time, just shifted by the wind velocity times the time difference [Taylor, 1938, Hickson, 2008].

This shows that a single phase screen $\phi(\vec{u}, t)$ (which contains Kolmogorov turbulence Φ_n) under Taylor frozen flow is related to a phase screen at a different time $\phi(\vec{u}, t - \tau)$ via the wind speed v_{wind}. Similarly, we can then say

$$B_\phi(\vec{u}, t) = B_\phi(\vec{u} - \vec{v}_{\text{wind}}\tau, t - \tau). \tag{2.24}$$

This implies the phase covariance function at one location and time $B_\phi(\vec{\xi}, t)$ in the pupil is

related to the phase covariance function at that location at a previous time $B_\phi(\vec{\xi}, 0)$, where $B_\phi(\vec{\xi}, 0)$ is a covariance related to the Kolmogorov phase covariance function. Since we know the Kolmogorov phase covariance function is non-zero as long as turbulence is present, this demonstrates that the phase covariance function at an arbitrary location and time $B_\phi(\vec{\xi}, \tau)$ is non-zero. Even if frozen flow is violated, as long as there is non-zero space-time covariance in the pupil, we expect non-zero space-time covariance in the image, as shown in Equation 2.22.

Rearranging Equation 2.21,

$$\langle S_\phi(\vec{x}_1, t) S_\phi^*(\vec{x}_2, t-\tau)\rangle = \int d\vec{\xi} \exp(2\pi i \vec{\xi}\cdot\vec{x}_2) B_\phi(\vec{\xi}, \tau) \int d\vec{u} \exp[-2\pi i \vec{u}\cdot(\vec{x}_1 - \vec{x}_2)] P(\vec{u}) P(\vec{u}+\vec{\xi}). \quad (2.25)$$

The latter integral is the Fourier transform of the overlap of displaced pupils. Defining this function,

$$\mathcal{P}(\vec{r}, \vec{\xi}) = \int d\vec{u} \exp(-2\pi i \vec{u}\cdot\vec{r}) P(\vec{u}) P(\vec{u}+\vec{\xi}), \quad (2.26)$$

we now have the space-time covariance of speckles as the product of the turbulence phase covariance function and $\mathcal{P}$, as follows:

$$\langle S_\phi(\vec{x}_1, t) S_\phi^*(\vec{x}_2, t-\tau)\rangle = \int d\vec{\xi} \exp(2\pi i \vec{\xi}\cdot\vec{x}_2) B_\phi(\vec{\xi}, \tau) \mathcal{P}(\vec{x}_1 - \vec{x}_2, \vec{\xi}). \quad (2.27)$$

This mathematical framework illustrates how the focal plane covariance is intimately related to pupil plane covariance in the high contrast imaging regime, with a perfect coronagraph and small phase errors. Looking at the overlap of displaced pupils, $\mathcal{P}(\vec{x}_1 - \vec{x}_2, \vec{\xi})$, the form of the expression suggests that covariance will be strongest at smaller spatial separations. Similarly, Equation 2.24 suggests that covariance will be strongest at smaller temporal separations. Overall, if there is non-zero space time covariance in the pupil plane, then we

will have non-zero space time covariance in the focal plane. We will test this further with simulations, as described in Section 2.3.

2.2.3 Space-Time KLIP

Recall that KLIP improves contrast by projecting away features that are spatially correlated in image sequences. We can extend the framework of KLIP [Soummer et al., 2012] to space-time covariances by using an image sequence instead of an image. Note that for the following mathematics we assume discrete time sequences, rather than continuous as in Section 2.2.2 above. Additionally, we assume regular and continuous time sampling for this implementation; however, this method can be extended easily to block-continuous sampling, which may be useful in future work.

All variables for the following mathematics are also described in Notation Glossary A. Baseline KLIP uses an image vector of length n_{p} (number of pixels in image) as its target image and a $n_p \times n_i$ matrix as the set of reference images to determine covariance between pixels, find eigenvectors of covariance, and project out the largest eigenvalue modes from the image. Similarly, space-time KLIP (referred to as stKLIP) uses an image sequence of length $n_s \times n_{\mathrm{p}}$ (number of images in the sequence times number of pixels per image), as shown in Equation 2.28, to perform those steps. Note that this is transposed compared to KLIP, which uses $n_{\mathrm{p}} \times n_s$.

It is then necessary to create a block diagonal covariance matrix of size $n_s \times n_{\mathrm{p}}$ by $n_s \times n_{\mathrm{p}}$, as illustrated in Figure 2.1, from the mean-subtracted image sequence. Each block is the covariance at a given time lag, with the block diagonal as lag zero (spatial covariance). If only lag zero is used, the mathematics here reduces down to baseline (spatial) KLIP, as described in Section 2.2.1. Lags should be chosen based on the translation time of the smallest relevant feature within the field of view at the focal plane up to the full crossing time of the wind across the telescope aperture. This is an additional tuneable parameter to consider when optimizing the algorithm, in addition to the number of modes.

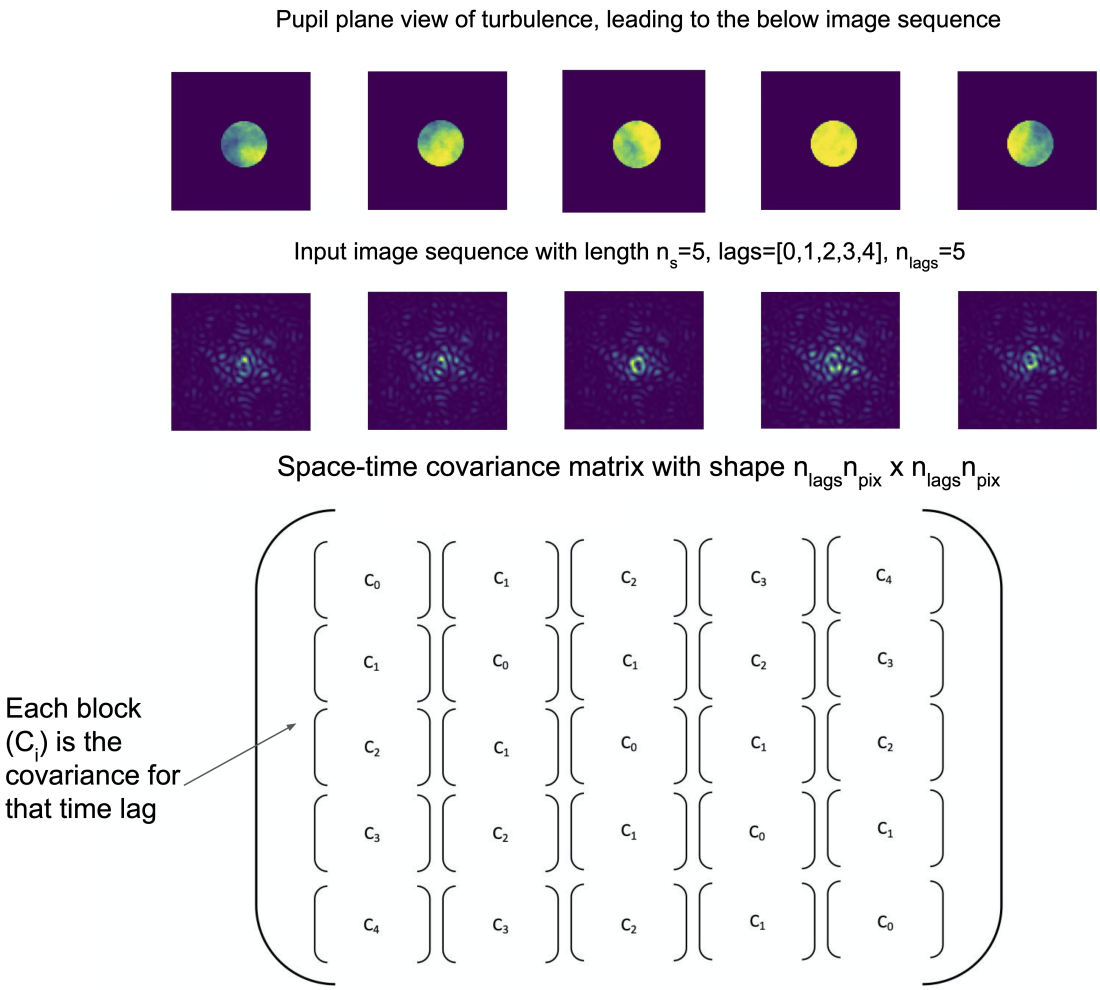

Figure 2.1: Diagram of stKLIP input sequence setup – translating phase screens (top) and resulting image sequence (middle) – with the corresponding block diagonal space-time covariance matrix (bottom). Each covariance block C_i is the covariance for a single lag, with shape $n_p \times n_p$, and together they create a single space-time covariance matrix C with size $n_s n_p \times n_s n_p$. The covariance matrix takes this form because the 2d images are flattened into 1d vectors, which are then joined to make an $n_p \times n_s$ 1d vector, which is multiplied by its transpose to create this matrix.

The following computations mirror baseline KLIP, but, in practice, are potentially more computationally expensive due to the larger size of the covariance matrix used in the eigen-decomposition. The steps of stKLIP are as follows:

1. Subtract the mean image over the whole reference set, then partition the reference set into image sequences. These image sequences have length $n_s = n_l = 2L + 1$ where L is the largest number of timesteps (lags) away from the central image and n_l is the total number of timesteps (lags) in the sequence. (The following steps will be repeated over each image sequence, such that every image, with the exception of L images at each end, is at some point the central image. Therefore, for n_i images, there will be $n_i - 2L$ image residuals at the end of this process.)

   Similarly to KLIP, the reference set/target image set S (which in this implementation are the same) are unraveled into one-dimensional vectors $\vec{s}$ of length $n_s \times n_p$, as seen below.

$$S = \begin{bmatrix} S_{1,1} & S_{1,2} & \dots & S_{1,n_p} \\ S_{2,1} & S_{2,2} & \dots & S_{2,n_p} \\ \vdots & \vdots & \ddots & \vdots \\ S_{n_s,1} & S_{n_s,2} & \dots & S_{n_s,n_p} \end{bmatrix} \tag{2.28}$$

$$\vec{s} = \begin{bmatrix} S_{1,1} \\ S_{1,2} \\ \vdots \\ S_{1,n_p} \\ \vdots \\ S_{n_s,n_p} \end{bmatrix} \tag{2.29}$$

2. Compute the $[n_s n_p, n_s n_p]$ size covariance matrix C of the image sequences. In practice, this is more straightforward when done by computing the covariance of each image pair (C_i) and then arranging them in the block diagonal ordering shown in Figure 2.1.

3. Perform an eigendecomposition on the covariance matrix, obtaining $n_s n_p$ eigenvalues ($\vec{\lambda}$) and a matrix eigenvectors (V) of size $[n_s n_p, n_s n_p]$ containing individual eigenvectors $\vec{v}$.

$$C\vec{v}_j = \lambda_j \vec{v}_j \tag{2.30}$$

$$\lambda_1 > \lambda_2 > \lambda_3 > \ldots \lambda_p \tag{2.31}$$

4. Choose a number of modes n_m, reducing the vector of eigenvalues and matrix of eigenvectors to sizes n_m and $[n_m, n_s n_p]$ respectively. The matrix of eigenvectors contains n_m rows of eigenvectors each with length $n_s n_p$, such that $V_{i,j} = (\vec{v}_j)_i$.

$$V = \begin{bmatrix} V_{1,1} & V_{1,2} & \ldots & V_{1,n_s n_p} \\ V_{2,1} & V_{1,1} & \ldots & V_{2,n_s n_p} \\ \vdots & \vdots & \ddots & \vdots \\ V_{m,1} & V_{m,2} & \ldots & V_{n_m,n_s n_p} \end{bmatrix} \tag{2.32}$$

5. Obtain image coefficients through inner product of chosen eigenvectors and image sequence, similar to Equation 2.10.

$$\vec{q} = V \cdot \vec{s} = \begin{bmatrix} q_1 \\ q_2 \\ \vdots \\ q_{n_m} \end{bmatrix} \tag{2.33}$$

6. Project the image sequence back into pixel space to obtain a reconstructed sequence $\hat{\vec{s}}$ with central image $\hat{\vec{\psi}}_k$, again mirroring Equation 2.11. Note: For ease of implementation, we have calculated the entire sequence, but projecting only onto the central image may improve efficiency.

$$\hat{\vec{s}} = \vec{q}^T \cdot V \tag{2.34}$$

$$\hat{\vec{\psi}}_k = [\hat{\vec{s}}_{n_p((n_l+1)/2-1)} \ldots \hat{\vec{s}}_{n_p(n_l+1)/2}] \tag{2.35}$$

7. Perform PSF subtraction using the central image.

$$\epsilon\vec{a}_k = \vec{s}_k - \hat{\vec{\psi}}_k \tag{2.36}$$

8. Iterate through the above steps such that each image is the central image of a sequence of length n_s, resulting in a set of residuals $\epsilon\vec{a}_{k,j} = [\epsilon_0\vec{a}_{k,0}, \epsilon_1\vec{a}_{k,1}, \ldots, \epsilon_{n_s}\vec{a}_{k,n_s}]$.

9. Compute mean of image sequence residuals to output an averaged residual, $\vec{r}_{k,\text{avg}}$.

$$\vec{r}_{k,\text{avg}} = \frac{1}{n_s}\sum_{j=0}^{n_s}\epsilon_j\vec{a}_{k,j} \tag{2.37}$$

Once our image sequence is projected into the new subspace in Step 6, we have two options for PSF subtraction: subtract the residuals from the whole sequence used, or subtract only from the central "target" image. We use a central target image to take advantage of speckle motions in timesteps both before and after. We then iterate through the full data set, as described in Step 8, performing stKLIP and PSF subtraction, so that each image is the central image of some image sequence with length $n_s = n_l = 2L+1$. This outputs a sequence of image residuals that is of length $n_i - 2L$. In Step 9, we then average over the number of timesteps to output an averaged residual.

There are possibilities for improving the algorithm, such as by exploiting the symmetry in the covariance matrix C in order to hasten the process of updating the eigenimages; however, we leave this for future work. Further improvements are discussed in Section 2.5.

2.3 Algorithm Development

In Section 2.2.2, we showed that we expect non-zero space-time covariance to exist in speckle noise. In Sections 2.2.1 and 2.2.3, we showed the mathematical framework for an algorithm to exploit these statistics for image processing and PSF subtraction.

In this section, we illustrate aberrations of increasing complexity to examine their covariance structure and test the application of stKLIP. These tests and simulations are described

in 2.3.1, for initial proof of concept. Section 2.3.2 describes the algorithm application to simulated data and calculations of possible contrast gains in the algorithm's current form; here we also discuss selection criteria for the choices of number of modes and lags. Analyzing these data sets also requires some computational optimization, which is described in 2.3.3. In the following Section 2.4, we will discuss the results of these applications of stKLIP.

2.3.1 Foundational Tests

Our first step was to create and implement simple test cases in one and two dimensions to demonstrate that our theoretical expectations from Section 2.2.2 are valid and ensure that our algorithm reduced image variance as expected. A one-dimensional case allows us to directly compare a simulated covariance matrix with one calculated from the analytic theory in Section 2.2.2, serving as a test of the relationship between pupil plane covariance and focal plane covariance. Then, a two-dimensional case serves as a first in implementing the algorithm, ensuring that the algorithm reduces variance on a well-understood simple case before moving onto more complex atmospheric simulations.

2.3.1.1 One-Dimensional Test of Pupil/Focal Covariance Relationship

To begin, we created a simple one-dimensional model of two interfering speckle PSFs, which are simply two sinusoids with slightly different frequencies in the pupil plane. We first use this simple sinusoidal model to compare the simulated space-time covariance to the predicted behavior from theory, to show how a set of input aberrations in the pupil plane corresponds with the resulting focal-plane space-time covariance. Although the algorithm does not require pupil plane covariances, this test is done to further establish the existence of the focal plane covariances that we seek to harness.

To create the 1-d speckle model, first we must create a grid setup for evaluating the wavefront in the pupil and focal planes. These are parameterized in units of D/λ and

λ/D respectively, where λ is our wavelength of observation, assuming monochromatic light. Keeping these units preserves the Fourier duality relationship, and they can be converted to more conventional units if the focal length is known.

The next critical piece is to define the entrance aperture in the pupil plane. This pupil function sets the amplitude A of the electric field ($E = Ae^{i\phi}$), and is simply a top-hat function ($\Pi(u)$, 1 inside a given region and 0 outside). We also apply a translating phase screen (shown in the top panel of Figure 2.2) to the pupil, which is where phase aberrations are accounted for. We use a simple perturbation of two superimposed sinusoids with similar periods/frequencies, so that the wings of their PSFs overlap. This set-up is like simulating one layer of frozen flow translating across the telescope's aperture. These perturbations are small ($\ll 1$ radian), consistent with the high-contrast regime.

We then perform the necessary Fourier transform to retrieve the focal-plane electric field. By doing this for the pupil function with no perturbations, we retrieve what we would see in an ideal case for a uniformly illuminated pupil; this is also what would be blocked if we had a perfect coronagraph. We subtract this "perfect" case from the case with the sinusoidal perturbation, performing the action of the coronagraph and suppressing light from the unaberrated portion of the wavefront.

A one-dimensional case (Figure 2.2) illustrates the relative evolution of two neighboring speckles created from atmospheric perturbations. Atmospheric theory (as in Section 2.2.2), in particular the frozen flow assumption, predicts a symmetrical space-time covariance structure, which can be computed for a 1-d model with a top-hat pupil function ($\Pi(u)$), two sinusoidal functions in the pupil, and no uniform illumination in the pupil ($C(x) = 0$). We carried out these calculations in two ways. First, we solved the integrals in Section 2.2.2 for the simple two sinusoid situation using Fast Fourier Transforms (FFTs). Second, we began with an array describing the sinusoidal "phase screen" and simulated propagation through an optical system using FFTs.

The variation in pupil and focal plane covariance over various time lags, as shown in

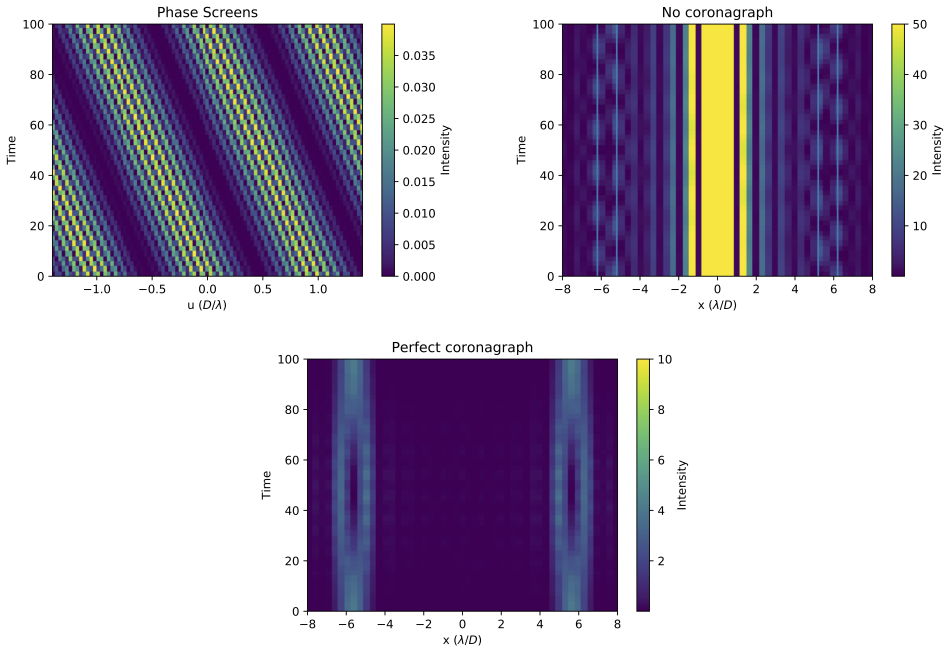

Figure 2.2: One-dimensional demonstration of speckle interference. Two sinusoidal perturbations in the pupil plane interfere to create moving speckles in the image plane. Top: 1d phase screen with interfering sinusoids over time. Middle: 1-d intensity over time without a coronagraph, showing the Airy pattern. Bottom: 1-d intensity over time with a coronagraph, with the speckles' relative evolution appearing more clearly due to the lack of coherent light, $C(\vec{x})$. This simulation is used as a test of the space-time speckle covariance theory in Section 2.2.2.

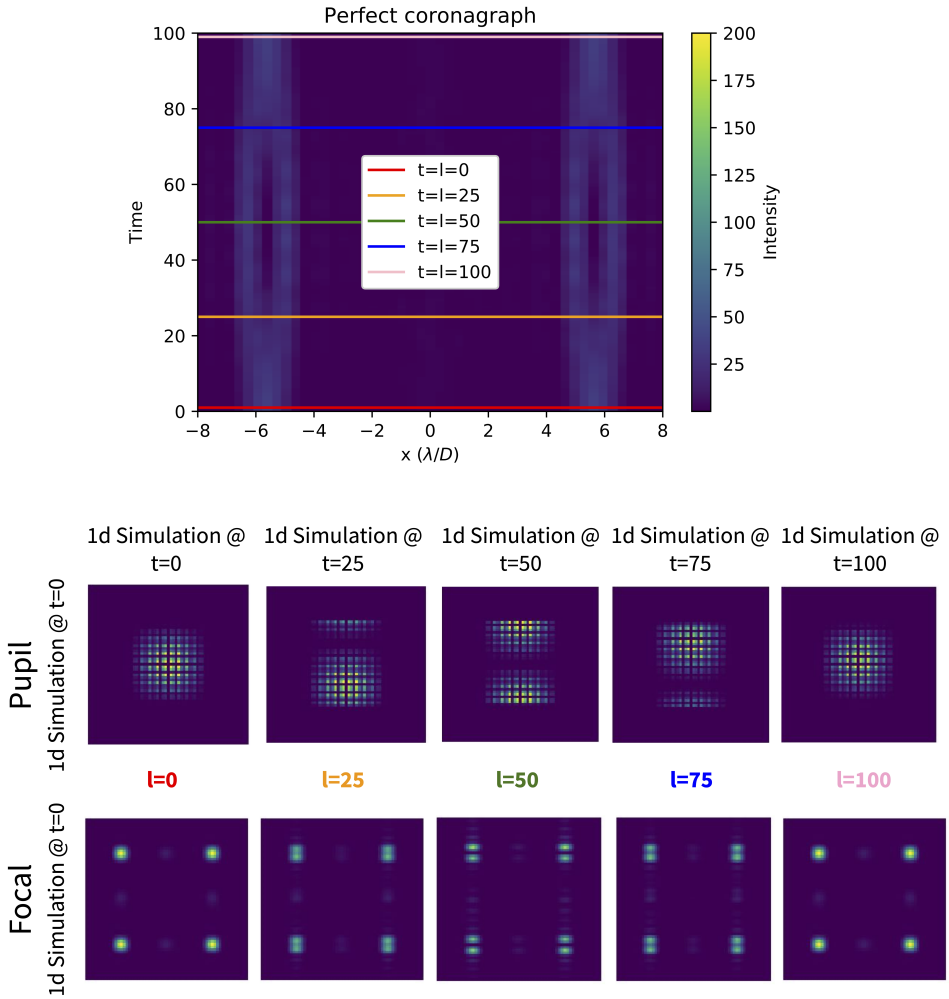

Figure 2.3: Space-time covariance matrices for pupil plane (middle) and focal plane (bottom) of a 1-d model of two sinusoids with different frequencies – as illustrated in the top panel of Figure 2.2 – with an annotated view of the simulation (top). These matrices show a symmetric pattern that changes with the number of lags used, due to the change in the speckles' relative locations. At lags 0 and 100, the peaks are due to the alignment of the speckles' peaks, as marked in the top panel; lag 25 illustrates the lower covariance when the speckles are in slightly different places, and lag 50 shows two lower intensity peaks when the speckles are separated. Importantly, for a given non-zero lag, there are non-zero terms, indicating that there are temporal correlations.

Figure 2.3, can be clearly interpreted based on the locations of the two interfering speckles. These matrices show a symmetric pattern that changes with the number of lags used, due to the change in the speckles' relative locations. At lags 0 and 100, the peaks are due to the alignment of the speckles' peaks, as marked in the top panel; lag 25 illustrates the lower covariance when the speckles are in slightly different places, and lag 50 shows two lower intensity peaks when the speckles are separated. Importantly, for a given non-zero lag, there are non-zero terms in both the pupil and focal plane covariances, indicating that there are temporal correlations.

This simulation further demonstrates the claim that a simplified frozen flow scenario in the pupil can create calculable space-time covariances in the focal plane, and validates our use of this simple test case to test stKLIP.

2.3.1.2 Two-Dimensional Test Case for Algorithm Development

In order to ensure that the algorithm is behaving according to our expectations – that it will reduce the image variance – we expand this one-dimensional test case into two-dimensions to make an image sequence of the two time-varying, interfering speckles. We use this idealized test case as a check against our expectations for our stKLIP implementation, and for a first test of efficacy, comparing the reduction in image variance between three data processing methods: mean-subtraction, KLIP, and stKLIP. The setup is the same as the above one-dimensional test case, but in two dimensions, with a circular aperture instead of a top hat as the pupil function. We create a series of images at various time steps as the input to stKLIP, shown in Figure 2.4.

Although there are two tuneable parameters for stKLIP — number of modes (e.g. number of eigenimages used in the projection) and number of lags, as described in Sections 2.2.1 and 2.2.3 — we only test one set of modes and lags (10 modes, 2 lags) with this simple test case and leave further exploration of these parameters for later testing (see Section 2.3.2). We similarly use 10 modes for KLIP to make the comparison fair.

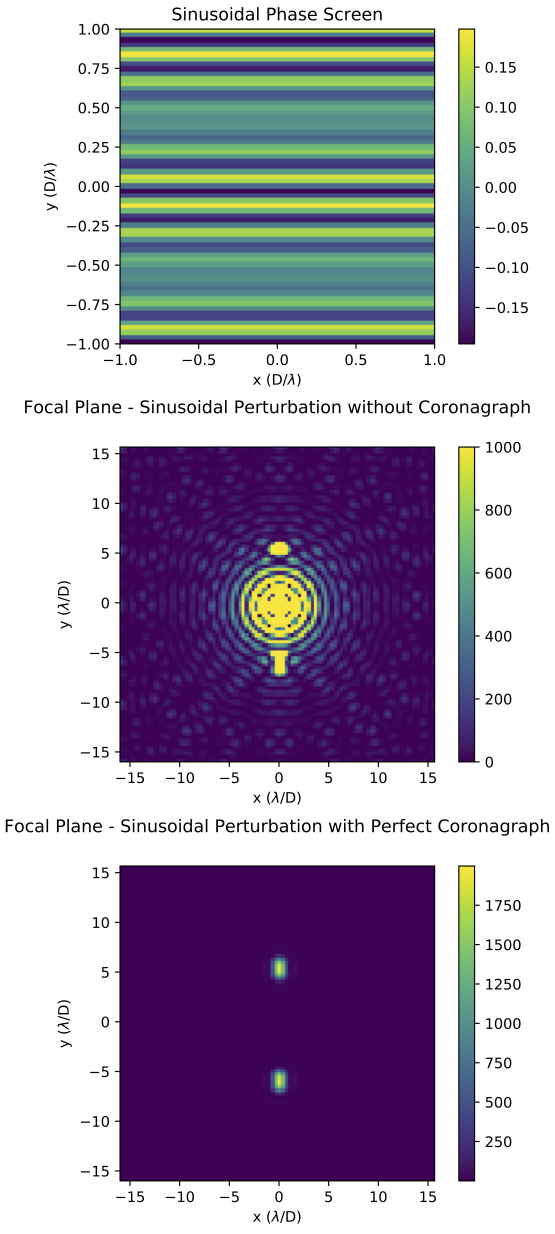

Figure 2.4: Two-dimensional test of speckle interference. A sinusoidal phase screen (top) produces a speckle pattern imposed on an Airy disk (middle). Subtracting the PSF of a model without perturbations, we simulate observations of this sinusoidal perturbation with a "perfect" coronagraph (bottom). All images depict the intensity ($I = |E|^2$). This simulation is used as a troubleshooting step for a first implementation of the stKLIP algorithm.

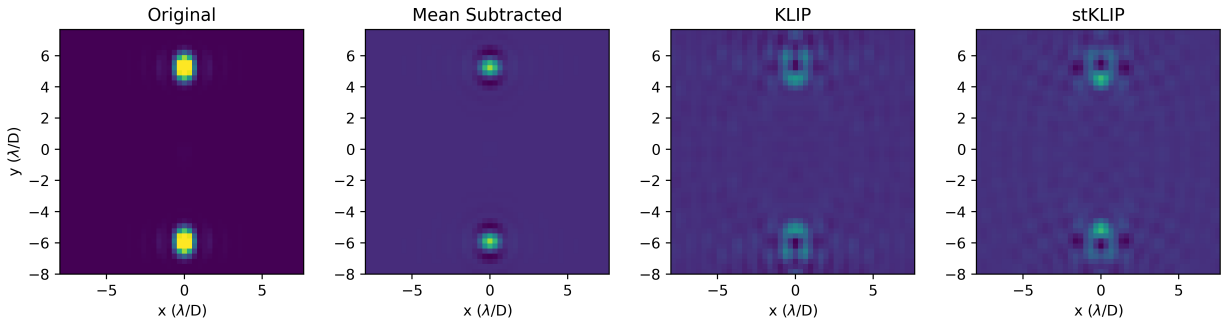

Figure 2.5: One frame of the input sequence (left) for the simple two-sinusoid test case with a coronagraph, with the residuals after PSF subtraction using mean-subtraction, KLIP, and stKLIP, showing a clear reduction in speckle intensity. Both stKLIP and baseline KLIP reduce image variance by a factor of at least 5.7 from the original image, an improvement over simple interventions like mean-subtraction. Although stKLIP does not improve upon KLIP in this limited test case, it is important to remember that we have not optimized for modes and lags in this scenario; this step was intended for troubleshooting, not rigorous characterization of the algorithm.

In this simple test case, KLIP and stKLIP reduce the variation in the image by factors of 6.8 and 5.7, respectively. Although stKLIP does not improve upon KLIP in this limited test case, it is important to remember that we have not optimized for modes and lags in this scenario; determination of performance is left for more rigorous and realistic tests in the following section, 2.3.2. They both outperform simple interventions, such as subtracting the mean of the image, in reducing the total variation in the image, as shown in Figure 2.5. To summarize, this 2d test was performed to demonstrate that the overall image variance decreases after projecting out modes of variation with stKLIP, as qualitatively expected, and in that sense the test can be considered successful.

2.3.2 Simulated AO Residual Tests

We then wanted to test stKLIP on a more realistic atmospheric phase screen and again measure potential contrast gains. To this end, we created a set of simulated observations to represent AO residuals and performed stKLIP on them for a variety of different modes and lags. We measure contrast curves and companion SNR for four methods of post-processing in order to understand the effectiveness of our new method: stKLIP, baseline/spatial KLIP, mean-subtraction, and no post-processing. Results from these tests are described in Section 2.4 and discussed further in Section 2.5. In this section, we first detail the methods used to create the simulated data set, then the methods for computing contrast curves and SNR on the processed data.

To create the simulated data set, we use a simulator specifically designed for high-contrast imaging with next-generation detectors, such as MKIDs, called `MEDIS` (the MKID Exoplanet Direct Imaging Simulator), the first end-to-end simulator for high contrast imaging instruments with photon counting detectors [Dodkins, 2018, Dodkins et al., 2020].

`MEDIS` generates atmospheric phase screens with `HCIPy` [Por et al., 2018]. These phase screens use models of Kolmogorov turbulence, and we use the simplest option of a single frozen flow layer. Then, `MEDIS` uses `PROPER` to propagate the light through the telescope under Fresnel diffraction, including both near- and far-field diffraction effects [Krist, 2007]. Separate wavefronts are propagated for each object in the field — the host star, and any companion planets. `MEDIS` also includes options to introduce coronagraph optics, aberrations (like non-common path errors), and realistic detectors. `MEDIS` outputs the electric field or intensity at specified locations in the optical chain, such as the pupil and focal planes in our case, as shown in Figure 2.6.

Given the wide range of parameters available in `MEDIS`, we had to make decisions on what to use for the `MEDIS` simulations used to test stKLIP. For these simulations, we implement a telescope with 10 meter diameter, similar to the Keck Telescopes. We begin with a case

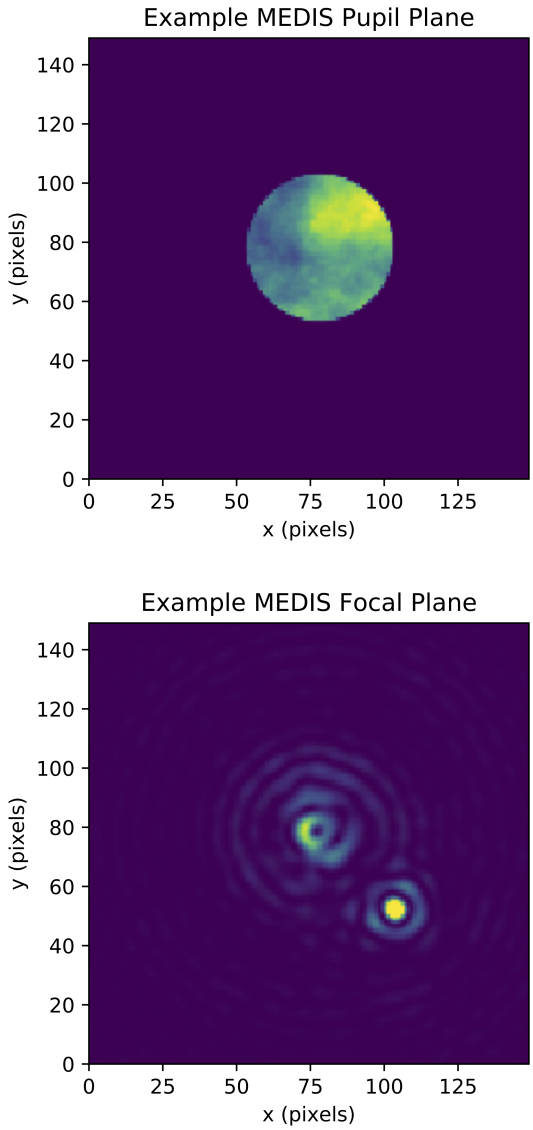

Figure 2.6: Examples of MEDIS simulations. (Top) Pupil plane, illustrating the phase screen. (Bottom) Focal plane, with a clearly bright companion object. These simulations are used as a preliminary test of stKLIP's efficacy and potential; however, there is a large parameter space to explore beyond the scope of this work.

without adaptive optics for simplicity. For this, the sampling rate needs to be a few milliseconds, a few times oversampled compared to the smallest temporally resolvable features given the field-of-view (FOV) under consideration. The number of frames is chosen to create a total observation time of 30 seconds (6,000 frames at 0.005 second sampling) to recreate a realistic observation and attain a sufficient number of independent samples. The grid size is significantly larger than the area of interest (256 $\times$ 256 pixels) to avoid edge effects. However, we choose a region size / FOV that is significantly smaller than our whole grid (100 $\times$ 100 pixels) to make this problem more computationally tractable.

The simulation includes atmospheric parameters, such as the Fried Parameter (r_0), a length scale for coherence in the atmosphere, and the structure constant (C_n), a description of turbulence strength over multiple atmospheric layers. The atmospheric model we use is a simple single layer of extremely mild Kolmogorov turbulence, with $r_0 > 10$ m, since we want $r_0 \gg D$ to stay in the high-contrast regime of small phase errors. Note: this simulated atmosphere is not realistic in ground-based imaging, but we chose these parameters to approximate the high-contrast regime without simulating adaptive optics and introducing additional parameters. While our numerical experiments will depend on the input power spectrum, our primary aim was to assess the characteristics of a second-order statistical analysis of the linearized system (Equation 2.13), rather than impacts of the particulars of the wavefront error power spectrum. It is worth exploring how different atmospheric conditions (e.g. a smaller r_0 value) would change the effectiveness of this method, but that is beyond the scope of this initial investigation.

We choose a vortex coronagraph [Mawet et al., 2009], since it is the closest to an "ideal" coronagraph of the options available in `MEDIS` (e.g. closest to perfect cancellation of the spatially coherent wave), thanks to its small inner working angle [Guyon et al., 2006]. We want an ideal detector since, for this initial investigation, we are not yet interested in how detector noise/error affects this method. We also include one companion object that would be readily detectable given current capabilities (a contrast of 5×10^3), in order to enable

SNR measurements of an injected companion for various post-processing methods including stKLIP. As mentioned in Section 2.2.2, lags should be chosen based on crossing times and relevant features. In these simulations, this ranges from 2 to 10 timesteps (0.01 to 0.05 seconds) for a wind speed of 5 m/s and 5 millisecond sampling. Future work should test a further range of lags, up to 400 timesteps (2 seconds, or one full crossing time), but our current method is computationally limited as mentioned in Section 2.3.3. In this investigation, we also test a range of modes from 1 to 500.

Although these simulations are computationally expensive, `MEDIS` is capable of parallel processing, except in cases where AO parameters require serialization. We take advantage of this capability by using UCLA's Hoffman2 Cluster. The resultant data sets are quite large, and require inventive ways of computing the necessary statistics without loading the full array into memory, described further in Section 2.3.3. These simulations show us how realistic space-time covariance differs from the idealized case, and allow us to begin to test the effectiveness of our new method.

Metrics of efficacy used in this study are measurements of variance, signal, noise, signal-to-noise ratios (SNR), and contrast curves. Variance is simply computed over the whole 100×100 pixel residual image using `numpy.var`. Signal is computed using aperture photometry (via `photutils`), centered on the simulated companion. Noise is similarly computed using aperture photometry by taking the standard deviation of a series of apertures in an annulus at the same separation as the simulated companion. SNR is then the ratio of these two measurements. Contrast curves are estimated using aperture photometry at various distances from the image center and dividing by the aperture photometry measurement of the unmasked (e.g. no coronagraph) peak, then adjusting by the signal throughput; the throughput here is estimated as the signal after processing divided by the signal before data processing. These various metrics are computed for the original images, as well as different post-processing scenarios, to understand the relative efficacy of stKLIP. Results are described in Section 2.4.

2.3.3 Iterative Statistics Calculations

There are two key computational challenges for large data sets such as those produced by `MEDIS`: memory access and computational complexity. Simulations with `MEDIS` for a realistic observing sequence based on our criteria above can be on the order of 100GB, which can pose challenges to RAM-based manipulation for the calculation of mean and covariance given our current computing resources. To address this problem, we implemented the framework for iterative statistics calculations set forth in [Savransky, 2015].

In order to perform a KLIP-style calculation, we first need to compute second-order statistical quantities for a data set of n samples $\vec{x}_i$, such as the mean and covariance. The formula for the calculating mean is:

$$\vec{\mu} \equiv \frac{1}{n}\sum_{i=1}^{n}\vec{x}_i \tag{2.38}$$

When the mean μ is estimated from the data, the sample covariance can be calculated as follows:

$$C \equiv \frac{1}{n-1}\sum_{i=1}^{n}(\vec{x}_i - \vec{\mu})(\vec{x}_i - \vec{\mu})^T. \tag{2.39}$$

These sums can be broken up into smaller iterative steps k, to make the calculation less memory intensive. For each step k, the mean can be updated with the formula

$$\vec{\mu}_k = \frac{(k-1)\vec{\mu}_{k-1} + \vec{x}_k}{k} \tag{2.40}$$

and the covariance can be updated by

$$S_k = \frac{k-2}{k-1}S_{k-1} + \frac{k}{(k-1)^2}(\vec{x}_k - \vec{\mu}_k)(\vec{x}_k - \vec{\mu}_k)^T. \tag{2.41}$$

However, Equation (2.41) is only applicable to the spatial covariance, e.g. a time lag of zero. The space-time covariance can be calculated as

$$S_l = \frac{1}{n-l-1}\sum_{i=1}^{n}(\vec{x}_i - \vec{\mu})(\vec{x}_{i-l} - \vec{\mu})^T. \tag{2.42}$$

Following a similar protocol to [Savransky, 2015], we derived an update formula for the space-time covariance:

$$S_l = \frac{1}{n-l-1}\left[\sum_{i=l}^{n}\vec{x}_i\vec{x}_{i-l}^{T} - (n-l)\vec{\mu}\vec{\mu}^{T} + \vec{\mu}^{T}\sum_{i=1}^{l-1}\vec{x}_i + \vec{\mu}\sum_{i=n-l-1}^{n}\vec{x}_i^{T} - 2l\vec{\mu}\vec{\mu}^{T}\right] \quad (2.43)$$

It is identical to Equation (2.41), except for the last 3 additional cross-terms. These cross-terms were directly calculated and determined to be negligibly small as the sample size becomes large relevant to the maximum lag, and thus would only be relevant in edge cases. For 1,000 samples, the error on the space-time covariance calculation is on the order of 10^{-4}% or less. For 10,000 samples, the error decreases to 10^{-6} to 10^{-7}%, indicating a trend of decreasing error for an increasing number of samples. We do not plan to use fewer than 1,000 samples in a data set, so we consider this approximation to the space-time covariance acceptable and have implemented it for the tests described in Section 2.3.2.

Although the mathematics laid out in this section make covariance calculations possible, the resulting covariance matrices can be quite large, on the order of 10GB for even short test cases with small FOVs. Even with sufficient RAM for manipulation, these large covariance matrices can lead to long computation times for following steps of the algorithm. The image size and sequence length of data sets used in our stKLIP method is therefore still currently limited by memory requirements and prohibitively long execution times. This is mostly due to the eigendecomposition calculations, since the full space-time covariance matrix needs to be loaded into memory for input into `scipy.linalg.eigh`. As we proceeded with larger data sets, we chose to perform a standard eigendecomposition with `scipy.linalg.eigh` using the default backend (C LAPACK `evr`) but limited the maximum number of eigenvalues/eigenvectors computed, since many of the smaller eigenvalues only capture noise and are not necessary for this process. There may be more optimal choices for the eigendecomposition algorithm, but such optimization is left for future work.

Another possible solution to mitigate this bottleneck would be using an iterative eigendecomposition. This could theoretically be done with the NIPALS (Nonlinear Iterative Partial

Least Squares) algorithm [Risvik, 2007]. However, applying the NIPALS algorithm is not straightforward for this problem; our space-time covariance matrix is currently assembled from various spatial covariance matrices, and considerable changes would need to be made to NIPALS to accommodate a space-time calculation instead of a solely spatial one, since the NIPALS algorithm relies on a data matrix as input instead of a covariance matrix. Future iterations of this algorithm could also make use of the `dask` package for parallelization of computations to help speed up run time, but as of this writing an eigendecomposition function (e.g. `dask.linalg.eigh`) was not yet implemented, although the similar `dask.linalg.svd` function could possibly be used. We leave such improvements in efficiency for future work.

2.4 Algorithm Performance on Simulated AO Residual Data

We have confirmed through theory (§2.2.2) and simulation (§2.3.1) that space-time covariances exist for speckles in a simple high-contrast imaging system in the regime of small phase errors and short exposures. In Section 2.2.3, we defined a new algorithm, similar to Karhunen-Loeve Image Processing, to take advantage of space-time covariances and improve final image contrast, with the eventual goal of detecting fainter companion objects. As shown in Section 2.3.2, we have developed an initial implementation of this space-time KLIP (stKLIP) algorithm, and demonstrated it on simulated data. In this section, we present the results of those demonstrations. It is worth noting that these tests on simulated data only explore a small range of parameter space, and are not indicative of the absolute potential of using space-time covariance in data processing. Instead, we present this as a first proof-of-concept for the possibility of this new method.

An example of the images input to and output by the stKLIP processing algorithm is shown in Figure 2.7, along with a comparison to two other data processing interventions, mean-subtraction (as in Equation 2.3) and KLIP. For this simulated data, mean-subtraction makes such a slight improvement that in the following figures we omit it from comparison

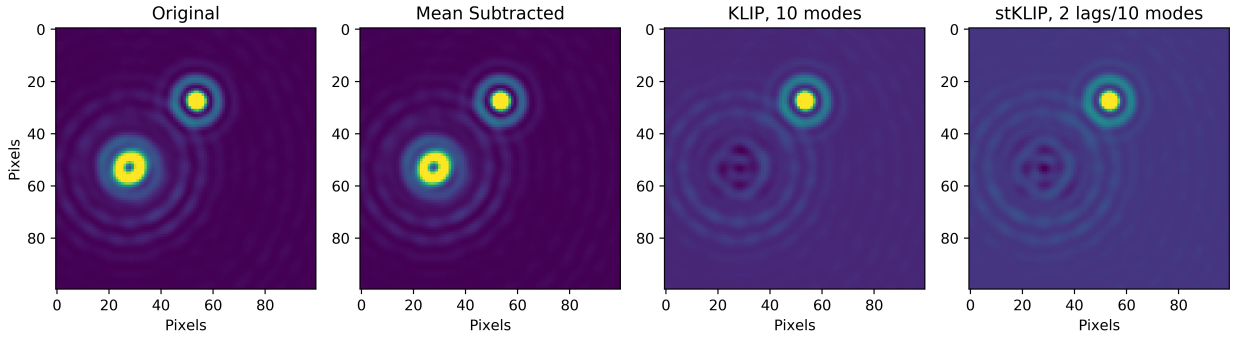

Figure 2.7: One frame of the input sequence (left) from `MEDIS`, with the residuals after PSF subtraction using mean-subtraction, KLIP, and stKLIP. Both stKLIP and baseline KLIP reduce image variance by a factor of ∼1.85 from the original image for the listed case of 10 modes and 2 timesteps lag in stKLIP.

plots, as it would be almost precisely coincident with the original image's metrics.

To quantitatively measure the efficacy of our stKLIP data processing algorithm, we computed total image variance, signal-to-noise ratios, and approximate contrast curves, as described in Section 2.3. To further determine the utility of this algorithm and characterize its dependence on the tuneable parameters, we also investigated the relationships between these efficacy metrics, the number of KL modes used, and the number of stKLIP lags used. We leave adjustments of the residual wavefront error statistics and companion location, among other parameters, and their effects on stKLIP's efficacy for future work.

Image variance is a primary metric for subtraction efficiency. Total image variance is reduced by almost half for both spatial / baseline KLIP and stKLIP within the first 10 modes, and variance approaches 0 around 50 modes. In this test, spatial and stKLIP are similar in their variance reduction abilities, and are both improvements on mean-subtraction and the original image. Image variance drops off steeply within the first 20 modes, indicating that most of the power is removed with only a few eigenimages required in the reconstruction. Given that only a small number of modes are required to remove the majority of the variance

in the image, future applications of this algorithm could exploit this fact to reduce the computational burden by only calculating the first n eigenvalues/eigenimages.

For both KLIP and stKLIP on these simulated data, signal starts to be lost around 5–10 modes and drops off more steeply after ∼30 modes. Space-time KLIP with 4, 5, 6, or 8 lags in this scenario shows a slight edge over baseline KLIP in signal retention, as shown in Figure 2.8. It is worth noting that the choice of optimal number of lags depends on the wind speed and region in the image that we are most interested in. Recall from Section 2.3.2 that this test uses $v = 5\,\mathrm{m/s}$, and the companion location can be seen in Figure 2.7. Noise reduction capabilities appear very similar between KLIP and stKLIP; after about 40–50 modes, so much of the image has been removed that noise approaches zero and shows small random fluctuations, indicating that these higher modes contain less information.

Signal-to-noise ratio (SNR) shows a 10–20% improvement over the original image within the first 40 modes, as shown in Figure 2.9. The 2nd peak in Figure 2.9 is possibly due to small number statistics (most of the signal has been removed by then) and not a real SNR improvement. It is worth noting that the SNR shown here could improve significantly if a method is implemented to retain signal and improve throughput, which we discuss more in the following section. We again see that there is a slight advantage for certain lags over spatial (lag=0) KLIP on the order of a few percent, indicating that there is possibility for properly tuned stKLIP to outperform KLIP.

Contrast curves (as shown in Figure 2.10) similarly show potential for up to 50% improvement depending on the number of modes, lags, and region of the image. Within 20 pixels, we see potential for up to 400% improvement, but with the caveat that this close to the coronagraphic mask, measurements of SNR and contrast are less reliable. A slight spread in the contrast curves for various lags, such as that seen around 30–40 pixels for 5 modes in Figure 2.10, indicates that it is necessary to strategically choose the number of lags used in stKLIP depending on the image region in which we want to optimize contrast. We will discuss these results and future work further in the following section.

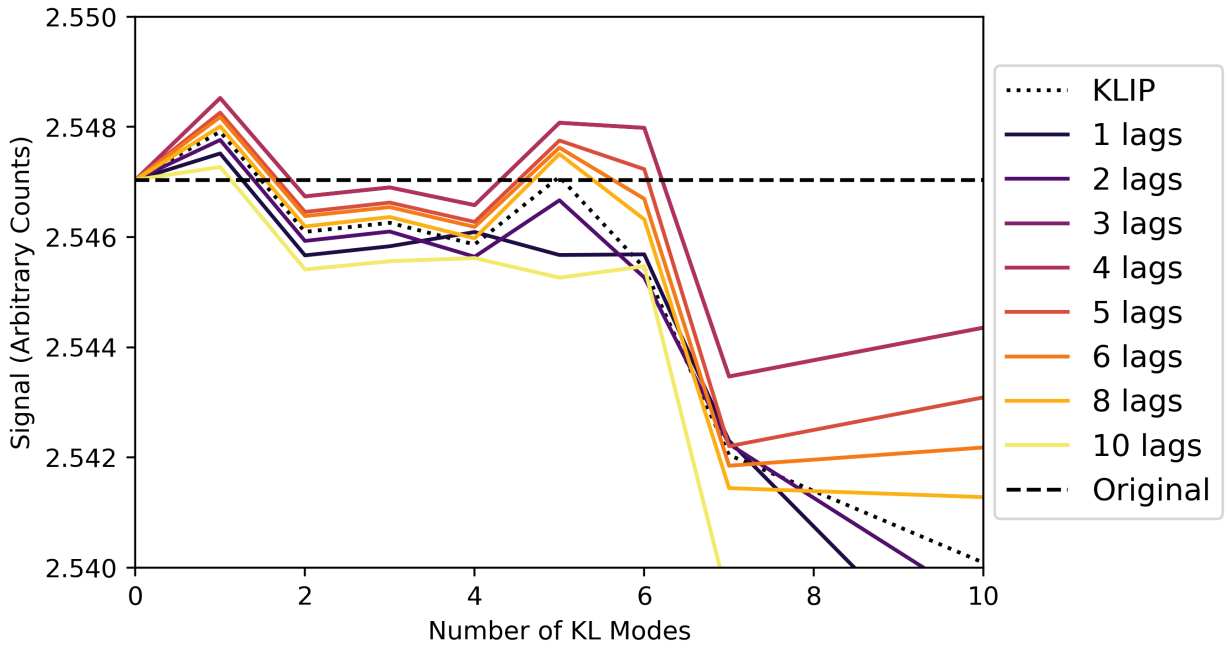

Figure 2.8: Companion signal over number of KL modes used in the model PSF subtraction; this figure shows that signal loss begins around 5 modes, indicating that future iterations of this algorithm would benefit heavily from implementing measures to prevent self-subtraction. Certain choices of lag (4, 5, 6, 8) show a minor improvement in signal retention over spatial (lag = 0) KLIP.

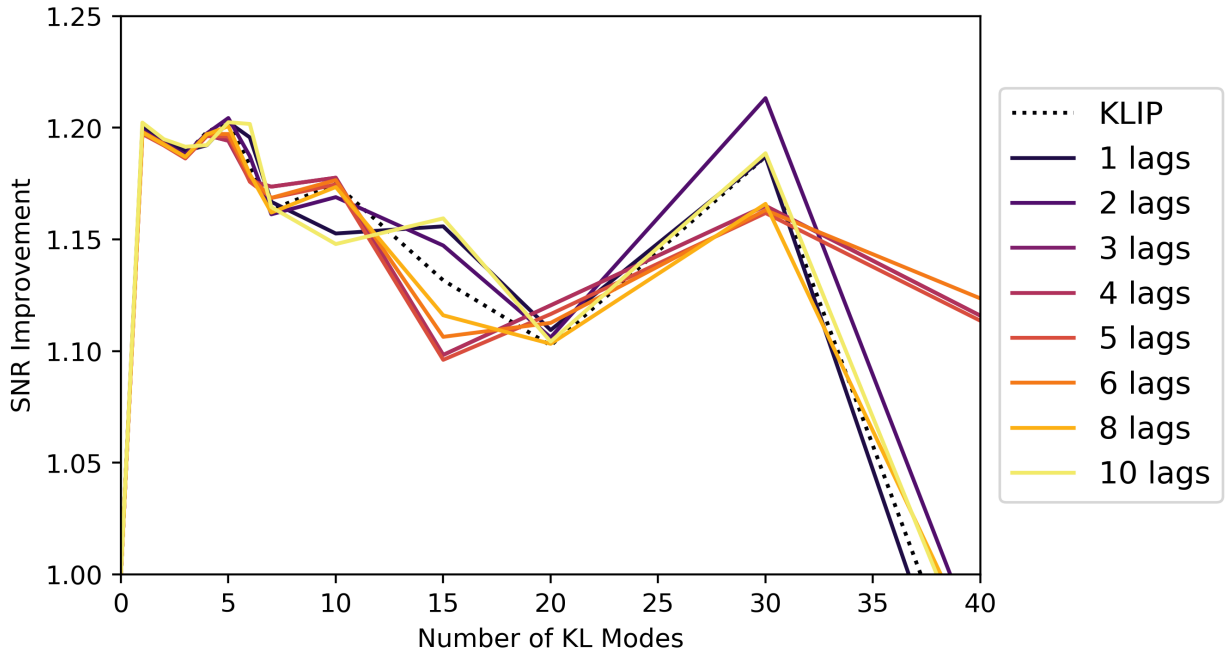

Figure 2.9: Companion signal-to-noise ratio (SNR) compared to the original image SNR over number of KL modes used in the model PSF subtraction; this figure shows a 10–20% improvement over the original image using stKLIP and KLIP, with stKLIP having a slight edge (on the order of a few percent) for certain choices of lag.

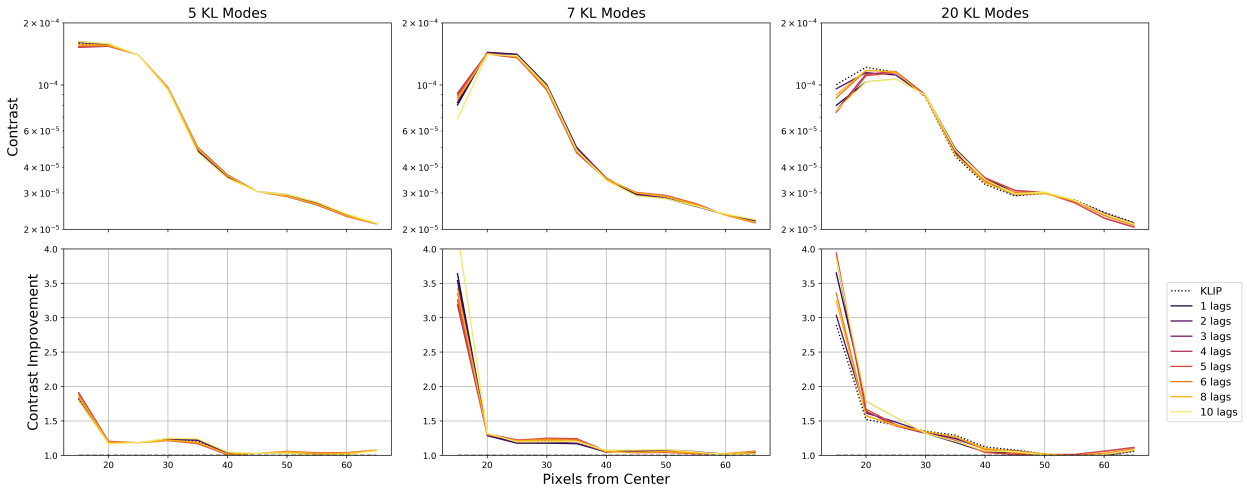

Figure 2.10: Contrast curves, as well as contrast improvement (a comparison to the original image's contrast curve), for three cases of KL modes: 5, 7, and 20. Each shows results for the image processed with baseline KLIP (0 lags) as well as stKLIP with a variety of lags. stKLIP is consistent with KLIP improvements, and in certain regions may show improvements depending on number of lags used.

2.5 Discussion

Overall, our tests on simulated data (Section 2.4) show that there is a demonstrated contrast gain (or equivalently, SNR improvement) of at least 10–20% from the original image using stKLIP with fewer than 40 modes. There is also evidence that stKLIP provides a slight advantage over spatial-only KLIP for certain choices of number of lags, number of modes, and location in image. However, the real potential for this method will be unlocked when the technique is safeguarded against self-subtraction and demonstrated on real data.

In this section, we first discuss how well the signal is retained for this new algorithm, and possibilities for future improvements to better avoid self-subtraction and retain signal in Section 2.5.1. Next, we discuss the relationship between the lag parameter and the optimized region of the target image in Section 2.5.2. Then we consider the addition of quasi-static speckles to our currently idealized, only atmospheric speckle regime in Section 2.5.3. Lastly, we propose other considerations for future work and implementations of this algorithm in Section 2.5.4.

2.5.1 Signal Retention

The signal clearly decreases beyond ∼5 KL modes as shown in Figure 2.8, indicating that we are not only subtracting from the noise but also the companion (known as self-subtraction). If we can find a way to reduce this self-subtraction and retain signal, we could potentially further improve the contrast gain. This could possibly be accomplished by masking the location of the planet or excluding regions with high spatial covariance but low temporal covariance, but further development is needed to enable this functionality. Depending on the masking implementation, this data processing method could be used for blind searches or characterization observations. In fact, it may be particularly suited to characterization observations due to the dependence on a specific image region from the nature of atmospheric speckles.

Based on previous work on LOCI (Locally Optimized Combination of Images) [Lafreniere et al., 2007, Marois et al., 2014, Thompson and Marois, 2021], we can expect additional contrast gains once masking is implemented. Additionally, there are other techniques used for KLIP to differentiate between signal and speckles, such as angular differential imaging (ADI, [Marois et al., 2006]), spectral differential imaging (SDI, [Marois et al., 2005]), and reference differential imaging (RDI, [Marois et al., 2003]). Similar efforts to increase the distance between the signal and the noise in the eigenimages may be useful for stKLIP.

Additionally, when the number of lags is zero, stKLIP simply reduces to baseline KLIP [Soummer et al., 2012] as mentioned in Section 2.2.3, and we have included spatial-only/baseline KLIP as a comparison for stKLIP in our analyses. It is worth noting, however, that KLIP is typically used on long-exposure images, a different regime than that for which stKLIP is useful. Additionally, we are comparing stKLIP to KLIP with no self-subtraction mitigation. Most current implementations of KLIP, such as pyKLIP [Wang et al., 2015], do have some sort of self-subtraction mitigation or method to increase spatial diversity implemented, such as forward modeling, angular differential imaging, or spectral differential imaging [Pueyo, 2016, Marois et al., 2006, Vigan et al., 2010]. Therefore, in practice, KLIP would currently have a significant advantage over stKLIP as implemented in this work. However, future work can adapt many of the existing methods and techniques from KLIP to improve the implementation of stKLIP and its resulting performance.

2.5.2 Optimization for Lags and Image Region

Despite KLIP's apparent advantages, it appears that, depending on the number of lags used and the location in the image, stKLIP can outperform KLIP by a few percent without self-subtraction implemented for either case as is done in our test. This is evident in Figure 2.10, showing detail of the region with highest contrast gain (other than near the central mask). The region of highest contrast gain will vary depending on the chosen lag as well as the atmospheric conditions creating the speckles in question. Optimization of input parameters

is a notoriously tricky problem for KLIP [Adams et al., 2021], and it appears stKLIP is subject to the same challenges.

The variation of optimal lag and image region is due to the relationship between the wind speed and spatial frequency, since wind speed and telescope diameter combine to determine the crossing time for one cycle of the spatial frequency as $t_{\text{cross}} = d_{\text{telescope}}/v_{\text{wind}}$. Spatial frequency in the pupil then corresponds to a location in the image plane. The effect of atmospheric parameters on speckle properties is further quantified in [Guyon, 2005] and speckle lifetimes are observed on shorter scales in [Goebel et al., 2018]. Empirical investigations of telescope telemetry and ambient weather conditions are also an ongoing area of study, especially with regards to predictive control [Guyon et al., 2019, Rudy et al., 2014, Hafeez et al., 2021], but that information may additionally be useful in determining optimal parameters for stKLIP on-sky. Additionally, using this information on the temporal/spatial locations of strongest correlations, it may be possible to reduce the matrix size or use only the most correlated images such as in T-LOCI [Marois et al., 2013].

For this work, we have been operating in the regime of milliseconds to track atmospheric speckle motions. However, in practice, the full 3D space-time correlation matrix will have power on multiple timescales, from that of atmospheric speckles to quasi-static speckles. It is outside the scope of this work to fully explore how space-time KLIP could be applied on multiple time domains, and there is additionally the caveat that computational complexity grows with longer timescales than those we have applied here.

2.5.3 Including Quasi-Static Speckles

As mentioned in Section 2.1, the scenario we have investigated is an idealized case — one in which quasi-static speckles are absent and our images are dominated entirely by atmospheric speckles. We are also working on short timescales, where the atmosphere is frozen at each time step. There is a timescale over which the intensity changes, which we are observing in this scenario, but there is also a timescale for changes in the electric field's phase. These phase

changes will only result in changes in intensity if superimposed onto a constant electric field, such as the case of non-coronagraphic imaging, or when quasi-static speckles are significant ($C(\vec{x})$ in Equation 2.15). This is another regime in which to explore algorithm performance, wherein quasi-static and atmospheric speckles co-exist and interact, possibly even changing the speckle lifetimes [Soummer and Aime, 2004, Fitzgerald and Graham, 2006, Bloemhof et al., 2001, Soummer and Aime, 2004]. In this regime, there will likely be additional space-time variation as "pinned" speckles oscillate. Given that the presence of quasi-static speckles will make visible the additional space-time variations in phase, it is possible that stKLIP will operate even more effectively with this additional information to exploit. However, additional quasi-static speckles will lead to additional photon noise, which may counteract any theoretical contrast gains from including phase information. (Note: recent work from [Mullen et al., 2019] shows that using KLIP on shorter exposures may even help remove quasi-static speckles more effectively, further bolstering the case for the stKLIP's effectiveness in this regime.) Additionally, the presence of atmospheric residuals could even provide information about the phase of quasi-static speckles, allowing them to be effectively nulled with a deformable mirror [Frazin, 2014, Frazin and Rodack, 2021]. Future simulations may explore this regime and determine if additional contrast gain is possible.

2.5.4 Considerations for Future Work

In this idealized test case, we also chose not to simulate adaptive optics corrections, instead leaving an investigation of how AO parameters affect space-time correlations and the resulting stKLIP processing for a future investigation. Since AO suppresses low frequencies and heaves high frequencies unchanged, although our total error is on par with an AO residual scenario, the overall shape of the power spectrum would be different. This would likely lead to weaker temporal correlations with AO. Previous work also shows that AO corrections do affect the lifetime of speckles [Males et al., 2021, Males and Guyon, 2017], so this will be an important factor to consider in future work.

Currently, we have yet to demonstrate the full potential of this algorithm, in part due to the high computational costs. To run stKLIP on a 100×100 pixel window of a simulated 30-second data set (with the parameters specified in Section 2.4) over a range of KLIP parameters, we required 128GB of RAM and approximately 400 hours of computation time. The high memory requirement is due to the eigendecomposition, since the space-time covariance matrix can become extremely large when including a large number of lags and must be loaded in fully to the eigendecomposition. As mentioned in Section 2.3.3, there are possible solutions to this challenge to reduce computational costs in less memory intensive implementations, or even analytical gains in efficiency that exploit symmetries inherent in the covariance matrix (shown in Figure 2.1) or focus on only the strongest correlations depending on the temporal and spatial scales of interest, but those are beyond the scope of this paper.

It may also be possible to reduce the number of eigenvalues/modes computed, which will reduce computation time and possibly memory consumption as well, given that we now know that values beyond ∼50 KL modes aren't of much use in our tested scenario, but the exact threshold will be dependent on the region of interest and number of lags used, among other factors. In future iterations, this code could also likely be improved by implementing this algorithm more optimally rather than in a high-level language, as the current implementation is in Python, and by using parallel processing.

2.6 Conclusion

Evolving atmospheric layers lead to time-varying speckles in the focal plane of an imaging system; for the high-contrast imaging regime, we have shown that spatio-temporal covariances in these speckles exist, and can be exploited for use in data processing to improve contrast. Our data processing tool has been implemented in Python, tested on a simple analytic test case to prove viability, and also tested on realistic simulations to understand

the effectiveness of this technique. We have shown there is potential for a contrast gain (or equivalently, SNR improvement) of at least 10–20% from the original image, with significant potential for an even larger gain if self-subtraction is adequately addressed. Additionally, we have shown evidence that the space-time nature of our algorithm, in its current form, may provide a slight advantage over spatial-only KLIP in certain cases, with significant potential for stronger improvement under different conditions and with improvements to the algorithm implementation. Although the SNR gains for this new method aren't fully developed, this initial work on space-time KLIP opens the door for the use of space-time covariances in high-contrast imaging, especially in the short timescale regime of atmospheric speckle lifetimes.

Future work can use our data processing tool to further explore the dependence of the space-time covariances and the resulting contrast improvements on various parameters, such as the type of coronagraph, AO performance, strength of quasi-static speckles, and atmospheric conditions. It would be particularly interesting to determine how AO affects these covariances, since AO is important in a realistic scenario for exoplanet imaging and affects the resulting speckle lifetimes and structures.

Future implementations of this algorithm will also need to consider how to minimize self-subtraction of the companion object, and overcome the memory and computational demands in the eigendecomposition. Further optimization of the tunable parameters is also necessary to optimize algorithm performance and implement this as a refined tool for exoplanet imaging. It would also be interesting to apply this tool to on-sky data, such as that from MEC on SCExAO at Subaru [Walter et al., 2020, 2018, Jovanovic et al., 2015b, Minowa et al., 2010], to determine potential on-sky contrast gains from this technique. Although this current work focuses on the use of speckle space-time covariances in post-processing, these covariances could even be used in real-time predictive control [Guyon et al., 2018]. Overall, the results in this work show that harnessing space-time covariances through "space-time KLIP" may be a promising technique to add to our toolkit for suppressing speckle noise in

exoplanet imaging while retaining signal throughput.

Notation Glossary A – Sections 2.1 & 2.3

Symbol	Definition
$I_\psi(k)$	Stellar PSF, as in Soummer et al. 2012
k	Pixel index
$T(k), \vec{t}$	Target image as in Soummer et al. 2012, and as in this work unrolled to 1-d and represented as a vector
$A(k), \vec{a}$	Faint astronomical signal (as above)
ϵ	True/false binary parameter
$\hat{I_\psi}(k), \vec{\hat{\psi}}$	Approximated PSF as in Soummer et al. 2012 and as a vector in this work, respectively
R	Matrix of reference images before mean subtraction
$\vec{r}$	Individual reference image
X	Mean image from reference set
M	Mean subtracted reference images
n_i	Number of images in reference set
n_p	Pixel count $n_x \times n_y$
n_x	Dimension 1 size
n_y	Dimension 2 size
n_m	Number of modes / eigenvectors chosen
i	Used as an arbitrary index
j	Used as an arbitrary index
C	Covariance matrix
$\vec{\lambda}$, λ	Vector of eigenvalues, eigenvalue
V	Matrix of eigenvectors/eigenimages

$\vec{v}$	Eigenvector
$\vec{q}$	Vector of coefficients
S, $\vec{s}$	Mean subtracted image sequences (in matrix and vector form)
$\vec{\hat{s}}$	Reconstructed image sequence
n_s	Number of images in sequence
L	Largest number of timesteps/lags in use as measured from the central image
n_l	Total number of timesteps/lags used, equal to n_s
$\vec{r}_{k,avg}$	Averaged residual from stKLIP

Notation Glossary B – Sections 2.2

Symbol	Definition
I	Intensity
$\vec{x}$	Location in image plane
$\vec{u}$	Location in pupil plane
t	Time
τ	Time step
Ψ_{pup}	Pupil amplitude
Ψ_{foc}	Focal amplitude
$\psi(\vec{u}, t)$	Pupil phase
$P(\vec{u})$	Pupil function
$C(\vec{x})$	Spatially coherent wavefront
$S_\phi(\vec{x}, t)$	Phase aberrations
ξ	Displacement in pupil
B_ϕ	phase covariance function
v_{wind}	Wind velocity

CHAPTER 3

Using Ground-Based Polarimetry to Monitor Plume Activity on Europa

3.1 Introduction

Multiple purpose-built instruments have been created for high-contrast imaging of exoplanets and planet-forming disks in the past decade. Although these instruments' main purpose is for extrasolar investigations, they can be powerful tools for solar system observations as well. Herein we present the first disk-resolved multiband infrared imaging polarimetry of Europa, one of Jupiter's four Galilean satellites and a popular target in the search for life in the solar system.

Unresolved polarimetric observations of the Galilean satellites were originally used in the 1970s and 1980s to determine Europa's surface composition, suggesting that it has a water ice surface [Dollfus, 1975, Mandeville et al., 1980], which we know today to be true from observations taken by the *Galileo* and *Juno* missions to Jupiter [Greeley et al., 1998, Szalay et al., 2024]. These observations, however, were quite limited in the range of phase angles and wavelengths probed; more recent disk-integrated polarimetric observations (e.g. Kiselev et al. [2017, 2022]) tracked the dependence of Europa's surface polarization on phase angle, and determined that sunlight scattering off the surface of Europa is linearly polarized between -0.4–0.4%, caused by a regolith layer with a high albedo. Spatially resolved polarimetry should be able to provide information on the grain sizes of the icy regolith across the surface, determining distinct compositional units indicative of differing geologic features, as well as

information on active processes like cryovolcanism, colloquially referred to as plumes [Poch et al., 2018, Sparks et al., 2022].

Unlike the well-established plumes on Enceladus [Hansen et al., 2006], the existence of plumes on Europa are still under debate, but are suspected due to its surface features and known subsurface ocean [Fagents et al., 2000, Melosh et al., 2004]. Water vapor consistent with plume activity on Europa was detected with *HST* observations circa 2012, but not in previous imaging, suggesting more variable plume activity on the timescales of years [Roth et al., 2014]. Follow up observations with *HST*/STIS similarly revealed images of possible plume activity, and recent searches for water vapor outgassing showed low levels with occasional stronger events, which may be considered indirect evidence of plume activity [Sparks et al., 2016, Paganini et al., 2020]. Additional monitoring of Europa's exosphere was obtained in 2018 with Keck/HIRES, but this work does not provide information on plume constraints [Brettle and Brown, 2018].

Plumes are an exciting window into the geology of icy outer solar system moons with subsurface oceans. *Cassini* observations of Enceladus's plumes have provided information on the geophysical mechanisms powering the plumes as well as the chemistry of the subsurface ocean — a key target of interest for habitability and astrobiology studies — even revealing signs of hydrothermal vents [Waite et al., 2017]. It is yet unclear where Europa's plumes originate — from evaporation or sublimation in pockets of liquid near the surface, or from nozzles originating deep in the subsurface ocean [Vorburger and Wurz, 2021]. Two key parameters in models of Europa's plumes are the spatial extent and column density, as different mechanisms will produce features with different sizes and flow rates. Location of plumes on the surface may correlate with existing surface features, again providing insight into how the plumes form. Additionally, others have hypothesized that Europa's plumes, similarly to those of Enceladus, may be tidally modulated, appearing when tidal stresses deepen cracks on the surface and allow water to escape [Quick et al., 2013, Rhoden et al., 2015].

Better constraints on the size and timing of Europa's plumes — as well as clearer evidence that they exist at all — will significantly constrain models of plume formation and deepen our understanding of subsurface ocean geology. These geological questions also have significant implications for astrobiology on Europa – similar to the previously described scenario on Enceladus.

Determining whether the plumes are periodic/predictable or stochastic could also assist in determining timing for mission plans, in preparation for two upcoming solar system missions: Europa Clipper [Phillips and Pappalardo, 2014], launching in 2024, and the European Space Agency's Jupiter Icy Moons Explorer (JUICE) [Grasset et al., 2013], launching in less than one year in April 2023. Understanding the timing of plumes is crucial for possible in-situ sampling, which could provide a direct observation of the subsurface ocean's composition, possibly including the molecular components of biology or even microbial life itself [Lorenz, 2016]. Space-based monitoring with *HST*, however, is challenging — as it is difficult to obtain sufficient time and cadence — but ground-based polarimetry (as first proposed by McCullough et al. 2020) could enable routine monitoring, providing data on both plume size and timing/variability to constrain features of plume activity and prepare for upcoming missions.

Ice particulates of size $\sim$1–2 microns should present a polarized signal in the infrared due to scattering. Additionally, this method of using imaging polarimetry allows direct detection of plumes across the disk of Europa — not limited to features located on the limb or detections of water vapor at non-specific locations as previous observations have been. This work is both a proof-of-concept, paving the way for future monitoring efforts, and an opportunity to learn more about the nature of Europa's plume activity, either via a positive detection or a constraint on the level of activity, and Europa's surface geology more generally.

We present observations taken with SCExAO/CHARIS infrared spectropolarimetry [Groff et al., 2016] on the Subaru Telescope of Europa in Section 3.2 with details of the data processing required for this unique dataset in Section 3.3. These data constitute the first disk-

Date (UT)	30 July 2023	
Instrument	SCExAO/CHARIS	
Filter	Broadband (JHK)	H
Exp. Time (s)	13	30
Tot. Time (min)	48	30

Table 3.1: Summary of observations of Europa with Subaru SCExAO/CHARIS.

resolved multiband infrared polarimetric imaging of Europa to be published. Preliminary analysis is presented in Section 3.4, and future work is detailed in Section 3.5.

3.2 CHARIS Observations

We observed Europa on 2023 July 29 UTC with Subaru SCExAO/CHARIS. At the time of observation, the system was a combination of extreme adaptive optics (SCExAO, the Subaru Coronagraphic Extreme Adaptive Optics system, Guyon et al. [2010], Vogt et al. [2010], Garrel et al. [2010]) to build off the initial wavefront correction from the facility's AO188 system [Hayano et al., 2008, Hayano et al., 2010], and the CHARIS instrument (the Coronagraphic High Angular Resolution Imaging Spectrograph) for infrared spectropolarimetric observations [Groff et al., 2015, 2016]. Observations are summarized in Table 3.1.

CHARIS observations were taken in broadband mode (simultaneous observations in J, H, and K bands -9- 1.16–2.37 μm with R$\sim$18) [Groff et al., 2016]) and so-called "high-resolution" H-band (centered on 1.63 μm, R$\sim$65), using natural guide star adaptive optics locked on Europa. Seeing conditions were steady at 0.4–0.6″ as recorded in the observing logs and by the MASS/DIMM data available from the CFHT seeing and mass profile records. The individual exposure time was 13 seconds for broadband and 30 seconds for H band, with total on-source integration times of 48 minutes and 30 minutes, respectively. All observations were taken without a coronagraph in the optical path, and without the instrument's usual

astrometric grid spots. We additionally observed a variety of stars for photometric and astrometric calibration (BD 343631, HD 239068, HD 236419, HD 236894, HIP 3373) on the same night for use in calibrations. Sky flats for calibration were taken at a similar separation to Europa for use in removing stray polarized light from bright nearby Jupiter.

Data "cubes" (with wavelength as the third dimension) were extracted from the raw CHARIS reads using the instrument's standard extraction pipeline (`CHARIS-DEP`) [Brandt et al., 2017]. Data cubes were then flat fielded and sky subtracted using a series of polarization flats taken on the same night with CHARIS and the aforementioned sky flats, via the instrument's standard data processing pipeline (`CHARIS-DPP`) Currie et al. [2018], Lawson et al. [2021]. Further calibration steps of image registration and spectrophotometric calibration for polarimetric data, however, are only implemented in the standard pipeline for observations using astrometric satellite spots and a central host star as the spectrophotometric reference; as a result, we perform these calibrations with processes tailored to this unique dataset as described in the following section.

3.3 Data Reduction and Processing

3.3.1 Image Registration

For image registration, we first split the images into left and right halves (i.e. separating each of the orthogonal polarization states that is imaged on the detector). We then use the nominal centers for the two polarization images on the detector, as listed in the `CHARIS-DPP` and adjusted by eye for a better match, to center the first image in the sequence, and align all subsequent frames to that centered frame via cross-correlation using `scikit-image`'s phase cross correlation function [van der Walt et al., 2014] to determine the pixel offset and `scipy.ndimage`'s shift function [Jones et al., 2001] to move each split frame to the correct centered position. We then create and apply a mask to the data to set all values outside the field of view to NaN, to prevent aliasing effects later on in the data reduction process

(particularly during the final step of polarized differential imaging, a.k.a. PDI, described further in Section 3.3.3).

3.3.2 Absolute Flux Calibration

For the broadband Europa data, we then perform the absolute flux calibration using the reference star HD 236894; these observations were also taken in broadband mode, with 16 second exposures for a total integration time of 8.5 minutes. HD 236894 is an O8V star with magnitude H (2MASS) = 8.877±0.026 [Cutri et al., 2003], listed as a polarization standard star in Heiles [2000]. These reference images are extracted using the same procedure as the target science data with the `CHARIS-DEP`, flat fielded with the `CHARIS-DPP`, and registered via cross-correlation. Notably, we do *not* use the `CHARIS-DPP` for sky subtraction here, as the only sky frames we have available from the night are from near Jupiter.

Instead, we perform sky subtraction via aperture photometry for the reference star data. We find the radius at which the signal is <0.5% of the point spread function (PSF) core, and use an annulus with that as the inner radius and the outer radius set by the limits of the field of view (FOV). We find the average pixel value in that annulus and use that as the noise value to subtract from each pixel in the image. Then, we take the median for each pixel across all sky subtracted reference star cubes and divide by the exposure time to create one master reference star cube with units of counts per second.

With this master reference star cube, we then extract the stellar flux for each wavelength slice in the cube. We again use aperture photometry (via `photutils` [Bradley et al., 2019]), here with an aperture of three times the full width at half maximum (FWHM) centered on the star. The FWHM is calculated as $\frac{1.02\lambda}{D}$ for each channel, and then converted to pixels using the CHARIS pixel scale 16.4±0.1 mas/pix. Given that our target science data is for an extended object, we must account for the finite aperture used in this process. We compute an encircled energy correction by deriving a curve of total flux versus radial distance from the star, and determining the fraction of flux contained at each radial location. After this

correction, we have a reference flux for each of the 22 CHARIS wavelength channels as if using an infinite aperture in counts/sec, hereafter referred to as the reference spectrum.

To convert to physical units, we then create a model data cube for the reference star using a Pickles model spectrum [Pickles, 1998] for an O9V star, the closest match in that spectral library to our reference star's classification, obtained via `pysynphot` [Lim et al., 2015]. We then compute the FWHM in pixels using the known central wavelength of the H-band filter and d$log\lambda$ value from the CHARIS data headers, and use this to convolve the model to the CHARIS resolution via a Gaussian with $\sigma = \frac{\mathrm{FWHM}}{2\sqrt{2\log 2}}$. The model is then interpolated to the CHARIS wavelength channels. To scale the model to the known stellar magnitude, we compute synthetic H-band photometry using the $\mathrm{H_{MKO}}$ filter transmission profile from the SVO Filter Profile Service [Rodrigo et al., 2012, Rodrigo and Solano, 2020] and the following equation from Tokunaga and Vacca [2005]:

$$\frac{\int F_\nu S_\nu / \nu d\nu}{\int S_\nu / \nu d\nu}. \tag{3.1}$$

where F_ν is the specific flux density, S_ν is the filter transmission profile, and ν is the frequency.

We convert the known stellar magnitude to Janskys using the 2MASS H-band zeropoint (1024 Jy) and the equation $F_\nu = \mathrm{ZP} \times 10^{-\mathrm{m}/2.5}$ [Cutri et al., 2003], and convert the model synthetic photometry to Janskys. We then fit for a scaling factor to scale the model to the known magnitude, resulting in a model spectrum at CHARIS resolution and wavelengths scaled to the known stellar flux.

Lastly, with this model spectrum (in Jy) and the aforementioned reference spectrum (in DN/s) we can divide the two to create a conversion factor in Jy/counts/second, which we can then use to convert our science target data to physical units by dividing by the target exposure time and multiplying by this conversion factor. Given that we are interested in the brightness of this extended object, we additionally convert to mJy/sq. arcsec by dividing by the subtended solid angle of a pixel in square arcseconds and converting from Jy to mJy.

3.3.3 Polarimetric Imaging via Double-Differencing

We then return to the `CHARIS-DPP` to complete the steps necessary to obtain images corresponding to the I, Q, and U components of the Stokes vector. Dual-band poalrimeters are generally insensitive to Stokes V (circular polarization) due to the retardance of the wave plate. The Stokes vector [Stokes, 1851] describes the elliptical polarization of light as:

$$S = \begin{bmatrix} I \\ Q \\ U \\ V \end{bmatrix}, \tag{3.2}$$

where I is the light's total intensity, Q and U are its two orthogonal linear polarization states, and V is its circular polarization, as illustrated in Figure 3.1. From the components of the Stokes vector, we can calculate the polarized intensity (PI), degree of linear polarization (DoLP), and angle of linear polarization (AoLP) as follows:

$$\text{PI} = \sqrt{Q^2 + U^2} \tag{3.3}$$

$$\text{DoLP} = \frac{\text{PI}}{I} = \frac{\sqrt{Q^2 + U^2}}{I} \tag{3.4}$$

$$\text{AoLP} = \frac{1}{2}\arctan\left(\frac{U}{Q}\right) \tag{3.5}$$

For an ideal polarimeter, if the incoming light is split into two orthogonal polarization states aligned with coordinate axes (I_1 and I_2), Stokes I and Q can be retrieved from adding and subtracting the intensity of I_1 and I_2 respectively:

$$I = I_1 + I_2 \tag{3.6}$$

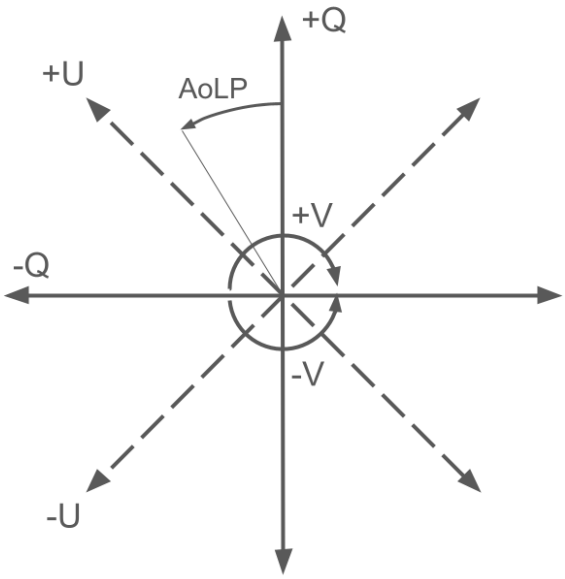

Figure 3.1: Diagram of the orientation of the Stokes vector components I, Q, U, and V, as well as the definition of the angle of linear polarization (AoLP). This visualization is as if the beam is propagating out of the page towards the observer, centered on the origin. Figure adapted from Fig. 1 of De Boer et al. [2020].

$$Q = I_1 - I_2 \tag{3.7}$$

Equivalently, we can describe the transmission for I_1 and I_2 as:

$$I_1 = \frac{1}{2}(I + Q) \tag{3.8}$$

$$I_2 = \frac{1}{2}(I - Q) \tag{3.9}$$

To obtain Stokes U, the angle of linear polarization must be rotated by 45° (i.e. by an additional optical component); then the above equations can be applied to retrieve $\pm U$.

In a polarimetric imaging instrument like SCExAO/CHARIS, simultaneous images of the field-of-view (FOV) are obtained in two orthogonal polarization states using a polarizing beam splitter, such as a Wollaston prism. Additionally, the system contains a half-wave plate (HWP) to rotate the polarization direction, allowing us to obtain Stokes I, Q, and U with some mitigation of instrumental polarization (IP) via double-differencing [Tinbergen, 2005, Witzel et al., 2011, Canovas et al., 2015, De Boer et al., 2020]. Stokes V (circularly polarized light) is unable to be measured by such a system. For the double-differencing procedure, images are recorded with four HWP angles; the HWP angle corresponds to half of the angle of linear polarization (e.g. a HWP angle of 22.5° creates a change of ΔAoLP = 45°) [Appenzeller, 1967, De Boer et al., 2020]. Two HWP angles (0° and 45°) are used to obtain $\pm Q$, and two (22.5° and 67.5°) are used to obtain $\pm U$ as follows, where Q^+, Q^-, U^+, and U^- correspond to the Stokes vectors obtained via single-difference (as in Equations 3.6 and 3.7 from each HWP angle (0, 22.5, 45, and 67.5°) respectively:

$$Q = \frac{1}{2}(Q^+ - Q^-) = \frac{1}{2}(I_1(0°) - I_2(0°) - I_1(45°) + I_2(45°)) \tag{3.10}$$

$$I_Q = \frac{1}{2}(I_{Q^+} - I_{Q^-}) = \frac{1}{2}(I_1(0°) + I_2(0°) + I_1(45°) + I_2(45°)) \tag{3.11}$$

$$U = \frac{1}{2}(U^+ - U^-) = \frac{1}{2}(I_1(22.5°) - I_2(22.5°) - I_1(67.5°) + I_2(67.5°)) \tag{3.12}$$

$$I_U = \frac{1}{2}(I_{U^+} - I_{U^-}) = \frac{1}{2}(I_1(22.5°) + I_2(22.5°) + I_1(67.5°) + I_2(67.5°)) \tag{3.13}$$

Double-differencing is able to remove IP downstream of the HWP in the telescope optics; however, further calibration is necessary to remove IP from the telescope mirrors, instrument optics upstream from the HWP, and crosstalk between polarization channels. For CHARIS, there exists a full Mueller matrix model of the instrumental polarization, which primarily arises from the image derotator (K-mirror), telescope mirrors, and the half-wave plate itself [van Holstein et al., 2020, GJ't Hart et al., 2021] as further described in Section 3.3.4.

In the `CHARIS-DPP` pipeline, these steps (double-differencing and instrumental polarization calibration) are collectively referred to as polarimetric differential imaging (PDI). PDI is a high-contrast imaging technique that is often used for detecting circumstellar disks, as in Chapter 5; this technique removes unwanted stellar light by relying on the fact that starlight is generally unpolarized, while light scattered off the small dust grains of a disk is polarized [Follette, 2023]. Although disk imaging is not the end goal of this particular investigation, the steps to processing dual-band polarimetry for our case and for traditional high-contrast imaging are largely the same, and result in total intensity and polarized intensity as shown in Figure 3.2, as well as Stokes Q and U images that display the typical "butterfly" pattern expected for a face-on, axisymmetric circular source as shown in Figure 3.3 [De Boer et al., 2020]. In each wavelength averaged image shown within, we have removed wavelength channel 12 due to a hot pixel over the disk of Europa interfering with image quality.

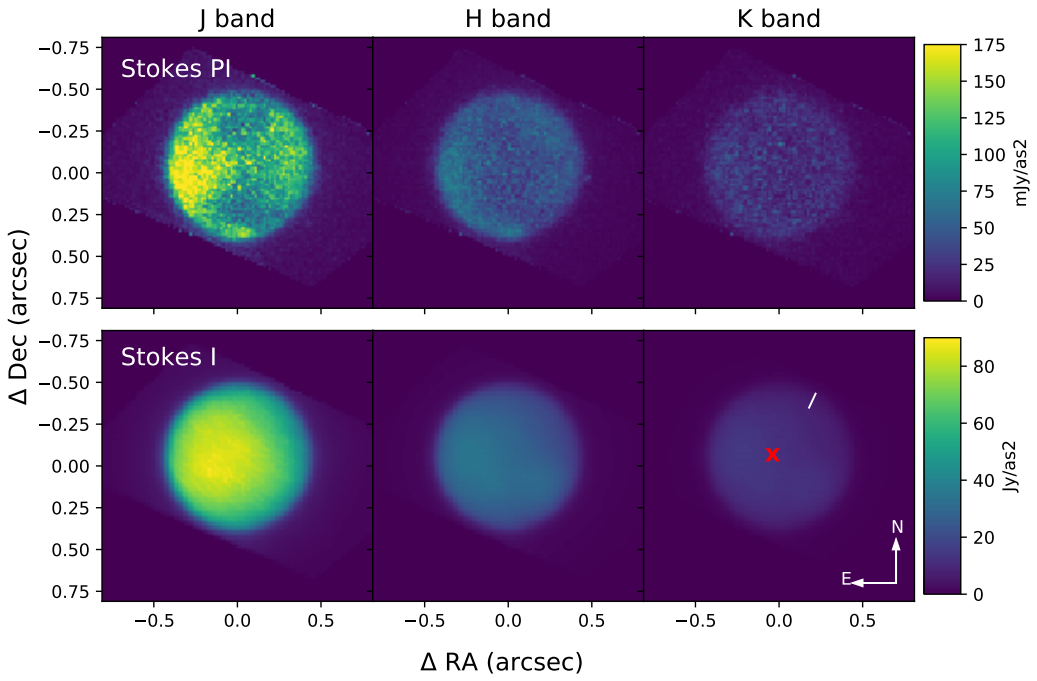

Figure 3.2: Preliminary reduction of broadband polarimetric imaging of Europa; columns correspond to the average flux density in the J band, H band, and K band respectively, rows correspond to total intensity and polarized intensity. Note the different color scaling in each (mJy vs. Jy), as Europa is significantly brighter in total intensity than in polarized light; additionally, Europa appears significantly brighter at J band. Images are shown with North up, East left; approximate positions of Europa's North Pole and the subsolar point (marked with a red $\times$) are indicated in the bottom right.

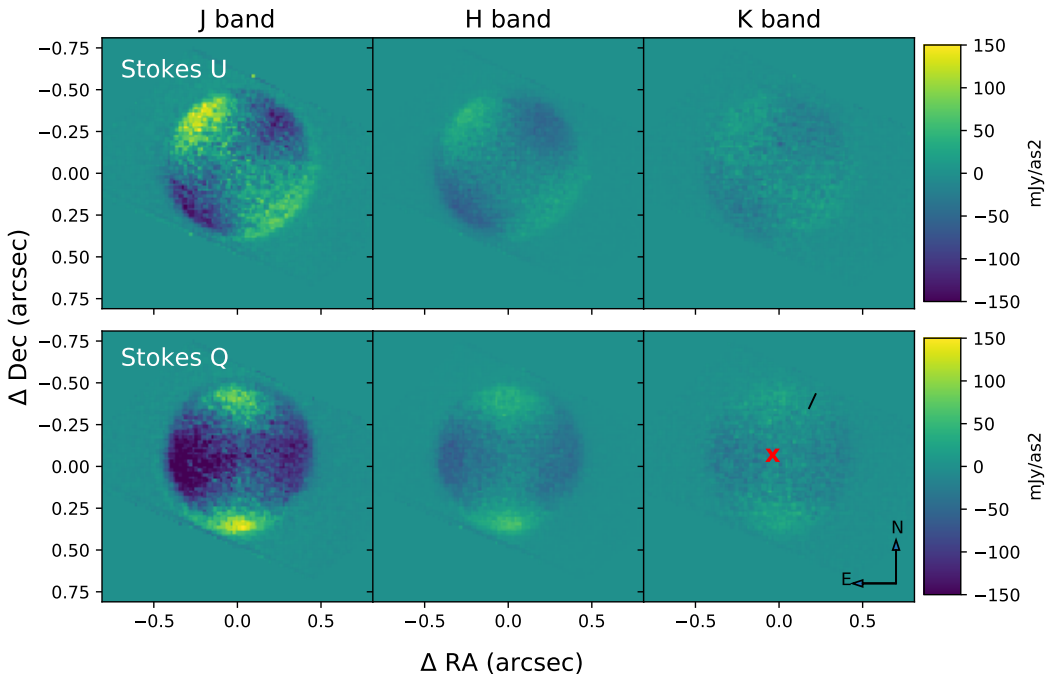

Figure 3.3: Preliminary reduction of broadband polarimetric imaging of Europa in Stokes Q and U showing the average flux density in each band. These images show a "butterfly" pattern as expected for a face-on, circular source [De Boer et al., 2020]. Images are shown with North up, East left; approximate positions of Europa's North Pole and the subsolar point (marked with a red $\times$) are indicated in the bottom right.

3.3.4 Instrumental Polarization Calibration

In a non-ideal polarimeter, there are multiple sources of error that must be accounted for and calibrated; the two most critical of these effects are polarization induced by the telescope and instrument optics (often simply referred to as instrumental polarization) and crosstalk (a form of "leakage" in which one polarization state is converted into another, usually between linear and circular polarization). IP is generally caused by diattenuation, in which an optical component has different reflectance or transmission properties depending on the polarization state. Crosstalk, on the other hand, is due to retardance, wherein a polarization state acquires a phase shift due to reflection or transmission [van Holstein et al., 2020].

It is possible to create a mathematical model of the polarization effects for an optical system, obtaining a Mueller matrix ($M_{\rm sys}$) to describe the transformation between the input Stokes vector ($\mathbf{S}_{\rm in}$) and the Stokes vectors $\mathbf{S}_{\rm rec}$ describing the light on each half of the detector (L/R):

$$\mathbf{S}_{\rm rec,L/R} = M_{\rm sys,L/R}\mathbf{S}_{\rm in} \tag{3.14}$$

or, equivalently:

$$\begin{bmatrix} I_{\rm rec,L/R} \\ Q_{\rm rec,L/R} \\ U_{\rm rec,L/R} \\ V_{\rm rec,L/R} \end{bmatrix} = \begin{bmatrix} I \to I & Q \to I & U \to I & V \to I \\ I \to Q & Q \to Q & U \to Q & V \to Q \\ I \to U & Q \to U & U \to U & V \to U \\ I \to V & Q \to V & U \to V & V \to V \end{bmatrix} \begin{bmatrix} I_{\rm in} \\ Q_{\rm in} \\ U_{\rm in} \\ V_{\rm in} \end{bmatrix} \tag{3.15}$$

where $M_{\rm sys}$ is the 4×4 Mueller matrix. $M_{\rm sys}$ can be written as the product of the Mueller matrices for each individual component, i.e. $M_n, M_{n-1} \cdots M_2 M_1$.

For CHARIS, the instrumental Mueller matrix model [van Holstein et al., 2020, GJ't Hart et al., 2021] accounts for the effects of the three main telescope mirrors (dependent on the parallactic angle a and the altitude angle p), the effects of the Wollaston (simply describing the left and right channels), the derotator/K-mirror (dependent on its angle θ and offset δ),

and the HWP (also dependent on its angle and offset). A simplified diagram of the Subaru SCExAO/CHARIS optical path, including these components, is shown in Figure 3.4. For components that can rotate the polarization angle, the model includes a rotation matrix $T(\theta)$:

$$T(\theta) = \begin{bmatrix} 1 & 0 & 0 & 0 \\ 0 & \cos(2\theta) & \sin(2\theta) & 0 \\ 0 & -\sin(2\theta) & \cos(2\theta) & 0 \\ 0 & 0 & 0 & 1 \end{bmatrix} \tag{3.16}$$

Each component in the model (the telescope mirrors, HWP, and derotator) also has a Mueller matrix that describes the optic's diattenuation (ϵ) and retardance (Δ):

$$M_{\text{component}} = \begin{bmatrix} 1 & \epsilon & 0 & 0 \\ \epsilon & 1 & 0 & 0 \\ 0 & 0 & \sqrt{1-\epsilon^2}\cos\Delta & \sqrt{1-\epsilon^2}\sin\Delta \\ 0 & 0 & -\sqrt{1-\epsilon^2}\sin\Delta & \sqrt{1-\epsilon^2}\cos\Delta \end{bmatrix} \tag{3.17}$$

The Wollaston prism has a simpler Mueller matrix that describes the split into the two orthogonal states:

$$M_{\text{W,L/R}} = \begin{bmatrix} 1 & \pm 1 & 0 & 0 \\ \pm 1 & 1 & 0 & 0 \\ 0 & 0 & 0 & 0 \\ 0 & 0 & 0 & 0 \end{bmatrix} \tag{3.18}$$

Combining these components, where $M_{\text{W,L/R}}$ describes the Wollaston, M_{der} describes the derotator, M_{HWP} describes the HWP, and M_{tel} describes the telescope mirrors, the model (as in van Holstein et al. [2020]) can be expressed as:

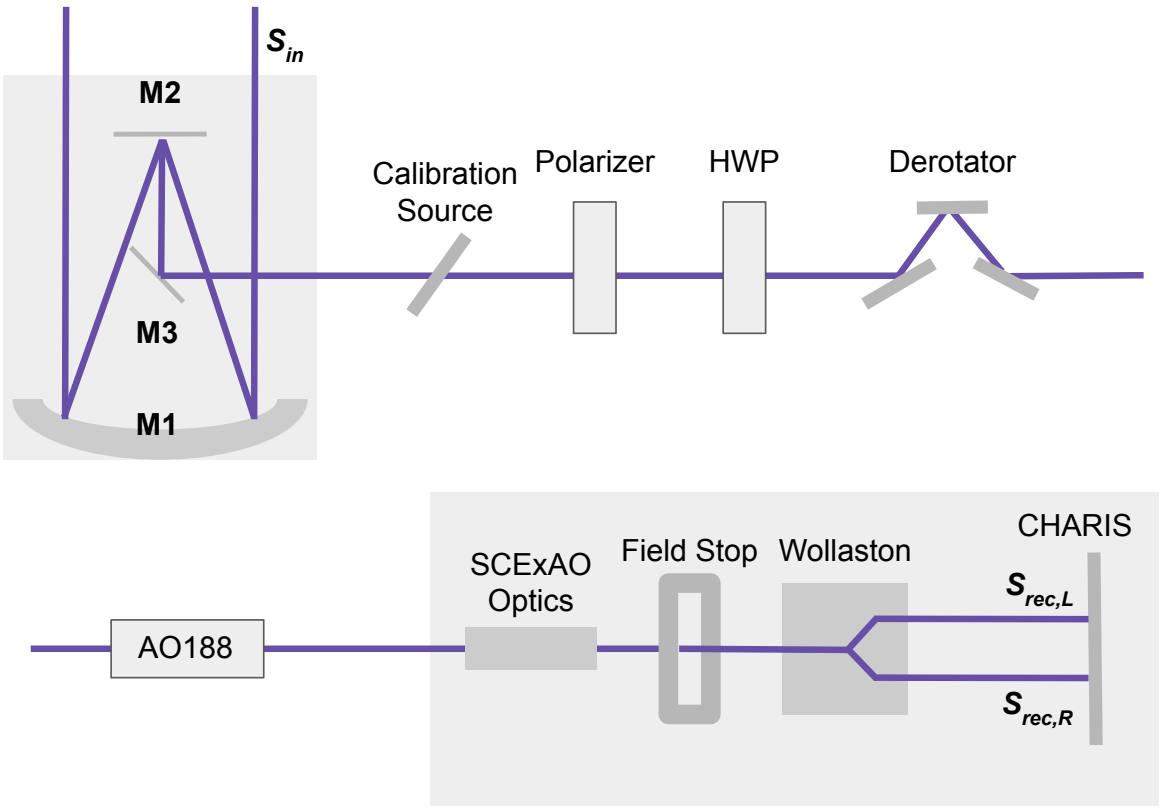

Figure 3.4: A simplified diagram illustrating the relevant components of the optical path from the Subaru telescope to SCExAO/CHARIS. Adapted from Fig. 1 in van Holstein et al. [2020].

$$\mathbf{S}_{\mathrm{rec,L/R}} = M_{/rmW,L/R} T(-\theta_{\mathrm{der}}, -\delta_{\mathrm{der}}) M_{\mathrm{der}} T(\theta_{\mathrm{der}}, \delta_{\mathrm{der}}) T(-\theta_{\mathrm{HWP}}, -\delta_{\mathrm{HWP}}) M_{\mathrm{HWP}} T(\theta_{\mathrm{HWP}}, \delta_{\mathrm{HWP}}) T(-a) M_{\mathrm{tel}} T(p) \mathbf{S}_{in} \quad (3.19)$$

van Holstein et al. [2020] implemented this model for CHARIS and fit values for the retardance of the HWP and derotator across all 22 wavelength channels recorded by CHARIS, providing a first-order calibration for instrumental polarization. GJ't Hart et al. [2021] then fully characterized the instrumental polarization effects for CHARIS spectropolarimetry, including the addition of physical models of the derotator and HWP retardance, the addition

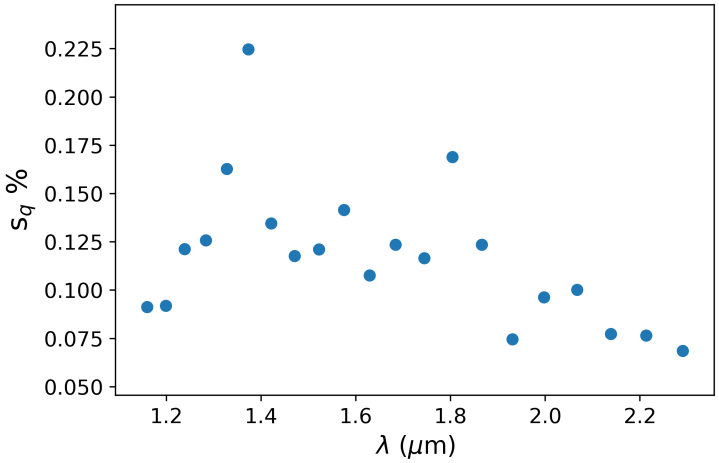

Figure 3.5: Polarimetric accuracy for SCExAO/CHARIS across the broadband wavelength channels for an 0.1% polarized source such as Europa. Polarimetric accuracy s_q is calculated as $s_q = |q|s_{rel} + s_{abs}$, as in GJ't Hart et al. [2021].

of a physical model of the tertiary mirror's diattenuation, and validation using both internal calibration sources and unpolarized standard star observations. These calibrations for instrumental polarization effects are included in the `CHARIS-DPP` PDI module. GJ't Hart et al. [2021] reports that the total polarimetric accuracy in normalized Stokes q (s_q) of CHARIS spectropolarimetry observations is 0.08% to 0.24% for a 1% polarized substellar companion, with an absolute accuracy s_{abs} of 0.067% to 0.22% and a relative accuracy s_{rel} of 0.41% to 2.5%. Polarimetric accuracy s_q is calculated as $s_q = |q|s_{rel} + s_{abs}$ where q is the polarized fraction Q/I_Q; accordingly, for our observations, we expect an accuracy of 0.07% to 0.22% for an 0.1% polarized source such as Europa in Stokes q, shown for each wavelength channel in Figure 3.5. Accuracy for Stokes u is calculated similarly, assuming a polarization fraction of 0.01% [Kiselev et al., 2022], and then used to calculate the accuracy in the degree of linear polarization $s_{DoLP} = \sqrt{q^2 s_q^2 + u^2 s_u^2}$; due to the extremely low expected signal in Stokes q (<0.01% according to measurements in Kiselev et al. [2022] for phase angle $\alpha \approx 11$), $s_q \approx s_{DoLP}$.

Although we observed unpolarized stars (BD+34 3631 and HD 239068, Heiles 2000) on the same night, these stars' polarization fraction uncertainties are the same order of magnitude as our observed signal; as a result of this fact and the already high accuracy of the existing CHARIS Mueller matrix model [GJ't Hart et al., 2021], we do not perform an additional instrumental polarization calibration with these observations. We do, however, leverage the large number of half-wave plate cycles as a confidence check on our polarization accuracy; the spread in polarization fraction across the 55 HWP cycles is substantially smaller than the accuracy calculated above (measurements of percent polarization fraction vary by ±0.08%, 0.01%, and 0.03% for J, H, and K bands respectively), and as such, we do not incorporate this spread as an additional error term.

3.3.5 Astrometric Calibration

The `CHARIS-DPP` corrects for a true north position angle (PA) offset relative to the recorded PA in the data headers, using the published value of -2.2±0.27° [Lawson et al., 2020]. It is worth noting, however, that recent work has reported a slightly different mean PA offset for some data sets, as in Chen et al. [2023]. However, a degree difference in PA would correspond to <1 pixel on the limb of Europa in our imagery, and therefore is negligible for our purposes.

3.3.6 High-resolution *H*-band Data

For the H-band CHARIS data, we complete the same data processing steps previously described for the broadband data. In this reduction, we use observations of HD 236894 (the same reference used for the broadband reduction) taken in spectral high-res H-band mode (R∼65.2) as our photometric reference. These calibrated H-band data are visualized for select wavelength channels in Figures 3.6 and 3.7.

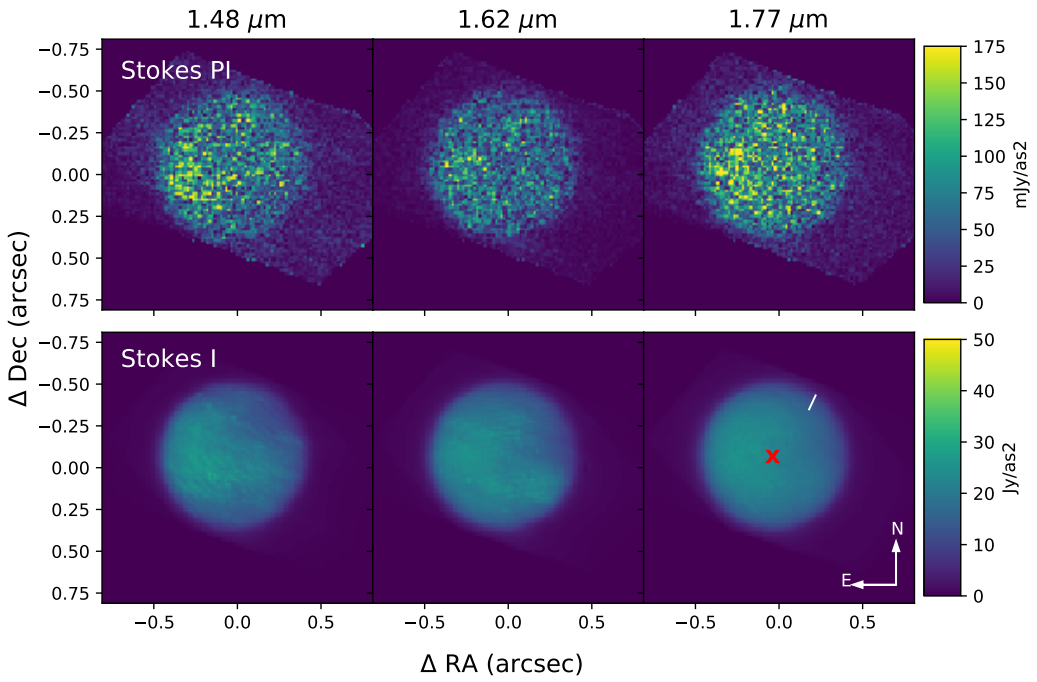

Figure 3.6: Preliminary reduction of polarimetric imaging of Europa in CHARIS high-resolution H-band mode; columns correspond to three wavelength channels within the data cube, rows correspond to total intensity, and polarized intensity. Note the different color scaling in each, as Europa is significantly brighter in total intensity than in polarized light. Images are shown with North up, East left; approximate positions of Europa's North Pole and the subsolar point (marked with a red x) are indicated in the bottom right.

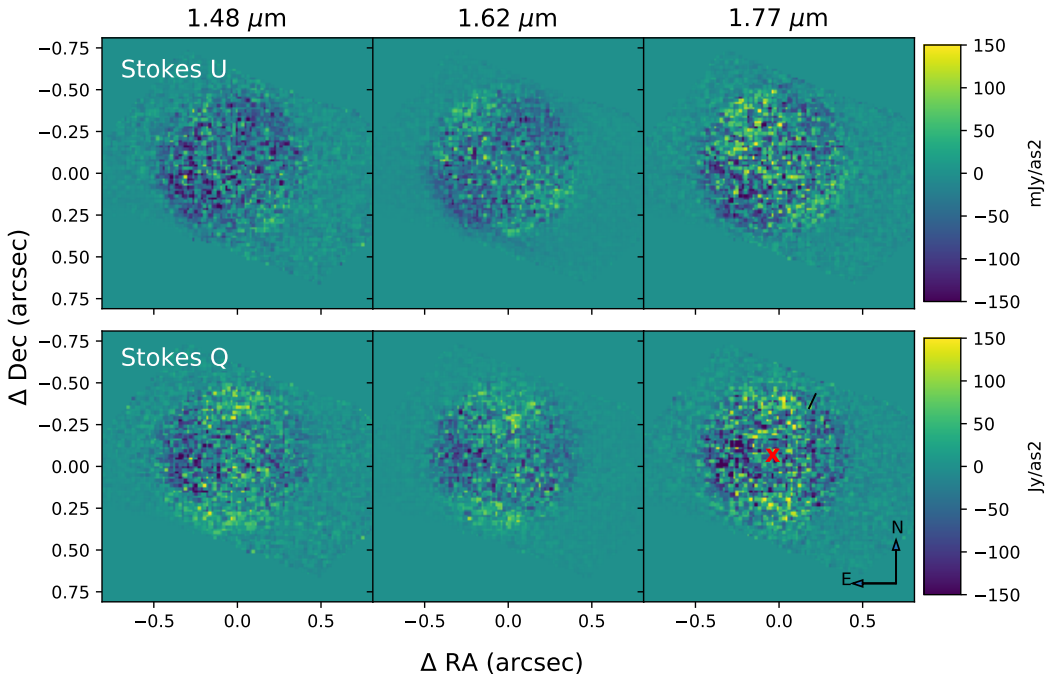

Figure 3.7: Preliminary reduction of CHARIS high-resolution H-band polarimetric imaging of Europa in Stokes Q and U. These images show a "butterfly" pattern as expected for a circular source. These images appear noisier because they are single wavelength channels instead of an average over a bandpass. Images are shown with North up, East left; and the subsolar point (marked with a red x) are indicated in the bottom right.

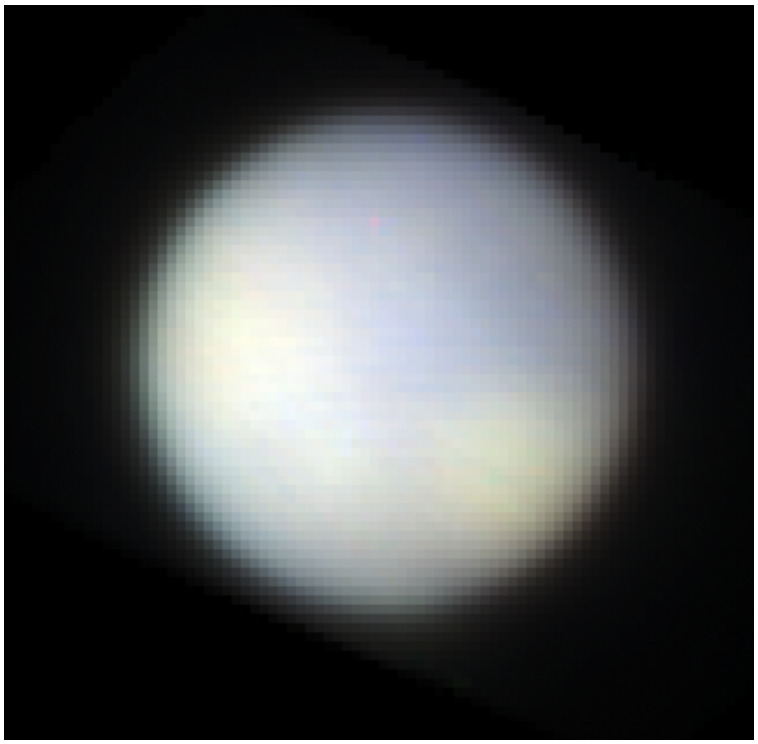

Figure 3.8: False color image of Europa in infrared total intensity as observed in CHARIS broadband mode. Red, green, and blue values correspond to K band, H band, and J band respectively.

3.4 Europa's Geologic Features

These unique data provide an opportunity to study Europa's surface features and characterize the scattering properties of the surface ice. Although similar resolved polarimetric imaging data have been collected with the *Hubble Space Telescope* (*HST*) in the visible (F435W) [Sparks et al., 2022], this is the first published resolved polarimetric dataset of Europa at infrared wavelengths. Here, we describe various geologic investigations that will be carried out with this dataset in future work. Additionally, a false color image of Europa in $J/H/K$ bands is provided in Figure 3.8, showing that we have resolved various geological units with distinct infrared colors.

3.4.1 Surface Scattering and Geologic Features

Using information from the JPL Horizons ephemeris [Giorgini, 2015], we are able to determine the orientation of Europa at the time of observation, enabling us to compare our observations with previously published maps and other results. The central point in our images (known as the subobserver point) corresponds to 3.54°N latitude and 113° to 117°W longitude on Europa. The range in longitude of the subobserver point is due to the long integration time, as Europa's rotation period is approximately 3.5 days; correspondingly, in our hour-long integration time, Europa will have rotated by approximately 4°.

At the time of observation, the subsolar point was located at 3.38°N 125–129°W; this can similar be described in terms of position angle in degrees and distance from the subobserver point in arcseconds, 72.53° and 0.09″. $> 98\%$ of Europa's surface was illuminated, with a solar phase angle $\alpha = 11.74$. Europa's North Pole, in terms of PA and distance from the subobserver point, was 342° and 0.432″. The disk of Europa had an angular diameter of 0.867″ and was separated from Jupiter by 169″ to 174.7″ during the observations. Currently, we do not correct for solar illumination, but plan to do so in future work, similar to the photometric correction in King et al. [2022]; this correction will affect the polarized intensity images, but not polarization fraction.

The known orientation of Europa implies that two known geographical features — Powys Regio and Tara Regio, as shown in Figure 3.9 — should be present in our images. Powys Regio and Tara Regio are regions of mottled chaos material, although Tara Regio also contains units of high-relative-brightness chaos material [Doggett et al., 2009]. "Chaos" on Europa refers to areas with disrupted ice, possibly originating from areas of shallow subsurface water [Schmidt et al., 2011]; this type of geologic structure potentially differs in composition and grain size from less disturbed areas on the surface, which are coated in irradiated sodium chloride [Trumbo et al., 2019], and therefore may present different polarimetric properties (e.g. degree of linear polarization, phase curve structure [Poch et al., 2018]). Tara Regio is an

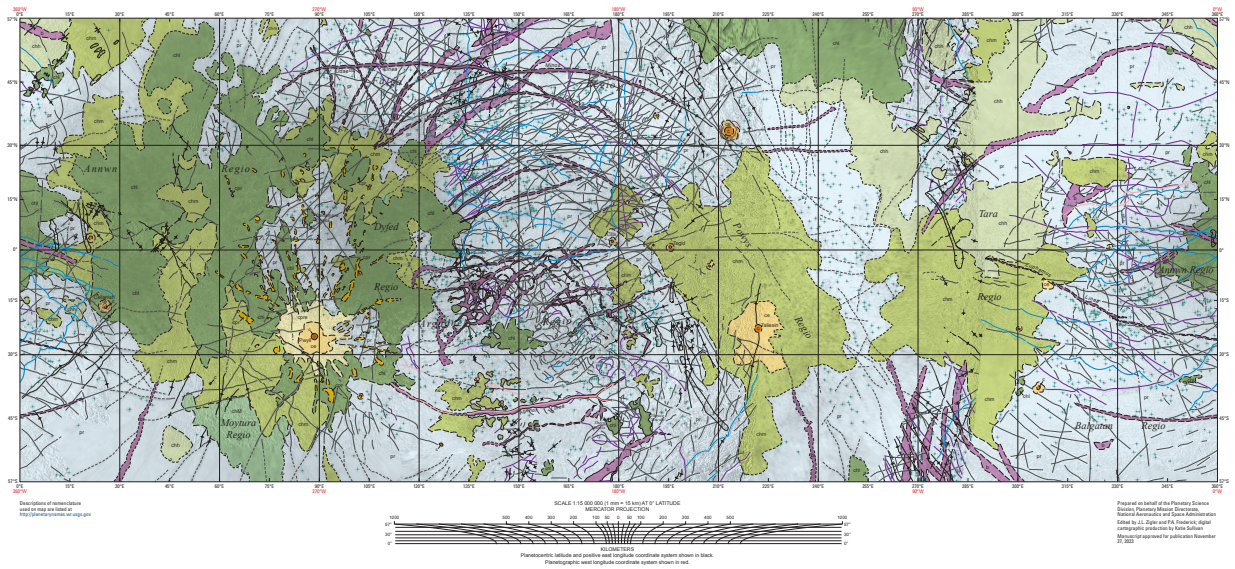

Figure 3.9: U.S. Geological Survey (USGS) geologic map of Europa's surface [Leonard et al., 2024]. At the time of our observations, the sub-observer point was located at approximately 3.5° N, 113 to 117° W. Due to the long integration time ($\sim$ 1 hour), surface features are slightly blurred, as Europa rotated by nearly 5 degrees longitude; however, there are brighter patches visible in our images, possibly corresponding to Powys Regio and Tara Regio. The subsolar point at the time of observations was approximately 3.4° N, 127° W.

area of particular interest due to the recent discovery of a concentration of CO_2 via *JWST* observations, which suggests interactions with the subsurface ocean [Trumbo and Brown, 2023]. Additionally, several large bands — locations where the terrain has been fractured by tectonic forces, likely due to a convecting layer of ice — are present to the South of Tara Regio [Howell and Pappalardo, 2018].

Previously, polarimetry has been used to determine properties of the surface ice of Europa, dating back to the 1970s when polarimetric observations supported the idea of a water ice surface [Dollfus, 1975]. Disk-integrated polarimetry has traced the surface polarization's behavior with phase angle α (e.g. Kiselev et al. [2009, 2017, 2022]), and our average degree of linear polarization across the surface is roughly in alignment with this work. Kiselev et al.

[2022] reports a degree of linear polarization of ≈0.1% for a phase angle of 11–12°, broadly in agreement with our measured values of 0.175±0.135%, 0.193±0.128%, and 0.248±0.087% for J, H, and K bands respectively. Measurements of polarization at various phase angles constrain the shape of the negative branch of polarization, which provides information on the size and scattering behavior of the grains; Kiselev et al. [2022] determined this polarization corresponds to backscattering off microscopic icy grains with a single-scattering albedo ∼0.985.

Other laboratory work has suggested that polarimetry can provide insight into not only grain size, but also the degree of sintering on an icy surface such as Europa's [Poch et al., 2018, Cerubini et al., 2018, 2020]. Sintering is the modification of ice grains' shapes as they are exposed to warmer temperatures, where they grow and coalesce to create a hardened icy surface; more sintered grains are larger, and depart from the spherical grain shape often assumed in Mie scattering calculations. This leads to changes in both the shape of the scattering phase curve and the degree of linear polarization; in particular, laboratory measurements have shown that the minimum depth of the negative portion of the polarimetric phase curve is shallower for larger grains, and the angle at which that minimum occurs decreases with sintering [Poch et al., 2018]. The properties of Europa's polarimetric phase curve suggest that it may have coarser and more sintered grains than other icy worlds like Enceladus [Poch et al., 2018]. With this resolved multiband polarimetric imaging from SCExAO/CHARIS, we can now investigate relationships between degree of polarization, spectroscopy, and more within distinct geographical units on Europa's surface. Similar work has been proposed in the visible with *HST*, describing how such an investigtion can provide insight into the porosity, composition, size, and shape of the icy regolith and even perhaps identify regions of recent ocean-surface ice interactions [Sparks et al., 2022]. Our infrared SCExAO/CHARIS data will complement those from *Hubble*, and may be compared to high spectral resolution infrared data such as those from VLT/SINFONI [Ligier et al., 2016].

3.4.2 Constraints on Plume Activity

The possibilities of cryovolcanism and the resulting water ice plumes are perhaps the most tantalizing subject within Europa's geology. As described earlier, there has not yet been an undisputed detection of plume activity on Europa; however, estimates from *HST* in 2014 claim observations consistent with a 10^{20} m^{-2} column density plume (similar to the column density of Enceladus plumes) 200 km in height [Roth et al., 2014, Paganini et al., 2020]. Such activity on Europa must also be weaker or more intermittent than that of Enceladus to account for the numerous non-detections of plumes over the past two decades. Additionally, recent observations with *JWST* did not detect plume activity, suggesting that any plumes on Europa are infrequent and/or quite weak [Villanueva et al., 2023].

Given the lack of plume detections on Europa, the majority of modeling of such processes has been done for Enceladus. Plumes on Enceladus are known to be quite consistent and quite large [Hansen et al., 2006], and therefore we have more information about their composition and other characteristics; from both in-situ measurements with *Cassini* and space telescope observations (e.g. *JWST*), these plumes have a measured flow rate of ∼300 kg/s. They originate from Enceladus's "tiger stripe" features, which have a spatial extent of approximately 100 km on the moon's surface, and can reach heights of up to 10,000 km [Hemingway et al., 2020, Villanueva et al., 2023]. These plumes are mainly composed of water, but have small amounts of CO, NH_3, C_2H_2, C_2H_4, CH_3OH, and O_2; they have a column density of 10^{14} to 10^{17} cm^{-2} depending on the molecular species [Hansen et al., 2020]. A majority of these particles are thought to be around 1 micron in size [Keat Yeoh et al., 2010].

With such small ice grains, we would expect the light scattered off of water ice plumes to be quite polarized according to Mie theory, in strong contrast with the low polarization of surface scattering described in the previous section. To calculate the polarization fraction and scattered intensity from a collection of grains originating from a plume, we use `pymiescatt` [Sumlin et al., 2018], a Python implementation of Bohren and Huffman's BHMIE code

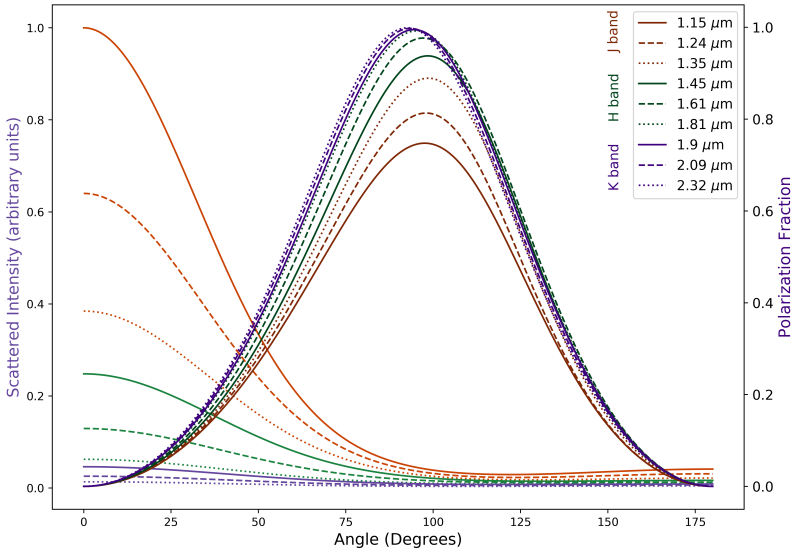

Figure 3.10: Normalized scattered intensity and polarization fraction for a distribution of water ice grains with diameters and number density as reported in [Keat Yeoh et al., 2010], computed using Mie theory for the approximate minimum, effective, and maximum wavelengths in J, H, and K bands and assuming unpolarized incident light. In H and K bands, the polarization fraction for scattering off water ice grains approaches 1.

which computes scattering efficiencies, angular scattering functions, and scattering matrix elements using Mie theory [Bohren and Huffman, 2008]. Assuming spherical grains with a given radius and number density (based on the particle size distribution of Enceladus-like plumes, as in Keat Yeoh et al. [2010] and McCullough et al. [2020]), and using the refractive index of water ice (1.31), we calculate curves of scattered intensity and polarization fraction versus scattering angle at J, H, and K bands as shown in Figure 3.10, illustrating the high polarization fractions expected for a collection of small ice particles.

It is worth noting, however, that the highest polarization fractions occur for scattering angles near 90° under Rayleigh scattering. If we assume there is only single scattering off an Enceladus-like plume, the range of scattering angles available is quite small due to the restrictions of the solar phase angle α; for Europa, the phase angle is at most $\approx$12°, which

corresponds to a scattering angle of ≈168°. Given that micron-sized grains are quite forward-scattering, such a high scattering angle corresponds to not only a low polarization fraction (<10%), but a lower overall scattered intensity; this is evident again in Figure 3.10. This polarization fraction may still be substantially larger than that of scattering off the surface ice, but the lower overall intensity would increase the difficulty of resolving a signal against the bright ($\sim$ 5 mag) background disk of Europa.

There is another case to consider on Europa that provides access to a much larger range of scattering angles, and thus a potentially higher polarization fraction for light scattered off the plumes. Light that initially scatters off Europa's icy surface (and is very slightly polarized) can then encounter the plume and become further polarized, which we refer to as the"double-scattering" scenario. The two cases of single scattering and double-scattering scattering are illustrated in Figure 3.11. A polarized signal from an icy plume would be dominated by the latter scenario.

Previous work by McCullough et al. [2020] predicted a plume signal on Europa — assuming an Enceladus-sized eruption and the above described double-scattering scenario — on the order of 10^{-15} W/m^2, with exact values depending on the solar phase angle at time of observation and the plume's location on the surface relative to the subsolar point. That work determined that such a plume should be detectable with the Gemini Planet Imager (GPI) [Macintosh et al., 2014b] with a signal-to-noise ratio of 7σ with a half-hour of observing time in H band.

Such a bright plume signal should similarly be readily observable with CHARIS in our 48 minute integration time. To isolate the plume signal, we attempt two approaches: calculating the polarization fraction (PF) and using a high-pass filter (HPF) on the polarized intensity (PI) images. To compute the polarization fraction, we divide the PI images by the double sum total intensity images (Stokes I), as shown in Figure 3.12. As a simple HPF, we subtract a version of the data smoothed with a σ=5 Gaussian from the image, shown in Figure 3.13.

A small bright feature at Δ RA 0.25" Δ Dec -0.15" is present only in polarization fraction

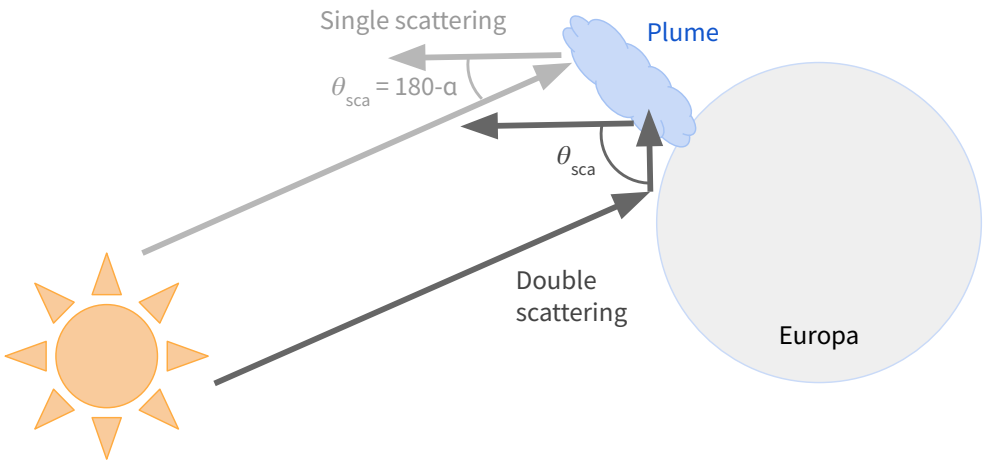

Figure 3.11: A cartoon illustrating the two scattering scenarios considered for a plume on Europa, reproduced from McCullough et al. [2020]. In the single scattering scenario, incident solar radiation directly scatters off the ice grains of the plume; due to the small solar phase angles at Europa's distance (α <12°), this mechanism has large scattering angles and therefore a lower polarization fraction and scattering efficiency. In the "double-scattering" scenario, incident light first reflects off Europa's surface before encountering the plume. This mechanism allows for a much larger range of scattering angles. It is worth noting that although this simple diagram is in 2D, the double scattering does not necessarily occur in a single plane.

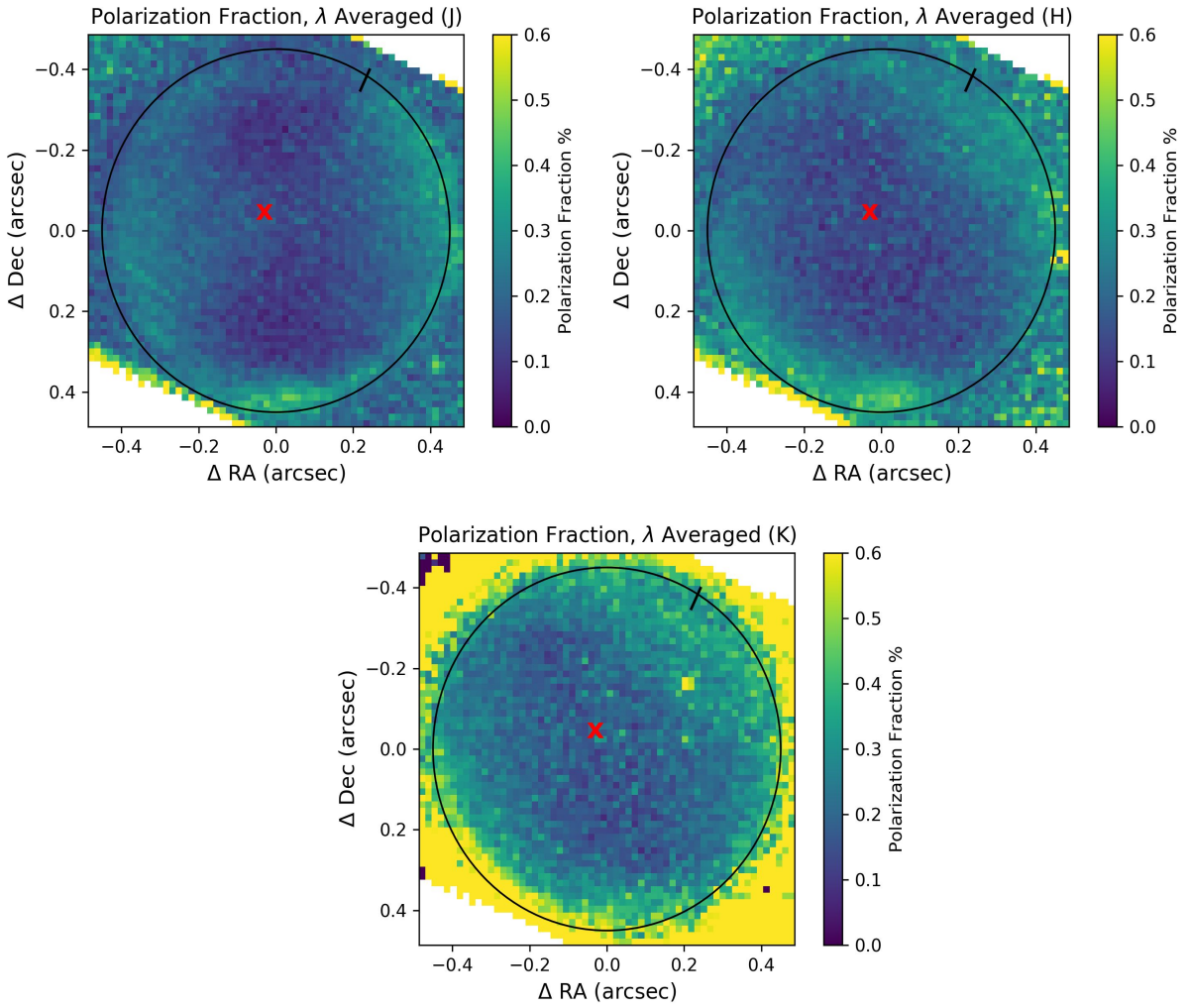

Figure 3.12: Average polarization fraction in each wavelength channel from the broadband $J/H/K$ CHARIS observations, with the disk of Europa approximately indicated with a circle and the North Pole (black dash) and subsolar point (red $\times$) marked. For $J/H/K$, our initial measurements of the average polarization fractions across the disk are 0.175±0.135%, 0.193±0.128%, and 0.248±0.087% respectively. Two notable features stand out: a circular marking at the bottom of the disk present across wavelength channels with a polarization fraction of roughly 0.4–0.5%, and a bright spot about 0.1″ from the North Pole only present in K band. Although the latter is likely an artifact as it is only present in one filter (K), the former may be a real astrophysical signal of unknown origin.

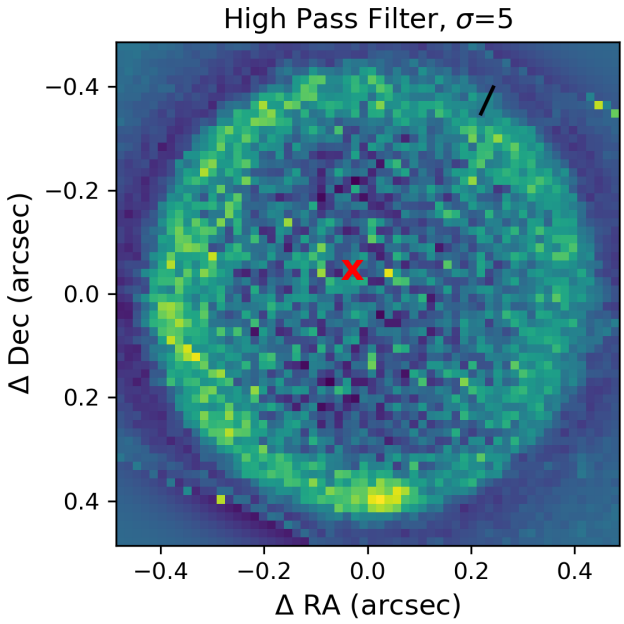

Figure 3.13: High-pass filtered image of Europa in polarized intensity (PI) averaged over $J/H/K$ bands. A bright marking at the bottom of the disk as seen in the image may be an astrophysical signal of interest; further work is needed to determine its nature. Approximate North Pole and subsolar point are marked as in other images in this section.

averaged over K band, but not the high-pass filtered images nor J and H polarization fraction; its extent is also smaller than 1 λ/D. As such, we regard it as a likely instrumental artifact.

An ovoid feature at Δ RA 0.1" Δ Dec 0.4" appears in the average polarization fraction for J, H, and K bands, as well as in a high-pass-filtered $J/H/K$ averaged polarized intensity image; this feature has a polarization fraction of roughly 0.4-0.5%, and further work is needed to determine its nature, as well as to place constraints on the presence and strength of plumes based on this imagery.

3.5 Conclusions and Future Work

In this chapter, I have presented the collection, reduction, and preliminary analysis of novel imagery of Europa's surface in polarized light using Subaru SCExAO/CHARIS. These data are the first disk-resolved multiband infrared imaging polarimetry of Europa to be published, and have potential to provide insight into the composition, grain size, degree of sintering, and more for Europa's icy regolith. Additionally, these data will be used to place constraints on cryovolcanic plume activity on Europa, as scattering off the micron-sized particulates in water ice plumes should present a strongly polarized signal, easily observable for an Enceladus-sized plume; this method may be useful for future monitoring of plumes, as ground-based observing is better suited to a long-term monitoring campaign than oversubscribed space telescope time.

At this time, preliminary data reduction and analysis reveals a region of interest on the Southeastern edge of Europa, although further investigation is needed to determine the true nature of this feature, whether it relates to surface geology, cryovolcanic activity, or another aspect of the Europa-Jupiter system. This investigation will include analysis of the feature's spectrum to learn more about its possible composition, as well as an analysis of the feature's presence and morphology across half-wave plate cycles; as described in Section 3.4.1, Europa

rotated by around 4° during our integration time, leading to a possible smearing of surface features, which we hope to mitigate by analyzing subsets of the full dataset.

To place real constraints on plume activity and determine if the feature of interest is consistent with plume activity, further improvements to the existing method of plume modeling from McCullough et al. [2020] are also necessary. Current modeling assumes a grain size distribution without a connection to underlying physical processes of cryovolcanism; we plan to apply theory of Europa's plume mechanics (e.g. Yeoh et al. [2015, 2017], Goldstein et al. [2018]) and existing software such as `DUDI` ("Dust Distribution," a Fortran-95 package modeling the ejection of material from a solar system body [Ershova and Schmidt, 2021, Ershova and Schmidt, 2021], translated into Python by undergraduate Eulrika Wu under my supervision in 2022 [Wu et al., 2023]) to predict plume signals and place constraints on plumes' size and perhaps their origin mechanism based on our observations. Additionally, prior modeling from McCullough et al. [2020] makes optimistic assumptions on the light incident on the plume in the double scattering scenario; we plan to undertake a more rigorous treatment of this scenario including polarization and attenuation from scattering off the surface, in addition to the already included albedo and surface illumination.

Additionally, there are a number of avenues for future work with this data set beyond the scope of this thesis, such as comparison to high-resolution spectroscopic mapping, description of the polarization of various compositional units, and measurements of infrared colors of various compositional units. We also have data from SCExAO/VAMPIRES [Norris et al., 2015, Lucas et al., 2022, Zhang et al., 2023] taken simultaneously with the SCExAO/CHARIS data presented within. These are visible light polarimetric images across four wavelength channels, and they provide an opportunity for future work to connect Europa's visible and infrared spectra from simultaneous observations and characterize geologic features; however, further work is needed to reduce the VAMPIRES data and correct for artifacts from instrumental polarization.

CHAPTER 4

Direct Spectroscopic Characterization of Cloudy L/T Transition Companion Brown Dwarf HIP 93398 B

4.1 Introduction

Brown dwarfs are substellar mass objects that may burn lithium or deuterium (∼13–∼80 $M_{\rm Jup}$), but are not sufficiently massive to sustain hydrogen fusion and enter the main sequence as a star [Hayashi and Nakano, 1963, Kumar, 1963]. Over their lifetimes, they cool and evolve through spectral types late-M, L, T, and Y [Marley, 1999, Mason, 2006]. Of particular interest is the L/T transition, a stage characterized by a major change in infrared color, but only a minor change in temperature; additionally, T dwarfs are characterized by methane absorption that is stronger in later-type objects [Burgasser et al., 2006b, Helling and Casewell, 2014]. As substellar objects cool, their atmospheric chemistries evolves, and various species of clouds are able to condense [Lodders and Fegley Jr, 2006, Kirkpatrick, 2005]. Multiple generations of substellar atmosphere models of increasing complexity in their treatment of atmospheric composition, cloud formation, and vertical transport, have been generated to describe the cooling evolution of brown dwarfs across their NIR spectra[Marley et al., 1996, Baraffe et al., 2002, Morley et al., 2014], such as the Sonora series of model grids [Marley et al., 2021, Morley et al., 2024, Mukherjee et al., 2024]. These models have also been used to estimate masses of directly-imaged substellar objects based on their observed luminosities and spectra. One of the key challenges of brown dwarf characterization is the degeneracy present between age, luminosity, and mass due to the way they cool over

time. Systems with independently-derived ages, masses, and spectral types are therefore key benchmarks for testing substellar atmosphere models, especially as these models increase in complexity, including factors such as disequilibrium chemistry and clouds [Marley and Robinson, 2015, Morley et al., 2024, Mukherjee et al., 2024].

Informed direct imaging searches using the Hipparcos-Gaia Catalog of Accelerations [Brandt, 2018, 2021] have recently yielded numerous discoveries of new brown dwarf companions [Fontanive et al., 2019, Bonavita et al., 2022, Franson and Bowler, 2023], including some that are amenable for direct spectroscopy such as those observed with the SCExAO/CHARIS instrument at Subaru Observatory [Guyon et al., 2010, Groff et al., 2016, Swimmer et al., 2022, Currie et al., 2021, Kuzuhara et al., 2022, Chilcote et al., 2021]. For systems with radial velocity measurements, it is also possible to determine a companion's dynamical mass, a measurement independent of models describing an object's luminosity evolution [Brandt et al., 2019]. To date, around 30 brown dwarf companions have been imaged and characterized using these combined techniques [Li et al., 2023].

Modeling the atmospheres of L/T transition objects has been a challenge for decades; accurate models require thorough line lists for a variety of molecules, many of which have only recently become available, and a consideration of many parameters, particularly gravity and metallicity, to which resulting spectra are quite sensitive [Morley et al., 2024]. Additionally, the treatment of clouds has been a major issue facing substellar atmosphere models, especially in finding self-consistent evolutionary and spectral models. Until recently, many models assumed cloud-free atmospheres, despite the fact that disequilibrium chemistry and clouds are known to be important factors in brown dwarf atmospheres, especially for L/T transition objects [Marley and Robinson, 2015].

Many brown dwarfs do agree with evolutionary models, supporting the models' validity (e.g. ε Indi BC; Chen et al. 2022). However, a few recently discovered T dwarfs show a slight tension with models (e.g. Oppenheimer et al. [1995], Cheetham et al. [2018], Bowler et al. [2021]). It has been suggested that this tension may be a result of an unresolved additional

companion, contributing to the measured mass but not substantially to the luminosity and observed spectrum. Alternatively, this tension may be due to missing physics in atmosphere models.

The massive companion brown dwarf HIP 93398 B was initially discovered with Keck/NIRC2 by Li et al. [2023] as one of the first objects whose location was predicted from radial velocity and astrometric accelerations prior to imaging, and suggested as another T dwarf in tension with evolution models. Here, we present follow-up imaging and spectroscopy of the object using Subaru SCExAO/CHARIS [Guyon et al., 2010, Groff et al., 2016]. We aim to more confidently establish this object's spectral type, determining whether or not it is in tension with brown dwarf cooling models as previously suggested. With a well-constrained dynamical mass and known spectral type, HIP 93398 B has the potential to serve as a benchmark brown dwarf for testing substellar atmosphere models.

In this work, we begin with an overview of the system's properties, including previously published information on the companion HIP 93398 B from the recent initial discovery by Li et al. [2023], in Section 4.2. We describe our new observations of the object using Subaru SCExAO/CHARIS in Section 4.3. Section 4.4 presents an update to the companion's orbital fit, and Section 4.5 presents spectral typing and photometry of HIP 93398 B, as well as a comparison to the newly updated Sonora Diamondback [Morley et al., 2024] substellar atmosphere models, which include both evolutionary and spectral models with clouds for warm L and early T dwarfs. Finally, we discuss the implications of these findings for the "overmassive T dwarf" problem and conclude in Section 4.6.

4.2 System Properties

HIP 93398 (HD 176535) is a main-sequence K3.5V star [Gondoin, 2020] at a distance of 36.99±0.03 parsecs, as measured by *Gaia* EDR3 [Gaia Collaboration et al., 2022]. Its properties are summarized in Table 4.1. This star has multiple age estimates with large

uncertainties, but no conclusive precise value. Measurements of the chromospheric index $\log R'_{\rm HK} = -4.732$ indicate that this star is old and inactive, with a weakly constrained age of 5.57 ± 4.84 Gyr [Gomes da Silva et al., 2021]. The system's isochronal age, based on a sample of FGK stars from the HARPS sample with *Gaia* parallaxes and using the PAdova and TRieste Stellar Evolution Code (PARSEC) [Bressan et al., 2012], is 5.21±4.68 Gyr [Delgado Mena et al., 2019b]. Meanwhile, the *Gaia* collaboration measures an isochronal age of $3.34^{+6.97}_{-0.61}$ Gyr with the PARSEC isochrones and their Fitting Location of Age and Mass with Evolution (FLAME) model [Gaia Collaboration et al., 2022]. Recent work from Li et al. [2023] uses S-index values of 0.43 [Gomes da Silva et al., 2021] and 0.63 [Delgado Mena et al., 2019b] and Bayesian-based method for age estimation developed by Brandt et al. [2014] to estimate an age of $3.59^{+0.87}_{-1.15}$ Gyr. In this paper, we adopt an age assumption of $3.59^{+0.87}_{-1.15}$ Gyr as in Li et al. [2023].

The recently discovered brown dwarf companion HIP 93398 B was inferred to be a T dwarf based on its age, mass, and luminosity [Li et al., 2023]. According to that work, the companion is on a $41.3^{+3.6}_{-3.1}$ year orbit, with a measured dynamical mass of $65.9^{+2.0}_{-1.7}\,M_{\rm Jup}$. The companion's other known properties are also listed in Table 4.2. This was one of the first companions with an astrometric location known prior to direct imaging. However, based on its derived bolometric luminosity (obtained by estimating W1 from L' and using relationships between W1 and bolometric luminosity), it is somewhat overmassive compared to expectations from evolutionary models, possibly indicating a tension between models and observations or that the companion is actually an unresolved binary [Li et al., 2023].

Property	Value	References
Host Star (A)		
ϖ (mas)	27.033±0.018	1
Distance (pc)	36.99±0.03	1
SpT	K3.5V	2,3
Mass ($M_\odot$)	0.72±0.02	4,5
Age (Gyr)	$3.59^{+0.87}_{-1.15}$	12
T_{eff} (K)	4727±104	6
[Fe/H] (dex)	-0.15±0.07	7
log(R'_{HK}) (dex)	-4.85	8
R'_X (dex)	<-4.28	9
log$g$ (dex)	$4.64^{+0.0846}_{-1.203}$	14
Gaia RUWE	1.019	1
Luminosity ($L_\odot$)	0.208±0.007	12
Gaia G (mag)	9.374±0.003	1
B_T (mag)	11.195±0.066	10
V_T (mag)	9.923±0.035	10
J (mag)	7.804±0.027	11
H (mag)	7.313±0.033	11
K_s (mag)	7.175±0.020	11

Table 4.1: Table summarizing the previously known and new properties of the host star HIP 93398 B. References abbreviated as (1) Gaia Collaboration et al. [2020a]; (2) Gray et al. [2006]; (3) Bourgés et al. [2014]; (4) Reiners and Zechmeister [2020]; (5) Delgado Mena et al. [2019a]; (6) Sousa et al. [2011]; (7) Gáspár et al. [2016]; (8) Pace [2013]; (9) Voges et al. [1999]; (10) Høg [2000]; (11) Cutri et al. [2003]; (12) Li et al. [2023]; (13) this work; and (14) Stassun [2019].

Companion (B)		
SpT	L9.0	13
Mass ($M_{\rm Jup}$)	$65.9^{+2.0}_{-1.7}$	12
H apparent (mag)	16.51±0.07	13
H absolute (mag)	13.67±0.07	13
J apparent (mag)	17.54±0.33	13
J absolute (mag)	14.70±0.33	13
L' apparent (mag)	16.31±0.07	12
L' absolute (mag)	13.47±0.07	12
$\log(L_{\rm bol}/L_{\odot})$	-5.26±0.07	12
Semimajor axis (AU)	$11.05^{+0.64}_{-0.56}$	12
Inclination (°)	$48.9^{+3.4}_{-3.7}$	12
Period (yr)	$40.6^{+3.9}_{-3.5}$	12
Eccentricity	$0.496^{+0.022}_{-0.020}$	12
Temperature (K)	1300^{+81}_{-150}	13

Table 4.2: Table summarizing the previously known and new properties of the companion HIP 93398 B. References abbreviated as (1) Gaia Collaboration et al. [2020a]; (2) Gray et al. [2006]; (3) Bourgés et al. [2014]; (4) Reiners and Zechmeister [2020]; (5) Delgado Mena et al. [2019a]; (6) Sousa et al. [2011]; (7) Gáspár et al. [2016]; (8) Pace [2013]; (9) Voges et al. [1999]; (10) Høg [2000]; (11) Cutri et al. [2003]; (12) Li et al. [2023]; (13) this work; and (14) Stassun [2019].

4.3 Observations and Data Reduction

The HD 176535 system was previously observed with the ESO HARPS spectrograph [Mayor et al., 2003, Trifonov et al., 2020] for radial velocity measurements, and its astrometric acceleration was identified via *Hipparcos* and *Gaia* data in the Hipparcos-Gaia Catalog of Accelerations [Brandt, 2018, 2021], allowing for the prediction of the astrometric location of the B companion in Li et al. [2023]. Li et al. [2023] also obtained L' band Keck/NIRC2 AO imaging data of the system, revealing the companion at the predicted astrometric location. In this work, we add follow-up imaging spectroscopy using the Coronagraphic High Angular Resolution Imaging Spectrograph [CHARIS, Groff et al., 2016] behind the Subaru Coronagraphic Extreme Adaptive Optics [SCExAO, Guyon et al., 2010, Jovanovic et al., 2015c] system on the 8.2-meter Subaru Telescope on Maunakea in Hawai'i.

4.3.1 SCExAO/CHARIS High-Contrast Imaging & Spectroscopy

We observed HIP 93398 on 2022 October 7 UTC in CHARIS broadband mode (simultaneous observations in J, H, and K bands – 1.16-2.37 μm with R$\sim$18 [Groff et al., 2016] and high-resolution H-band (centered on 1.63 μm, $R \approx 65$). We additionally acquired high-resolution J-band data (centered on 1.24 μm with $R \approx 75$) on 2023 September 1 UTC. Seeing conditions were a steady $\sim$0.″5 across the 2022 night and were variable between $\sim$0.″5-0.″8 on the 2023 night , according to the MASS/DIMM data available from the CFHT seeing and mass profile records. The individual exposure time was 60 seconds for broadband, 40 seconds for J band, and 60 seconds for H band, with total on-source integration times of 34 minutes, 80 minutes, and 82 minutes. All observations were taken with the instrument's 139 mas coronagraph. Observations and measured companion characteristics are summarized in Table 4.3.

For these observations, an initial wavefront correction was applied by AO188 [Hayano et al., 2008], followed by higher-order corrections from SCExAO [Guyon et al., 2010, Jovanovic et al., 2015c]. A Lyot coronagraph within SCExAO with $3\lambda/D$ inner working angle

Filter	Date (UT)	Sep.(mas)	PA (°)
Broadband	2022-10-07	368 ± 11	96.7 ± 1.0
H	2022-10-07	370 ± 11	96.7 ± 1.0
J	2023-09-01	387 ± 11	99.9 ± 1.0

Table 4.3: SCExAO/CHARIS observations and relative astrometry of HIP 93398 AB. Similar to Li et al. [2023], we adopt 3% fractional errors for separation and 3% for position angle.

then masks the central star for observation with the CHARIS integral field spectrograph (IFS). The IFS allows for spectral differential imaging (SDI; Oppenheimer and Hinkley 2009), and the observations were performed using SCExAO's pupil-tracking mode to enable angular differential imaging (ADI; Marois et al. 2006). All observations also included "satellite spots" created by modulations imposed on the SCExAO deformable mirror for astrometric and spectrophotometric calibration, using a $15\lambda/D$ separation and 0.05 μm amplitude [Jovanovic et al., 2015a, Sahoo et al., 2020].

4.3.2 Data Reduction with CHARIS-DEP & pyklip-CHARIS

Data cubes (with wavelength as the third dimension) were extracted from the raw CHARIS data and calibrated using the instrument's standard pipeline (`CHARIS-DEP`) from Brandt et al. [2017], which includes crosstalk corrections and removal of correlated noise. We then performed PSF subtraction using `pyklip-CHARIS` [Chen et al., 2023][1].

First, `pyklip-CHARIS` uses the satellite spots to locate the image centroid in preparation for Karhunen-Loéve Image Processing (KLIP) [Soummer et al., 2012]. We perform KLIP using both ADI and SDI with the following parameters: 9 annuli, 4 subsections, 1 pixel movement, and 1, 20, and 50 as the maximum number of basis vectors used in noise reconstruction for PSF subtraction. The KLIP PSF-subtracted images are shown in Figure

[1]Detailed information and tutorials on CHARIS-specific additions to `pyklip` can be found at `https://pyklip.readthedocs.io/en/latest/instruments/CHARIS.html`

4.1.

After the initial KLIP reduction, we perform forward modeling (KLIP-FM, Pueyo [2016], Wang et al. [2016]) to model the companion PSF and fit for its astrometry, testing 1, 20, and 50 KL modes to find a balance between oversubtraction and sufficient noise removal. Using an estimate of the companion's location and a known instrumental PSF, KLIP-FM produces the PSF-subtracted image from data and a forward-modeled companion PSF at the estimated location. We then convert the PSF model flux to the flux of the unocculted star using the satellite spot flux and a known reference-spot-to-star ratio as reported in Currie et al. [2020]. Pending calibration results from the CHARIS team indicate that this ratio may not be stable over time, and as a result we use the latest value for data taken with the default satellite spot modulation frequency after May 2022 of $1.25\times10^{-3} \pm 1.30 \times 10^{-4}$ (Kellen Lawson & Thayne Currie, priv. comm., Currie et al. [2020]).

The forward model is then fit using a Markov-Chain Monte Carlo (MCMC; implemented in `emcee` from Foreman-Mackey et al. 2013) to approximate the posteriors of the RA and Dec offsets, a flux scaling factor for the model, the companion separation, and the position angle (PA). For this MCMC implementation, we use uniform priors, 100 walkers with 2000 steps, 400 of which are discarded as burn-in. The maximum likelihood values of the posteriors from the MCMC are adopted as the raw astrometric values, i.e. before including instrumental calibration uncertainties. For CHARIS, we use uncertainties of 0.05 mas (30% of a lenslet) on the position of the central star, a lenslet scale of 16.15±0.10 mas/lenslet [Kuzuhara et al., 2022], the uncertainty of the aforementioned satellite spot/host star contrast, and a PA offset of $2\overset{\circ}{.}0 \pm 0\overset{\circ}{.}4$ [Chen et al., 2023].

KLIP-FM also allows us to extract the companion's spectrum, which, for the broadband data, we then convert from contrast to physical units. This requires the observed magnitude of the host star (listed in Table 4.3), the contrast between the unocculted star and our PSF model, and a stellar model spectrum for the host star, for which we use a Castelli/Kurucz model [Castelli and Kurucz, 2003] implemented in `pysynphot` [STScI Development Team,

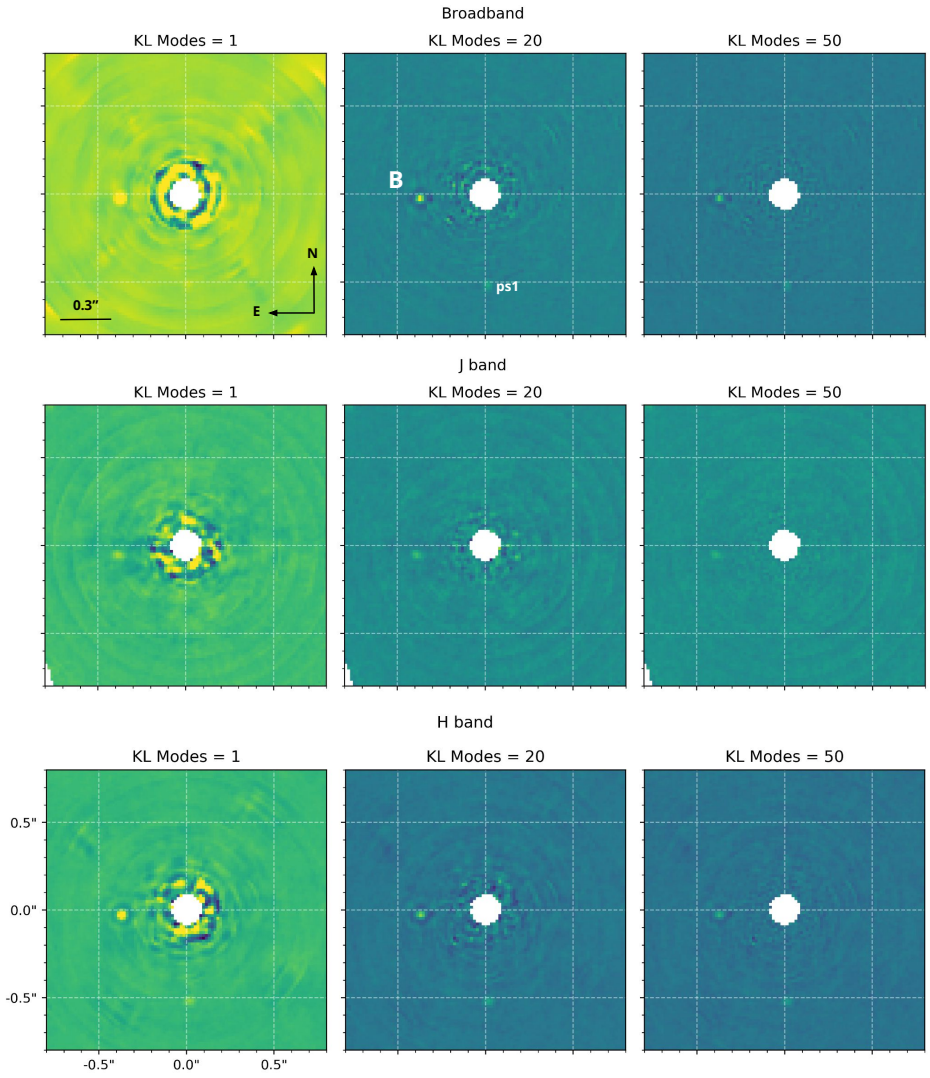

Figure 4.1: PSF-subtracted images of HIP 93398 B as seen with SCExAO/CHARIS in broadband (top), J band (middle), and H band (bottom). Each set of images shows the reduction with 1 KL mode, 20 KL modes, and 50 KL modes. The more KL modes included, the higher the risk of oversubtraction. A second, fainter point source (labeled as ps1) is also visible in the 2022 broadband and H-band images; this is investigated and found to be a background source in Section 4.3.3. J and H band are shown with the same color stretch (maximum value = 20, arbitrary units/detector counts), while broadband uses a different scaling (maximum value = 50).

2013] with stellar parameters $T_{\rm eff} = 4727\,{\rm K}$, [Fe/H] $= -0.15$, and $\log g = 4.64$ as referenced in Table 4.1 above. This calibration can be expressed as

$$F_{\rm companion} = \frac{F_{\rm companion}}{F_{\rm spot}} \times \frac{F_{\rm spot}}{F_{\rm star}} \times F_{\rm star}, \tag{4.1}$$

where $F_{\rm companion}/F_{\rm spot}$ is the raw contrast spectrum previously extracted, $F_{\rm spot}F_{\rm star}$ is the star-to-spot ratio previously used, and $F_{\rm star}$ is the stellar model flux calibrated to the observed magnitude. This results in a calibrated spectrum in flux density units, F_λ (erg s^{-1} cm^{-2} Å^{-1}). Error bars on this spectrum are estimated by injecting and recovering synthetic sources at an annulus of the same separation as the companion, resulting in the spectrum shown in Figure 4.2. We do not report an absolute flux calibration for J band, due to the poorer quality of the J-band data resulting from variable seeing during those observations. Additionally, the H-band absolute flux calibration differs slightly from the broadband calibration. We have included this difference in the error on our reported H band magnitude; however, for color measurements, we use H and J both derived from broadband, as the relative calibration between bands in that observation is more reliable. In Figure 4.2, include both H and J spectral data with an arbitrary scaling factor to compare their overall shape with that of the calibrated broadband and H band spectra. Subtle differences in the spectra as shown in Figure 4.2 should be interpreted with caution, as no color correction has been applied to account for the different bandpasses between the higher-resolution and broadband modes; additionally, the discrepancy between the H band and broadband data is larger than it appears in Figure 4.2, but is included in the error budget on our derived photometry.

4.3.3 Background Object Identification

An additional point source with an H-band apparent magnitude of ∼17 was detected in the 2022 data set at $180° \pm 5.0$4 PA and 515 ± 15.5 mas separation in the broadband and H-band images. We believe this to be a background object, based on its spectrum as shown in Figure 4.3. We perform a least squares fit to a grid of normalized Castelli-Kurucz model

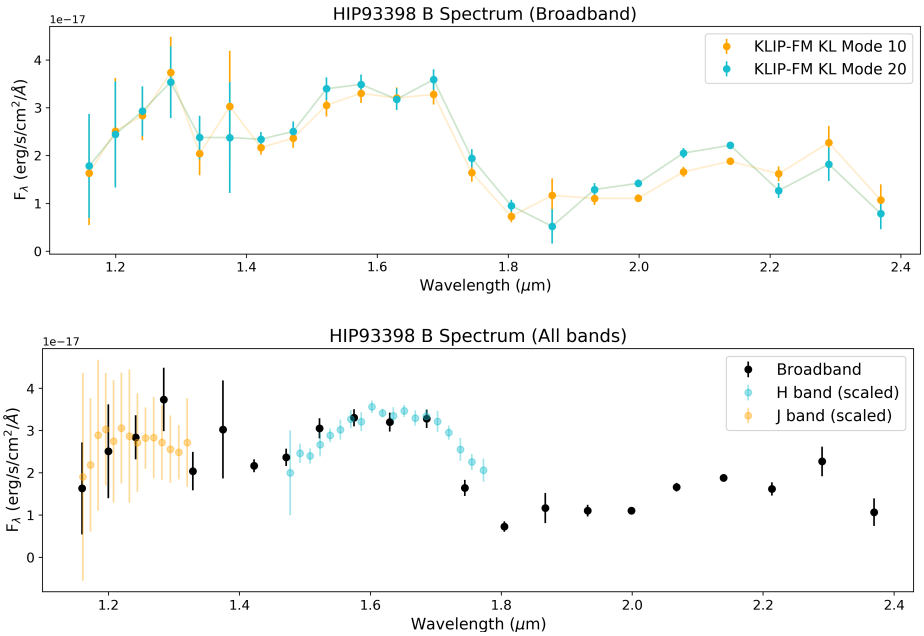

Figure 4.2: Extracted spectra of HIP 93398 B from the broadband and high-resolution H-band data. Methane absorption features are visible at 1.6 and 2.2 μm. (Top) Two extractions are shown: one using 10 KL modes in the reduction (orange), and one using 20 KL modes (blue). (Bottom) Broadband data with J- and H-band high resolution superimposed on top, and scaled to near the broadband flux calibration for illustration purposes. It is worth noting that the J and H band data points are not necessarily directly comparable to the broadband data points, as these are monochromatic flux densities over a finite bandpass and no color correction has been applied.

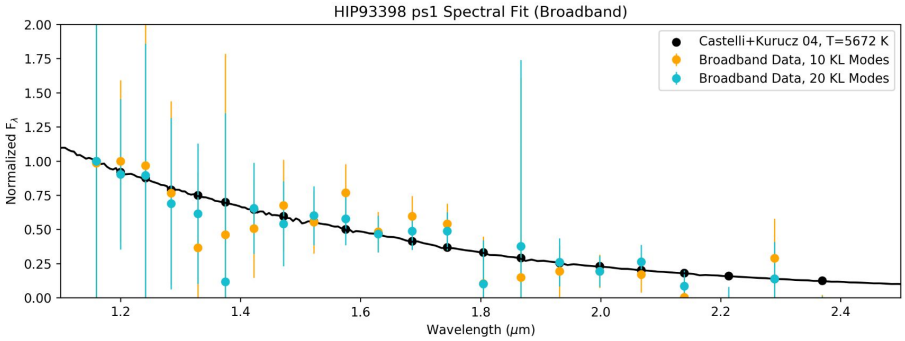

Figure 4.3: Extracted spectrum of HIP 93398 C from our SCExAO/CHARIS broadband data shown with Castelli-Kurucz 04 model stellar atmosphere fits [Castelli and Kurucz, 2004]. The best fit model atmospheres indicate a stellar object with a temperature between 3800-5700 K.

stellar atmospheres [Castelli and Kurucz, 2004] for the broadband and H-band data each separately, as well as together using all available data. The best fit model ($\chi^2_\nu = 0.13$) to the broadband data is a star with $T_{\rm eff} = 5672\,{\rm K}$, solar metallicity, and $\log g = 4.95$. As a result, we conclude that this is likely a background star with temperature 3800-5700 K.

Using our broadband data, we determine an observed apparent K-band magnitude of 18.6±1.37. We use this apparent K-band magnitude to determine a distance estimate using the surface brightness color relation, as described in Pietrzyński et al. [2019]. For this calculation, we assume a $V - K$ color (1.53) and radius ($0.93 R_\odot$) typical for a star near the best fit temperature [Cox, 2015, Zombeck, 2006], and derive a distance of ≈10.4 kpc, a reasonable distance for a background star in the direction of the Galactic center.

Given the lack of a second detection in the 2023 dataset, we are also unable to establish common proper motion for this point source with the host star; however, due to the poor seeing conditions of the 2023 J-band epoch, we also cannot use this non-detection to rule out common proper motion.

4.4 Orbital Fitting

Li et al. [2023] indicated a need for future data to further refine the orbital constraints for HIP 93398 B. Our recent epoch of data from 2023 Sept 1 is sufficiently removed from the observations in Li et al. [2023] that the object would have shown substantial motion (≈2-3° PA and 0.2" separation); accordingly, we perform a joint fit using our new epoch of relative astrometry from Subaru/CHARIS, existing Keck/NIRC2 relative astrometry [Li et al., 2023], HARPS radial velocities (RVs) [Trifonov et al., 2020], and stellar absolute astrometry from the HGCA [Brandt, 2018, 2021, Gaia Collaboration et al., 2020b, 2022].We do not include our 2022 Subaru/CHARIS astrometry in the fit, as it does not provide additional leverage and, although consistent, has larger errors than the existing 2022 Keck/NIRC2 relative astrometry.

We fit this combined data using the Bayesian orbit fitting code `orvara` [Brandt et al., 2021], which fits Keplerian orbits using the `ptemcee` parallel-tempered affine-invariant MCMC algorithm [Vousden et al., 2016, Foreman-Mackey et al., 2013] and nine parameters describing the companion's orbit: semi-major axis (a), inclination (i), longitude of ascending node (Ω), time of periastron passage (T_0), eccentricity and argument of periastron ($\sqrt{e}\sin\omega$ and $\sqrt{e}\cos\omega$), companion (secondary) mass (M_s), and host star mass (M_*). We use log-uniform priors for semi-major axis and companion mass, a geometric prior for inclination, and a Gaussian prior for host star mass based on previously published stellar mass values of 0.72 ± 0.02 $M_\odot$. For this MCMC, we use 10 temperatures, 100 walkers, 200,000 steps, and discard 500 of those steps as burn-in. Figure 4.4 illustrates the orbital fit for HIP 93398 B using `orvara`, compared with both absolute and relative astrometry. Our orbital fit is in agreement with that of Li et al. [2023] within 1σ.

As a check for consistency, we additionally fit for the orbit of HIP 93398 B using the HGCA module of `orbitize!` [Blunt et al., 2020], an alternative open-source orbit fitting code for directly imaged objects. By default, `orbitize!` uses uniform priors, except for

Parameter	Li et al. [2023]	This Work (orvara)	This Work (orbitize!)
Mass ($M_{\rm Jup}$)	$65.9^{+2.0}_{-1.7}$	$66.9^{+2.3}_{-2.1}$	$60.3^{+18.8}_{-8.1}$
Semimajor Axis a (au)	$11.05^{+0.64}_{-0.56}$	$11.02^{+0.62}_{-0.51}$	$12.17^{+1.8}_{-1.2}$
Eccentricity e	$0.50^{+0.022}_{-0.022}$	$0.49^{+0.021}_{-0.018}$	$0.49^{+0.11}_{-0.12}$
Inclination i (°)	$49.8^{+3.4}_{-3.7}$	$49.1^{+3.5}_{-3.7}$	$56.6^{+12.9}_{-11.7}$

Table 4.4: Companion mass and selected orbital parameters for HIP 93398 B from both `orvara` [Brandt et al., 2021] and `orbitize!` [Blunt et al., 2020], compared with previously published values from Li et al. [2023].

semi-major axis (log uniform), inclination (sine), parallax (Gaussian), companion mass (log uniform), and host star mass (Gaussian). We use`orbitize!`'s default priors (except on the stellar mass, for which we use the above Gaussian prior), `ptemcee`, and the above data, except for the HARPS RVs. For clear comparison to the results from `orvara`, this parallel-tempered MCMC also used 10 temperatures, 100 walkers, 500 burn-in steps, and 200,000 total steps in the chain. Values from `orbitize!` are in agreement within error bars with both the Li et al. [2023] values and our `orvara` fit results. We report updates to a subset of the parameters fit by `orvara` and `orbitize!`–M_s, a, e, and i–and compare them to the constraints from Li et al. [2023] in Table 4.4. Although this additional epoch of relative astrometry only marginally improves constraints on the system's orbit and companion mass, we confirm that this object is firmly in the brown dwarf regime at ∼66 $M_{\rm Jup}$, with a semi-major axis of ≈11 au and moderate eccentricity around ≈0.5 in line with results for the eccentricity distribution of directly imaged brown dwarfs from Bowler et al. [2020].

4.5 Spectral Analysis

Using the age of the system and HIP 93398 B's mass as listed in Table 4.1, evolutionary models predict the companion to have a temperature of ∼1200–1400 K and a luminosity

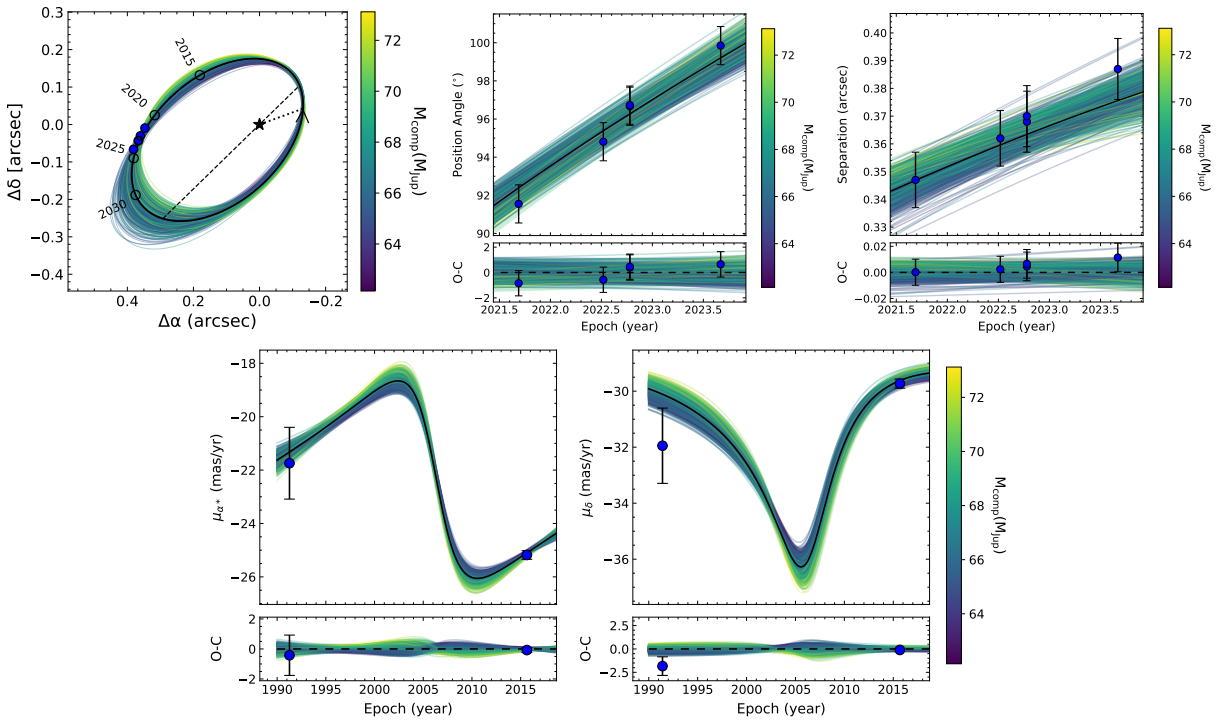

Figure 4.4: Orbital fits for HIP 93398 B using `orvara` [Brandt et al., 2021]. Randomly drawn orbits from the MCMC chain are color-coded by companion mass and plotted against (top) the object's apparent position, measured position angle, and measured separation; and (bottom) absolute astrometry [Brandt, 2021]. A companion mass of $\approx$66 $M_{\rm Jup}$ is favored, in agreement with past work, cementing this object firmly in the brown dwarf regime.

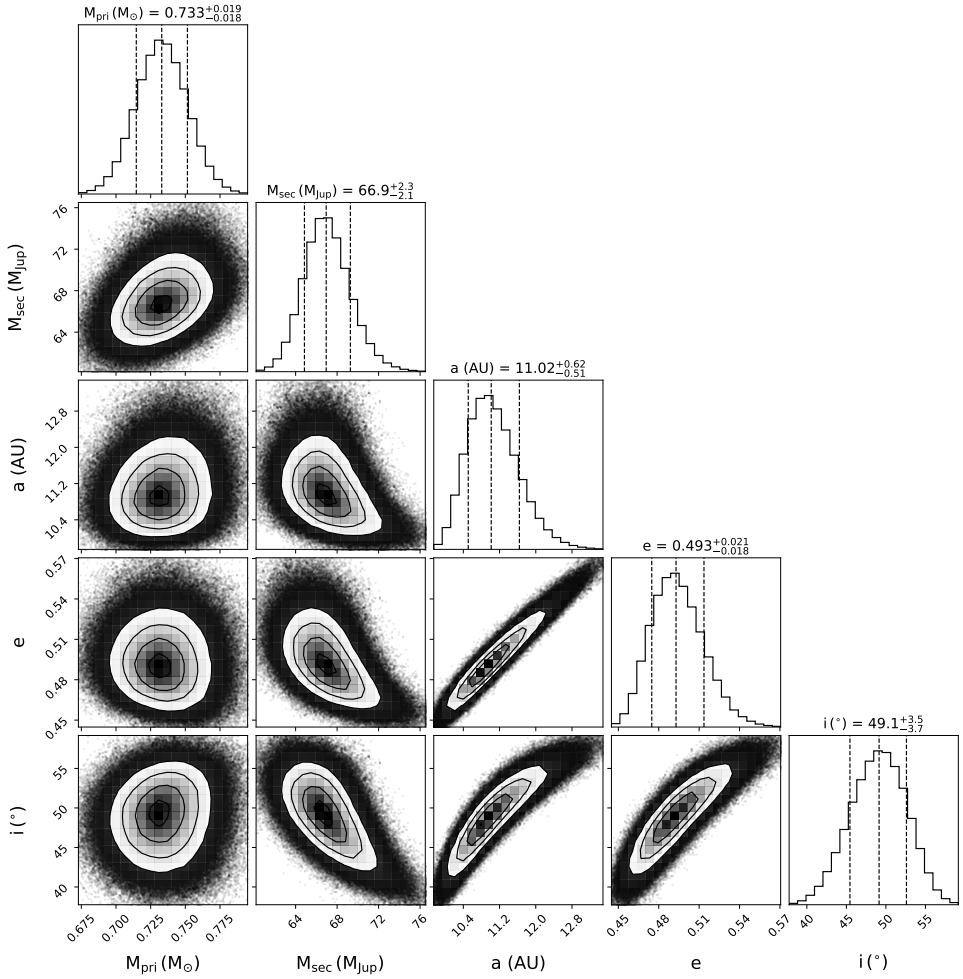

Figure 4.5: Corner plot for a subset of fit parameters from `orvara`: stellar mass, companion mass, semimajor axis, eccentricity, and inclination. The posteriors are nearly Gaussian.

$log(L_{bol}/L_{\odot})$ of ∼-4.5. This is in tension with the values derived by Li et al. [2023], where $log(L_{bol}/L_{\odot})$ = -5.26±0.07 and T_{eff} ∼900–1000 K, and is fainter and cooler than predicted by evolutionary models. In this section, we extract J, H, and K band photometry to compute a revised bolometric luminosity, and then use our new spectral observations to determine a spectral type for the object.

4.5.1 Photometry and Colors

J-, H-, and K-band photometry are primarily derived from the calibrated broadband spectrum, due to the more reliable relative calibration between the two channels in that observation, which will be crucial for determining colors. We compute the photometry in each band by integrating the observed flux multiplied by the transmission profile for each filter (J_{MKO}, H_{MKO}, and K_{MKO}, from Rodrigo and Solano [2020]) over its bandpass via the following equation as in Tokunaga and Vacca [2005],

$$\langle F_\nu \rangle = \frac{\int F_\nu(\nu) S(\nu)/\nu \, d\nu}{\int S(\nu)/\nu \, d\nu}, \tag{4.2}$$

where $\langle F_\nu \rangle$ is the monochromatic flux density (erg/s/cm^2/Hz) for the resulting photometry, F_ν is the observed monochromatic flux density (erg/s/cm^2/Hz), $S(\nu)$ is the filter transmission function, and ν represents the frequencies in each bandpass. Monochromatic flux densities are then converted to Vega magnitudes using the MKO filter zero points. As mentioned earlier in Section 4.3, we do not attempt an absolute flux calibration for the J-band high-res observations due to data quality, and we incorporate the discrepancy between the H-band as measured in broadband and as measured in high-res mode as part of the error on the reported photometry.

Then, to place HIP 93398 B in context with other substellar objects, we use our newly derived J, H, and K magnitudes, along with the previously published L' magnitude from [Li et al., 2023], to compute its $J - H$, $J - K$ and $H - L'$ colors. We determine that $J - H$ = 1.03 ± 0.69, $J - K$ = 1.58±0.41 and $H - L'$ = 0.20 ± 0.57 for HIP 93398 B. In Figure

4.6, HIP 93398 B is shown alongside a sample of field and companion M-, L-, and T-dwarfs from the Ultracool Sheet [Best et al., 2024]. In $J - H$ color space, HIP 93398 B is aligned with other L/T transition objects, while in $H - L'$ it is somewhat of an outlier, along with a few other young companions, namely HD 984 B Meshkat et al. [2015], Liu et al. [2016], HD 1160 B [Maire et al., 2016, Garcia et al., 2017, Nielsen et al., 2012], and HIP 78530 B [Bailey et al., 2013, Lachapelle et al., 2015, Kouwenhoven et al., 2005, Lafrenière et al., 2011]. These three comparison objects have all been identified as much younger (<120 Myr) late M-dwarfs, with masses ranging from ∼25-125 $M_{\rm Jup}$. Although there is low precision on HIP 93398 B's age measurement, even the lowest bounds indicate this object is at least 500 Myr old. The strange $H - L'$ color alternatively may be explained by systematic errors in the reported L' magnitude from Li et al. [2023]; however, a full re-analysis of those data is beyond the scope of this paper.

Additionally, we derive a bolometric luminosity for HIP 93398 B via the methods described in **?** and Sanghi et al. [2023]. We first use the **?** polynomial relationship between the object's absolute H band magnitude M_H and its effective temperature $T_{\rm eff}$, resulting in a temperature of 1280^{+156}_{-138} K for HIP 93398 B. Assuming a radius of R∼1$R_{\rm Jup}$ and using the Stefan-Boltzmann law, this results in a luminosity $log(L_{\rm bol}/L_\odot)$ of -4.65$^{+0.19}_{-0.22}$ dex. Using the polynomial relationships between bolometric luminosity and J, H, and K magnitudes from Sanghi et al. [2023], we obtain $log(L_{\rm bol}/L_\odot)$ = -4.65± 0.15, -4.64±0.23, and -4.63±0.08 respectively. The value we report in Table 4.1 is that of the H band magnitude derived bolometric luminosity from the Sanghi et al. [2023], as that relationship is described as the most reliable in that work.

4.5.2 Spectral Standards and Empirical Spectra

We first compare HIP 93398 B's CHARIS spectra (reduced with 10 KL modes) to spectral standards from the SpeX Prism Library Analysis Toolkit (`SPLAT`) [Burgasser and Splat Development Team, 2017]. Using `SPLAT`'s classifyByStandard routine, we determine that the

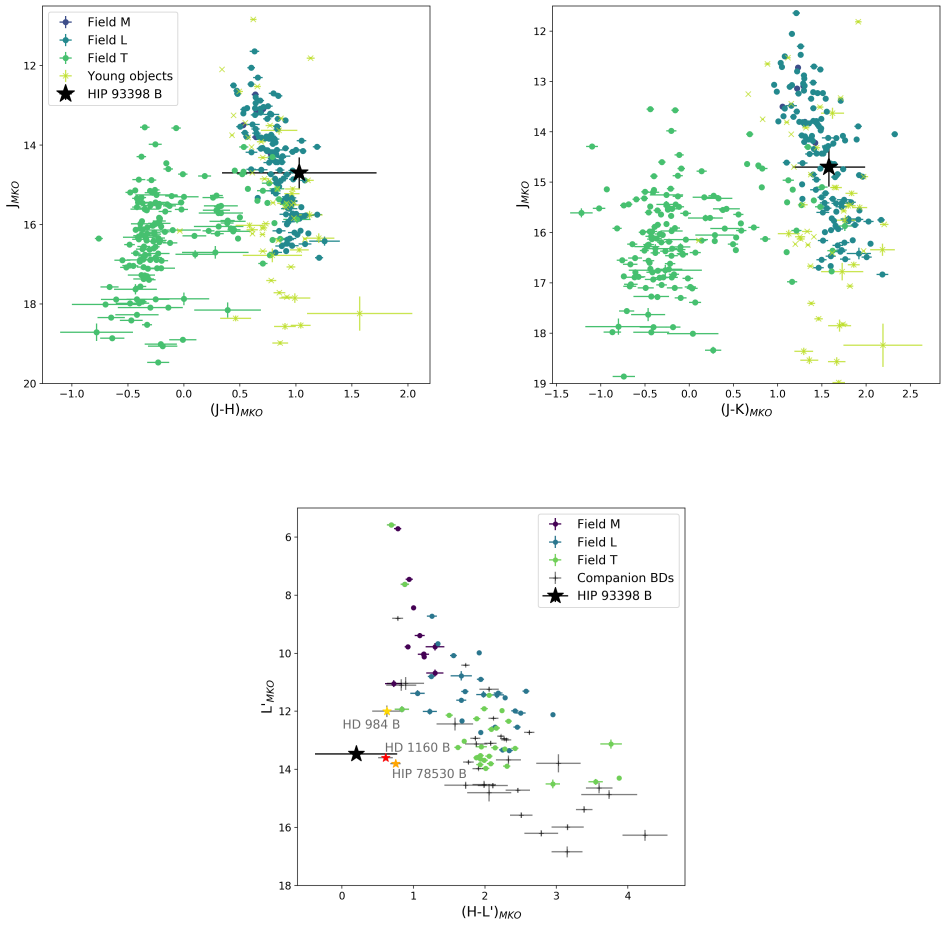

Figure 4.6: Color magnitude diagrams for $J-H$, $J-K$, and $H-L'$ colors. HIP 93398 B is shown in the context of a number of other field dwarfs and young companion brown dwarfs, as reported in the Ultracool Sheet [Best et al., 2024]. HIP 93398 B is aligned with other L/T transition objects in $J-H$ and $J-K$ color space, while in $H-L'$ it is an outlier, somewhat nearby a few other companion BDs, namely HD 984 B (yellow, Meshkat et al. [2015], Liu et al. [2016]), HD 1160 B (red, Maire et al. [2016], Garcia et al. [2017], Nielsen et al. [2012]), and HIP 78530 B (orange, Bailey et al. [2013], Lachapelle et al. [2015], Kouwenhoven et al. [2005], Lafrenière et al. [2011]). The strange $H-L'$ color may be explained by systematic errors in the reported L' magnitude from Li et al. [2023]; however, a full re-analysis of those data is beyond the scope of this paper.

broadband spectra and the H-band spectra are each best matched with an L9.0 standard (DENIS-P J0255-4700, Burgasser et al. [2006a]). The uncertainty-weighted mean classifications calculated by `SPLAT` are L5.0±4.5 and L9.0±0.6 respectively. The higher uncertainty on the broadband classification in this routine is likely due to the larger errors present in J band in the broadband data set.

We also compared the HIP 93398 B broadband spectrum to templates from the SpeX Prism Library [Burgasser, 2014], and we present the 5 best fit spectra in Figure 4.7 along with their reduced chi squared (χ^2_ν) values. These spectra are — in order of best fit — the L9.0 dwarf 2MASS J11181292-0856106 [Kirkpatrick et al., 2010], L4.0 dwarf 2MASS J01341675-0546530 [Kellogg et al., 2017], L5.0 dwarf 2MASS J16231308+3950419 [Kellogg et al., 2015], T1.0 dwarf WISE J005757.63+201304.2 [Kirkpatrick et al., 2014], and L5.0 dwarf SDSS J164916.89+464340.0 [Chiu et al., 2006]. These spectral types are NIR spectral types as given by the SpeX Prism Library [Burgasser, 2014]. Template matches support the classification of HIP 93398B as L5.0-9.0 type, establishing it as an L/T transition object.

4.5.3 Comparison to Substellar Atmosphere Model Spectra and Evolutionary Models

We then fit HIP 93398 B's broadband $J/H/K$ and high-resolution H-band CHARIS spectra independently to substellar atmospheres from the Sonora Diamondback [Morley et al., 2024] model grids. For this portion of the analysis, we omit the high-resolution J-band data due to its larger error bars from poorer seeing conditions. Sonora Diamondback models are the recently-released successor to the well-established Sonora Bobcat models, and include the effects of clouds on substellar spectra (unlike Bobcat, which only included cloud-free models). These models cover effective temperatures from 900 to 2400 K, surface gravities $\log g = 3.5 - -5.5$, metallicities [M/H] $= -0.5$, 0.0, and $+0.5$, plus cloud sedimentation efficiency $f_{\rm sed}$ [Ackerman and Marley, 2001] values from 1 to 8. Both models are appropriate for a large range of masses of substellar objects.

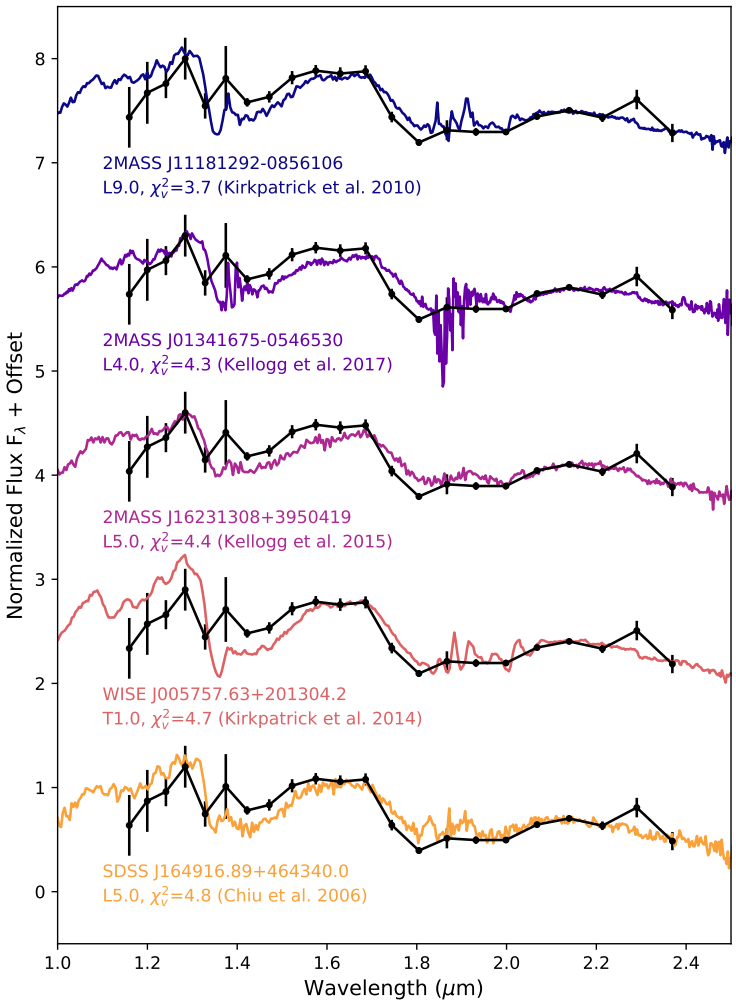

Figure 4.7: CHARIS broadband spectra of HIP 93398 B (black) compared to the five best fit template spectra from the SpeX Prism Library [Burgasser, 2014] via the `SPLAT` package Burgasser and Splat Development Team [2017]. These template matches support the idea that HIP 93398 B is an late-L type L/T transition object. Other than the T1 spectrum pictured, other T0/T1 spectra are substantially worse fits for the data (χ^2_ν >6). The CHARIS data shown within are from a reduction using 10 KL modes.

For comparison to our spectra, we used a Gaussian filter to convolve and resample the model spectra to the CHARIS resolutions for broadband ($R \sim 18.4$) and H-band ($R \sim 65$) observations. For each spectrum in the model grid, we determine an optimal scaling factor to the data via χ^2 minimization, and then compare these independent reduced chi squared χ^2_ν values across the grid to find the best fit model. The best fit model for H band has $T_{\rm eff} = 1300$ K, $\log g = 3.5$, Solar metallicity, and cloud parameter $f_{\rm sed} = 4$. The best fit model for the broadband data has $T_{\rm eff} = 1200$ K, $\log g = 5.0$, metallicity [M/H] $= +0.5$, and cloud parameter $f_{\rm sed} = 4$. These best fit spectra are shown compared to our data in Figure 4.8. However, it is unlikely for a companion to have a substantially different metallicity from its primary (in this case, near solar metallicity), and for an object of this mass and R$\sim$1 $R_{\rm Jup}$, we would expect a surface gravity around log$g$=5.0. If we assume solar metallicity and log$g$=5.0, the best fit broadband spectrum has $T_{\rm eff} = 1100$ K and $f_{\rm sed} = 4$. Additionally, spectra from atmospheres with the same temperature, log$g$, and metallicity but different $f_{\rm sed}$ values are shown in Figure 4.9, highlighting the importance of clouds in reproducing the relatively flat spectrum observed for this object.

Maps of χ^2 across the model grid points are also shown in Figure 4.10, and they illustrate the favored parameter space for each data set; [M/H] < 0 and models with no clouds or thin clouds ($f_{\rm sed} = 8$) are clearly disfavored, while a fairly broad range of temperatures are preferred, especially for the H-band data. We calculate constraints on temperature from this information by marginalizing over metallicity, sedimentation efficiency, and $\log g$, resulting in a temperature of 1200^{+140}_{-130} K derived from the broadband data and 2000^{+260}_{-470} K from the H band data. These values agree at the 2σ level, and the marginalized posterior distributions show a strongly peaked Gaussian for the broadband fit, but a much broader skew normal distribution, allowing for cooler temperatures, for the H band fit. The skewness of the H-band temperature distribution is visually evident in Figure 4.8. Additionally, the H band high-resolution data only probes a small part of wavelength space, and therefore has less leverage to discriminate between models. As a result, we adopt the broadband-data derived

temperature for the remaining discussion.

Additionally, we compare the spectrum-derived temperature of HIP 93398 B and its independently-derived age to evolutionary models for both cloud-free and "hybrid" (i.e. including clouds) models from Sonora Diamondback. As described in [Morley et al., 2024], the inclusion of clouds can change the predicted temperature for an object by ∼100–200 K and, therefore, has a significant effect on the predicted evolutionary track for a given mass of object. In Figures 4.11 and 4.12, we place HIP 93398 B in the context of evolution models for various substellar object masses assuming solar metallicity. HIP 93398's temperature, spanning ∼1000–1500 K when considering estimates from both spectra and photometry, as well as its revised luminosity, are consistent with both cloudy and cloud-free evolutionary tracks for its mass as shown in Figures 4.11 and 4.12. If the temperature is lower as suggested by spectral fits alone, there would be a notable disagreement with cloud-free evolutionary tracks. The agreement with evolutionary models is also not particularly sensitive to age if the object were to be older, as was estimated by some methods in Section 4.1.

4.6 Discussion and Conclusions

Li et al. [2023] suggested HIP 93398 B to be a likely T6 dwarf based on inference from other analogous substellar objects with similar masses and ages. However, the additional information provided herein from the object's spectra suggest that this is not the case, as HIP 93398 B is more likely a late L dwarf near the L/T transition and with a temperature of approximately 1100–1300 K. Its location at the L/T transition is supported by multiple lines of evidence: spectral typing via standards, temperatures derived from substellar atmosphere models, $J - H$ and $J - K$ colors, and position on color-magnitude diagrams. HIP 93398 B's estimated bolometric luminosity $log(L_{\rm bol}/L_{\odot})$ = -4.64±0.23 is also significantly brighter than the estimate from Li et al. [2023]'s L' photometry of -5.26±0.07; this revised bolometric luminosity is similar to that of L5 gamma dwarf 2MASS J03264225-2102057 [Gizis

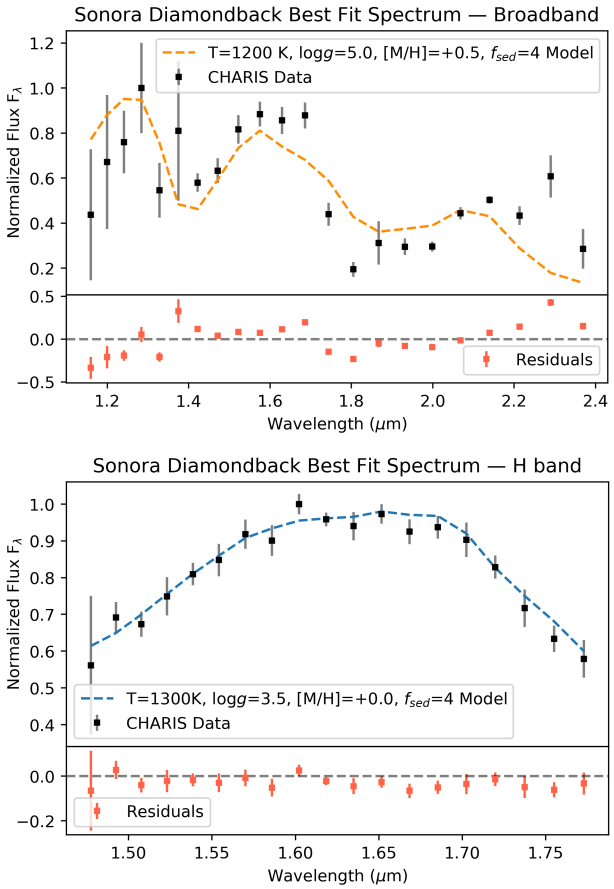

Figure 4.8: CHARIS spectra of HIP 93398 B (black) compared to the best fit substellar atmosphere spectral models from Sonora Diamondback [Morley et al., 2024]. The H-band best fit model spectra are shown in blue (bottom), the broadband best fit model spectra are shown in orange (top), and residuals are shown in red below the spectra. The predicted temperatures for this object based on the best fit models are within expectations for its designation as an L/T transition object (∼1100–1400 K; Dupuy and Liu [2012], Vos et al. [2019]). It is worth noting that if we assume log$g$=5.0 (an expected value for this size of object) and solar metallicity (similar to its host star), the best-fit broadband temperature changes slightly to 1100 K, but the preferred cloud parameter value remains the same.

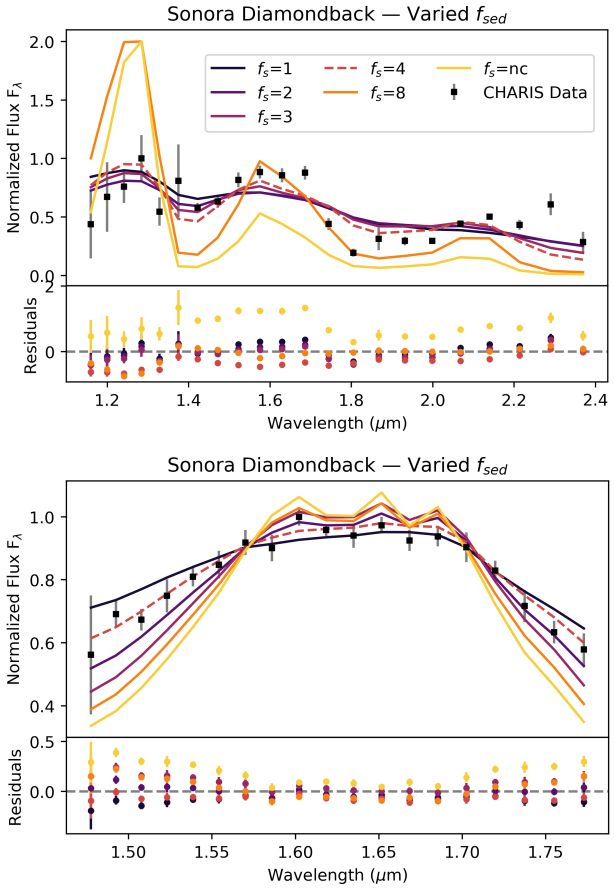

Figure 4.9: CHARIS spectra of HIP 93398 B (black) compared to the best fit substellar atmosphere spectral models from Sonora Diamondback [Morley et al., 2024] with varying values of $f_{\rm sed}$ (a parameterization of cloud thickness) at constant temperature and $\log g$ (1200 and 1300 K, 3.5 and 4.5 dex, the best fit values for the broadband and H band spectra respectively), where the best fit value is indicated with a dashed line. This object is best fit with models that include clouds with low-to-mid sedimentation efficiency, indicating the possible presence of thick clouds; although the degree of cloudiness isn't well constrained, clouds are necessary to reproduce the flatness of our observed spectrum.

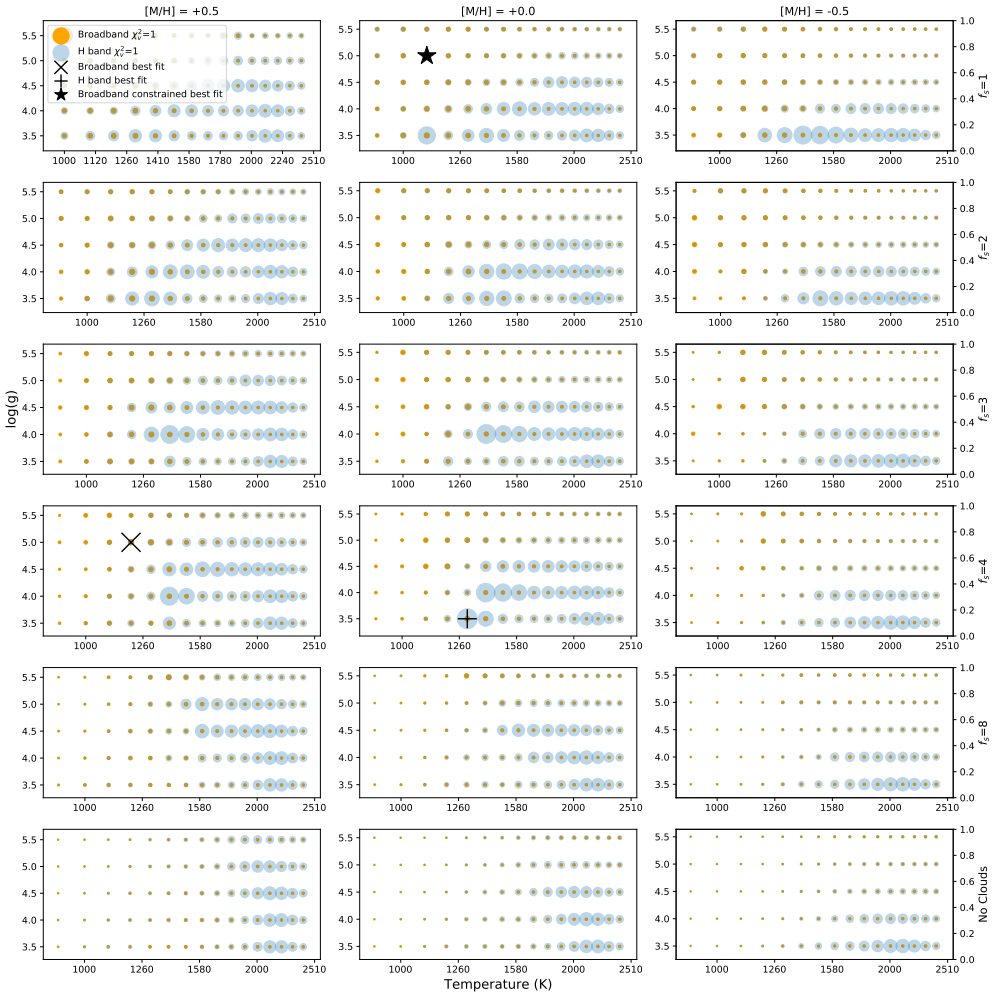

Figure 4.10: Fit metrics across the Sonora Diamondback model grid for both H band (blue) and broadband (orange) CHARIS data for the three available metallicities: +0.5 (left), +0.0 (middle), and −0.5 (right). Best fit models are shown in black crosses, with a black star for the "constrained" best fit value, where we assumed solar metallicity and $\log g = 5.0$. A larger marker size corresponds to a smaller χ^2 value (i.e. a better fit, where the size of $\chi^2_\nu = 1$ is shown in the legend). Models without clouds–similar to those from the previous generation of models, e.g. Sonora Bobcat–indicate a higher temperature >2000 K; however, cloudy models and metallicity ≥0.0 are significantly favored overall and, for the broadband data, indicate a lower temperature around 1200–1600 K, in line with expectations for an L/T transition object and in agreement with evolutionary models, as shown in Figure 4.11.

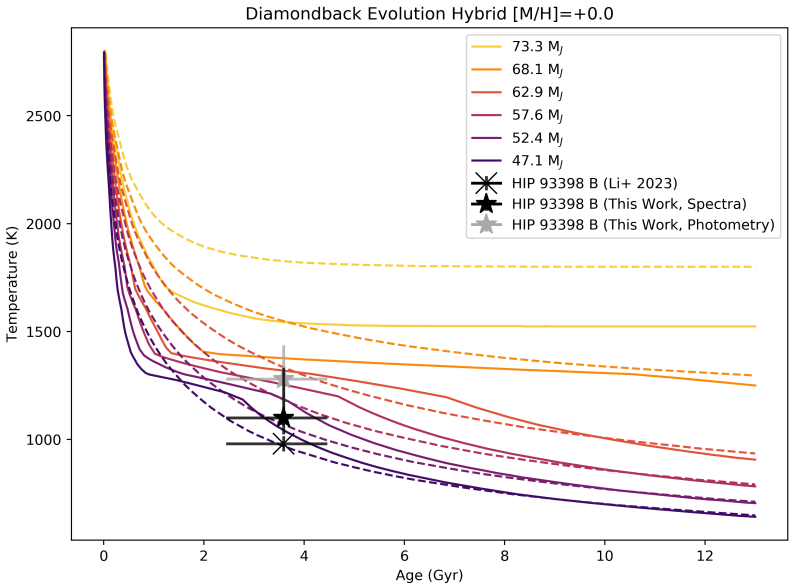

Figure 4.11: Age and temperature of HIP 93398 B derived from Diamondback model spectra fitting to broadband data and from photometric polynomial relationships, compared to Diamondback evolutionary models for solar metallicity. Hybrid models including clouds are shown in solid lines, while cloudless models are indicated with dashed lines. The temperature values derived from photometry are consistent with either cloudy or cloudless models, while the lower temperatures derived from spectra require clouds to be consistent with evolutionary tracks.

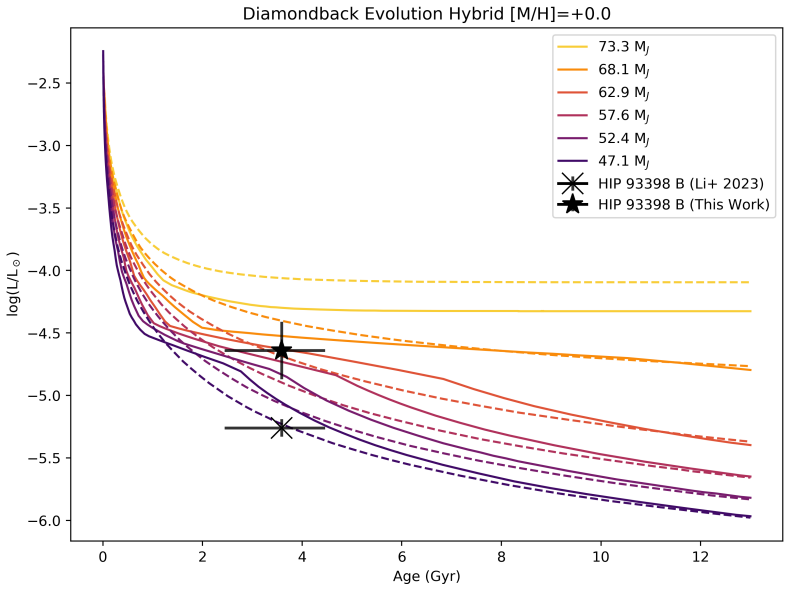

Figure 4.12: Age and luminosity of HIP 93398 B derived from photometric polynomial relationships, compared to Diamondback evolutionary modelsfor solar metallicity. Hybrid models including clouds are shown in solid lines, while cloudless models are indicated with dashed lines. Similar to the previous figure for age and temperature, these data do not support the tension between the known dynamical mass ($\sim$66 M_{Jup}) and the mass predicted by evolution models for both cloudy and cloudless models.

et al., 2003], L7 dwarf 2MASSW J0030300-145033 [Kirkpatrick et al., 2000], and L7.5 dwarf SDSSp J042348.57-041403.5 [Geballe et al., 2002]. Perhaps most notably, modeling fits to this spectrum clearly indicate that some amount of clouds are likely present in HIP 93398 B's atmosphere, although further modeling work would be needed to determine the cloud composition and characteristics.

Additionally, the classification of HIP 93398 B as a late-L dwarf resolves the previously proposed tension between evolutionary models and dynamical masses, particularly when clouds are included. Li et al. [2023] determined that their T6 classification and dynamical mass measurement justified the addition of HIP 93398 B to a growing list of brown dwarfs that may challenge existing evolutionary models, as they are overmassive and underluminous compared to model predictions. However, our spectral classification leads to a substantially higher model-dependent $T_{\rm eff}$ and also a higher luminosity, resolving this issue. Using the newest generation of substellar evolution models (Sonora Diamondback; Morley et al. [2024]) — which include clouds, an important feature for objects at the L/T transition and a key factor in brown dwarf atmospheres [Marley and Robinson, 2015] — the dynamical mass measurement is now in agreement with the spectrum-derived temperature and independently measured age.

In this work, we presented follow-up spectroscopic imaging on recently-discovered directly imaged brown dwarf companion HIP 93398 B using Subaru SCExAO/CHARIS in broadband ($J/H/K$), H band, and J band. Using a new epoch of data from 2023 combined with existing relative astrometry, HARPS RVs, and *Hipparcos*/*Gaia* absolute astrometry, we support previous measurements of the object's dynamical mass of $\sim$66 $M_{\rm Jup}$, establishing this object as an old ($3.59^{+0.87}_{-1.15}$ Gyr) and massive brown dwarf companion. Spectral analysis reveals this object to be a cloudy L/T transition brown dwarf, contrary to previous classifications as a T dwarf. =With the revised spectral type, temperature, and luminosity in evolutionary models (e.g. Sonora Diamondback), HIP 93398 B is no longer in tension with evolutionary predictions; although there are a handful of such T class objects that are in disagreement

with evolutionary models (e.g. Gl 229 B, Calamari et al. [2022]), HIP 93398 B does not seem to be among them.

Instead, the case of HIP 93398 B points to the importance of cloud physics in brown dwarf atmospheric and cooling models. Comparing so-called "overmassive" T dwarfs with new generations of substellar atmosphere models featuring clouds and disequilibrium chemistry may resolve some of the disagreement between models and observations. The growing sample of brown dwarfs with dynamical mass measurements, identified by HGCA-informed surveys like HIP 93398 B, will be key for continued testing of substellar atmosphere models.

CHAPTER 5

High-Contrast Polarimetric Imaging of the Low-Inclination Debris Disk Around HD 156623

5.1 Introduction

High-contrast imaging is extremely useful for spatially resolving debris disks, the extrasolar analogs of our solar system's interplanetary dust/Kuiper Belt [Mann et al., 2006]. Debris disks represent a later stage of a system's formation and evolution, wherein the circumstellar disk has evolved and lost most of its gas content. They also have low optical depth, and their dust is thought to be replenished by collisions and/or sublimation of planetesimals [Wyatt, 2008]. Imaging of debris disks provides significant information about the system beyond what an infrared excess measurement alone can provide, such as grain properties and disk morphology [Hughes et al., 2018]. Longer-wavelength observations (e.g. those from ALMA, the Atacama Large Millimeter Array) are able to resolve the thermal emission of disks, providing information on the distribution of large grains and the presence of gas in a system. In the near-infrared and optical, however, we are able to trace smaller grains, and polarimetric scattered light observations can reveal additional information about a disk's composition and structure. Morphological information can even reveal signs of a planetary companion, as demonstrated by the disk warp that led to the discovery of β Pictoris b [Roques et al., 1994, Lagrange et al., 2010].

The Gemini Planet Imager (GPI) [Macintosh et al., 2008, 2014a], a ground-based adaptive-optics (AO) instrument dedicated to high-contrast discovery and characterization of exoplan-

ets (formerly at Gemini South), has also imaged multiple debris disks with its integral-field spectrometer and dual-channel polarimeter [Esposito et al., 2020]. In addition to the planet search component of the Gemini Planet Imager Exoplanet Survey (GPIES), whose results are reported in Nielsen et al. [2019], Esposito et al. [2020] reports on a survey of debris disks with GPI. This survey resolved 26 debris disks and 3 protoplanetary/transitional disks, several of which were resolved in scattered light for the first time.

One of these newly resolved disks was HD 156623, a debris disk around a 16 Myr-old A0V star in Sco-Cen, at a distance of ∼112 pc [Houk and Fuentes-Williams, 1982, Gaia Collaboration, 2018]. HD 156623 is a low-inclination disk (≈ 35°), detected by GPI only in polarized light [Esposito et al., 2020]. This system lacks a visible inner clearing unlike many other imaged debris disks, including others in Sco-Cen [Bonnefoy et al., 2021]; close to the star, dust is usually cleared by Poynting-Robertson drag, accretion, stellar radiation pressure, and/or blowout from stellar winds on short timescales [Wyatt, 2008, Hughes et al., 2018], and a planet, if present, can sculpt a sharp inner edge of a debris disk (e.g. Engler et al. [2020], Pearce et al. [2024]). Additionally, prior observations in thermal emission via ALMA imaging from Lieman-Sifry et al. [2016] reported evidence for an inner clearing and showed significant CO gas mass, leading to the "hybrid" disk label given to this system. There is still significant debate on the mechanism that leads to the observed gas mass; either primordial gas has been retained (i.e. due to shielding by carbon atoms from photodissociation of CO) [Kral et al., 2019, Moór et al., 2019, Marino et al., 2020] or secondary gas has been re-generated via collisions, sublimation, or another process [Péricaud et al., 2017, Hales et al., 2019, Moór et al., 2017, Beust et al., 1990].

In this work, we aim to perform more detailed modeling of the disk around HD 156623 as seen in polarized infrared scattered light by GPI, with particular interest in constraining the presence and location of the hidden inner edge of the debris disk. In Sections 5.2 and 5.3 respectively, we include information on the host star HD 156623 and observations done by the Gemini Planet Imager with relevant information on the data reduction. In

Section 5.4, we present scattered light imagery models from `MCFOST` and the resulting best-fit parameters for the disk geometry [Pinte et al., 2006, 2009, Pinte, 2022]. In Section 5.5, we present empirical measurements of radial brightness profiles, scattering phase function, and polarization fraction. We then present analysis of the system's spectral energy distribution (SED) in Section 5.6. These measurements and insights into the inner edge location and minimum grain size in the context of this gas-rich disk are then discussed in Section 5.7.

5.2 Previous Observations of HD 156623

HD 156623 (HIP 84881) is an A0V star with a parallax of 9.2±0.03 mas [Houk and Fuentes-Williams, 1982, Gaia Collaboration, 2018, Brown et al., 2021]. Stellar parameters are summarized in Table 5.1. It exhibits pulsations consistent with zero-age main sequence (ZAMS) δ Scutis stars, and it is a member of the Upper Centaurus-Lupus subgroup of the Sco-Cen association, which contains stars of a wide-range of ages from ∼3 to 19 Myr [Pecaut and Mamajek, 2016, Mellon et al., 2019, Ratzenböck et al., 2023]. This star system appears to be relatively young — 16±7 Myr according to Mellon et al. [2019].

HD 156623 has been covered by many ground-based photometric surveys and space-based missions–including *WISE* [Cutri et al., 2012, Wright et al., 2010], 2MASS [Skrutskie et al., 2006], *IRAS* [Neugebauer et al., 1984, Beichman et al., 1988], and Tycho [Høg et al., 2000, Pickles and Depagne, 2010]–which is useful for constructing an SED as described in Section 5.6. Data from *WISE* indicate an infrared excess for HD 156623 of $L/L_* = 4.33\times10^{-3}$ [Rizzuto et al., 2012].

The disk around HD 156623 was also previously observed with ALMA, which marginally resolved the disk and found a strong ^{12}CO(2-1) signature, indicating the presence of a mass of CO gas $\geq 3.9 \cdot 10^{-4} M_\oplus$ [Lieman-Sifry et al., 2016]. Lieman-Sifry et al. [2016] also reports a 1240 μm continuum flux for HD 156623 of 720±110 μJy. Further detections of CO gas with APEX and IRAM were also completed in Péricaud et al. [2017].

Parameter	Value	Reference
D (pc)	111.75 ± 0.96	Gaia et al. [2018]
Age (Myr)	16 ± 7	Mellon et al. [2019]
$T_{\rm eff}$ (K)	9040^{+240}_{-160}	Mellon et al. [2019]
M_* ($M_\odot$)	$1.90^{+0.05}_{-0.04}$	Esposito et al. [2020]
L_* ($L_\odot$)	13.06 ± 1.80	Esposito et al. [2020]
R_* ($R_\odot$)	1.51 ± 0.09	Mellon et al. [2019]
I (mag)	7.1	Esposito et al. [2020]
H (mag)	7.0	Esposito et al. [2020]
$L_{\rm IR}/L_*$	$4.3{\cdot}10^{-3}$	Rizzuto et al. [2012]

Table 5.1: Summary of parameters for HD 156623. Magnitudes are synthetic photometry in Cousins I [Bessell et al., 1998] and 2MASS H [Skrutskie et al., 2006] as calculated by Esposito et al. [2020].

5.3 Observations and Data Reduction

5.3.1 Gemini Planet Imager Observations

GPI observations resolved the disk in scattered light using GPI's polarimetric mode, which uses a half-wave plate for modulation and a Wollaston prism beam splitter for analysis [Perrin et al., 2010, 2014]. The polarimetric data presented herein were first published as part of a larger survey in Esposito et al. [2020]. In total intensity, GPI uses angular differential imaging (ADI) to create angular diversity that can be exploited to improve the images' final contrast [Marois et al., 2006]. Observations in pol mode result in measurements of the Stokes $\mathcal{I}$, $\mathcal{Q}$, and $\mathcal{U}$ vectors. Most data products for debris disks — including those used in this work — use azimuthal Stokes vectors, $\mathcal{Q}_\phi$ and $\mathcal{U}_\phi$ (described below in Equations 5.1 and 5.2, where ϕ is the azimuthal angle around the star measured counterclockwise starting from North), which is useful for understanding polarization relative to the central star [Schmid

Date (UT)	**Mode**	$t_{\mathbf{exp}}$ **(s)**	$t_{\mathbf{int}}$ **(s)**	ΔPA (°)
2019 Apr 27	Pol	88.74	2129.81	28.2
2017 Apr 21	Pol	59.65	954.34	11.2

Table 5.2: GPI observations of HD 156623. The debris disk was detected in both polarimetric observations, and for the purposes of this investigation we focus on the higher-quality, longer–exposure data from 2019. The following observation parameters are provided: exposure time ($t_{\rm exp}$), total integration time ($t_{\rm int}$), and field rotation (ΔPA, degrees). All observations were taken in the H band.

et al., 2006, Millar-Blanchaer et al., 2015].

$$\mathcal{Q}_\phi = \mathcal{Q}\cos 2\phi + \mathcal{U}\sin 2\phi \tag{5.1}$$

$$\mathcal{U}_\phi = -\mathcal{Q}\sin 2\phi + \mathcal{U}\cos 2\phi \tag{5.2}$$

$\mathcal{Q}_\phi$ then contains all polarized light from the debris disk that is aligned perpendicular or parallel to a vector from the host star to a given pixel. $\mathcal{U}_\phi$ then contains polarized light oriented 45° to this vector, which we expect to be devoid of signal for an optically thin debris disk (discussed further in Esposito et al. [2020]). GPI images also include four "satellite" spots, reference images of the occulted star used for astrometric and photometric calibrations [Sivaramakrishnan and Oppenheimer, 2006, Esposito et al., 2020].

The effective outer radius of the full circular field of view in reduced images is 1.4″ from the star, with radial separations up to 1.8″ visible over limited ranges of position angle (PA). The field of view size of each frame is 2.6″ x 2.6″, and we use the GPI pixel scale value of 14.166 ± 0.007 mas lenslet^{-1} [Konopacky et al., 2014, De Rosa et al., 2015, 2020]. The minimum projected separation viewable in the data is 0.123″, set by the edge of the focal plane mask (FPM, De Rosa et al. [2015]).

We observed HD 156623 on 2017 Apr 21 and 2019 Apr 27. A summary of the observations

are listed in Table 5.2. The debris disk around HD 156623 was detected by GPI in H band (λ_c=1.65 μm) polarized light ($\mathcal{Q}_\phi$), in both 2017 and 2019. In 2017, sixteen 60-second exposures were taken in H band polarimetry mode with the wave plate rotating between exposures (typically 22.5° per move as described by Perrin et al. [2015]), with 11.2° of field rotation and approximately 1.15 arcsec seeing. In 2019, twenty four 88-second exposures were taken in H band polarimetry mode with 28.2° of field rotation and ∼0.39 arcsec seeing. The 2019 data was higher quality and is what will be used in our analysis.

5.3.2 Data Reduction and Polarized Differential Imaging

Data for HD 156623 were reduced using the standard GPI Data Reduction Pipeline (DRP), documented in Perrin et al. [2014], Perrin et al. [2016], and Wang et al. [2018]. The data reduction procedure for polarimetry data in particular, as well as sources of noise in GPI polarimetric data, are further described in Perrin et al. [2015] and Section 4.1 of Esposito et al. [2020]; this reduction, however, is an improved reduction from that presented in Esposito et al. [2020] due to the quadropole correction described later in this section. The GPI DRP completes dark subtraction, flexure correction, field distortion correction, destriping, bad pixel corrections, and other calibrations specific to the GPI instrument, such as a cleaning procedure to account for biasing between orthogonal polarization channels [Perrin et al., 2014, 2015, Wiktorowicz et al., 2014, Konopacky et al., 2014]. After the standard DRP, the series of reduced polarimetric observations is converted into a single data cube containing the Stokes vectors $\mathcal{I}$, $\mathcal{Q}$, $\mathcal{U}$, and $\mathcal{V}$, before then converting $\mathcal{Q}$ and $\mathcal{U}$ to radial Stokes vectors ($\mathcal{Q}_\phi$ and $\mathcal{U}_\phi$) as previously described [Perrin et al., 2015]. This data reduction pipeline produces images in units of analog-to-digital units per coadd (ADU coadd^{-1}); using the measured flux of the satellite spots, which are themselves images of the host star, and the star's known H band magnitude (see Table 5.1) we converted those detector units into surface brightness units of mJy arcsec^{-2} for the subsequent analysis, as in Wang et al. [2014], Hung et al. [2016], and Esposito et al. [2020]. The calibration factor for this data reduction was $6.41\times10^{-9}\pm$

0.27×10^{-9} Jy/(ADU/coadd). Additionally, an extra instrumental polarization subtraction–a quadrupole modulation of the total intensity pattern scaled to data and subtracted for each waveplate modulation–was applied to the data to remove an instrumental polarization effect seen in GPI images [De Rosa et al., 2020].

Polarized intensity frames from the standard data reduction readily show the disk, due to the natural separation of unpolarized stellar light and polarized light scattered from the disk. For total intensity, we must complete stellar point spread function (PSF) subtraction, for which we use the `pyKLIP` package [Wang et al., 2015]. `pyKLIP` uses Karhunen-Loéve Image Processing (KLIP), a form of principal components analysis, to create a model of the stellar PSF using its dominant modes of variation for PSF subtraction [Soummer et al., 2012]. For polarimetric GPI data, the total intensity is the sum of the two orthogonal polarization states, plus any unpolarized light. We employ ADI in our reduction for total intensity data taken with GPI polarimetry mode. Parameters for the `pyKLIP` reduction generally must be chosen with care to maximize the signal from the disk, avoiding self-subtraction [Milli et al., 2012] while also reducing contamination from the stellar PSF. For this particular disk, which is faint relative to the stellar halo in total intensity, we use a particularly unaggressive implementation of KLIP, using one annulus and one subsection in the subtraction as recommended by `pyKLIP` documentation. We additionally test multiple KL modes (1, 5, 10, 20, 50) and use `pyKLIP`'s minimum rotation (`minrot` = 3) criterion for basis vector selection, as is recommended to avoid self-subtraction. Even after applying PSF-subtraction, however, we were unable to recover the disk in total intensity light, as shown in Figure 5.1. Although other recent algorithms have focused on improving this issue of self-subtraction (e.g. non-negative matrix factorization (NMF), Ren et al. [2018]), we do not pursue additional reductions in this work; although such algorithms may be able to recover the disk's general morphology, we choose to focus on the polarized intensity detection which already provides such morphological information. Additionally, low-inclination and radially extended disks are particularly challenging to retrieve in total intensity with an ADI

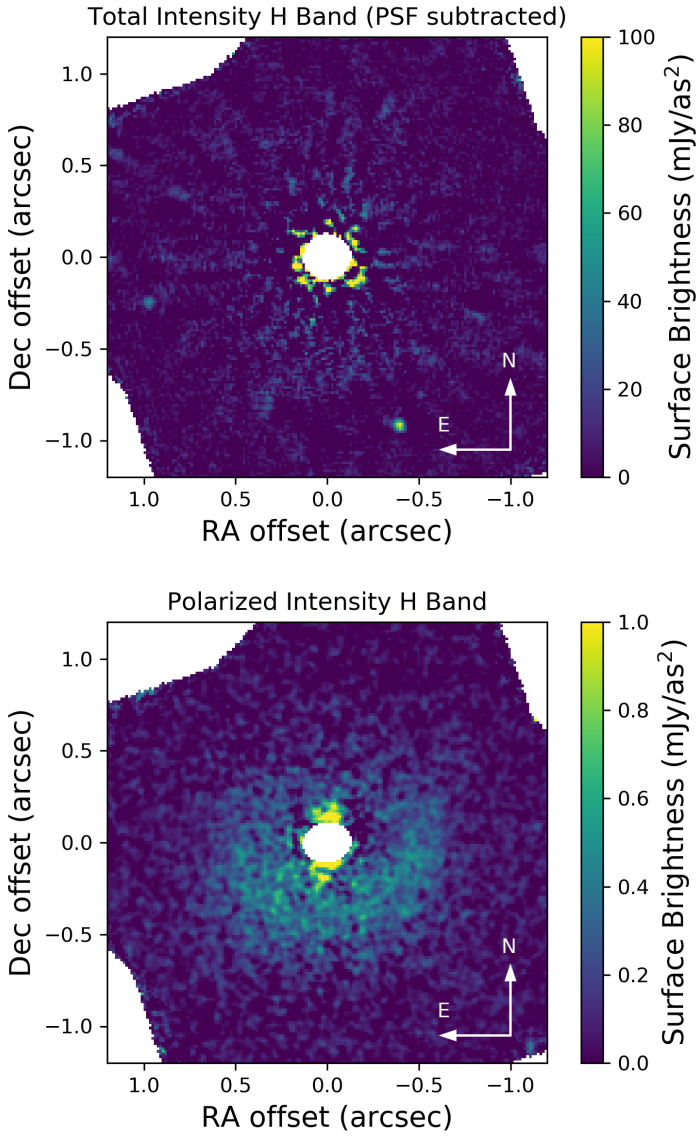

Figure 5.1: PSF-subtracted total intensity GPI H band image of HD 156623 using 5 KL modes (top) and polarized intensity GPI H band image of HD 156623 smoothed with a 2 pixel wide Gaussian kernel for visualization (bottom). The debris disk is only detected in polarized light, with a signal-to-noise ratio of ∼2-3 per resolution element. The point sources visible in the total intensity image were determined to be unbound background stars in Esposito et al. [2020].

approach. The point sources in total intensity were already determined by Esposito et al. [2020] to be unbound background objects and are thus not considered in our analysis of this system.

5.4 Disk Morphology

In this section, we reproduce the modeling originally presented in Esposito et al. [2020] to show the scattered light model disk images and quality of fit to the data, which were not provided in that work, with the goal of constraining the inner edge from our imagery. This modeling is nearly identical to that of Esposito et al. [2020], but run with a 40% longer chain. This leads to a small improvement in the quality of the results due to more total samples of the posterior. We use these morphological results (namely position angle, inclination, and radius constraints) to guide our measurements of the disk's brightness profiles and phase function, calculated in Section 5.5.

As in Esposito et al. [2020], morphological parameters of the disk were estimated by comparison to models from the Monte Carlo radiative transfer code `MCFOST` [Pinte et al., 2006, 2009]. `MCFOST` is a radiative transfer code that uses Monte Carlo and ray tracing methods to produce models of observables (scattered-light imagery, millimeter and infrared visibilities, line maps, SEDs, dust temperature distributions) for circumstellar environments such as protoplanetary and debris disks. Models were fit to Stokes $\mathcal{Q}_\phi$, $\mathcal{Q}$ and $\mathcal{U}$ data simultaneously, as $\mathcal{Q}_\phi$ is the only available data with the quadrupole noise signal removed. Following the procedure in Esposito et al. [2018], our models assume Mie scattering from spherical grains in an azimuthally-symmetric, optically-thin disk centered on the star, observed at 1.65 microns (the H band peak wavelength). We additionally use the same disk parameters and procedure as described in Esposito et al. [2020], as summarized below. The disk has a vertical structure where the scale height is a constant fraction of the radius, set to 0.055, a value consistent with measured values for similar disks in the literature and consistent with modeled vertical

structure assuming the effects of radiation pressure and collisions [Esposito et al., 2018, Millar-Blanchaer et al., 2015, Krist et al., 2005, Thébault, 2009]. The surface density is described by a smoothed broken/two-component power law, with two different fixed power law indices: one for the disk interior to a critical radius (R_c), set to $\alpha_{in} = -3.5$, and one for the disk exterior to R_c, set to $\alpha_{out} = 1.5$ as in Esposito et al. [2020]; these values were manually tuned to a reasonable by-eye match in that work, and we have adopted the same parameter choice for consistency. The following model parameters were left free to vary in the fit: the minimum grain size (a_{min}), grain porosity, dust mass (within the grain size distribution used) M_d, disk position angle (PA), inclination (i), dust inner radius R_{in}, dust outer radius R_{out}, and the critical radius R_c at which the inner and outer surface density profiles cross. Although the α power law exponents can theoretically be used to define a disk edge where the signal falls below the noise, R_{in} and R_{out} are included as free parameters to be able to define an edge that is more abrupt than that from a smoothly declining power law, e.g. from planet sculpting. Additionally, we do not expect the dust mass M_d to be physically meaningful; instead, it essentially functions as a scaling factor for the global surface brightness of the disk. PA is defined as the angle counterclockwise from North to the projected major axis of the disk.

We used a parallel-tempered MCMC with three temperatures, each with 120 walkers. Walkers were initialized randomly from a uniform distribution and then simulated for 3500 iterations. We discarded the first 2900 iterations as "burn-in" where the ensemble of walkers had not yet converged to their peak in posterior space, and used the final 600 iterations of the zeroth temperature walkers (equivalent to 2.16×10^5 models) for the disk parameter value estimates, which are summarized in Table 5.4. "Max Lk Value" contains the values for the maximum likelihood model, which is shown in Figure 5.3 and the adjacent column shows the median values with a 1-sigma confidence interval. A corner plot of posteriors from the MCMC is shown in Figure 5.2. Multiple parameters have slightly multimodal or non-Gaussian posteriors, and as such the 1σ values should be interpreted with caution for

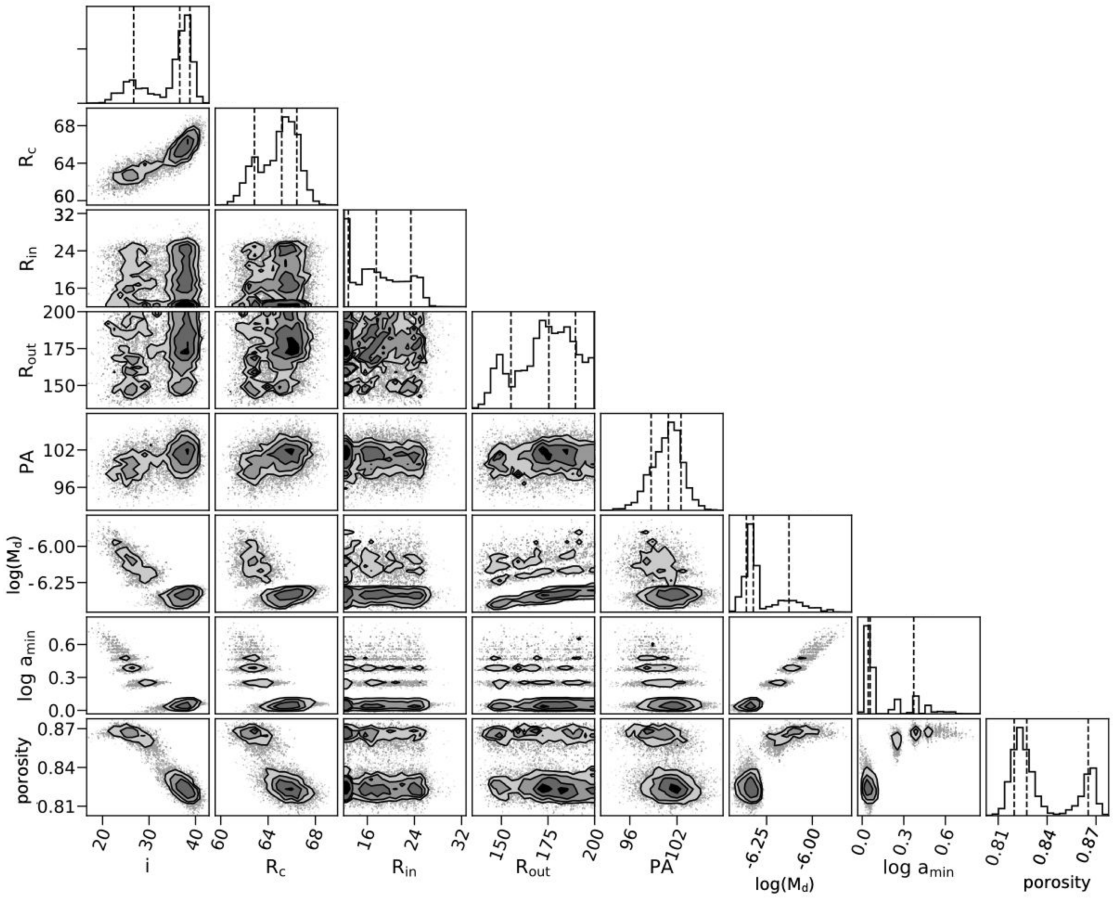

Figure 5.2: Corner plot of posteriors from `MCFOST` modeling of scattered light imaging.

those parameters; parameters with strongly non-Gaussian posteriors are reported as either maximum likelihood values or 99.7% confidence upper/lower limits. Similar to Esposito et al. [2020], we aim for a model that constrains the necessary morphological parameters with sufficient accuracy for our purposes, while acknowledging that a more complex / physically-motivated treatment of grain properties is necessary to truly reproduce the observed scattered light distribution.

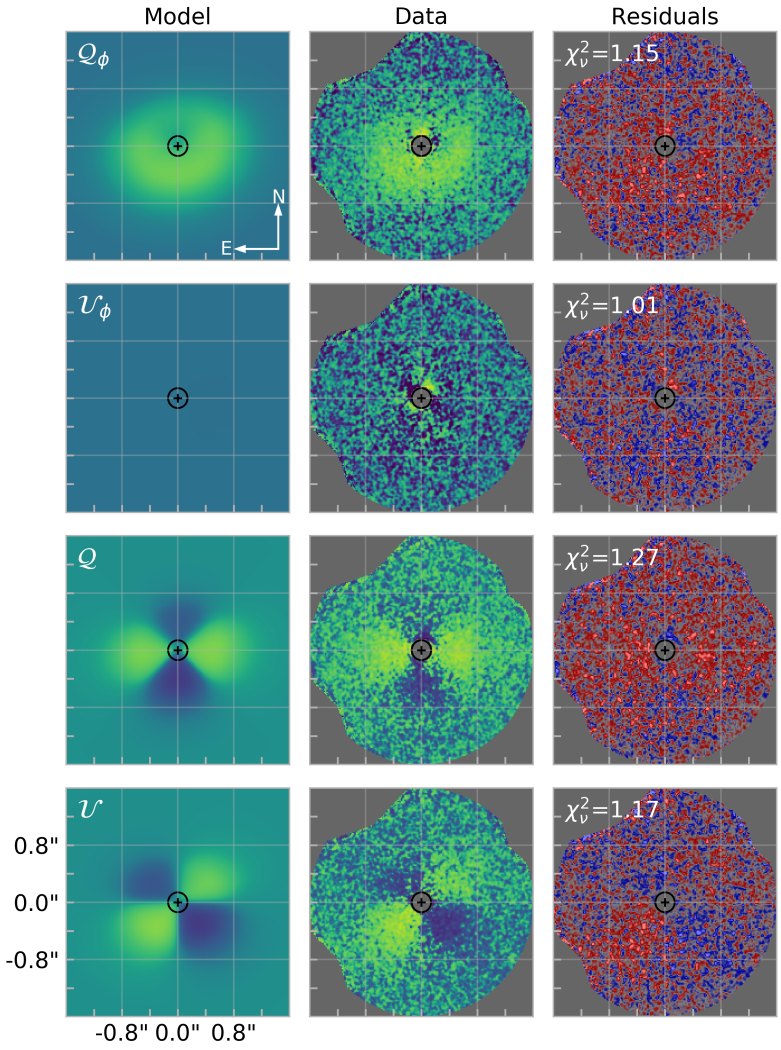

Figure 5.3: `MCFOST` maximum likelihood scattered light model of HD 156623 with data and residuals for Stokes $\mathcal{Q}_\phi$, $\mathcal{U}_\phi$, $\mathcal{Q}$, and $\mathcal{U}$, drawn from only the last 600 iterations (i.e. excluding burn-in).

Best-Fit Morphological Parameters

Parameter	**Max. Lk. Value**	**50 $\pm$ 1σ**	**Value from Esposito et al. [2020]**
PA (deg)	102.081	$100.9^{+1.6}_{-2.2}$	$100.9^{+1.9}_{-2.2}$
Inclination (deg)	38.978	$36.6^{+2.1}_{-9.9}$	$34.9^{+3.6}_{-9.5}$
$R_{\rm in}$ (AU)	12.707	< 26.6	< 26.7 (99.7% confidence)
$R_{\rm out}$(AU)	184.482	> 139.2	> 139.3 (99.7% confidence)
$R_{\rm c}$(AU)	67.113	$65.2^{+1.3}_{-2.3}$	64.4$\pm$1.8

Other Parameters Used

Parameter	**Free/Fixed**	**Max Lk. or Fixed Value**	**Value from Esposito et al. [2020]**
$a_{\rm min}$ (μm)	Free	1.13	1.19
$M_{\rm d}$ (log$M_{\odot}$)	Free	-6.31	$-6.31^{+0.21}_{-0.05}$
Porosity (%)	Free	0.82	0.84
$\alpha_{\rm in}$	Fixed	1.5	1.5
$\alpha_{\rm out}$	Fixed	-3.5	-3.5
β	Fixed	1	1
H_0/r_H	Fixed	0.055	0.055

Table 5.3: Summary of retrieved disk parameters from `MCFOST` from the final 600 iterations (i.e. excluding burn-in). The top section outlines the best fit morphological parameters adopted for our analysis, alongside the values from Esposito et al. [2020] which are generally in agreement. The bottom section describes parameters which are not necessarily physically meaningful in this application and should be interpreted with caution, but are included here for reproduciblity of our models.

5.5 Brightness and Scattering

5.5.1 Radial Brightness Profiles

Radial brightness profiles allow for further investigation of both the inner clearing and the outer radius of the disk, e.g. determining when the observed data is consistent with zero disk signal, in addition to the above modeling with `MCFOST`.

To that end, we measure radial brightness profiles (Figure 5.5) for various position angles. To compute these profiles, we first deproject the disk based on our determined value of inclination, such that each radial cut traverses the same distance from the center of the disk, using the Python package `diskmap` [Stolker et al., 2016]. Zero position angle is defined counterclockwise from North, as described earlier. Radial brightness profiles are the average of a wedge at the given angle range that is **5** pixels long in the radial direction and 45° (∼5–80 pixels depending on the radial distance from the center) wide, with its error as the variance of that slice of the wedge. Pixels within 15 AU of the center are masked, as this region is within the influence of the FPM (FPM) and therefore contains large errors. To determine a rough estimate for the visual outer radius of the disk–i.e. where the disk signal is dominant over the noise–in our data, we rebin the brightness profiles to 5 pixel wide annuli, and determine where the signal becomes consistent with zero by 2σ in our images at each angle. We average those measurements across azimuthal angles to find a visual outer radius of ∼78 AU. This visual outer radius is not an inherent property of the disk, but instead a quantitatively-derived limit for where the image is dominated by the signal instead of the noise for use in further calculations, e.g. the scattering phase functions in Section 5.5.2. We additionally compute radial surface density profiles (Figure 5.6) by correcting the brightness profiles by a factor of $1/r^2$, as shown in Figure 5.4. As an independent check on the disk morphology, we fit a smoothly broken power law (as defined via MCFOST and below in Equation 5.3) to the average measured surface density profile using least-squares, shown in Figure 5.4.

$$\rho(r,z) \propto \frac{\exp[-|z|/H(r)^{\gamma}]}{[(r/r_c)^{-2\alpha_{\rm in}} + (r/r_c)^{-2\alpha_{\rm out}}]^{1/2}} \tag{5.3}$$

We set the z coordinate to a constant for simplicity, use the same formalism for $H(r) = H_0(r/r_H)^{\beta}$ as Esposito et al. [2020] where β=0 and H_0/r_H=0.055, set the exponent γ=1, and leave r_c, $\alpha_{\rm in}$, and $\alpha_{\rm out}$ as free parameters, along with an arbitrary scaling/normalization factor N. The best fit values for the average radial surface density profile are N=1.73±0.13, r_c=78.8±6.0 AU, $\alpha_{\rm in}$=0.58±0.15, and $\alpha_{\rm out}$=-1.31±0.15. These differ significantly from the scattered-light modeling values for r_c, $\alpha_{\rm in}$, and $\alpha_{\rm out}$. These differences may be explained simply by the fact that $\alpha_{\rm in}$ and $\alpha_{\rm out}$ were fixed in the `MCFOST` models, as r_c is expected to vary with any change in the power law exponents. Additionally, this average profile may be biased due to a lower SNR detection of the back-scattering half of the disk, where the outer edge is much less well-defined, or a different scattering phase function than that assumed by `MCFOST`, which may change the ratio of surface brightness to surface density.

5.5.2 Observed Polarized Scattering Phase Functions

Scattering phase functions (SPFs) describe the fraction of light scattered into a solid angle by a single dust grain, and their shapes are determined by the properties of the dust itself; therefore, they are often used as a probe of the grain size, porosity, composition, and shape of a disk's dust grains.

We make several assumptions in this calculation, similar to those used for geometric modeling; that is, we take the disk to be azimuthally symmetric (but radially varying, related to the observed surface brightness) and optically thin, with the previously-described morphological parameters inferred via `MCFOST`. We also assume that scattering is independent of azimuthal angle (e.g. only the scattering angle θ is a variable in our equations), which is true for a spherical grain by symmetry and a good approximation for randomly oriented

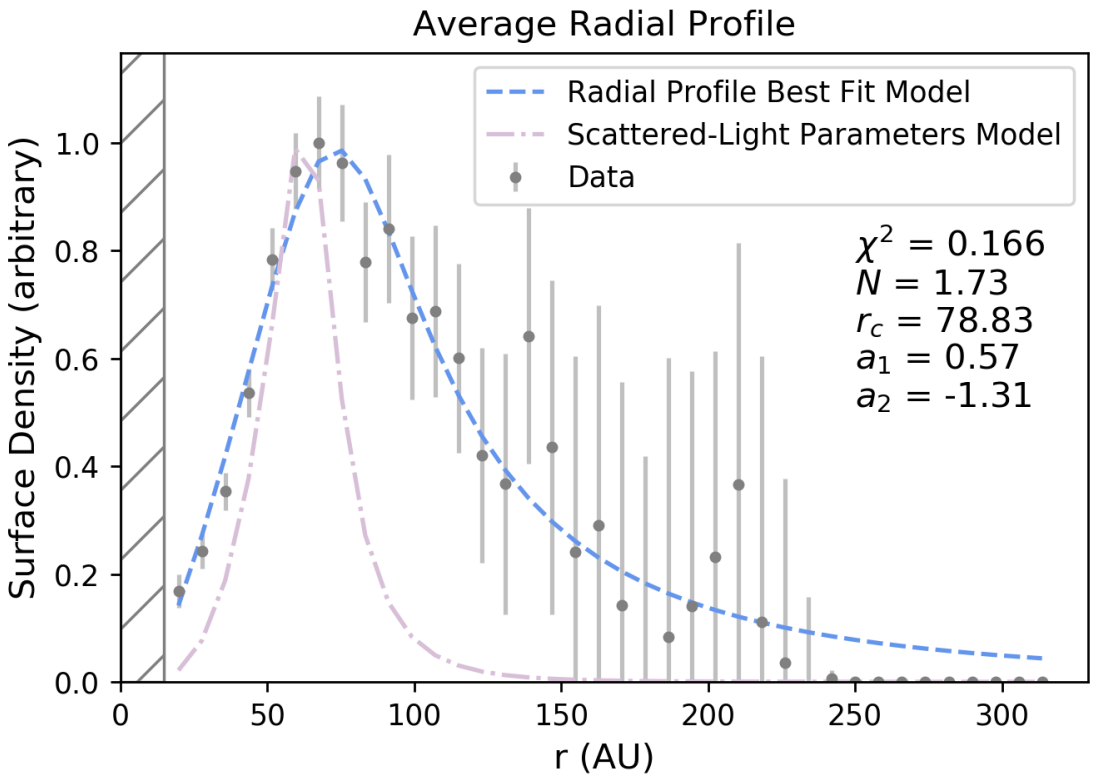

Figure 5.4: The average radial surface density profile (grey points with error bars) fit with a smoothly-broken two-component power law (the dashed blue line). The hatched region on the left marks the limits from the FPM as in other figures, and the dot-dash light purple curve represents the radial profile determined by scattered-light modeling. The values derived from this average surface density profile for r_c, $\alpha_{\rm in}$, and $\alpha_{\rm out}$ are substantially different from those determined via scattered-light modeling, perhaps due to a difference in the scattering phase function or bias due to the low SNR detection of the back-scattering portion of the disk; alternatively, these differences may simply be an artifact of the different modeling approaches.

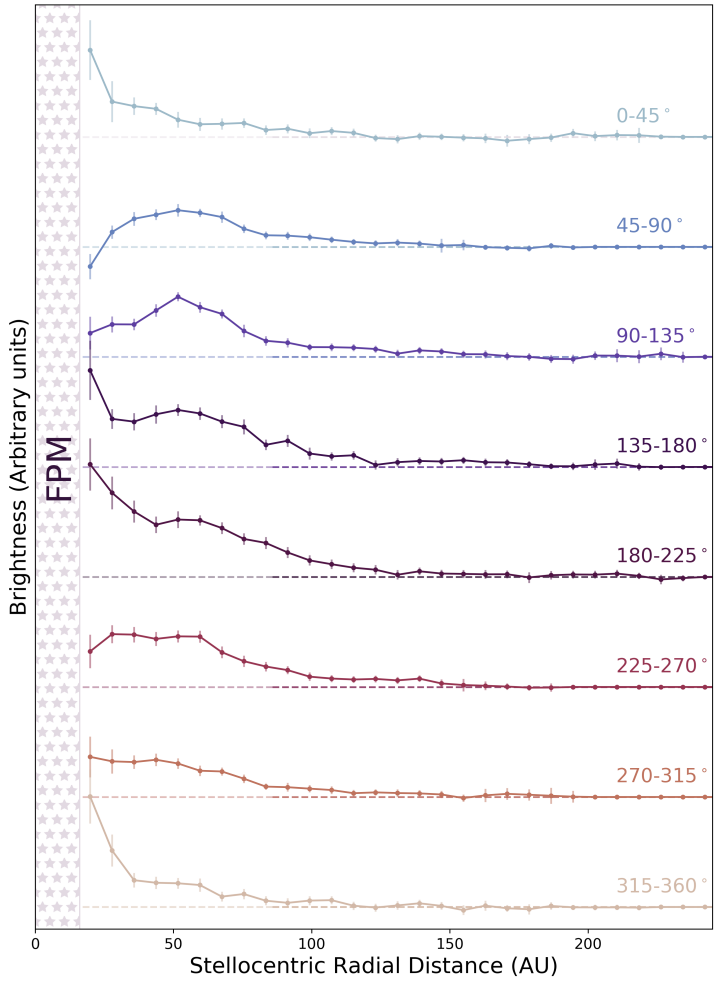

Figure 5.5: Measured brightness curves along the radial direction of HD 156623's deprojected disk for various angles. The region covered by the FPM is blocked out (hatched in light purple, labeled FPM), and it is clear that in most cases, the inner hole is unresolved, with the exception of possibly PA 45-90° and PA 90-235°. Each profile is arbitrarily offset for clarity, and the dashed lines correspond to zero for each profile depicted.

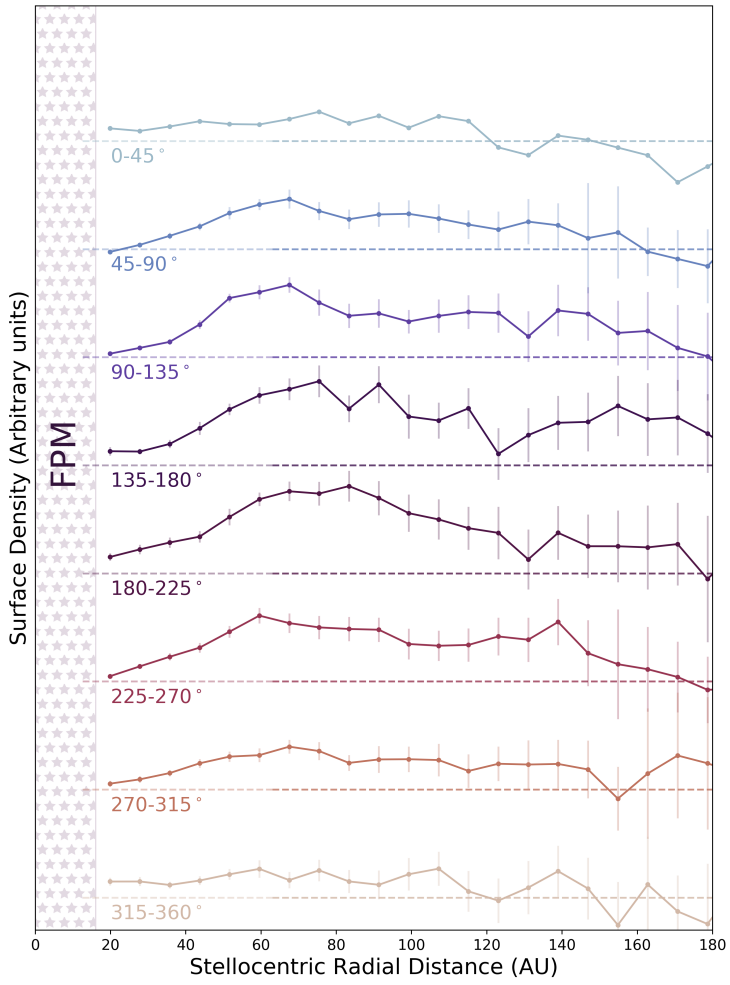

Figure 5.6: Surface density (brightness corrected by a factor of $1/r^2$) profiles along the radial direction of HD 156623's deprojected disk for various angles. The region covered by the FPM is blocked out (hatched in light purple, labeled FPM). Each profile is arbitrarily offset for clarity, and the dashed lines correspond to zero for each profile depicted.

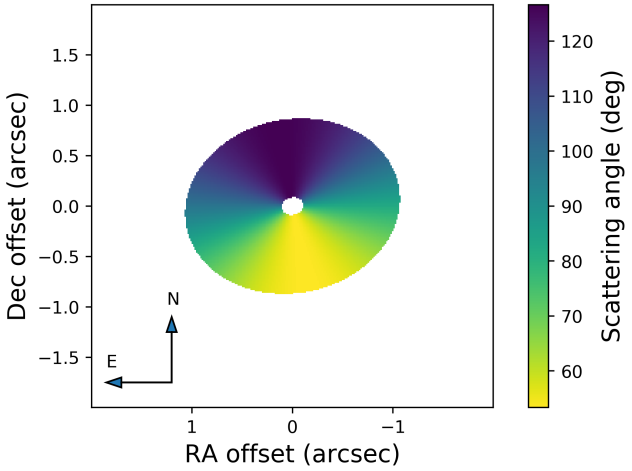

Figure 5.7: Diagram with the scattering angle across the disk of HD 156623, assuming the geometric parameters defined in Section 5.4. The most forward scattering occurs in the southwest, and the most back scattering occurs in the northeast.

non-spherical grains. The expression for a normalized SPF is then as follows:

$$f(\theta) \sim \frac{B_{\rm obs}(r,\theta)}{\rho(r)} \cdot r^2 \tag{5.4}$$

where $f(\theta)$ is the SPF, solely dependent on scattering angle and radially varying properties, $B_{\rm obs}(r,\theta)$ is the observed brightness at a given radius r and PA θ, $\rho(r)$ is the surface density of the disk, derived from the observed radial brightness profile, and r is the radius from the central star.

Given that this disk does not have a clearly defined single ring at which to compute a SPF, SPFs were instead determined by taking measurements of $B_{\rm obs}(r,\theta)$ at multiple radii around the disk, then averaging over the varying radii. For this specific calculation, we limit the range over which we compute the SPF to the annuli beyond the FPM and within the visual outer radius as determined by the radial brightness curves; this range is 15 AU (at the FPM limit) to 78 AU. Since we do assume the disk's surface density can vary radially, we retain $\rho(r)$ and r in our calculations, even though they are constants for a given radius. The disk surface density, $\rho(r)$, was approximated using the average best fit radial brightness

profile where the peak surface brightness was normalized to 1.

Scattering angle (θ) for each point in the disk is determined analytically, as shown in Figure 5.7, following the above geometric assumptions. This disk is most forward scattering around ∼200° PA, with a scattering angle of 54°, and most backward scattering near ∼10° PA with a scattering angle of 126°.

HD 156623's debris disk appears slightly asymmetric in visual inspection, particularly in the northwest quadrant, so SPFs were measured separately for the East and West halves of the disk (divided approximately along the minor axis), as shown in Figure 5.8. Errors were derived by the variance of pixels in each annulus, similar to the procedure for the radial brightness profiles, and propagated appropriately through the calculation. There is a slight asymmetry that is most pronounced near the eastern ansae (∼80–95°), consistent with the brightness asymmetry described in Crotts et al. [2024] that suggests the disk may be eccentric or experiencing more frequent collisions on the Eastern half. However, it is also worth noting that in our calculation, there is an implicit assumption that the density is azimuthally constant and radially varying. As a result, even if there is a true increase in brightness at those angles, there may not be a corresponding overbrightness in the SPF if we do not assume this symmetry.

We additionally fit a Henyey-Greenstein SPF [Henyey and Greenstein, 1941] to each of our observed scattering SPFs divided by a Rayleigh polarization curve (approximating the total intensity SPF), also shown in Figure 5.8. The Henyey-Greenstein (HG) function $p(\theta)$ is an empirical description, not based in Mie theory or another physical scenario, and it is calculated as

$$p(\theta) = \frac{1}{4\pi} \frac{1 - g^2}{[1 + g^2 - 2g\cos\theta]^{3/2}} \tag{5.5}$$

where g is the Henyey-Greenstein asymmetry parameter ($g = \cos\theta$, ranging from -1 to 1) and θ is the scattering angle. For debris disks, which are typically forward scattering, g is

Band	**Source**	λ_{eff} (μm)	**Flux (Jy)**	**References**
B	Tycho 2	0.44	4.75±0.10	Hog et al. [2000], Cox [2015]
V	Tycho 2	0.55	4.71±0.1	Hog et al. [2000], Cox [2015]
J	2MASS	1.24	2.33±0.05	Cohen et al. [2003], Skrutskie et al. [2006]
H	2MASS	1.66	1.47±0.03	Cohen et al. [2003], Skrutskie et al. [2006]
K_s	2MASS	2.16	1.05±0.02	Cohen et al. [2003], Skrutskie et al. [2006]
W1	ALLWISE	3.35	0.502±0.027	Wright et al. [2010], Mainzer et al. [2011]
W2	ALLWISE	4.6	0.30 ±0.010	Wright et al. [2010], Mainzer et al. [2011]
S9W	*AKARI*	9	0.215±0.015	Murakami et al. [2007], Ishihara et al. [2010]
W3	ALLWISE	11.6	0.155±0.007	Wright et al. [2010], Mainzer et al. [2011]
W4	ALLWISE	22.1	0.626±0.036	Wright et al. [2010], Mainzer et al. [2011]
	ALMA	1240	0.00072±0.00011	Lieman-Sifry et al. [2016]

Table 5.4: Summary of photometry used in creating the spectral energy distribution for HD 156623.

greater than 0. For the Eastern half of the disk, the HG function is a poor fit, even with the best fit value $g = 0.33$; however, the HG function with $g = 0.45$ is a reasonable approximation for the Western half. These g values are broadly consistent with similar measurements for other low-inclination debris disks as summarized by Hughes et al. [2018], supporting the ideas that disk dust may not obey one Henyey-Greenstein SPF at all scattering angles and that best-fit g values may correlate with the range of scattering angles probed. Although the HG function is not inherently physically informative, we do not pursue physical dust model fits to our phase function given the limited range of scattering angles for the available data. Additionally, there is still an asymmetry in the derived total intensity SPF–albeit less pronounced–again mirroring findings from Crotts et al. [2024].

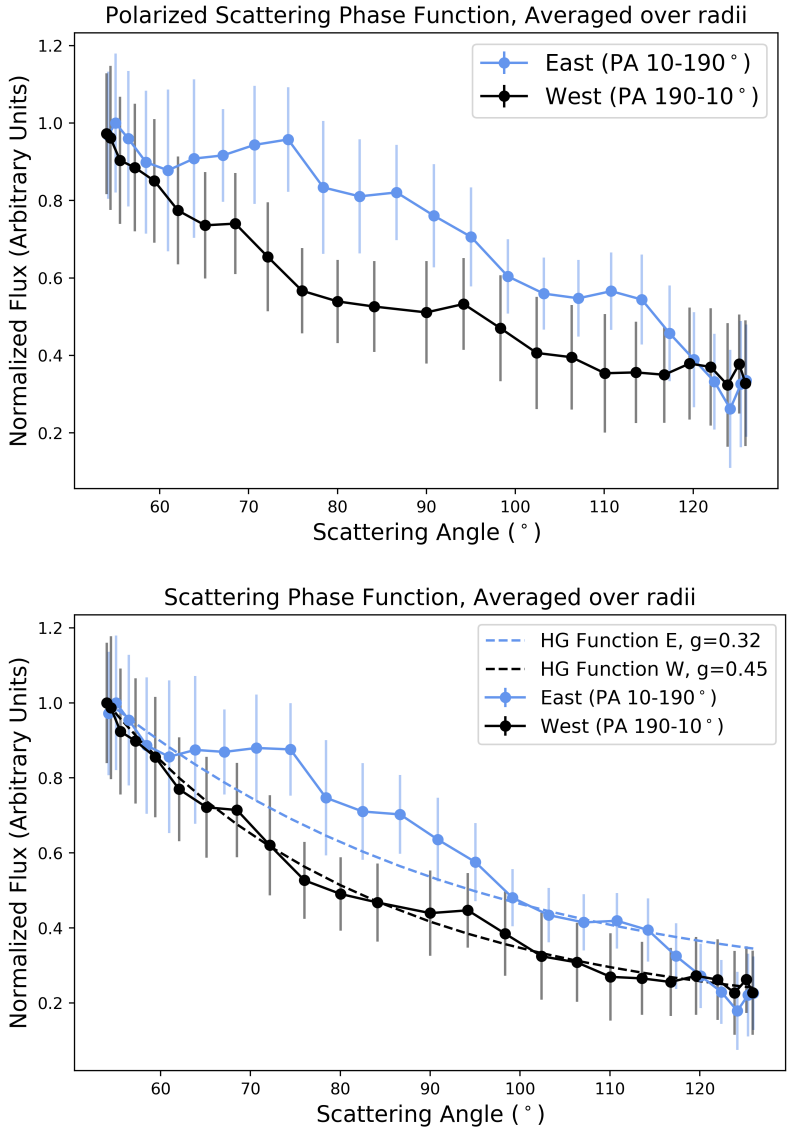

Figure 5.8: (Left) Measured polarized light scattering phase function for the disk, split between the Eastern and Western halves of the disk as defined by the approximate minor axis. We observe an asymmetry between the Eastern and Western halves, consistent with recent findings in Crotts et al. [2024] suggesting this disk may be slightly eccentric. (Right) The measured East/West SPFs divided by a Rayleigh polarization curve, along with Henyey–Greenstein functions fit to each SPF. There is a lesser but still distinct asymmetry between the two halves of the disk, and the Henyey-Greenstein function is a poor fit for the Eastern half.

5.6 Thermal Emission

The main goal of our investigation of HD 156623's SED is to constrain the location of the disk's unseen inner edge. Photometric measurements of HD 156623 were acquired from a variety of sources, ranging from visible to mid-infrared to millimeter ALMA observations. Most measurements were obtained in magnitudes from the IRSA or Vizier databases, and then converted to Janskys using the zero points provided by each mission/project's documentation. These observations and their references are summarized in Table 5.4; all data listed here are before color corrections, as we instead treat points with large bandpasses (namely W3/W4 and AKARI S9W) using synthetic photometry as described below. Although photometric data from *IRAS* were available for this object, they were not used due to poor data quality flags present in the catalog. Given the wide bandpasses of the *WISE* W3/W4 [Wright et al., 2010] and *AKARI* S9W [Fujiwara et al., 2010] filters, we compute synthetic photometry by integrating the model flux multiplied by the transmission profile for each filter (from Rodrigo and Solano [2020]) over its bandpass via the following equation as in Tokunaga and Vacca [2005]:

$$\langle F_\nu \rangle = \frac{\int F_\nu(\nu) S(\nu)/\nu \, d\nu}{\int S(\nu)/\nu \, d\nu} \tag{5.6}$$

where $\langle F_\nu \rangle$ is the monochromatic flux density (erg/s/cm^2/Hz) for our synthetic photometry, F_ν is the monochromatic flux density (erg/s/cm^2/Hz) from the object, $S(\nu)$ is the filter transmission function, and ν represents the frequencies in the bandpass. Additional absolute calibration uncertainties were incorporated for the WISE data points [Cutri et al., 2012] and AKARI data points [TanabÉ et al., 2008].

We initially fit a simple model consisting of two single-temperature blackbody curves for the stellar emission plus the disk's thermal emission to these monochromatic flux densities using a Levenberg-Marquardt least-squares fit implemented in `scipy`. The free parameters included are disk temperature (T_d) and a parameter proportional to the disk emitting area (A). The stellar radius (R_*) and temperature (T_*) are set using the values in Table 5.1 from

Mellon et al. [2019]. The best-fit dust temperature is 184±23 K with a reduced chi squared χ^2_ν value of 1.088, corresponding to a radius of $8.49^{+2.60}_{-1.78}$ AU if treated as an equilibrium temperature for a grain radiating as a blackbody. It is additionally worth noting that radii derived from SEDs are known to be underestimates; i.e. they are often smaller than the inner radii derived from resolved observations [Wyatt, 2008, Pawellek and Krivov, 2015, Pawellek et al., 2021, Booth et al., 2013, Hom et al., 2020].

Given the poor fit at long wavelengths while using a single-temperature blackbody to represent thermal emission from dust, we subsequently tested a model for the spectral energy distribution using a single-temperature blackbody plus an additional modified wavelength-dependent emissivity, following the formalism in Backman et al. [1992]. Again, this model does not assume a spatial distribution or grain size distribution. In this model, grains of a characteristic size $\sim\lambda_0/2\pi$ radiate with a modified emissivity ϵ_ν as follows:

$$\epsilon_\nu = \begin{cases} \frac{\lambda_0}{\lambda} & \lambda > \lambda_0 \\ 1 & \text{otherwise} \end{cases} \tag{5.7}$$

This model was again fit using the `scipy` implementation of a Levenberg-Marquardt least-squares fit, now for both temperature and λ_0. The best-fit disk temperature for this model is 140±23 K with a χ^2_ν value of 1.21, corresponding to a radius of $14.7^{+6.34}_{-3.85}$ AU, with λ_0 unconstrained (best fit value of 219 μm, corresponding to a characteristic grain size of $\sim$35 μm). These models are visualized in Figure 5.9. Neither model is able to capture the 9μm *AKARI* point, and a modified emissivity is necessary to reproduce the flux observed by ALMA.

However, these simple models do not explicitly fit for the inner radius we are interested in, as they assume a single temperature across the entire disk. To constrain the inner radius, we then compute the SED for a spatially resolved, azimuthally symmetric disk using `MCFOST`. We set up this resolved model using a Kurucz 9000 K model atmosphere [Castelli and Kurucz, 2004] and the same parameters and assumptions (e.g. Mie scattering, dust grain size and

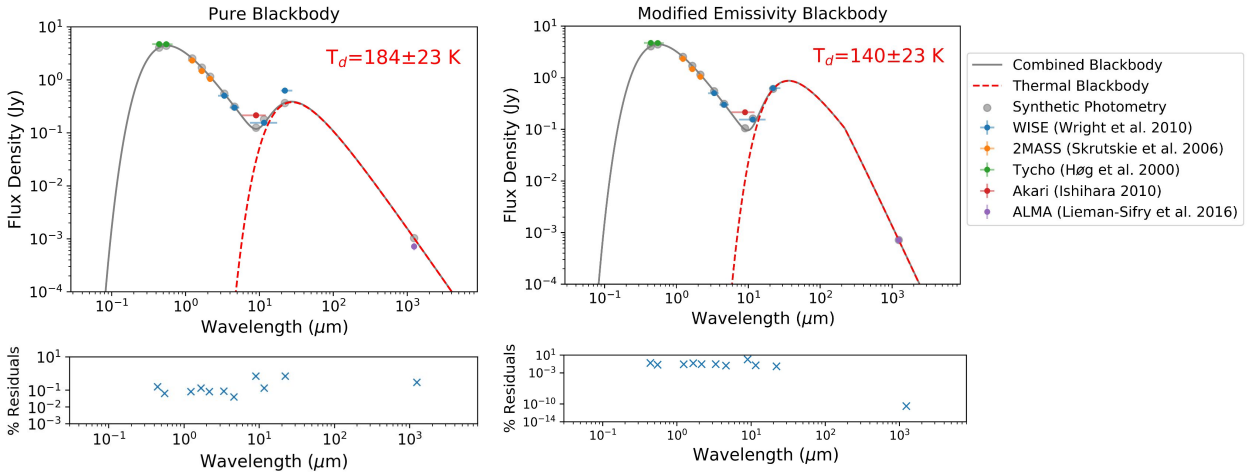

Figure 5.9: Single-component blackbody models using best-fit values to available photometry for HD 156623, with fractional residuals shown below. The dust's blackbody contribution to the SED is plotted in red. (Left) For a a simple single-component blackbody SED, the photometry is best fit with temperature T = 184±23 K. (Right) For a modified-emissivity single-component blackbody SED, the photometry is best fit with T = 140±23 K and λ_0 = 219 μm. Neither model is able to capture the 9μm AKARI point, and a modified emissivity is necessary to reproduce the flux observed by ALMA.

composition) as the scattered-light model in Section 5.4, leaving only $r_{\rm in}$, $a_{\rm min}$, and $M_{\rm d}$ as free parameters. We explore the posterior for those parameters again with a Goodman and Weare [2010] affine invariant MCMC ensemble sampler using the `emcee` package with 16 walkers and uniform priors, with bounds on the priors for $r_{\rm in}$ ($0< r_{\rm in} <15$) and $\log a_{\rm min}$ ($-2< \log a_{\rm min} <1$). Walkers were initialized randomly from a uniform distribution and then simulated for 1500 iterations. We discarded the first 100 iterations as "burn-in" where the ensemble of walkers had not yet converged to their peak in posterior space, and used the remaining 1400 iterations (equivalent to 2.2×10^4 models) for the disk parameter value estimates. The maximum likelihood model SED is shown compared to available photometry in Figure 5.10, and a corner plot of the approximate posteriors is shown in Figure 5.11.

Scattered-light image modeling is limited by the focal-plane mask in its determination of $r_{\rm in}$, resulting in a maximum likelihood value that corresponds to the FPM edge ($\sim$12–15 AU) and a 3σ upper limit of $<$26.6 AU; SED modeling, on the other hand, returns a maximum likelihood value of 2.37 AU and is limited by the prior bound at zero, resulting in an upper limit of $<$13.4 at 99.7% confidence ($<$8.85 AU at 95% confidence). The value for $\log(M_{\rm d})$ should be considered as a scaling factor more than a physically relevant value, as we assume a sparse grain density and do not consider dynamical effects like collisions; for the sake of reproducing our modeling, the value for $\log(M_{\rm d})$ for the maximum-likelihood model shown in Figure 5.10 is -7.02. The minimum grain size $a_{\rm min}$ is much smaller as suggested by SED modeling, $<$0.21 μm at compared to $\sim$1 μm from scattered-light image modeling. For comparison, the blowout size for the system is around 3.5 μm, as further discussed in Section 5.7. This $a_{\rm min}$ value from SED modeling reached a bound on the prior at 0.01 μm, suggesting that the Dohnanyi size distribution or other grain characteristics we have assumed may not fully describe this system; however, given the limited number of photometric data points currently available (four data points–AKARI 9μm, W3, W4, and ALMA–and currently three free parameters), we choose not to add further free parameters to our model in this work. This best-fit MCFOST SED model has $\chi^2_\nu = 1.11$, similar to the

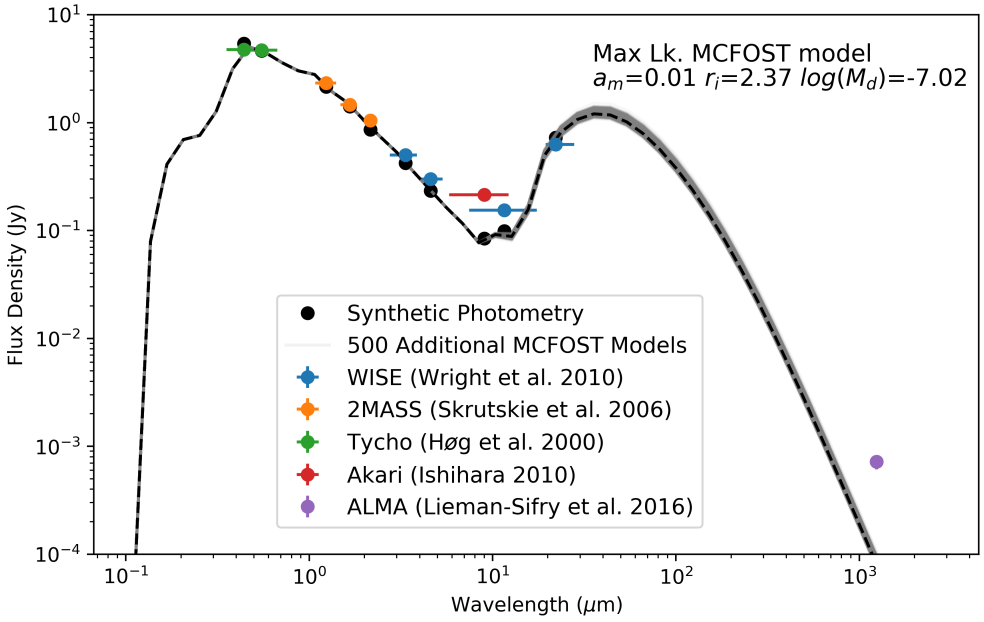

Figure 5.10: Maximum likelihood SED model from `MCFOST` (as a dashed black line, with synthetic photometric points marked) compared to available photometry (colored according to its source). The best fit model requires sub-blowout size grains and a close-in inner radius around ∼3 AU. 500 additional SED models randomly drawn from the post-burn-in MCMC are plotted in grey.

simpler models above. Again, the *AKARI* and ALMA points are not fit well by this model; we discuss this discrepancy–as well as the discrepancy in $a_{\rm min}$–further in Section 5.7. The maximum temperatures calculated by `MCFOST` at $r_{\rm in}$ and $R_{\rm c}$ at the disk midplane in the best fit model are ∼500 K and 355 K respectively.

5.7 Discussion

All SED fits are unable to capture the *AKARI* data point (the red point in Figure 5.9), and no single model we have tested is able to satisfactorily explain the entire set of photometric data points available. `MCFOST` modeling similarly has trouble reproducing the *AKARI* point,

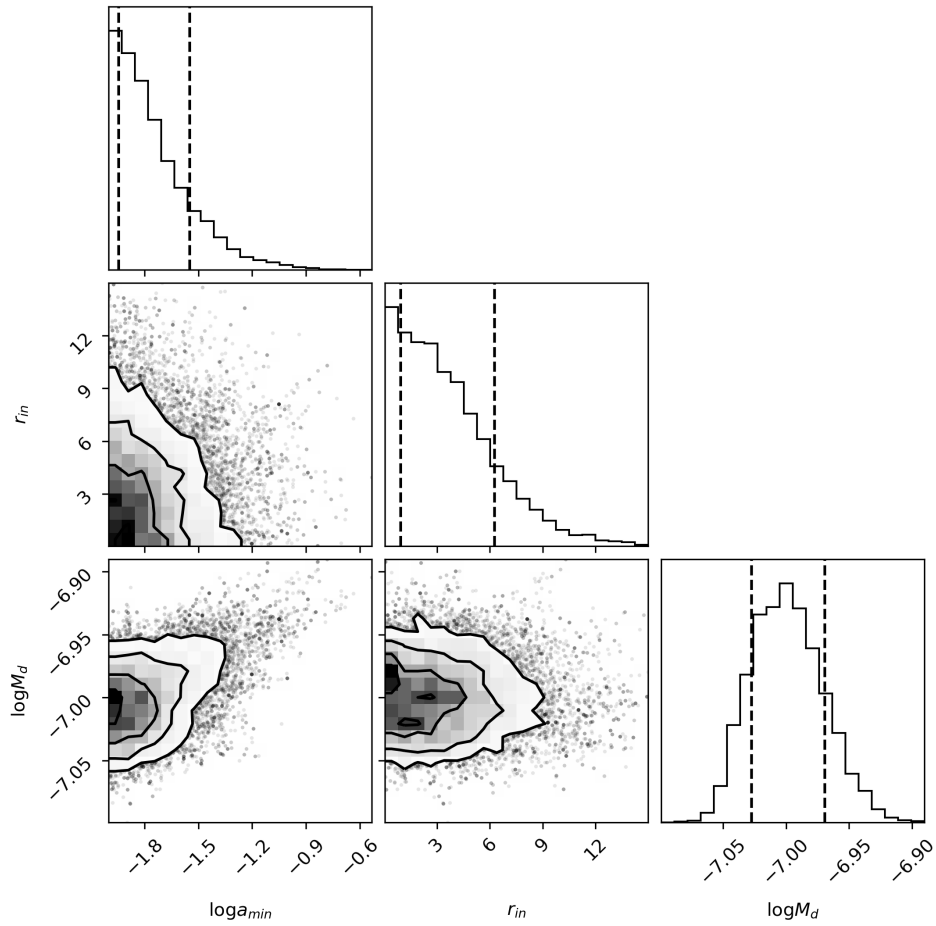

Figure 5.11: Corner plot for MCMC fit with photometry and `MCFOST` SED models. The reported value for $r_{\rm in}$ is an upper bound (< 13.43 AU at 99.7% confidence), as seen in the posterior distribution. Additionally, the value for $\log a_{\rm min}$ is also only an upper limit of -0.685 (0.21 μm); this suggests that different assumptions for the grain composition and/or size distribution may be needed to fully understand the minimum grain size of this system.

as well as the long wavelength flux measured by ALMA, indicating that different assumptions for grain composition and/or size distribution may be needed; given the limited number of photometric points available, exploring those as free parameters in a model is beyond the scope of this work. However, based on our modeling, it appears that–under the assumptions described in our work–the thermal signature of the disk is best explained by a population of close-in warm dust with sub-blowout size grains, and a modified emissivity trend at longer wavelengths. One could additionally imagine that the debris disk has two components: a cold outer disk imaged by GPI and ALMA, and a separate warm inner belt that is behind the GPI FPM and unresolved by ALMA, but also boosts the 9 μm emission as seen by *AKARI*. Future work may include exploring two-component models, and further observations (e.g. *JWST*/MIRI spectroscopy) are necessary to better define the shape of the spectrum through the mid-infrared.

The radiative transfer modeling of the scattered light data is limited by the focal-plane mask, initially constraining $r_{\rm in}$ to be less than 26.6 AU. Single-component blackbody fits to the SED suggest an inner edge of ∼8-15 AU (not accounting for non-blackbody behavior of real dust grains or the possibility of grain overheating; e.g. Pawellek and Krivov [2015], Morales et al. [2011]), and disk models with `MCFOST` fit to the SED constrain the edge to $<$ 13.4 AU. However, it is again worth noting that even the best fit SED model is unable to reproduce both the 9 μm excess and the long wavelength flux observed by ALMA, indicating that different assumptions on the grain properties or surface density distribution (e.g. inner and outer power laws) are necessary to fully explain this system; given the lack of photometry at this time, we leave this endeavor for future work. Lieman-Sifry et al. [2016] similarly constrains the inner radius of this disk using ALMA data and SED modeling, with a best fit value of $r_{in} = 10$ AU from a visibility-only fit and $r_{in} = 2.99$ AU from a simultaneous visibility and SED fit. Our result is in agreement with these values within 1σ. This $<$ 13.4 AU inner edge is certainly unique; HD 156623 is one of few known low-inclination debris disks in Sco-Cen imaged in scattered light (which is biased towards edge-on disks) where the inner clearing

is not visible due to its location behind the FPM [Bonnefoy et al., 2021]. Additionally, this modeling assumes a certain power law for surface density; different assumptions in that value may lead to significant changes in the value of $r_{\rm in}$, possibly explaining the slight differences between our estimate and that of Lieman-Sifry et al. [2016].

The blowout grain size of this system is estimated as ∼3.5 μm, according to Arnold et al. [2019] which uses the equation below [Burns et al., 1979] to compute the blowout size for HR 4796, a similar temperature A-type star.

$$a_{\rm BO} = 1.152 \langle Q_{\rm pr} \rangle \left(\frac{L_*}{L_\odot} \right) \left(\frac{M_*}{M_\odot} \right)^{-1} (1 - \mathcal{P}) \left(\frac{\rho}{\rm g/cm^3} \right)^{-1} \tag{5.8}$$

where L_* is the stellar luminosity is solar luminosities, M_* is the stellar mass in solar masses, $\mathcal{P}$ is the grain porosity (assumed to be zero), ρ is the grain density (assumed to be 3.3 g/cm^3 from Draine and Lee [1984], Draine [2003]), and $\langle Q_{\rm pr} \rangle$ is the average radiation pressure efficiency, calculated from grain scattering properties through:

$$\langle Q_{\rm pr} \rangle = \frac{1}{n} \sum_{i=\nu_{\rm min}}^{\nu_{\rm max}} [F_{\nu,*} Q_{\rm abs,i} + (1 - g) Q_{\rm sca,i}]. \tag{5.9}$$

where $\nu_{\rm min}$ is the lowest frequency used in the calculation, $\nu_{\rm max}$ is the highest frequency used in the calculation, $F_{\nu,*}$ is the stellar spectrum at a given frequency, $Q_{\rm abs,i}$ is the absorption coefficient for a given frequency, g is the asymmetry parameter, $Q_{\rm sca,i}$ is the scattering coefficient for a given frequency, and n is the number of frequency samples used. We will adopt the blowout size of 3.5 μm for the remainder of this discussion which assumes astrosilicate grains as we have in our modeling.

Values for the minimum grain size from both scattered-light image modeling and SED modeling are in significant disagreement with the calculated blowout size; additionally, these values constrain the minimum grain size from different data and different assumptions on the physics of grain interactions with light, as the image modeling value is derived from the polarized scattering phase function and the SED modeling value is derived from thermal equilibrium. `MCFOST` scattered-light image modeling reports the maximum likelihood value

for a_{min} as 1.13 μm, with smaller peaks in the probability distribution around 1.35–1.82 μm as shown in Figure 5.2, and SED modeling suggests $< 1\mu$m; however, these values are much smaller than the minimum dust grain size predicted by the blowout size of 3.5 microns. Lieman-Sifry et al. [2016] provides additional evidence for sub-blowout size grains via their simultaneous model fits to their observed ALMA visibilities and the SED, finding a minimum grain size around $\sim$1 μm, in agreement with our scattered-light modeling. This discrepancy from the blowout size could indicate a rapid re-supply of small grains, possibly from ongoing collisions; however, this blowout size could alternatively indicate that we have underestimated the minimum grain size from radiative transfer and grain modeling due to our assumptions on grain properties [Grigorieva et al., 2007] and/or the use of Mie theory, which is known to be a poor representation of true grain properties. However, if the grains are, in fact, porous as indicated by our radiative transfer modeling, the blowout size could be significantly larger, making this discrepancy even larger. The blowout timescale is approximately the free-fall time, which is short, on the order of orbital timescales. As a result, the blowout timescale should be the dominant timescale for this system. The collision timescale, which dominates the dust replenishment, is $\sim 10^2$ yr–substantially longer than the blowout timescale.

As HD 156623 is known to host a gas-rich disk, gas drag could change the blowout size and associated timescales–that is, small dust grains may be coupled to the gas, enabling their retention and explaining the observed inner edge and sub-blowout size grains. In Lieman-Sifry et al. [2016], HD 156623 has one of the strongest CO J = 2-1 detections out of their sample in Sco-Cen; perhaps this system has a particularly high gas mass, and therefore greater influence of gas drag on the dust dynamics. The sample of Sco-Cen disks from Lieman-Sifry et al. [2016] also suggests a correlation between the presence of gas and sub-blowout grains, as seen in this system. Further modeling is needed to fully understand the impact of the presence of gas in this disk.

5.8 Conclusions

We have (1) presented analysis of the morphology of the possible "hybrid" debris disk around HD 156623 in H band polarized scattered light, (2) presented an empirical measurement of the brightness/surface density profile and scattering phase function for HD 156623's debris disk, and 3) determined that the inner radius of the disk is likely close to the star to $<$ 13.4 AU via SED modeling and imaging. Our work suggests that HD 156623 retains sub-blowout size grains, and gas drag may be a key influence on the dust population of this debris disk, in line with findings from Lieman-Sifry et al. [2016]. However, we acknowledge the numerous degeneracies present in this type of debris disk data, as the observed scattered-light distribution is a complicated and difficult-to-disentangle combination of disk geometry, grain size distribution, grain properties (e.g. porosity, scattering efficiency), and more [Stark et al., 2014]. Future work should consider obtaining additional mid-infrared photometry (e.g. from *JWST*) to further constrain the debris disk SED, and testing more complex models, such as a two-component dust population or simultaneously modeling the gas and dust components of the disk to explore how gas drag impacts small grain retention in this system.

CHAPTER 6

Conclusions

This thesis aims to highlight the deep, critical connection between astronomical instrumentation and cutting-edge astronomical discoveries, especially in the context of high-contrast imaging and (exo-)planetary science. Additionally, these investigations contribute to our understanding of the formation of planetary systems, our ability to detect and characterize exoplanetary systems, and our search for habitable conditions beyond Earth – topics that were all recently prioritized by the Astro2020 Decadal Survey [NASEM, 2021].

In Chapter 2, I developed a new framework for harnessing both spatial and temporal information to remove speckle noise from high-contrast imaging data. To utilize this space-time covariance, our new approach uses a Karhunen-Loéve transform on an image sequence, as opposed to a set of single reference images as in previous applications of Karhunen-Loéve Image Processing (KLIP) for high-contrast imaging. With the recent development of photon-counting detectors, such as microwave kinetic inductance detectors (MKIDs), this technique now has the potential to improve contrast when used as a post-processing step. Preliminary testing on simulated data shows this technique can improve contrast by at least 10–20% from the original image, with significant potential for further improvement. For certain choices of parameters, this algorithm may provide larger contrast gains than spatial-only KLIP.

In Chapter 3, I presented the first resolved infrared polarimetric imaging of Europa, one of the most promising targets for the search for life in the solar system. Although no strong plumes were detected in this data, this work illustrates the sensitivity and capabilities of existing polarimetric instruments, and the potential for high-contrast imaging systems to

contribute to solar system science. Additionally, we intend to continue analysis of this data set for other geologic information and/or fainter plume signals.

In Chapter 4, I revised the spectral type classification of brown dwarf companion HIP 93398 B with new spectroscopic observations from Subaru SCExAO/CHARIS. Spectral typing via empirical templates, temperatures derived by fitting substellar atmosphere models, and $J-H$, $J-K$ and $H-L'$ colors all suggest that this object is instead a late-L dwarf near the L/T transition (T = 1200^{+140}_{-130} K) with moderate to thick clouds present in its atmosphere. When compared with the latest generation of evolution models that account for clouds with our revised luminosity and temperature for the object, the previously suggested tension between the model-independent mass/age and model predictions is resolved, illustrating the importance of cloud physics in brown dwarf cooling models.

Finally, in Chapter 5, I analyzed the first scattered light detection of the debris disk around HD 156623, as imaged by the Gemini Planet Imager in polarized light. I used radiative transfer models to constrain the geometric parameters of the disk based on scattered light data, and thermal models to constrain the unresolved inner radius based on the system's spectral energy distribution (SED). I also computed a measurement of the polarized scattering phase function, adding to the existing sample of empirical phase function measurements. I found that HD 156623's debris disk inner radius is constrained to less than 26.6 AU from scattered light imagery and less than 13.4 AU from SED modeling at a 99.7% confidence interval, and suggest that gas drag may play a role in retaining sub-blowout size dust grains so close to the star.

In this thesis, I have presented novel contributions to both high-contrast imaging techniques and our understanding of planetary systems. These works provide insight into detections of extrasolar planets, the nature of oceans beyond Earth, the atmospheres of giant planets and brown dwarfs, and the mechanisms of planet formation – all topics for which we need to improve our understanding in order to reach the eventual goal of identifying habitable worlds beyond Earth.

Bibliography

A. S. Ackerman and M. S. Marley. Precipitating condensation clouds in substellar atmospheres. *The Astrophysical Journal*, 556(2):872, 2001.

J. Adams, J. Wang, and K. I. Follette. Optimization Techniques for Exoplanet Direct Imaging. In *American Astronomical Society Meeting Abstracts*, volume 53 of *American Astronomical Society Meeting Abstracts*, page 344.05, Jan. 2021.

C. Aime and R. Soummer. The Usefulness and Limits of Coronagraphy in the Presence of Pinned Speckles. ApJ, 612(1):L85–L88, Sept. 2004. doi: 10.1086/424381.

C. Aime and R. Soummer. The usefulness and limits of coronagraphy in the presence of pinned speckles. *The Astrophysical Journal Letters*, 612(1):L85, 2004.

C. Aime, J. Borgnino, F. Martin, R. Petrov, G. Ricort, and S. Kadiri. Contribution to the space-time study of stellar speckle patterns. *Journal of the Optical Society of America A*, 3:1001–1009, July 1986. doi: 10.1364/JOSAA.3.001001.

I. Appenzeller. A new polarimeter for faint astronomical objects. *Publications of the Astronomical Society of the Pacific*, pages 136–139, 1967.

J. A. Arnold, A. J. Weinberger, G. Videen, and E. S. Zubko. The effect of dust composition and shape on radiation-pressure forces and blowout sizes of particles in debris disks. *The Astronomical Journal*, 157(4):157, 2019.

H. W. Babcock. The possibility of compensating astronomical seeing. *Publications of the Astronomical Society of the Pacific*, 65(386):229–236, 1953.

D. Backman, F. Gillett, and F. Witteborn. Infrared observations and thermal models of the beta pictoris disk. *Astrophysical Journal, Part 1 (ISSN 0004-637X), vol. 385, Feb. 1, 1992, p. 670-679.*, 385:670–679, 1992.

V. Bailey, P. M. Hinz, T. Currie, K. Y. L. Su, S. Esposito, J. M. Hill, W. F. Hoffmann, T. Jones, J. Kim, J. Leisenring, M. Meyer, R. Murray-Clay, M. J. Nelson, E. Pinna, A. Puglisi, G. Rieke, T. Rodigas, A. Skemer, M. F. Skrutskie, V. Vaitheeswaran, and J. C. Wilson. A Thermal Infrared Imaging Study of Very Low Mass, Wide-separation Brown Dwarf Companions to Upper Scorpius Stars: Constraining Circumstellar Environments. ApJ, 767(1):31, Apr. 2013. doi: 10.1088/0004-637X/767/1/31.

I. Baraffe, G. Chabrier, F. Allard, and P. H. Hauschildt. Evolutionary models for low-mass stars and brown dwarfs: Uncertainties and limits at very young ages. A&A, 382:563–572, Feb. 2002. doi: 10.1051/0004-6361:20011638.

C. Beichman, G. Neugebauer, H. Habing, P. Clegg, and T. J. Chester. Infrared astronomical satellite (iras) catalogs and atlases. volume 1: Explanatory supplement. In *Infrared astronomical satellite (IRAS) catalogs and atlases. Volume 1: Explanatory supplement*, volume 1, 1988.

M. S. Bessell, F. Castelli, and B. Plez. Model atmospheres broad-band colors, bolometric corrections and temperature calibrations for O - M stars. A&A, 333:231–250, May 1998.

W. M. Best, E. A. Magnier, M. C. Liu, K. M. Aller, Z. Zhang, W. Burgett, K. Chambers, P. Draper, H. Flewelling, N. Kaiser, et al. Photometry and proper motions of m, l, and t dwarfs from the pan-starrs1 3π survey. *The Astrophysical Journal Supplement Series*, 234 (1):1, 2017.

W. M. Best, M. C. Liu, E. A. Magnier, and T. J. Dupuy. A volume-limited sample of ultracool dwarfs. i. construction, space density, and a gap in the l/t transition. *The Astronomical Journal*, 161(1):42, 2020.

W. M. J. Best, T. J. Dupuy, M. C. Liu, A. Sanghi, R. J. Siverd, and Z. Zhang. The UltracoolSheet: Photometry, Astrometry, Spectroscopy, and Multiplicity for 4000+ Ultracool

Dwarfs and Imaged Exoplanets, Feb. 2024. URL https://doi.org/10.5281/zenodo.10573247.

H. Beust, A. Lagrange-Henri, A. Vidal-Madjar, and R. Ferlet. The beta pictoris circumstellar disk. x-numerical simulations of infalling evaporating bodies. *Astronomy and Astrophysics (ISSN 0004-6361), vol. 236, no. 1, Sept. 1990, p. 202-216.*, 236:202–216, 1990.

J.-L. Beuzit, A. Vigan, D. Mouillet, K. Dohlen, R. Gratton, A. Boccaletti, J.-F. Sauvage, H. M. Schmid, M. Langlois, C. Petit, et al. Sphere: the exoplanet imager for the very large telescope. *Astronomy & Astrophysics*, 631:A155, 2019.

N. A. Bharmal. Frozen flow or not? investigating the predictability of the atmosphere. In *Journal of Physics: Conference Series*, volume 595, page 012003. IOP Publishing, 2015.

E. E. Bloemhof, R. G. Dekany, M. Troy, and B. R. Oppenheimer. Behavior of Remnant Speckles in an Adaptively Corrected Imaging System. ApJ, 558(1):L71–L74, Sept. 2001. doi: 10.1086/323494.

S. Blunt, J. J. Wang, I. Angelo, H. Ngo, D. Cody, R. J. De Rosa, J. R. Graham, L. Hirsch, V. Nagpal, E. L. Nielsen, L. Pearce, M. Rice, and R. Tejada. orbitize!: A Comprehensive Orbit-fitting Software Package for the High-contrast Imaging Community. AJ, 159(3):89, Mar. 2020. doi: 10.3847/1538-3881/ab6663.

C. F. Bohren and D. R. Huffman. *Absorption and scattering of light by small particles*. John Wiley & Sons, 2008.

M. Bonavita, C. Fontanive, R. Gratton, K. Mužić, S. Desidera, D. Mesa, B. Biller, A. Scholz, A. Sozzetti, and V. Squicciarini. Results from The COPAINS Pilot Survey: four new BDs and a high companion detection rate for accelerating stars. MNRAS, 513(4):5588–5605, July 2022. doi: 10.1093/mnras/stac1250.

C. Z. Bond, S. Cetre, S. Lilley, P. Wizinowich, D. Mawet, M. Chun, E. Wetherell, S. Jacobson, C. Lockhart, E. Warmbier, et al. Adaptive optics with an infrared pyramid wavefront sensor at keck. *Journal of Astronomical Telescopes, Instruments, and Systems*, 6(3):039003–039003, 2020.

M. Bonnefoy, J. Milli, F. Menard, P. Delorme, A. Chomez, M. Bonavita, A.-M. Lagrange, A. Vigan, J. Augereau, J. Beuzit, et al. Narrow belt of debris around the sco-cen star hd 141011. *Astronomy & Astrophysics*, 655:A62, 2021.

M. Booth, G. Kennedy, B. Sibthorpe, B. C. Matthews, M. C. Wyatt, G. Duchêne, J. Kavelaars, D. Rodriguez, J. S. Greaves, A. Koning, et al. Resolved debris discs around a stars in the herschel debris survey. *Monthly Notices of the Royal Astronomical Society*, 428(2): 1263–1280, 2013.

W. J. Borucki, D. Koch, G. Basri, N. Batalha, T. Brown, D. Caldwell, J. Caldwell, J. Christensen-Dalsgaard, W. D. Cochran, E. DeVore, et al. Kepler planet-detection mission: introduction and first results. *Science*, 327(5968):977–980, 2010.

L. Bourgés, S. Lafrasse, G. Mella, O. Chesneau, J. L. Bouquin, G. Duvert, A. Chelli, and X. Delfosse. The JMMC Stellar Diameters Catalog v2 (JSDC): A New Release Based on SearchCal Improvements. In N. Manset and P. Forshay, editors, *Astronomical Data Analysis Software and Systems XXIII*, volume 485 of *Astronomical Society of the Pacific Conference Series*, page 223, May 2014.

B. P. Bowler, S. C. Blunt, and E. L. Nielsen. Population-level eccentricity distributions of imaged exoplanets and brown dwarf companions: dynamical evidence for distinct formation channels. *The Astronomical Journal*, 159(2):63, 2020.

B. P. Bowler, M. Endl, W. D. Cochran, P. J. MacQueen, J. R. Crepp, G. W. Doppmann, S. Dulz, T. D. Brandt, G. Mirek Brandt, Y. Li, T. J. Dupuy, K. Franson, K. M. Kratter, C. V. Morley, and Y. Zhou. The McDonald Accelerating Stars Survey (MASS): Discovery

of a Long-period Substellar Companion Orbiting the Old Solar Analog HD 47127. ApJ, 913(2):L26, June 2021. doi: 10.3847/2041-8213/abfec8.

L. Bradley, B. Sipőcz, T. Robitaille, E. Tollerud, Z. Vinícius, C. Deil, K. Barbary, H. M. Günther, M. Cara, I. Busko, S. Conseil, M. Droettboom, A. Bostroem, E. M. Bray, L. A. Bratholm, T. Wilson, M. Craig, G. Barentsen, S. Pascual, A. Donath, J. Greco, G. Perren, P. L. Lim, and W. Kerzendorf. astropy/photutils: v0.6, Jan. 2019. URL https://doi.org/10.5281/zenodo.2533376.

B. R. Brandl, T. Agócs, G. Aitink-Kroes, T. Bertram, F. Bettonvil, R. Van Boekel, O. Boulade, M. Feldt, A. Glasse, A. Glauser, et al. Status of the mid-infrared e-elt imager and spectrograph metis. In *Ground-based and Airborne Instrumentation for Astronomy VI*, volume 9908, pages 633–647. SPIE, 2016.

T. D. Brandt. The Hipparcos-Gaia Catalog of Accelerations. ApJS, 239(2):31, Dec. 2018. doi: 10.3847/1538-4365/aaec06.

T. D. Brandt. The Hipparcos-Gaia Catalog of Accelerations: Gaia EDR3 Edition. ApJS, 254(2):42, June 2021. doi: 10.3847/1538-4365/abf93c.

T. D. Brandt, M. Kuzuhara, M. W. McElwain, J. E. Schlieder, J. P. Wisniewski, E. L. Turner, J. Carson, T. Matsuo, B. Biller, M. Bonnefoy, C. Dressing, M. Janson, G. R. Knapp, A. Moro-Martín, C. Thalmann, T. Kudo, N. Kusakabe, J. Hashimoto, L. Abe, W. Brandner, T. Currie, S. Egner, M. Feldt, T. Golota, M. Goto, C. A. Grady, O. Guyon, Y. Hayano, M. Hayashi, S. Hayashi, T. Henning, K. W. Hodapp, M. Ishii, M. Iye, R. Kandori, J. Kwon, K. Mede, S. Miyama, J. I. Morino, T. Nishimura, T. S. Pyo, E. Serabyn, T. Suenaga, H. Suto, R. Suzuki, M. Takami, Y. Takahashi, N. Takato, H. Terada, D. Tomono, M. Watanabe, T. Yamada, H. Takami, T. Usuda, and M. Tamura. The Moving Group Targets of the SEEDS High-contrast Imaging Survey of Exoplanets and Disks: Results and Observations from the First Three Years. ApJ, 786(1):1, May 2014. doi: 10.1088/0004-637X/786/1/1.

T. D. Brandt, M. Rizzo, T. Groff, J. Chilcote, J. P. Greco, N. J. Kasdin, M. A. Limbach, M. Galvin, C. Loomis, G. Knapp, M. W. McElwain, N. Jovanovic, T. Currie, K. Mede, M. Tamura, N. Takato, and M. Hayashi. Data reduction pipeline for the CHARIS integral-field spectrograph I: detector readout calibration and data cube extraction. *Journal of Astronomical Telescopes, Instruments, and Systems*, 3:048002, Oct. 2017. doi: 10.1117/1.JATIS.3.4.048002.

T. D. Brandt, T. J. Dupuy, and B. P. Bowler. Precise Dynamical Masses of Directly Imaged Companions from Relative Astrometry, Radial Velocities, and Hipparcos-Gaia DR2 Accelerations. AJ, 158(4):140, Oct. 2019. doi: 10.3847/1538-3881/ab04a8.

T. D. Brandt, T. J. Dupuy, Y. Li, G. M. Brandt, Y. Zeng, D. Michalik, D. C. B. Gagliuffi, and V. Raposo-Pulido. orvara: An efficient code to fit orbits using radial velocity, absolute, and/or relative astrometry. *The Astronomical Journal*, 162(5):186, 2021.

A. Bressan, P. Marigo, L. Girardi, B. Salasnich, C. Dal Cero, S. Rubele, and A. Nanni. PARSEC: stellar tracks and isochrones with the PAdova and TRieste Stellar Evolution Code. MNRAS, 427(1):127–145, Nov. 2012. doi: 10.1111/j.1365-2966.2012.21948.x.

H. K. Brettle and M. E. Brown. Investigating the Variability of Europa's Exosphere with Keck HIRES. In *AAS/Division for Planetary Sciences Meeting Abstracts #50*, volume 50 of *AAS/Division for Planetary Sciences Meeting Abstracts*, page 403.04, Oct. 2018.

A. G. Brown, A. Vallenari, T. Prusti, J. De Bruijne, C. Babusiaux, M. Biermann, O. Creevey, D. Evans, L. Eyer, A. Hutton, et al. Gaia early data release 3-summary of the contents and survey properties. *Astronomy & Astrophysics*, 649:A1, 2021.

A. J. Burgasser. The spex prism library: 1000+ low-resolution, near-infrared spectra of ultracool m, l, t and y dwarfs. *arXiv preprint arXiv:1406.4887*, 2014.

A. J. Burgasser and Splat Development Team. The SpeX Prism Library Analysis Toolkit (SPLAT): A Data Curation Model. In *Astronomical Society of India Conference Series*,

volume 14 of *Astronomical Society of India Conference Series*, pages 7–12, Jan. 2017. doi: 10.48550/arXiv.1707.00062.

A. J. Burgasser, T. Geballe, S. Leggett, J. D. Kirkpatrick, and D. A. Golimowski. A unified near-infrared spectral classification scheme for t dwarfs. *The Astrophysical Journal*, 637 (2):1067, 2006a.

A. J. Burgasser, J. D. Kirkpatrick, K. L. Cruz, I. N. Reid, S. K. Leggett, J. Liebert, A. Burrows, and M. E. Brown. Hubble space telescope nicmos observations of t dwarfs: brown dwarf multiplicity and new probes of the l/t transition. *The Astrophysical Journal Supplement Series*, 166(2):585, 2006b.

J. A. Burns, P. L. Lamy, and S. Soter. Radiation forces on small particles in the solar system. *Icarus*, 40(1):1–48, 1979.

M. P. Cagigal and V. F. Canales. Experimental checking of the Rician statistics in partially compensated wave fronts. *Optical Engineering*, 40:2690–2697, Dec. 2001. doi: 10.1117/1.1417495.

E. Calamari, J. K. Faherty, B. Burningham, E. Gonzales, D. Bardalez-Gagliuffi, J. M. Vos, M. Gemma, N. Whiteford, and J. Gaarn. An atmospheric retrieval of the brown dwarf gliese 229b. *The Astrophysical Journal*, 940(2):164, 2022.

B. Calvin, M. P. Fitzgerald, M. A. van Kooten, J. Fowler, R. Jensen-Clem, B. L. Gerard, and S. Ragland. The use of spatial-temporal correlations to identify dynamic environmental changes affecting adaptive optics system performance. In *Adaptive Optics Systems VIII*, volume 12185, pages 2542–2552. SPIE, 2022.

V. F. Canales and M. P. Cagigal. Rician Distribution to Describe Speckle Statistics in Adaptive Optics. Appl. Opt., 38(5):766–771, Feb. 1999. doi: 10.1364/AO.38.000766.

H. Canovas, F. Ménard, J. De Boer, C. Pinte, H. Avenhaus, and M. Schreiber. Nonazimuthal linear polarization in protoplanetary disks. *Astronomy & Astrophysics*, 582:L7, 2015.

A. L. Carter, S. Hinkley, J. Kammerer, A. Skemer, B. A. Biller, J. M. Leisenring, M. A. Millar-Blanchaer, S. Petrus, J. M. Stone, K. Ward-Duong, et al. The jwst early release science program for direct observations of exoplanetary systems i: High-contrast imaging of the exoplanet hip 65426 b from 2 to 16 μm. *The Astrophysical journal letters*, 951(1): L20, 2023.

F. Castelli and R. L. Kurucz. New Grids of ATLAS9 Model Atmospheres. In N. Piskunov, W. W. Weiss, and D. F. Gray, editors, *Modelling of Stellar Atmospheres*, volume 210, page A20, Jan. 2003. doi: 10.48550/arXiv.astro-ph/0405087.

F. Castelli and R. L. Kurucz. New grids of atlas9 model atmospheres. *arXiv preprint astro-ph/0405087*, 2004.

R. Cerubini, O. Poch, A. Pommerol, H.-M. Schmid, B. Jost, Y. Brouet, and N. Thomas. Polarimetry of water ice particles providing insights on grain size and degree of sintering on icy planetary surfaces. In *European Planetary Science Congress (EPSC 2018)*, volume 12, pages EPSC2018–83. Copernicus, 2018.

R. Cerubini, A. Pommerol, O. Poch, and N. Thomas. Polarized reflectance of flash-frozen ice particles. In *Lunar and Planetary Science Conference*, number 2326, page 2141, 2020.

A. Cheetham, D. Ségransan, S. Peretti, J. B. Delisle, J. Hagelberg, J. L. Beuzit, T. Forveille, M. Marmier, S. Udry, and F. Wildi. Direct imaging of an ultracool substellar companion to the exoplanet host star HD 4113 A. A&A, 614:A16, June 2018. doi: 10.1051/0004-6361/201630136.

M. Chen, Y. Li, T. D. Brandt, T. J. Dupuy, C. V. Cardoso, and M. J. McCaughrean. Precise dynamical masses of ε indi ba and bb: Evidence of slowed cooling at the l/t transition. *The Astronomical Journal*, 163(6):288, 2022.

M. Chen, J. J. Wang, T. D. Brandt, T. Currie, J. Lozi, J. Chilcote, and M. Vincent. Post-processing CHARIS integral field spectrograph data with PYKLIP. *RAS Techniques and Instruments*, 2(1):620–636, Jan. 2023. doi: 10.1093/rasti/rzad039.

J. Chilcote, Q. Konopacky, R. J. De Rosa, R. Hamper, B. Macintosh, C. Marois, M. D. Perrin, D. Savransky, R. Soummer, J.-P. Véran, et al. Gpi 2.0: upgrading the gemini planet imager. In *Ground-based and Airborne Instrumentation for Astronomy VIII*, volume 11447, pages 394–407. SPIE, 2020.

J. Chilcote, T. Tobin, T. Currie, T. D. Brandt, T. D. Groff, M. Kuzuhara, O. Guyon, J. Lozi, N. Jovanovic, A. Sahoo, et al. Scexao/charis direct imaging of a low-mass companion at a saturn-like separation from an accelerating young a7 star. *The Astronomical Journal*, 162(6):251, 2021.

K. Chiu, X. Fan, S. K. Leggett, D. A. Golimowski, W. Zheng, T. R. Geballe, D. P. Schneider, and J. Brinkmann. Seventy-One New L and T Dwarfs from the Sloan Digital Sky Survey. AJ, 131(5):2722–2736, June 2006. doi: 10.1086/501431.

M. Cohen, W. A. Wheaton, and S. Megeath. Spectral irradiance calibration in the infrared. xiv. the absolute calibration of 2mass. *The Astronomical Journal*, 126(2):1090, 2003.

A. N. Cox. *Allen's astrophysical quantities*. Springer, 2015.

K. A. Crotts, B. C. Matthews, G. Duchêne, T. M. Esposito, R. Dong, J. Hom, R. Oppenheimer, M. Rice, S. G. Wolff, C. H. Chen, et al. A uniform analysis of debris disks with the gemini planet imager. i. an empirical search for perturbations from planetary companions in polarized light images. *The Astrophysical Journal*, 961(2):245, 2024.

T. Currie, T. D. Brandt, T. Uyama, E. L. Nielsen, S. Blunt, O. Guyon, M. Tamura, C. Marois, K. Mede, M. Kuzuhara, et al. Scexao/charis near-infrared direct imaging, spectroscopy, and forward-modeling of κ and b: A likely young, low-gravity superjovian companion. *The Astronomical Journal*, 156(6):291, 2018.

T. Currie, O. Guyon, J. Lozi, A. Sahoo, S. Vievard, V. Deo, J. Chilcote, T. Groff, T. D. Brandt, K. Lawson, et al. On-sky performance and recent results from the subaru coronagraphic extreme adaptive optics system. In *Adaptive Optics Systems VII*, volume 11448, pages 1468–1487. SPIE, 2020.

T. Currie, T. D. Brandt, M. Kuzuhara, J. Chilcote, E. Cashman, R. Y. Liu, K. Lawson, T. Tobin, G. M. Brandt, O. Guyon, J. Lozi, V. Deo, S. Vievard, K. Ahn, and N. Skaf. A new type of exoplanet direct imaging search: a SCExAO/CHARIS survey of accelerating stars. In S. B. Shaklan and G. J. Ruane, editors, *Techniques and Instrumentation for Detection of Exoplanets X*, volume 11823 of *Society of Photo-Optical Instrumentation Engineers (SPIE) Conference Series*, page 1182304, Sept. 2021. doi: 10.1117/12.2595001.

T. Currie, B. Biller, A.-M. Lagrange, C. Marois, O. Guyon, E. Nielsen, M. Bonnefoy, and R. De Rosa. Direct imaging and spectroscopy of extrasolar planets. *arXiv preprint arXiv:2205.05696*, 2022.

R. Cutri et al. Vizier online data catalog: Wise all-sky data release (cutri+ 2012). *VizieR Online Data Catalog*, pages II–311, 2012.

R. M. Cutri, M. F. Skrutskie, S. van Dyk, C. A. Beichman, J. M. Carpenter, T. Chester, L. Cambresy, T. Evans, J. Fowler, J. Gizis, E. Howard, J. Huchra, T. Jarrett, E. L. Kopan, J. D. Kirkpatrick, R. M. Light, K. A. Marsh, H. McCallon, S. Schneider, R. Stiening, M. Sykes, M. Weinberg, W. A. Wheaton, S. Wheelock, and N. Zacarias. VizieR Online Data Catalog: 2MASS All-Sky Catalog of Point Sources (Cutri+ 2003). *VizieR Online Data Catalog*, art. II/246, June 2003.

J. C. Dainty, D. R. Hennings, and K. A. Odonnell. Space-time correlation of stellar speckle patterns. *Journal of the Optical Society of America (1917-1983)*, 71:490–492, Apr. 1981.

J. De Boer, M. Langlois, R. G. van Holstein, J. H. Girard, D. Mouillet, A. Vigan, K. Dohlen, F. Snik, C. U. Keller, C. Ginski, et al. Polarimetric imaging mode of vlt/sphere/irdis-i.

description, data reduction, and observing strategy. *Astronomy & Astrophysics*, 633:A63, 2020.

R. J. De Rosa, E. L. Nielsen, S. C. Blunt, J. R. Graham, Q. M. Konopacky, C. Marois, L. Pueyo, J. Rameau, D. M. Ryan, J. J. Wang, et al. Astrometric confirmation and preliminary orbital parameters of the young exoplanet 51 eridani b with the gemini planet imager. *The Astrophysical Journal Letters*, 814(1):L3, 2015.

R. J. De Rosa, T. M. Esposito, A. Gibbs, V. P. Bailey, M. P. Fitzgerald, J. Chilcote, G. Duchêne, Q. Konopacky, B. Macintosh, M. A. Millar-Blanchaer, M. M. Nguyen, E. L. Nielsen, M. D. Perrin, J. Rameau, and J. J. Wang. Gemini Planet Imager observational calibrations XV: instrument calibrations after six years on sky. In C. J. Evans, J. J. Bryant, and K. Motohara, editors, *Ground-based and Airborne Instrumentation for Astronomy VIII*, volume 11447 of *Society of Photo-Optical Instrumentation Engineers (SPIE) Conference Series*, page 114475A, Dec. 2020. doi: 10.1117/12.2561071.

R. J. De Rosa, M. M. Nguyen, J. Chilcote, B. Macintosh, M. D. Perrin, Q. Konopacky, J. J. Wang, G. Duchêne, E. L. Nielsen, J. Rameau, et al. Revised astrometric calibration of the gemini planet imager. *Journal of Astronomical Telescopes, Instruments, and Systems*, 6(1):015006–015006, 2020.

N. R. Deacon, M. C. Liu, E. A. Magnier, K. M. Aller, W. M. Best, T. Dupuy, B. P. Bowler, A. W. Mann, J. A. Redstone, W. S. Burgett, et al. Wide cool and ultracool companions to nearby stars from pan-starrs 1. *The Astrophysical Journal*, 792(2):119, 2014.

E. Delgado Mena, A. Moya, V. Adibekyan, M. Tsantaki, J. I. González Hernández, G. Israelian, G. R. Davies, W. J. Chaplin, S. G. Sousa, A. C. S. Ferreira, and N. C. Santos. Abundance to age ratios in the HARPS-GTO sample with Gaia DR2. Chemical clocks for a range of [Fe/H]. A&A, 624:A78, Apr. 2019a. doi: 10.1051/0004-6361/201834783.

E. Delgado Mena, A. Moya, V. Adibekyan, M. Tsantaki, J. I. González Hernández, G. Israelian, G. R. Davies, W. J. Chaplin, S. G. Sousa, A. C. S. Ferreira, and N. C. Santos. Abundance to age ratios in the HARPS-GTO sample with Gaia DR2. Chemical clocks for a range of [Fe/H]. A&A, 624:A78, Apr. 2019b. doi: 10.1051/0004-6361/201834783.

R. Dodkins. *Development of MKID Instrumentation for exoplanet direct imaging.* PhD thesis, University of Oxford, 2018.

R. H. Dodkins, K. K. Davis, B. Lewis, S. Mahashabde, B. A. Mazin, I. A. Lipartito, N. Fruitwala, K. O'Brien, and N. Thatte. First principle simulator of a stochastically varying image plane for photon-counting high contrast applications. *Publications of the Astronomical Society of the Pacific*, 132(1016):104503, 2020.

T. Doggett, R. Greeley, P. Figueredo, and K. Tanaka. Geologic stratigraphy and evolution of europa's surface. *Europa*, page 137, 2009.

A. Dollfus. Optical polarimetry of the galilean satellites of jupiter. *Icarus*, 25(3):416–431, 1975.

B. T. Draine. Interstellar dust grains. *Annual Review of Astronomy and Astrophysics*, 41 (1):241–289, 2003.

B. T. Draine and H. M. Lee. Optical Properties of Interstellar Graphite and Silicate Grains. ApJ, 285:89, Oct. 1984. doi: 10.1086/162480.

T. J. Dupuy and A. L. Kraus. Distances, luminosities, and temperatures of the coldest known substellar objects. *Science*, 341(6153):1492–1495, 2013.

T. J. Dupuy and M. C. Liu. The Hawaii Infrared Parallax Program. I. Ultracool Binaries and the L/T Transition. ApJS, 201(2):19, Aug. 2012. doi: 10.1088/0067-0049/201/2/19.

T. J. Dupuy and M. C. Liu. The hawaii infrared parallax program. i. ultracool binaries and the l/t transition. *The Astrophysical Journal Supplement Series*, 201(2):19, 2012.

N. Engler, C. Lazzoni, R. Gratton, J. Milli, H. M. Schmid, G. Chauvin, Q. Kral, N. Pawellek, P. Thébault, A. Boccaletti, et al. Hd 117214 debris disk: scattered-light images and constraints on the presence of planets. *Astronomy & Astrophysics*, 635:A19, 2020.

A. Ershova and J. Schmidt. DUDI. Fast code for modeling two-body dynamics of dust ejected from an atmosphereless body. In *AAS/Division for Planetary Sciences Meeting Abstracts*, volume 53 of *AAS/Division for Planetary Sciences Meeting Abstracts*, page 308.02, Oct. 2021.

A. Ershova and J. Schmidt. Two-body model for the spatial distribution of dust ejected from an atmosphereless body. *Astronomy & Astrophysics*, 650:A186, 2021.

T. M. Esposito, G. Duchêne, P. Kalas, M. Rice, É. Choquet, B. Ren, M. D. Perrin, C. H. Chen, P. Arriaga, E. Chiang, E. L. Nielsen, J. R. Graham, J. J. Wang, R. J. De Rosa, K. B. Follette, S. M. Ammons, M. Ansdell, V. P. Bailey, T. Barman, J. Sebastián Bruzzone, J. Bulger, J. Chilcote, T. Cotten, R. Doyon, M. P. Fitzgerald, S. J. Goodsell, A. Z. Greenbaum, P. Hibon, L.-W. Hung, P. Ingraham, Q. Konopacky, J. E. Larkin, B. Macintosh, J. Maire, F. Marchis, C. Marois, J. Mazoyer, S. Metchev, M. A. Millar-Blanchaer, R. Oppenheimer, D. Palmer, J. Patience, L. Poyneer, L. Pueyo, A. Rajan, J. Rameau, F. T. Rantakyrö, D. Ryan, D. Savransky, A. C. Schneider, A. Sivaramakrishnan, I. Song, R. Soummer, S. Thomas, J. K. Wallace, K. Ward-Duong, S. Wiktorowicz, and S. Wolff. Direct Imaging of the HD 35841 Debris Disk: A Polarized Dust Ring from Gemini Planet Imager and an Outer Halo from HST/STIS. AJ, 156:47, Aug. 2018. doi: 10.3847/1538-3881/aacbc9.

T. M. Esposito, P. Kalas, M. P. Fitzgerald, M. A. Millar-Blanchaer, G. Duchene, J. Patience, J. Hom, M. D. Perrin, R. J. De Rosa, E. Chiang, et al. Debris disk results from the gemini planet imager exoplanet survey's polarimetric imaging campaign. *The Astronomical Journal*, 160(1):24, 2020.

S. A. Fagents, R. Greeley, R. J. Sullivan, R. T. Pappalardo, L. M. Prockter, G. S. Team, et al. Cryomagmatic mechanisms for the formation of rhadamanthys linea, triple band margins, and other low-albedo features on europa. *Icarus*, 144(1):54–88, 2000.

C. Fassino, G. Pistone, and M. P. Rogantin. Computing the moments of the complex gaussian: Full and sparse covariance matrix. *Mathematics*, 7(3), 2019. ISSN 2227-7390. doi: 10.3390/math7030263. URL https://www.mdpi.com/2227-7390/7/3/263.

M. P. Fitzgerald and J. R. Graham. Speckle Statistics in Adaptively Corrected Images. ApJ, 637(1):541–547, Jan. 2006. doi: 10.1086/498339.

O. Flasseur, L. Denis, É. Thiébaut, and M. Langlois. Exoplanet detection in angular differential imaging by statistical learning of the nonstationary patch covariances-the paco algorithm. *Astronomy & Astrophysics*, 618:A138, 2018.

K. B. Follette. An introduction to high contrast differential imaging of exoplanets and disks. *Publications of the Astronomical Society of the Pacific*, 135(1051):093001, 2023.

C. Fontanive, Mužić, K. , M. Bonavita, and B. Biller. A new method for target selection in direct imaging programmes with COPAINS. MNRAS, 490(1):1120–1134, Nov. 2019. doi: 10.1093/mnras/stz2587.

D. Foreman-Mackey, D. W. Hogg, D. Lang, and J. Goodman. emcee: The MCMC Hammer. PASP, 125(925):306, Mar. 2013. doi: 10.1086/670067.

K. Franson and B. P. Bowler. Dynamical Mass of the Young Brown Dwarf Companion PZ Tel B. AJ, 165(6):246, June 2023. doi: 10.3847/1538-3881/acca18.

R. A. Frazin. Simultaneous ultra-high contrast imaging and determination of time-dependent, non-common path aberrations in the presence of detector noise. In L. M. Stepp, R. Gilmozzi, and H. J. Hall, editors, *Ground-based and Airborne Telescopes V*,

volume 9145, pages 1368 – 1374. International Society for Optics and Photonics, SPIE, 2014. doi: 10.1117/12.2054356. URL https://doi.org/10.1117/12.2054356.

R. A. Frazin and A. T. Rodack. Millisecond exoplanet imaging: Ii. regression equations and technical discussion. *J. Opt. Soc. Am. A*, 38(10):1557–1569, Oct 2021. doi: 10.1364/JOSAA.426339. URL http://opg.optica.org/josaa/abstract.cfm?URI=josaa-38-10-1557.

H. Fujiwara, D. Ishihara, S. Oyabu, A. Salama, S. Takita, and I. Yamamura. Akari/irc all-sky survey point source catalogue version 1.0–release note (rev. 1)–. *AKARI*, 2010.

C. Gaia, A. Brown, A. Vallenari, T. Prusti, J. De Bruijne, C. Babusiaux, Á. Juhász, G. Marschalkó, G. Marton, L. Molnár, et al. Gaia data release 2 summary of the contents and survey properties. *Astronomy & Astrophysics*, 616(1), 2018.

Gaia Collaboration. VizieR Online Data Catalog: Gaia DR2 (Gaia Collaboration, 2018). *VizieR Online Data Catalog*, art. I/345, Apr. 2018.

Gaia Collaboration, A. Helmi, F. van Leeuwen, P. J. McMillan, D. Massari, T. Antoja, A. C. Robin, L. Lindegren, U. Bastian, F. Arenou, and et al. Gaia Data Release 2. The kinematics of globular clusters and dwarf galaxies around the Milky Way (Corrigendum). A&A, 642:C1, Oct. 2020a. doi: 10.1051/0004-6361/202039217.

Gaia Collaboration, A. Helmi, F. van Leeuwen, P. J. McMillan, D. Massari, T. Antoja, A. C. Robin, L. Lindegren, U. Bastian, F. Arenou, and et al. Gaia Data Release 2. The kinematics of globular clusters and dwarf galaxies around the Milky Way (Corrigendum). A&A, 642:C1, Oct. 2020b. doi: 10.1051/0004-6361/202039217.

Gaia Collaboration, S. A. Klioner, L. Lindegren, F. Mignard, J. Hernández, M. Ramos-Lerate, U. Bastian, M. Biermann, A. Bombrun, A. de Torres, and et al. Gaia Early Data Release 3. The celestial reference frame (Gaia-CRF3). A&A, 667:A148, Nov. 2022. doi: 10.1051/0004-6361/202243483.

E. V. Garcia, T. Currie, O. Guyon, K. G. Stassun, N. Jovanovic, J. Lozi, T. Kudo, D. Doughty, J. Schlieder, J. Kwon, T. Uyama, M. Kuzuhara, J. C. Carson, T. Nakagawa, J. Hashimoto, N. Kusakabe, L. Abe, W. Brandner, T. D. Brandt, M. Feldt, M. Goto, C. A. Grady, Y. Hayano, M. Hayashi, S. S. Hayashi, T. Henning, K. W. Hodapp, M. Ishii, M. Iye, M. Janson, R. Kandori, G. R. Knapp, T. Matsuo, M. W. McElwain, S. Miyama, J. I. Morino, A. Moro-Martin, T. Nishimura, T. S. Pyo, E. Serabyn, T. Suenaga, H. Suto, R. Suzuki, Y. H. Takahashi, H. Takami, M. Takami, N. Takato, H. Terada, C. Thalmann, E. L. Turner, M. Watanabe, J. Wisniewski, T. Yamada, T. Usuda, and M. Tamura. SCExAO and GPI Y JHBand Photometry and Integral Field Spectroscopy of the Young Brown Dwarf Companion to HD 1160. ApJ, 834(2):162, Jan. 2017. doi: 10.3847/1538-4357/834/2/162.

V. Garrel, O. Guyon, P. Baudoz, F. Martinache, F. Vogt, Y. Takashi, Y. Kaito, and F. Cantalloube. The subaru coronagraphic extreme ao (scexao) system: visible imaging mode. In *Adaptive Optics Systems II*, volume 7736, pages 1991–1996. SPIE, 2010.

A. Gáspár, G. H. Rieke, and N. Ballering. The Correlation between Metallicity and Debris Disk Mass. ApJ, 826(2):171, Aug. 2016. doi: 10.3847/0004-637X/826/2/171.

T. R. Geballe, G. R. Knapp, S. K. Leggett, X. Fan, D. A. Golimowski, S. Anderson, J. Brinkmann, I. Csabai, J. E. Gunn, S. L. Hawley, G. Hennessy, T. J. Henry, G. J. Hill, R. B. Hindsley, Ž. Ivezić, R. H. Lupton, A. McDaniel, J. A. Munn, V. K. Narayanan, E. Peng, J. R. Pier, C. M. Rockosi, D. P. Schneider, J. A. Smith, M. A. Strauss, Z. I. Tsvetanov, A. Uomoto, D. G. York, and W. Zheng. Toward Spectral Classification of L and T Dwarfs: Infrared and Optical Spectroscopy and Analysis. ApJ, 564(1):466–481, Jan. 2002. doi: 10.1086/324078.

T. D. Gebhard, M. J. Bonse, S. P. Quanz, and B. Schölkopf. Half-sibling regression meets exoplanet imaging: Psf modeling and subtraction using a flexible, domain knowledge-driven, causal framework. *arXiv preprint arXiv:2204.03439*, 2022.

J. D. Giorgini. Status of the JPL Horizons Ephemeris System. In *IAU General Assembly*, volume 29, page 2256293, Aug. 2015.

J. E. Gizis, I. N. Reid, G. R. Knapp, J. Liebert, J. D. Kirkpatrick, D. W. Koerner, and A. J. Burgasser. Hubble Space Telescope Observations of Binary Very Low Mass Stars and Brown Dwarfs. AJ, 125(6):3302–3310, June 2003. doi: 10.1086/374991.

J. GJ't Hart, R. G. van Holstein, S. P. Bos, J. Ruigrok, F. Snik, J. Lozi, O. Guyon, T. Kudo, J. Zhang, N. Jovanovic, et al. Full characterization of the instrumental polarization effects of the spectropolarimetric mode of scexao/charis. In *Polarization Science and Remote Sensing X*, volume 11833, pages 148–174. SPIE, 2021.

S. Gladysz, N. Yaitskova, and J. C. Christou. Statistics of intensity in adaptive-optics images and their usefulness for detection and photometry of exoplanets. *Journal of the Optical Society of America A*, 27(11):A64–A75, Nov. 2010. doi: 10.1364/JOSAA.27.000A64.

A. Glindemann, R. G. Lane, and J. C. Dainty. Simulation of Time-evolving Speckle Patterns Using Kolmogorov Statistics. *Journal of Modern Optics*, 40(12):2381–2388, Dec. 1993. doi: 10.1080/09500349314552401.

S. Goebel. From Lab Testing to Science: Applying SAPHIRA HgCdTe L-APD Detectors to Adaptive Optics. *arXiv e-prints*, art. arXiv:1807.04903, July 2018.

S. B. Goebel, O. Guyon, D. N. B. Hall, N. Jovanovic, J. Lozi, and F. Martinache. Measurements of Speckle Lifetimes in Near-infrared Extreme Adaptive Optics Images for Optimizing Focal Plane Wavefront Control. PASP, 130(992):104502, Oct. 2018. doi: 10.1088/1538-3873/aad8ed.

D. B. Goldstein, M. Hedman, M. Manga, M. Perry, J. Spitale, and B. Teolis. Enceladus plume dynamics: from surface to space. *Enceladus and the icy moons of Saturn*, 175, 2018.

J. Gomes da Silva, N. C. Santos, V. Adibekyan, S. G. Sousa, T. L. Campante, P. Figueira, D. Bossini, E. Delgado-Mena, M. J. P. F. G. Monteiro, P. de Laverny, A. Recio-Blanco, and C. Lovis. Stellar chromospheric activity of 1674 FGK stars from the AMBRE-HARPS sample. I. A catalogue of homogeneous chromospheric activity. A&A, 646:A77, Feb. 2021. doi: 10.1051/0004-6361/202039765.

P. Gondoin. Chromospheric activity of nearby Sun-like stars. R'_{HK} index signature of a recent burst of star formation. A&A, 641:A110, Sept. 2020. doi: 10.1051/0004-6361/202038291.

J. Goodman and J. Weare. Ensemble samplers with affine invariance. *Communications in applied mathematics and computational science*, 5(1):65–80, 2010.

O. Grasset, M. Dougherty, A. Coustenis, E. Bunce, C. Erd, D. Titov, M. Blanc, A. Coates, P. Drossart, L. Fletcher, et al. Jupiter icy moons explorer (juice): An esa mission to orbit ganymede and to characterise the jupiter system. *Planetary and Space Science*, 78:1–21, 2013.

R. O. Gray, C. J. Corbally, R. F. Garrison, M. T. McFadden, E. J. Bubar, C. E. McGahee, A. A. O'Donoghue, and E. R. Knox. Contributions to the Nearby Stars (NStars) Project: Spectroscopy of Stars Earlier than M0 within 40 pc-The Southern Sample. AJ, 132(1): 161–170, July 2006. doi: 10.1086/504637.

R. Greeley, R. Sullivan, J. Klemaszewski, K. Homan, J. W. Head III, R. T. Pappalardo, J. Veverka, B. E. Clark, T. V. Johnson, K. P. Klaasen, et al. Europa: initial galileo geological observations. *Icarus*, 135(1):4–24, 1998.

A. Grigorieva, P. Artymowicz, and P. Thébault. Collisional dust avalanches in debris discs. *Astronomy & Astrophysics*, 461(2):537–549, 2007.

T. D. Groff, N. J. Kasdin, M. A. Limbach, M. Galvin, M. A. Carr, G. Knapp, T. Brandt, C. Loomis, N. Jarosik, K. Mede, et al. The charis ifs for high contrast imaging at subaru.

In *Techniques and Instrumentation for Detection of Exoplanets VII*, volume 9605, pages 457–466. SPIE, 2015.

T. D. Groff, J. Chilcote, N. J. Kasdin, M. Galvin, C. Loomis, M. A. Carr, T. Brandt, G. Knapp, M. A. Limbach, O. Guyon, et al. Laboratory testing and performance verification of the charis integral field spectrograph. In *Ground-based and Airborne Instrumentation for Astronomy VI*, volume 9908, page 99080O. International Society for Optics and Photonics, 2016.

O. Guyon. Limits of adaptive optics for high-contrast imaging. *The Astrophysical Journal*, 629(1):592, 2005.

O. Guyon. Extreme adaptive optics. *Annual Review of Astronomy and Astrophysics*, 56: 315–355, 2018.

O. Guyon and J. Males. Adaptive optics predictive control with empirical orthogonal functions (eofs). *arXiv preprint arXiv:1707.00570*, 2017.

O. Guyon, E. Pluzhnik, M. J. Kuchner, B. Collins, and S. Ridgway. Theoretical limits on extrasolar terrestrial planet detection with coronagraphs. *The Astrophysical Journal Supplement Series*, 167(1):81, 2006.

O. Guyon, F. Martinache, V. Garrel, F. Vogt, K. Yokochi, and T. Yoshikawa. The subaru coronagraphic extreme ao (scexao) system: wavefront control and detection of exoplanets with coherent light modulation in the focal plane. In *Adaptive optics systems II*, volume 7736, pages 792–800. SPIE, 2010.

O. Guyon, N. Jovanovic, J. Lozi, J. Males, F. Martinache, B. Mazin, B. Norris, and P. Pathak. Subaru coronagraphic extreme adaptive optics (scexao): wavefront control optimized for high-contrast imaging (conference presentation). In *Techniques and Instrumentation for Detection of Exoplanets VIII*, volume 10400, page 1040017. International Society for Optics and Photonics, 2017.

O. Guyon, B. Mazin, M. Fitzgerald, D. Mawet, C. Marois, A. Skemer, J. Lozi, and J. Males. Wavefront control architecture and expected performance for the TMT Planetary Systems Imager. In L. M. Close, L. Schreiber, and D. Schmidt, editors, *Adaptive Optics Systems VI*, volume 10703 of *Society of Photo-Optical Instrumentation Engineers (SPIE) Conference Series*, page 107030Z, July 2018. doi: 10.1117/12.2314331.

O. Guyon, A. Sevin, D. Gratadour, J. Bernard, H. Ltaief, D. Sukkari, S. Cetre, N. Skaf, J. Lozi, F. Martinache, et al. The compute and control for adaptive optics (cacao) real-time control software package. In *Adaptive Optics Systems VI*, volume 10703, page 107031E. International Society for Optics and Photonics, 2018.

O. Guyon, J. Lozi, S. Vievard, A. Sahoo, N. Jovanovic, T. Currie, P. Pathak, F. Martinache, T. Kudo, M. Tamura, G. Singh, C. Clergeon, Y. Minowa, Y. Ono, E. Mieda, B. Mazin, A. Walter, N. Cvetojevic, S. Lacour, E. Huby, B. Norris, A. Wong, M. Ireland, C. Schwab, T. Feger, P. Tuthill, T. Lagadec, T. Groff, J. Chilcote, T. Brandt, D. Hall, S. Goebel, F. Snik, D. Doelman, S. Bos, H. Kawahara, T. Kotani, D. Mawet, R. Belikov, E. Bendek, A. Sevin, D. Gratadour, H. Ltaief, J. Males, Z. Jin, N. Murakami, J. Knight, and J. Kasdin. The SCExAO High Contrast Imaging Platform: Current and Upcoming Capabilities. In *American Astronomical Society Meeting Abstracts #233*, volume 233 of *American Astronomical Society Meeting Abstracts*, page 104.03, Jan. 2019.

R. Hafeez, F. Archinuk, S. Fabbro, H. Teimoorinia, and J.-P. Véran. Forecasting Wavefront Corrections in an Adaptive Optics System. *arXiv e-prints*, art. arXiv:2112.01437, Dec. 2021.

A. Hales, U. Gorti, J. M. Carpenter, M. Hughes, and K. Flaherty. Modeling the spatial distribution and origin of co gas in debris disks. *The Astrophysical Journal*, 878(2):113, 2019.

C. Hansen, L. Esposito, J. Colwell, A. Hendrix, G. Portyankina, A. Stewart, and R. West.

The composition and structure of enceladus' plume from the complete set of cassini uvis occultation observations. *Icarus*, 344:113461, 2020.

C. J. Hansen, L. Esposito, A. Stewart, J. Colwell, A. Hendrix, W. Pryor, D. Shemansky, and R. West. Enceladus' water vapor plume. *Science*, 311(5766):1422–1425, 2006.

Y. Hayano, H. Takami, O. Guyon, S. Oya, M. Hattori, Y. Saito, M. Watanabe, N. Murakami, Y. Minowa, M. Ito, S. Colley, M. Eldred, T. Golota, M. Dinkins, N. Kashikawa, and M. Iye. Current status of the laser guide star adaptive optics system for Subaru Telescope. In N. Hubin, C. E. Max, and P. L. Wizinowich, editors, *Adaptive Optics Systems*, volume 7015 of *Society of Photo-Optical Instrumentation Engineers (SPIE) Conference Series*, page 701510, July 2008. doi: 10.1117/12.789992.

Y. Hayano, H. Takami, S. Oya, M. Hattori, Y. Saito, M. Watanabe, O. Guyon, Y. Minowa, S. E. Egner, M. Ito, et al. Commissioning status of subaru laser guide star adaptive optics system. In *Adaptive Optics Systems II*, volume 7736, pages 260–267. SPIE, 2010.

C. Hayashi and T. Nakano. Evolution of Stars of Small Masses in the Pre-Main-Sequence Stages. *Progress of Theoretical Physics*, 30(4):460–474, Oct. 1963. doi: 10.1143/PTP.30.460.

C. Heiles. 9286 stars: an agglomeration of stellar polarization catalogs. *The Astronomical Journal*, 119(2):923, 2000.

C. Helling and S. Casewell. Atmospheres of brown dwarfs. *The Astronomy and Astrophysics Review*, 22(1):80, 2014.

D. J. Hemingway, M. L. Rudolph, and M. Manga. Cascading parallel fractures on enceladus. *Nature Astronomy*, 4(3):234–239, 2020.

L. G. Henyey and J. L. Greenstein. Diffuse radiation in the galaxy. *Astrophysical Journal, vol. 93, p. 70-83 (1941).*, 93:70–83, 1941.

G. Herriot, D. Andersen, J. Atwood, P. Byrnes, M.-A. Boucher, C. Boyer, K. Caputa, C. Correia, J. Dunn, B. Ellerbroek, et al. Tmt nfiraos: adaptive optics system for the thirty meter telescope. In *Adaptive Optics Systems III*, volume 8447, pages 613–621. SPIE, 2012.

P. Hickson. Fundamentals of atmospheric and adaptive optics. *The University of British Columbia: Vancouver, BC, Canada*, pages 1–68, 2008.

S. Hinkley, A. L. Carter, S. Ray, A. Skemer, B. Biller, E. Choquet, M. A. Millar-Blanchaer, S. Sallum, B. Miles, N. Whiteford, et al. The jwst early release science program for the direct imaging and spectroscopy of exoplanetary systems. *Publications of the Astronomical Society of the Pacific*, 134(1039):095003, 2022.

E. Høg. Tycho Star Catalogs: The 2.5 Million Brightest Stars. In P. Murdin, editor, *Encyclopedia of Astronomy and Astrophysics*, page 2862. Astronomy and Astrophysics, 2000. doi: 10.1888/0333750888/2862.

E. Høg, C. Fabricius, V. V. Makarov, S. Urban, T. Corbin, G. Wycoff, U. Bastian, P. Schwekendiek, and A. Wicenec. The Tycho-2 catalogue of the 2.5 million brightest stars. A&A, 355:L27–L30, Mar. 2000.

E. Hog, C. Fabricius, V. V. Makarov, S. Urban, T. Corbin, G. Wycoff, U. Bastian, P. Schwekendiek, and A. Wicenec. The tycho-2 catalogue of the 2.5 million brightest stars. Technical report, Naval Observatory Washington DC, 2000.

J. Hom, J. Patience, T. M. Esposito, G. Duchêne, K. Worthen, P. Kalas, H. Jang-Condell, K. Saboi, P. Arriaga, J. Mazoyer, et al. First resolved scattered-light images of four debris disks in scorpius-centaurus with the gemini planet imager. *The Astronomical Journal*, 159 (1):31, 2020.

N. Houk and T. Fuentes-Williams. Vol. 3 of the michigan catalogue of two-dimensional

spectral types (-40° to-26°) and future plans. In *Bulletin of the American Astronomical Society*, volume 14, page 615, 1982.

S. M. Howell and R. T. Pappalardo. Band formation and ocean-surface interaction on europa and ganymede. *Geophysical Research Letters*, 45(10):4701–4709, 2018.

A. M. Hughes, G. Duchêne, and B. C. Matthews. Debris disks: structure, composition, and variability. *Annual Review of Astronomy and Astrophysics*, 56:541–591, 2018.

L.-W. Hung, S. Bruzzone, M. A. Millar-Blanchaer, J. J. Wang, P. Arriaga, S. Metchev, M. P. Fitzgerald, A. Sivaramakrishnan, and M. D. Perrin. Gemini planet imager observational calibration xii: photometric calibration in the polarimetry mode. In *Ground-based and Airborne Instrumentation for Astronomy VI*, volume 9908, pages 1044–1056. SPIE, 2016.

D. Ishihara, T. Onaka, H. Kataza, A. Salama, C. Alfageme, A. Cassatella, N. Cox, P. Garcia-Lario, C. Stephenson, M. Cohen, et al. The akari/irc mid-infrared all-sky survey. *Astronomy & Astrophysics*, 514:A1, 2010.

R. Jensen-Clem, C. Z. Bond, S. Cetre, E. McEwen, P. Wizinowich, S. Ragland, D. Mawet, and J. Graham. Demonstrating predictive wavefront control with the keck ii near-infrared pyramid wavefront sensor. In *Techniques and Instrumentation for Detection of Exoplanets IX*, volume 11117, page 111170W. International Society for Optics and Photonics, 2019.

E. Jones, T. Oliphant, P. Peterson, et al. SciPy: Open source scientific tools for Python, 2001. URL http://www.scipy.org/.

N. Jovanovic, O. Guyon, F. Martinache, P. Pathak, J. Hagelberg, and T. Kudo. Artificial Incoherent Speckles Enable Precision Astrometry and Photometry in High-contrast Imaging. ApJ, 813(2):L24, Nov. 2015a. doi: 10.1088/2041-8205/813/2/L24.

N. Jovanovic, F. Martinache, O. Guyon, C. Clergeon, G. Singh, T. Kudo, V. Garrel, K. Newman, D. Doughty, J. Lozi, J. Males, Y. Minowa, Y. Hayano, N. Takato, J. Morino, J. Kuhn,

E. Serabyn, B. Norris, P. Tuthill, G. Schworer, P. Stewart, L. Close, E. Huby, G. Perrin, S. Lacour, L. Gauchet, S. Vievard, N. Murakami, F. Oshiyama, N. Baba, T. Matsuo, J. Nishikawa, M. Tamura, O. Lai, F. Marchis, G. Duchene, T. Kotani, and J. Woillez. The Subaru Coronagraphic Extreme Adaptive Optics System: Enabling High-Contrast Imaging on Solar-System Scales. PASP, 127(955):890, Sept. 2015b. doi: 10.1086/682989.

N. Jovanovic, F. Martinache, O. Guyon, C. Clergeon, G. Singh, T. Kudo, V. Garrel, K. Newman, D. Doughty, J. Lozi, J. Males, Y. Minowa, Y. Hayano, N. Takato, J. Morino, J. Kuhn, E. Serabyn, B. Norris, P. Tuthill, G. Schworer, P. Stewart, L. Close, E. Huby, G. Perrin, S. Lacour, L. Gauchet, S. Vievard, N. Murakami, F. Oshiyama, N. Baba, T. Matsuo, J. Nishikawa, M. Tamura, O. Lai, F. Marchis, G. Duchene, T. Kotani, and J. Woillez. The Subaru Coronagraphic Extreme Adaptive Optics System: Enabling High-Contrast Imaging on Solar-System Scales. PASP, 127(955):890, Sept. 2015c. doi: 10.1086/682989.

N. J. Kasdin, V. P. Bailey, B. Mennesson, R. T. Zellem, M. Ygouf, J. Rhodes, T. Luchik, F. Zhao, A. E. Riggs, B.-J. Seo, et al. The nancy grace roman space telescope coronagraph instrument (cgi) technology demonstration. In *Space Telescopes and Instrumentation 2020: Optical, Infrared, and Millimeter Wave*, volume 11443, pages 300–313. SPIE, 2020.

S. Keat Yeoh, T. Chapman, D. Goldstein, P. Varghese, and L. Trafton. Hybrid simulation of the gas/particle plume of enceladus. In *AAS/Division for Planetary Sciences Meeting Abstracts# 42*, volume 42, pages 25–05, 2010.

K. Kellogg, S. Metchev, K. Geißler, S. Hicks, J. D. Kirkpatrick, and R. Kurtev. A targeted search for peculiarly red l and t dwarfs in sdss, 2mass, and wise: discovery of a possible l7 member of the tw hydrae association. *The Astronomical Journal*, 150(6):182, 2015.

K. Kellogg, S. Metchev, P. A. Miles-Páez, and M. E. Tannock. A statistical survey of peculiar l and t dwarfs in sdss, 2mass, and wise. *The Astronomical Journal*, 154(3):112, 2017.

O. King, L. N. Fletcher, and N. Ligier. Compositional mapping of europa using mcmc modeling of near-ir vlt/sphere and galileo/nims observations. *The Planetary Science Journal*, 3(3):72, 2022.

J. D. Kirkpatrick. New spectral types l and t. *Annu. Rev. Astron. Astrophys.*, 43:195–245, 2005.

J. D. Kirkpatrick, I. N. Reid, J. Liebert, J. E. Gizis, A. J. Burgasser, D. G. Monet, C. C. Dahn, B. Nelson, and R. J. Williams. 67 Additional L Dwarfs Discovered by the Two Micron All Sky Survey. AJ, 120(1):447–472, July 2000. doi: 10.1086/301427.

J. D. Kirkpatrick, D. L. Looper, A. J. Burgasser, S. D. Schurr, R. M. Cutri, M. C. Cushing, K. L. Cruz, A. C. Sweet, G. R. Knapp, T. S. Barman, et al. Discoveries from a near-infrared proper motion survey using multi-epoch two micron all-sky survey data. *The Astrophysical Journal Supplement Series*, 190(1):100, 2010.

J. D. Kirkpatrick, A. Schneider, S. Fajardo-Acosta, C. R. Gelino, G. N. Mace, E. L. Wright, S. E. Logsdon, I. S. McLean, M. C. Cushing, M. F. Skrutskie, et al. The allwise motion survey and the quest for cold subdwarfs. *The Astrophysical Journal*, 783(2):122, 2014.

N. Kiselev, V. Rosenbush, F. Velichko, and S. Zaitsev. Polarimetry of the galilean satellites and jupiter near opposition. *Journal of Quantitative Spectroscopy and Radiative Transfer*, 110(14-16):1713–1718, 2009.

N. Kiselev, V. Rosenbush, V. Afanasiev, S. Zaitsev, S. Kolesnikov, and D. Shakhovskoy. Polarimetric properties of icy moons of the outer planets. In *Radiation mechanisms of astrophysical objects: classics today*, pages 203–209. Print Publishing House Yerevan, Armenia, 2017.

N. Kiselev, V. Rosenbush, K. Muinonen, L. Kolokolova, A. Savushkin, and N. Karpov. New polarimetric data for the galilean satellites: Europa observations and modeling. *The Planetary Science Journal*, 3(6):134, 2022.

A. N. Kolmogorov. Dissipation of energy in locally isotropic turbulence. In *Akademiia Nauk SSSR Doklady*, volume 32, page 16, 1941.

Q. M. Konopacky, S. J. Thomas, B. A. Macintosh, D. Dillon, N. Sadakuni, J. Maire, M. Fitzgerald, S. Hinkley, P. Kalas, T. Esposito, et al. Gemini planet imager observational calibrations v: astrometry and distortion. In *Ground-based and Airborne Instrumentation for Astronomy V*, volume 9147, pages 2585–2600. SPIE, 2014.

M. B. N. Kouwenhoven, A. G. A. Brown, H. Zinnecker, L. Kaper, and S. F. Portegies Zwart. The primordial binary population. I. A near-infrared adaptive optics search for close visual companions to A star members of Scorpius OB2. A&A, 430:137–154, Jan. 2005. doi: 10.1051/0004-6361:20048124.

Q. Kral, S. Marino, M. C. Wyatt, M. Kama, and L. Matra. Imaging [ci] around hd 131835: reinterpreting young debris discs with protoplanetary disc levels of co gas as shielded secondary discs. *Monthly Notices of the Royal Astronomical Society*, 489(3):3670–3691, 2019.

J. E. Krist. High-contrast imaging with the hubble space telescope: performance and lessons learned. In *Optical, Infrared, and Millimeter Space Telescopes*, volume 5487, pages 1284–1295. SPIE, 2004.

J. E. Krist. Proper: an optical propagation library for idl. In *Optical Modeling and Performance Predictions III*, volume 6675, page 66750P. International Society for Optics and Photonics, 2007.

J. E. Krist, D. Ardila, D. Golimowski, M. Clampin, H. Ford, G. Illingworth, G. Hartig, F. Bartko, N. Benítez, J. Blakeslee, et al. Hubble space telescope advanced camera for surveys coronagraphic imaging of the au microscopii debris disk. *The Astronomical Journal*, 129(2):1008, 2005.

S. S. Kumar. The Structure of Stars of Very Low Mass. ApJ, 137:1121, May 1963. doi: 10.1086/147589.

M. Kuzuhara, T. Currie, T. Takarada, T. D. Brandt, B. Sato, T. Uyama, M. Janson, J. Chilcote, T. Tobin, K. Lawson, et al. Direct-imaging discovery and dynamical mass of a substellar companion orbiting an accelerating hyades sun-like star with scexao/charis. *The Astrophysical Journal Letters*, 934(2):L19, 2022.

F.-R. Lachapelle, D. Lafrenière, J. Gagné, R. Jayawardhana, M. Janson, C. Helling, and S. Witte. Characterization of Low-mass, Wide-separation Substellar Companions to Stars in Upper Scorpius: Near-infrared Photometry and Spectroscopy. ApJ, 802(1):61, Mar. 2015. doi: 10.1088/0004-637X/802/1/61.

D. Lafreniere, C. Marois, R. Doyon, D. Nadeau, and É. Artigau. A new algorithm for point-spread function subtraction in high-contrast imaging: a demonstration with angular differential imaging. *The Astrophysical Journal*, 660(1):770, 2007.

D. Lafrenière, R. Jayawardhana, M. Janson, C. Helling, S. Witte, and P. Hauschildt. Discovery of an ~23 M $_{Jup}$ Brown Dwarf Orbiting ~700 AU from the Massive Star HIP 78530 in Upper Scorpius. ApJ, 730(1):42, Mar. 2011. doi: 10.1088/0004-637X/730/1/42.

A. M. Lagrange, M. Bonnefoy, G. Chauvin, D. Apai, D. Ehrenreich, A. Boccaletti, D. Gratadour, D. Rouan, D. Mouillet, S. Lacour, and M. Kasper. A Giant Planet Imaged in the Disk of the Young Star β Pictoris. *Science*, 329(5987):57, July 2010. doi: 10.1126/science.1187187.

K. Lake, V. Isgar, I. Baker, M. Herrington, L. Hipwood, C. Maxey, H. Weller, K. Barnes, and M. Hicks. Developments in the saphira family of hgcdte apd infrared arrays for low flux sensing: present and future. In *Sensors, Systems, and Next-Generation Satellites XXIV*, volume 11530, page 115300H. International Society for Optics and Photonics, 2020.

K. Lawson, T. Currie, J. P. Wisniewski, M. Tamura, G. Schneider, J.-C. Augereau, T. D. Brandt, O. Guyon, N. J. Kasdin, T. D. Groff, J. Lozi, J. Chilcote, K. Hodapp, N. Jovanovic, F. Martinache, N. Skaf, E. Akiyama, T. Henning, G. R. Knapp, J. Kwon, S. Mayama, M. W. McElwain, M. L. Sitko, R. Asensio-Torres, T. Uyama, and K. Wagner. SCExAO/CHARIS Near-infrared Integral Field Spectroscopy of the HD 15115 Debris Disk. AJ, 160(4):163, Oct. 2020. doi: 10.3847/1538-3881/ababa6.

K. Lawson, T. Currie, J. P. Wisniewski, J. Hashimoto, O. Guyon, T. D. Groff, J. Lozi, T. D. Brandt, J. Chilcote, V. Deo, et al. High-contrast integral field spectropolarimetry of planet-forming disks with scexao/charis. In *Techniques and Instrumentation for Detection of Exoplanets X*, volume 11823, pages 110–129. SPIE, 2021.

E. J. Leonard, D. A. Patthoff, and D. A. Senske. Global geologic map of europa. Technical report, US Geological Survey, 2024.

Y. Li, T. D. Brandt, G. M. Brandt, Q. An, K. Franson, T. J. Dupuy, M. Chen, R. Bowens-Rubin, B. L. Lewis, B. P. Bowler, A. Gibbs, R. Kiman, J. Faherty, T. Currie, R. Jensen-Clem, H. Zhang, E. Contreras-Martinez, M. P. Fitzgerald, B. A. Mazin, and M. Millar-Blanchaer. Surveying nearby brown dwarfs with HGCA: direct imaging discovery of a faint, high-mass brown dwarf orbiting HD 176535 A. MNRAS, 522(4):5622–5637, July 2023. doi: 10.1093/mnras/stad1315.

J. Lieman-Sifry, A. M. Hughes, J. M. Carpenter, U. Gorti, A. Hales, and K. M. Flaherty. Debris disks in the scorpius–centaurus ob association resolved by alma. *The Astrophysical Journal*, 828(1):25, 2016.

N. Ligier, F. Poulet, J. Carter, R. Brunetto, and F. Gourgeot. Vlt/sinfoni observations of europa: New insights into the surface composition. *The Astronomical Journal*, 151(6):163, 2016.

P. Lim, R. Diaz, and V. Laidler. Pysynphot user's guide. *STScI, Baltimore, MD*, 2015.

M. C. Liu, T. J. Dupuy, and K. N. Allers. The Hawaii Infrared Parallax Program. II. Young Ultracool Field Dwarfs. ApJ, 833(1):96, Dec. 2016. doi: 10.3847/1538-4357/833/1/96.

M. C. Liu, T. J. Dupuy, and K. N. Allers. The hawaii infrared parallax program. ii. young ultracool field dwarfs. *The Astrophysical Journal*, 833(1):96, 2016.

K. Lodders and B. Fegley Jr. Chemistry of low mass substellar objects. In *Astrophysics Update 2*, pages 1–28. Springer, 2006.

J. D. Long and J. R. Males. Unlocking Starlight Subtraction in Full-data-rate Exoplanet Imaging by Efficiently Updating Karhunen-Loève Eigenimages. AJ, 161(4):166, Apr. 2021. doi: 10.3847/1538-3881/abe12b.

R. D. Lorenz. Europa ocean sampling by plume flythrough: astrobiological expectations. *Icarus*, 267:217–219, 2016.

J. Lozi, O. Guyon, N. Jovanovic, S. Goebel, P. Pathak, N. Skaf, A. Sahoo, B. Norris, F. Martinache, M. N'Diaye, et al. Scexao, an instrument with a dual purpose: perform cutting-edge science and develop new technologies. In *Adaptive Optics Systems VI*, volume 10703, pages 1266–1277. SPIE, 2018.

M. Lucas, M. Bottom, O. Guyon, J. Lozi, B. Norris, V. Deo, S. Vievard, K. Ahn, N. Skaf, and P. Tuthill. A visible-light lyot coronagraph for scexao/vampires. In *Ground-based and Airborne Instrumentation for Astronomy IX*, volume 12184, pages 1443–1455. SPIE, 2022.

B. Lyot. The study of the solar corona and prominences without eclipses (george darwin lecture, 1939). *Monthly Notices of the Royal Astronomical Society, Vol. 99, p. 580*, 99: 580, 1939.

B. Macintosh, J. R. Graham, P. Ingraham, Q. Konopacky, C. Marois, M. Perrin, L. Poyneer, B. Bauman, T. Barman, A. S. Burrows, A. Cardwell, J. Chilcote, R. J. De Rosa, D. Dillon, R. Doyon, J. Dunn, D. Erikson, M. P. Fitzgerald, D. Gavel, S. Goodsell, M. Har-

tung, P. Hibon, P. Kalas, J. Larkin, J. Maire, F. Marchis, M. S. Marley, J. McBride, M. Millar-Blanchaer, K. Morzinski, A. Norton, B. R. Oppenheimer, D. Palmer, J. Patience, L. Pueyo, F. Rantakyro, N. Sadakuni, L. Saddlemyer, D. Savransky, A. Serio, R. Soummer, A. Sivaramakrishnan, I. Song, S. Thomas, J. K. Wallace, S. Wiktorowicz, and S. Wolff. First light of the gemini planet imager. *Proceedings of the National Academy of Sciences*, 111(35):12661–12666, 2014a. ISSN 0027-8424. doi: 10.1073/pnas.1304215111. URL https://www.pnas.org/content/111/35/12661.

B. Macintosh, J. R. Graham, P. Ingraham, Q. Konopacky, C. Marois, M. Perrin, L. Poyneer, B. Bauman, T. Barman, A. S. Burrows, et al. First light of the gemini planet imager. *proceedings of the National Academy of Sciences*, 111(35):12661–12666, 2014b.

B. A. Macintosh, J. R. Graham, D. W. Palmer, R. Doyon, J. Dunn, D. T. Gavel, J. Larkin, B. Oppenheimer, L. Saddlemyer, A. Sivaramakrishnan, et al. The gemini planet imager: from science to design to construction. In *Adaptive Optics Systems*, volume 7015, page 701518. International Society for Optics and Photonics, 2008.

N. Madhusudhan. Exoplanetary atmospheres: key insights, challenges, and prospects. *Annual Review of Astronomy and Astrophysics*, 57(1):617–663, 2019.

A. Mainzer, J. Bauer, T. Grav, J. Masiero, R. Cutri, J. Dailey, P. Eisenhardt, R. McMillan, E. Wright, R. Walker, et al. Preliminary results from neowise: an enhancement to the wide-field infrared survey explorer for solar system science. *The Astrophysical Journal*, 731(1):53, 2011.

A. L. Maire, M. Bonnefoy, C. Ginski, A. Vigan, S. Messina, D. Mesa, R. Galicher, R. Gratton, S. Desidera, T. G. Kopytova, M. Millward, C. Thalmann, R. U. Claudi, D. Ehrenreich, A. Zurlo, G. Chauvin, J. Antichi, A. Baruffolo, A. Bazzon, J. L. Beuzit, P. Blanchard, A. Boccaletti, J. de Boer, M. Carle, E. Cascone, A. Costille, V. De Caprio, A. Delboulbé, K. Dohlen, C. Dominik, M. Feldt, T. Fusco, J. H. Girard, E. Giro, D. Gisler,

L. Gluck, C. Gry, T. Henning, N. Hubin, E. Hugot, M. Jaquet, M. Kasper, A. M. Lagrange, M. Langlois, D. Le Mignant, M. Llored, F. Madec, P. Martinez, D. Mawet, J. Milli, O. Möller-Nilsson, D. Mouillet, T. Moulin, C. Moutou, A. Origné, A. Pavlov, C. Petit, J. Pragt, P. Puget, J. Ramos, S. Rochat, R. Roelfsema, B. Salasnich, J. F. Sauvage, H. M. Schmid, M. Turatto, S. Udry, F. Vakili, Z. Wahhaj, L. Weber, and F. Wildi. First light of the VLT planet finder SPHERE. II. The physical properties and the architecture of the young systems PZ Telescopii and HD 1160 revisited. A&A, 587:A56, Mar. 2016. doi: 10.1051/0004-6361/201526594.

J. R. Males and O. Guyon. Ground-based adaptive optics coronagraphic performance under closed-loop predictive control, 2017.

J. R. Males and O. Guyon. Ground-based adaptive optics coronagraphic performance under closed-loop predictive control. *Journal of Astronomical Telescopes, Instruments, and Systems*, 4(1):019001, 2018.

J. R. Males, M. P. Fitzgerald, R. Belikov, and O. Guyon. The Mysterious Lives of Speckles. I. Residual Atmospheric Speckle Lifetimes in Ground-based Coronagraphs. PASP, 133 (1028):104504, Oct. 2021. doi: 10.1088/1538-3873/ac0f0c.

J.-C. Mandeville, J. E. Geake, and A. Dollfus. Reflectance polarimetry of callisto and the evolution of the galilean. *Icarus*, 41(3):343–355, 1980.

I. Mann, M. Köhler, H. Kimura, A. Cechowski, and T. Minato. Dust in the solar system and in extra-solar planetary systems. *The Astronomy and Astrophysics Review*, 13(3):159–228, 2006.

S. Marino, M. Flock, T. Henning, Q. Kral, L. Matrà, and M. Wyatt. Population synthesis of exocometary gas around a stars. *Monthly Notices of the Royal Astronomical Society*, 492(3):4409–4429, 2020.

M. Marley. From Giant Planets to Cool Stars. PASP, 111(766):1591–1592, Dec. 1999. doi: 10.1086/316463.

M. S. Marley and T. D. Robinson. On the cool side: modeling the atmospheres of brown dwarfs and giant planets. *Annual Review of Astronomy and Astrophysics*, 53:279–323, 2015.

M. S. Marley, D. Saumon, T. Guillot, R. S. Freedman, W. B. Hubbard, A. Burrows, and J. I. Lunine. Atmospheric, Evolutionary, and Spectral Models of the Brown Dwarf Gliese 229 B. *Science*, 272(5270):1919–1921, June 1996. doi: 10.1126/science.272.5270.1919.

M. S. Marley, D. Saumon, C. Visscher, R. Lupu, R. Freedman, C. Morley, J. J. Fortney, C. Seay, A. J. Smith, D. Teal, et al. The sonora brown dwarf atmosphere and evolution models. i. model description and application to cloudless atmospheres in rainout chemical equilibrium. *The Astrophysical Journal*, 920(2):85, 2021.

C. Marois, R. Doyon, R. Racine, and D. Nadeau. Efficient speckle noise attenuation in faint companion imaging. *Publications of the Astronomical Society of the Pacific*, 112(767):91, 2000.

C. Marois, R. Doyon, D. Nadeau, R. Racine, and G. A. H. Walker. Effects of Quasi-Static Aberrations in Faint Companion Searches. In C. Aime and R. Soummer, editors, *EAS Publications Series*, volume 8 of *EAS Publications Series*, pages 233–243, Jan. 2003. doi: 10.1051/eas:2003067.

C. Marois, R. Doyon, D. Nadeau, R. Racine, M. Riopel, P. Vallée, and D. Lafrenière. TRIDENT: An Infrared Differential Imaging Camera Optimized for the Detection of Methanated Substellar Companions. PASP, 117(833):745–756, July 2005. doi: 10.1086/431347.

C. Marois, D. Lafreniere, R. Doyon, B. Macintosh, and D. Nadeau. Angular differential imaging: A powerful high-contrast imaging technique. *The Astrophysical Journal*, 641(1):

556–564, Apr 2006. ISSN 1538-4357. doi: 10.1086/500401. URL http://dx.doi.org/10.1086/500401.

C. Marois, D. Lafrenière, R. Doyon, B. Macintosh, and D. Nadeau. Angular Differential Imaging: A Powerful High-Contrast Imaging Technique. ApJ, 641(1):556–564, Apr. 2006. doi: 10.1086/500401.

C. Marois, D. Lafreniere, R. Doyon, B. Macintosh, and D. Nadeau. Angular differential imaging: a powerful high-contrast imaging technique. *The Astrophysical Journal*, 641(1): 556, 2006.

C. Marois, B. Macintosh, T. Barman, B. Zuckerman, I. Song, J. Patience, D. Lafrenière, and R. Doyon. Direct imaging of multiple planets orbiting the star hr 8799. *science*, 322 (5906):1348–1352, 2008.

C. Marois, C. Correia, J.-P. Véran, and T. Currie. Tloci: A fully loaded speckle killing machine. *Proceedings of the International Astronomical Union*, 8(S299):48–49, 2013.

C. Marois, C. Correia, R. Galicher, P. Ingraham, B. Macintosh, T. Currie, and R. De Rosa. Gpi psf subtraction with tloci: the next evolution in exoplanet/disk high-contrast imaging. In *Adaptive Optics Systems IV*, volume 9148, page 91480U. International Society for Optics and Photonics, 2014.

J. W. Mason. *Astrophysics update*. Springer, 2006.

D. Mawet, E. Serabyn, K. Liewer, R. Burruss, J. Hickey, and D. Shemo. The vector vortex coronagraph: laboratory results and first light at palomar observatory. *The Astrophysical Journal*, 709(1):53, 2009.

M. Mayor and D. Queloz. A jupiter-mass companion to a solar-type star. *nature*, 378(6555): 355–359, 1995.

M. Mayor, F. Pepe, D. Queloz, F. Bouchy, G. Rupprecht, G. Lo Curto, G. Avila, W. Benz, J. L. Bertaux, X. Bonfils, T. Dall, H. Dekker, B. Delabre, W. Eckert, M. Fleury, A. Gilliotte, D. Gojak, J. C. Guzman, D. Kohler, J. L. Lizon, A. Longinotti, C. Lovis, D. Megevand, L. Pasquini, J. Reyes, J. P. Sivan, D. Sosnowska, R. Soto, S. Udry, A. van Kesteren, L. Weber, and U. Weilenmann. Setting New Standards with HARPS. *The Messenger*, 114:20–24, Dec. 2003.

B. A. Mazin, B. Bumble, S. R. Meeker, K. O'Brien, S. McHugh, and E. Langman. A superconducting focal plane array for ultraviolet, optical, and near-infrared astrophysics. *Optics express*, 20(2):1503–1511, 2012.

J. McCullough, B. Macintosh, M. Millar-Blanchaer, L. Schaefer, D. Schroeder, and R. De Rosa. Detection sensitivity for the gemini planet imager (gpi) to potential europa plumes. *AGU Fall Meeting Abstracts*, 2020.

S. R. Meeker, B. A. Mazin, A. B. Walter, P. Strader, N. Fruitwala, C. Bockstiegel, P. Szypryt, G. Ulbricht, G. Coiffard, B. Bumble, et al. Darkness: a microwave kinetic inductance detector integral field spectrograph for high-contrast astronomy. *Publications of the Astronomical Society of the Pacific*, 130(988):065001, 2018.

S. N. Mellon, E. E. Mamajek, K. Zwintz, T. J. David, R. Stuik, G. J. J. Talens, P. Dorval, O. Burggraaff, M. A. Kenworthy, J. I. Bailey III, et al. Discovery of δ scuti pulsations in the young hybrid debris disk star hd 156623. *The Astrophysical Journal*, 870(1):36, 2019.

H. Melosh, A. Ekholm, A. Showman, and R. Lorenz. The temperature of europa's subsurface water ocean. *Icarus*, 168(2):498–502, 2004.

D. Mendis and M. Rosenberg. Annu. rev. astron. astrophys. *Annu. Rev. Astron. Astrophys*, 32:419, 1994.

T. Meshkat, M. Bonnefoy, E. E. Mamajek, S. P. Quanz, G. Chauvin, M. A. Kenworthy, J. Rameau, M. R. Meyer, A. M. Lagrange, J. Lannier, and P. Delorme. Discovery of a

low-mass companion to the F7V star HD 984. MNRAS, 453(3):2378–2386, Nov. 2015. doi: 10.1093/mnras/stv1732.

M. A. Millar-Blanchaer, J. R. Graham, L. Pueyo, P. Kalas, R. I. Dawson, J. Wang, M. D. Perrin, B. Macintosh, S. M. Ammons, T. Barman, et al. β pictoris'inner disk in polarized light and new orbital parameters for β pictoris b. *The Astrophysical Journal*, 811(1):18, 2015.

J. Milli, D. Mouillet, A.-M. Lagrange, A. Boccaletti, D. Mawet, G. Chauvin, and M. Bonnefoy. Impact of angular differential imaging on circumstellar disk images. *Astronomy & Astrophysics*, 545:A111, 2012.

Y. Minowa, Y. Hayano, S. Oya, M. Watanabe, M. Hattori, O. Guyon, S. Egner, Y. Saito, M. Ito, H. Takami, V. Garrel, S. Colley, T. Golota, and M. Iye. *Performance of Subaru adaptive optics system AO188*, volume 7736 of *Society of Photo-Optical Instrumentation Engineers (SPIE) Conference Series*, page 77363N. SPIE, 2010. doi: 10.1117/12.857818.

A. Moór, M. Curé, Á. Kóspál, P. Ábrahám, T. Csengeri, C. Eiroa, D. Gunawan, T. Henning, A. M. Hughes, A. Juhász, et al. Molecular gas in debris disks around young a-type stars. *The Astrophysical Journal*, 849(2):123, 2017.

A. Moór, Q. Kral, P. Ábrahám, Á. Kóspál, A. Dutrey, E. Di Folco, A. M. Hughes, A. Juhász, I. Pascucci, and N. Pawellek. New millimeter co observations of the gas-rich debris disks 49 cet and hd 32297. *The Astrophysical Journal*, 884(2):108, 2019.

A. M. Moore, J. E. Larkin, S. A. Wright, B. Bauman, J. Dunn, B. Ellerbroek, A. C. Phillips, L. Simard, R. Suzuki, K. Zhang, et al. The infrared imaging spectrograph (iris) for tmt: instrument overview. In *Ground-based and Airborne Instrumentation for Astronomy V*, volume 9147, pages 787–798. SPIE, 2014.

F. Y. Morales, G. Rieke, M. Werner, G. Bryden, K. Stapelfeldt, and K. Su. Common warm

dust temperatures around main-sequence stars. *The Astrophysical Journal Letters*, 730 (2):L29, 2011.

C. V. Morley, M. S. Marley, J. J. Fortney, R. Lupu, D. Saumon, T. Greene, and K. Lodders. Water Clouds in Y Dwarfs and Exoplanets. ApJ, 787(1):78, May 2014. doi: 10.1088/0004-637X/787/1/78.

C. V. Morley, S. Mukherjee, M. S. Marley, J. J. Fortney, C. Visscher, R. Lupu, E. Gharib-Nezhad, D. Thorngren, R. Freedman, and N. Batalha. The sonora substellar atmosphere models. iii. diamondback: Atmospheric properties, spectra, and evolution for warm cloudy substellar objects. *arXiv preprint arXiv:2402.00758*, 2024.

S. Mukherjee, J. J. Fortney, C. V. Morley, N. E. Batalha, M. S. Marley, T. Karalidi, C. Visscher, R. Lupu, R. Freedman, and E. Gharib-Nezhad. The sonora substellar atmosphere models. iv. elf owl: Atmospheric mixing and chemical disequilibrium with varying metallicity and c/o ratios. *The Astrophysical Journal*, 963(1):73, 2024.

W. I. Mullen, B. Macintosh, J. Chilcote, and J.-B. Ruffio. Speckle evolution and post-processing contrast improvements with short exposure imaging on the Gemini Planet Imager. In *American Astronomical Society Meeting Abstracts #233*, volume 233 of *American Astronomical Society Meeting Abstracts*, page 140.38, Jan. 2019.

W. I. Mullen, B. Macintosh, J. Chilcote, and J.-B. Ruffio. Speckle evolution and post-processing contrast improvements with short exposure imaging on the gemini planet imager. In *American Astronomical Society Meeting Abstracts# 233*, volume 233, pages 140–38, 2019.

H. Murakami, H. Baba, P. Barthel, D. L. Clements, M. Cohen, Y. Doi, K. Enya, E. Figueredo, N. Fujishiro, H. Fujiwara, et al. The infrared astronomical mission akari. *Publications of the Astronomical Society of Japan*, 59(sp2):S369–S376, 2007.

NASA Exoplanet Science Institute. Planetary systems table, 2020. URL https://catcopy.ipac.caltech.edu/dois/doi.php?id=10.26133/NEA12.

NASEM. *Pathways to Discovery in Astronomy and Astrophysics for the 2020s*. The National Academies Press, Washington, DC, 2021. ISBN 978-0-309-46586-1. doi: 10.17226/26141. URL https://www.nap.edu/catalog/26141/pathways-to-discovery-in-astronomy-and-astrophysics-for-the-2020s.

G. Neugebauer, H. J. Habing, R. van Duinen, H. H. Aumann, B. Baud, C. A. Beichman, D. A. Beintema, N. Boggess, P. E. Clegg, T. de Jong, J. P. Emerson, T. N. Gautier, F. C. Gillett, S. Harris, M. G. Hauser, J. R. Houck, R. E. Jennings, F. J. Low, P. L. Marsden, G. Miley, F. M. Olnon, S. R. Pottasch, E. Raimond, M. Rowan-Robinson, B. T. Soifer, R. G. Walker, P. R. Wesselius, and E. Young. The Infrared Astronomical Satellite (IRAS) mission. ApJ, 278:L1–L6, Mar. 1984. doi: 10.1086/184209.

E. L. Nielsen, M. C. Liu, Z. Wahhaj, B. A. Biller, T. L. Hayward, A. Boss, B. Bowler, A. Kraus, E. L. Shkolnik, M. Tecza, M. Chun, F. Clarke, L. M. Close, C. Ftaclas, M. Hartung, J. R. Males, I. N. Reid, A. J. Skemer, S. H. P. Alencar, A. Burrows, E. de Gouveia Dal Pino, J. Gregorio-Hetem, M. Kuchner, N. Thatte, and D. W. Toomey. The Gemini NICI Planet-Finding Campaign: Discovery of a Multiple System Orbiting the Young A Star HD 1160. ApJ, 750(1):53, May 2012. doi: 10.1088/0004-637X/750/1/53.

E. L. Nielsen, R. J. De Rosa, B. Macintosh, J. J. Wang, J.-B. Ruffio, E. Chiang, M. S. Marley, D. Saumon, D. Savransky, S. M. Ammons, et al. The gemini planet imager exoplanet survey: giant planet and brown dwarf demographics from 10 to 100 au. *The Astronomical Journal*, 158(1):13, 2019.

B. Norris, G. Schworer, P. Tuthill, N. Jovanovic, O. Guyon, P. Stewart, and F. Martinache. The vampires instrument: imaging the innermost regions of protoplanetary discs with polarimetric interferometry. *Monthly Notices of the Royal Astronomical Society*, 447(3): 2894–2906, 2015.

K. A. Odonnell, B. J. Brames, and J. C. Dainty. Measurements of the spatial-temporal statistics of stellar speckle patterns at Mauna Kea, Hawaii. *Optics Communications*, 41 (2):79–82, Mar. 1982. doi: 10.1016/0030-4018(82)90321-2.

B. R. Oppenheimer and S. Hinkley. High-Contrast Observations in Optical and Infrared Astronomy. ARA&A, 47(1):253–289, Sept. 2009. doi: 10.1146/annurev-astro-082708-101717.

B. R. Oppenheimer and S. Hinkley. High-contrast observations in optical and infrared astronomy. *Annual Review of Astronomy and Astrophysics*, 47, 2009.

B. R. Oppenheimer, S. R. Kulkarni, K. Matthews, and T. Nakajima. Infrared Spectrum of the Cool Brown Dwarf Gl 229B. *Science*, 270(5241):1478–1479, Dec. 1995. doi: 10.1126/science.270.5241.1478.

B. R. Oppenheimer, C. Beichman, D. Brenner, R. Burruss, E. Cady, J. Crepp, L. Hillenbrand, S. Hinkley, E. R. Ligon, T. Lockhart, I. Parry, L. Pueyo, E. Rice, L. C. Roberts, J. Roberts, M. Shao, A. Sivaramakrishnan, R. Soummer, G. Vasisht, F. Vescelus, J. K. Wallace, C. Zhai, and N. Zimmerman. Project 1640: the world's first ExAO coronagraphic hyperspectral imager for comparative planetary science. In B. L. Ellerbroek, E. Marchetti, and J.-P. Véran, editors, *Adaptive Optics Systems III*, volume 8447 of *Society of Photo-Optical Instrumentation Engineers (SPIE) Conference Series*, page 844720, July 2012. doi: 10.1117/12.926419.

G. Pace. Chromospheric activity as age indicator. An L-shaped chromospheric-activity versus age diagram. A&A, 551:L8, Mar. 2013. doi: 10.1051/0004-6361/201220364.

L. Paganini, G. L. Villanueva, L. Roth, A. Mandell, T. Hurford, K. D. Retherford, and M. J. Mumma. A measurement of water vapour amid a largely quiescent environment on europa. *Nature astronomy*, 4(3):266–272, 2020.

N. Pawellek and A. V. Krivov. The dust grain size–stellar luminosity trend in debris discs. *Monthly Notices of the Royal Astronomical Society*, 454(3):3207–3221, 2015.

N. Pawellek, M. Wyatt, L. Matra, G. Kennedy, and B. Yelverton. A 75 per cent occurrence rate of debris discs around f stars in the β pic moving group. *Monthly Notices of the Royal Astronomical Society*, 502(4):5390–5416, 2021.

T. D. Pearce, A. V. Krivov, A. A. Sefilian, M. R. Jankovic, T. Löhne, T. Morgner, M. C. Wyatt, M. Booth, and S. Marino. The effect of sculpting planets on the steepness of debris-disc inner edges. *Monthly Notices of the Royal Astronomical Society*, 527(2):3876–3899, 2024.

M. J. Pecaut and E. E. Mamajek. The star formation history and accretion-disc fraction among the k-type members of the scorpius–centaurus ob association. *Monthly Notices of the Royal Astronomical Society*, 461(1):794–815, 2016.

J. Péricaud, E. Di Folco, A. Dutrey, S. Guilloteau, and V. Piétu. The hybrid disks: a search and study to better understand evolution of disks. *Astronomy & Astrophysics*, 600:A62, 2017.

M. D. Perrin, J. R. Graham, J. E. Larkin, S. Wiktorowicz, J. Maire, S. Thibault, M. P. Fitzgerald, R. Doyon, B. A. Macintosh, D. T. Gavel, et al. Imaging polarimetry with the gemini planet imager. In *Adaptive Optics Systems II*, volume 7736, page 77365R. International Society for Optics and Photonics, 2010.

M. D. Perrin, J. Maire, P. Ingraham, D. Savransky, M. Millar-Blanchaer, S. G. Wolff, J.-B. Ruffio, J. J. Wang, Z. H. Draper, N. Sadakuni, et al. Gemini planet imager observational calibrations i: Overview of the gpi data reduction pipeline. *Ground-based and Airborne Instrumentation for Astronomy V*, 9147:1168–1180, 2014.

M. D. Perrin, G. Duchene, M. Millar-Blanchaer, M. P. Fitzgerald, J. R. Graham, S. J. Wiktorowicz, P. G. Kalas, B. Macintosh, B. Bauman, A. Cardwell, et al. Polarimetry with the gemini planet imager: methods, performance at first light, and the circumstellar ring around hr 4796a. *The Astrophysical Journal*, 799(2):182, 2015.

M. D. Perrin, P. Ingraham, K. B. Follette, J. Maire, J. J. Wang, D. Savransky, P. Arriaga, V. P. Bailey, S. Bruzzone, J. K. Chilcote, et al. Gemini planet imager observational calibrations xi: pipeline improvements and enhanced calibrations after two years on sky. In *Ground-based and Airborne Instrumentation for Astronomy VI*, volume 9908, pages 1010–1022. SPIE, 2016.

C. B. Phillips and R. T. Pappalardo. Europa clipper mission concept: Exploring jupiter's ocean moon. *Eos, Transactions American Geophysical Union*, 95(20):165–167, 2014.

A. Pickles and E. Depagne. All-Sky Spectrally Matched UBVRI - ZY and ugriz Magnitudes for Stars in the Tycho2 Catalog. PASP, 122(898):1437, Dec. 2010. doi: 10.1086/657947.

A. J. Pickles. A Stellar Spectral Flux Library: 1150-25000 Å. PASP, 110(749):863–878, July 1998. doi: 10.1086/316197.

G. Pietrzyński, D. Graczyk, A. Gallenne, W. Gieren, I. Thompson, B. Pilecki, P. Karczmarek, M. Górski, K. Suchomska, M. Taormina, et al. A distance to the large magellanic cloud that is precise to one per cent. *Nature*, 567(7747):200–203, 2019.

C. Pinte. pymcfost. https://github.com/cpinte/pymcfost, 2022.

C. Pinte, F. Ménard, G. Duchêne, and P. Bastien. Monte carlo radiative transfer in protoplanetary disks. *Astronomy & Astrophysics*, 459(3):797–804, 2006.

C. Pinte, T. Harries, M. Min, A. Watson, C. Dullemond, P. Woitke, F. Ménard, and M. Durán-Rojas. Benchmark problems for continuum radiative transfer-high optical depths, anisotropic scattering, and polarisation. *Astronomy & Astrophysics*, 498(3):967–980, 2009.

O. Poch, R. Cerubini, A. Pommerol, B. Jost, and N. Thomas. Polarimetry of water ice particles providing insights on grain size and degree of sintering on icy planetary surfaces. *Journal of Geophysical Research: Planets*, 123(10):2564–2584, 2018.

E. H. Por, S. Y. Haffert, V. M. Radhakrishnan, D. S. Doelman, M. Van Kooten, and S. P. Bos. High Contrast Imaging for Python (HCIPy): an open-source adaptive optics and coronagraph simulator. In *Adaptive Optics Systems VI*, volume 10703 of *Proc. SPIE*, 2018. doi: 10.1117/12.2314407. URL https://doi.org/10.1117/12.2314407.

L. Pueyo. Detection and Characterization of Exoplanets using Projections on Karhunen Loeve Eigenimages: Forward Modeling. ApJ, 824(2):117, June 2016. doi: 10.3847/0004-637X/824/2/117.

L. Pueyo. Detection and characterization of exoplanets using projections on karhunen–loeve eigenimages: Forward modeling. *The Astrophysical Journal*, 824(2):117, 2016.

L. C. Quick, O. S. Barnouin, L. M. Prockter, and G. W. Patterson. Constraints on the detection of cryovolcanic plumes on europa. *Planetary and Space Science*, 86:1–9, 2013.

R. Racine, G. A. Walker, D. Nadeau, R. Doyon, and C. Marois. Speckle noise and the detection of faint companions. *Publications of the Astronomical Society of the Pacific*, 111 (759):587, 1999.

R. Racine, G. A. H. Walker, D. Nadeau, R. Doyon, and C. Marois. Speckle Noise and the Detection of Faint Companions. PASP, 111(759):587–594, May 1999. doi: 10.1086/316367.

S. Ragland, D. Mawet, C. Alvarez, K. Matthews, C. Bond, S. Cetre, J.-R. Delorme, S. Lilley, N. Jovanovic, G. Ruane, et al. High contrast imaging upgrades for the keck adaptive optics imager. In *6th International Conference on Adaptive Optics for Extremely Large Telescopes, AO4ELT 2019*, 2019.

S. Ratzenböck, J. E. Großschedl, J. Alves, N. Miret-Roig, I. Bomze, J. Forbes, A. Goodman, Á. Hacar, D. Lin, S. Meingast, et al. The star formation history of the sco-cen association-coherent star formation patterns in space and time. *Astronomy & Astrophysics*, 678:A71, 2023.

A. Reiners and M. Zechmeister. Radial Velocity Photon Limits for the Dwarf Stars of Spectral Classes F-M. ApJS, 247(1):11, Mar. 2020. doi: 10.3847/1538-4365/ab609f.

B. Ren, L. Pueyo, G. B. Zhu, J. Debes, and G. Duchêne. Non-negative matrix factorization: robust extraction of extended structures. *The Astrophysical Journal*, 852(2):104, 2018.

A. R. Rhoden, T. A. Hurford, L. Roth, and K. Retherford. Linking europa's plume activity to tides, tectonics, and liquid water. *Icarus*, 253:169–178, 2015.

G. R. Ricker, J. N. Winn, R. Vanderspek, D. W. Latham, G. Á. Bakos, J. L. Bean, Z. K. Berta-Thompson, T. M. Brown, L. Buchhave, N. R. Butler, et al. Transiting exoplanet survey satellite. *Journal of Astronomical Telescopes, Instruments, and Systems*, 1(1): 014003–014003, 2015.

H. Risvik. Principal component analysis (pca) & nipals algorithm, 2007.

A. C. Rizzuto, M. J. Ireland, and D. B. Zucker. Wise circumstellar discs in the young sco-cen association. *Monthly Notices of the Royal Astronomical Society: Letters*, 421(1):L97–L101, 2012.

F. Roddier, J. Gilli, and G. Lund. On the origin of speckle boiling and its effects in stellar speckle interferometry. *Journal of Optics*, 13(5):263, 1982.

F. Roddier, J. M. Gilli, and G. Lund. On the origin of speckle boiling and its effects in stellar speckle interferometry. *Journal of Optics*, 13:263–271, Oct. 1982. doi: 10.1088/0150-536X/13/5/002.

C. Rodrigo and E. Solano. The SVO Filter Profile Service. In *XIV.0 Scientific Meeting (virtual) of the Spanish Astronomical Society*, page 182, July 2020.

C. Rodrigo and E. Solano. The svo filter profile service. In *XIV. 0 Scientific Meeting (virtual) of the Spanish Astronomical Society*, page 182, 2020.

C. Rodrigo, E. Solano, and A. Bayo. SVO Filter Profile Service Version 1.0. IVOA Working Draft 15 October 2012, Oct. 2012.

F. Roques, H. Scholl, B. Sicardy, and B. A. Smith. Is there a planet around β pictoris? perturbations of a planet on a circumstellar dust disk: 1. the numerical model. *Icarus*, 108(1):37–58, 1994.

L. Roth, J. Saur, K. D. Retherford, D. F. Strobel, P. D. Feldman, M. A. McGrath, and F. Nimmo. Transient water vapor at europa's south pole. *science*, 343(6167):171–174, 2014.

A. R. Rudy, S. Srinath, L. Poyneer, S. M. Ammons, D. Gavel, R. Kupke, D. Dillon, and C. Rockosi. Progress towards wind predictive control on ShaneAO: test bench results. In E. Marchetti, L. M. Close, and J.-P. Vran, editors, *Adaptive Optics Systems IV*, volume 9148 of *Society of Photo-Optical Instrumentation Engineers (SPIE) Conference Series*, page 91481Z, July 2014. doi: 10.1117/12.2057194.

A. Sahoo, O. Guyon, J. Lozi, J. Chilcote, N. Jovanovic, T. Brandt, T. Groff, and F. Martinache. Precision photometric and astrometric calibration using alternating satellite speckles. *The Astronomical Journal*, 159(6):250, 2020.

M. Samland, J. Bouwman, D. Hogg, W. Brandner, T. Henning, and M. Janson. Trap: A temporal systematics model for improved direct detection of exoplanets at small angular separations. *Astronomy & Astrophysics*, 646:A24, 2021.

A. Sanghi, M. C. Liu, W. M. Best, T. J. Dupuy, R. J. Siverd, Z. Zhang, S. A. Hurt, E. A. Magnier, K. M. Aller, and N. R. Deacon. The hawaii infrared parallax program. vi. the fundamental properties of 1000+ ultracool dwarfs and planetary-mass objects using optical to mid-infrared spectral energy distributions and comparison to bt-settl and atmo 2020 model atmospheres. *The Astrophysical Journal*, 959(1):63, 2023.

D. Savransky. Sequential covariance calculation for exoplanet image processing. *The Astrophysical Journal*, 800(2):100, 2015.

R. J. Scaddan and J. G. Walker. Statistics of stellar speckle patterns. Appl. Opt., 17: 3779–3784, Dec. 1978. doi: 10.1364/AO.17.003779.

J. Schlaerth, A. Vayonakis, P. Day, J. Glenn, J. Gao, S. Golwala, S. Kumar, H. LeDuc, B. Mazin, J. Vaillancourt, et al. A millimeter and submillimeter kinetic inductance detector camera. *Journal of Low Temperature Physics*, 151(3-4):684–689, 2008.

H. Schmid, F. Joos, and D. Tschan. Limb polarization of uranus and neptune-i. imaging polarimetry and comparison with analytic models. *Astronomy & Astrophysics*, 452(2): 657–668, 2006.

B. Schmidt, D. Blankenship, G. Patterson, and P. Schenk. Active formation of 'chaos terrain'over shallow subsurface water on europa. *Nature*, 479(7374):502–505, 2011.

A. C. Schneider, J. A. Munn, F. J. Vrba, J. Bruursema, S. E. Dahm, S. J. Williams, M. C. Liu, and B. N. Dorland. Astrometry and photometry for 1000 l, t, and y dwarfs from the ukirt hemisphere survey. *The Astronomical Journal*, 166(3):103, 2023.

A. Sivaramakrishnan and B. R. Oppenheimer. Astrometry and photometry with coronagraphs. *The Astrophysical Journal*, 647(1):620, 2006.

M. Skrutskie, R. Cutri, R. Stiening, M. Weinberg, S. Schneider, J. Carpenter, C. Beichman, R. Capps, T. Chester, J. Elias, et al. The two micron all sky survey (2mass). *The Astronomical Journal*, 131(2):1163, 2006.

M. F. Skrutskie, R. M. Cutri, R. Stiening, M. D. Weinberg, S. Schneider, J. M. Carpenter, C. Beichman, R. Capps, T. Chester, J. Elias, J. Huchra, J. Liebert, C. Lonsdale, D. G. Monet, S. Price, P. Seitzer, T. Jarrett, J. D. Kirkpatrick, J. E. Gizis, E. Howard, T. Evans, J. Fowler, L. Fullmer, R. Hurt, R. Light, E. L. Kopan, K. A. Marsh, H. L. McCallon,

R. Tam, S. Van Dyk, and S. Wheelock. The Two Micron All Sky Survey (2MASS). AJ, 131(2):1163–1183, Feb. 2006. doi: 10.1086/498708.

B. A. Smith and R. J. Terrile. A Circumstellar Disk around β Pictoris. *Science*, 226(4681): 1421–1424, Dec. 1984. doi: 10.1126/science.226.4681.1421.

R. Soummer. Apodized pupil lyot coronagraphs for arbitrary telescope apertures. *The Astrophysical Journal*, 618(2):L161, 2004.

R. Soummer and C. Aime. Statistics of pinned speckles in direct and coronagraphic high-contrast imaging. In D. B. Calia, B. L. Ellerbroek, and R. Ragazzoni, editors, *Advancements in Adaptive Optics*, volume 5490, pages 495 – 503. International Society for Optics and Photonics, SPIE, 2004. doi: 10.1117/12.551985. URL https://doi.org/10.1117/12.551985.

R. Soummer and C. Aime. Statistics of pinned speckles in direct and coronagraphic high-contrast imaging. In D. Bonaccini Calia, B. L. Ellerbroek, and R. Ragazzoni, editors, *Advancements in Adaptive Optics*, volume 5490 of *Society of Photo-Optical Instrumentation Engineers (SPIE) Conference Series*, pages 495–503, Oct. 2004. doi: 10.1117/12.551985.

R. Soummer, A. Ferrari, C. Aime, and L. Jolissaint. Speckle noise and dynamic range in coronagraphic images. *The Astrophysical Journal*, 669(1):642, 2007.

R. Soummer, L. Pueyo, and J. Larkin. Detection and characterization of exoplanets and disks using projections on karhunen-loève eigenimages. *The Astrophysical Journal Letters*, 755(2):L28, 2012.

S. G. Sousa, N. C. Santos, G. Israelian, M. Mayor, and S. Udry. Spectroscopic stellar parameters for 582 FGK stars in the HARPS volume-limited sample. Revising the metallicity-planet correlation. A&A, 533:A141, Sept. 2011. doi: 10.1051/0004-6361/201117699.

W. B. Sparks, K. P. Hand, M. A. McGrath, E. Bergeron, M. Cracraft, and S. E. Deustua. PROBING FOR EVIDENCE OF PLUMES ON EUROPA WITH HST/STIS. *Astrophysical Journal*, 829(2):121, sep 2016. doi: 10.3847/0004-637x/829/2/121. URL https://doi.org/10.3847/0004-637x/829/2/121.

W. B. Sparks, J. Bailey, L. Bergeron, K. Bott, D. V. Cotton, T. Germer, J. Grunsfeld, K. P. Hand, L. Kolokolova, M. A. McGrath, and O. Poch. Probing the icy regoliths of Europa with imaging polarimetry. HST Proposal. Cycle 30, ID. #17163, June 2022.

C. C. Stark, G. Schneider, A. J. Weinberger, J. H. Debes, C. A. Grady, H. Jang-Condell, and M. J. Kuchner. Revealing asymmetries in the hd 181327 debris disk: a recent massive collision or interstellar medium warping. *The Astrophysical Journal*, 789(1):58, 2014.

K. G. Stassun. VizieR Online Data Catalog: TESS Input Catalog - v8.0 (TIC-8) (Stassun+, 2019). *VizieR Online Data Catalog*, art. IV/38, Nov. 2019.

S. Steiger, T. Currie, T. D. Brandt, O. Guyon, M. Kuzuhara, J. Chilcote, T. D. Groff, J. Lozi, A. B. Walter, N. Fruitwala, et al. Scexao/mec and charis discovery of a low-mass, 6 au separation companion to hip 109427 using stochastic speckle discrimination and high-contrast spectroscopy. *The Astronomical Journal*, 162(2):44, 2021.

G. G. Stokes. On the composition and resolution of streams of polarized light from different sources. *Transactions of the Cambridge Philosophical Society*, 9:399, 1851.

T. Stolker, C. Dominik, M. Min, A. Garufi, G. D. Mulders, and H. Avenhaus. Scattered light mapping of protoplanetary disks. A&A, 596:A70, Dec. 2016. doi: 10.1051/0004-6361/201629098.

STScI Development Team. pysynphot: Synthetic photometry software package. Astrophysics Source Code Library, record ascl:1303.023, Mar. 2013.

B. J. Sumlin, W. R. Heinson, and R. K. Chakrabarty. Retrieving the aerosol complex refractive index using pymiescatt: A mie computational package with visualization capabilities. *Journal of Quantitative Spectroscopy and Radiative Transfer*, 205:127–134, 2018.

N. Swimmer, T. Currie, S. Steiger, G. M. Brandt, T. D. Brandt, O. Guyon, M. Kuzuhara, J. Chilcote, T. Tobin, T. D. Groff, J. Lozi, I. Bailey, John I., A. B. Walter, N. Fruitwala, N. Zobrist, J. P. Smith, G. Coiffard, R. Dodkins, K. K. Davis, M. Daal, B. Bumble, S. Vievard, N. Skaf, V. Deo, N. Jovanovic, F. Martinache, M. Tamura, N. J. Kasdin, and B. A. Mazin. SCExAO and Keck Direct Imaging Discovery of a Low-mass Companion Around the Accelerating F5 Star HIP 5319. AJ, 164(4):152, Oct. 2022. doi: 10.3847/1538-3881/ac85a8.

J. Szalay, F. Allegrini, R. Ebert, F. Bagenal, S. Bolton, S. Fatemi, D. McComas, A. Pontoni, J. Saur, H. Smith, et al. Oxygen production from dissociation of europa's water-ice surface. *Nature astronomy*, pages 1–10, 2024.

T. TanabÉ, I. Sakon, M. Cohen, T. Wada, Y. Ita, Y. Ohyama, S. Oyabu, K. Uemizu, T. Takagi, D. Ishihara, et al. Absolute photometric calibration of the infrared camera (irc) aboard akari. *Publications of the Astronomical Society of Japan*, 60(sp2):S375–S388, 2008.

G. I. Taylor. The spectrum of turbulence. *Proceedings of the Royal Society of London. Series A-Mathematical and Physical Sciences*, 164(919):476–490, 1938.

P. Thébault. Vertical structure of debris discs. *Astronomy & Astrophysics*, 505(3):1269–1276, 2009.

W. Thompson and C. Marois. Improved contrast in images of exoplanets using direct snr optimization. *arXiv preprint arXiv:2103.09252*, 2021.

J. Tinbergen. Astronomical polarimetry. *Astronomical Polarimetry*, 2005.

A. Tokunaga and W. Vacca. The mauna kea observatories near-infrared filter set. iii. isophotal wavelengths and absolute calibration. *Publications of the Astronomical Society of the Pacific*, 117(830):421, 2005.

T. Trifonov, L. Tal-Or, M. Zechmeister, A. Kaminski, S. Zucker, and T. Mazeh. Public HARPS radial velocity database corrected for systematic errors. A&A, 636:A74, Apr. 2020. doi: 10.1051/0004-6361/201936686.

S. K. Trumbo and M. E. Brown. The distribution of co2 on europa indicates an internal source of carbon. *Science*, 381(6664):1308–1311, 2023.

S. K. Trumbo, M. E. Brown, and K. P. Hand. Sodium chloride on the surface of europa. *Science advances*, 5(6):eaaw7123, 2019.

N. W. Tuchow, C. C. Stark, and E. Mamajek. Hpic: the habitable worlds observatory preliminary input catalog. *The Astronomical Journal*, 167(3):139, 2024.

T. Uyama, B. Ren, D. Mawet, G. Ruane, C. Z. Bond, J. Hashimoto, M. C. Liu, T. Muto, J.-B. Ruffio, N. Wallack, et al. Early high-contrast imaging results with keck/nirc2-pwfs: The sr 21 disk. *The Astronomical Journal*, 160(6):283, 2020.

S. van der Walt, J. L. Schönberger, J. Nunez-Iglesias, F. Boulogne, J. D. Warner, N. Yager, E. Gouillart, T. Yu, and the scikit-image contributors. scikit-image: image processing in python. *PeerJ*, 2:e453, jun 2014. ISSN 2167-8359. doi: 10.7717/peerj.453. URL https://doi.org/10.7717/peerj.453.

R. G. van Holstein, S. P. Bos, J. Ruigrok, J. Lozi, O. Guyon, B. Norris, F. Snik, J. Chilcote, T. Currie, T. D. Groff, et al. Calibration of the instrumental polarization effects of scexao-charis'spectropolarimetric mode. In *Ground-based and Airborne Instrumentation for Astronomy VIII*, volume 11447, pages 1113–1126. SPIE, 2020.

M. A. van Kooten, R. Jensen-Clem, C. Bond, S. Cetre, S. Ragland, P. Wizinowich, D. Mawet, and J. Fowler. Status of predictive wavefront control on keck ii adaptive optics bench. In *Techniques and Instrumentation for Detection of Exoplanets X*, volume 11823, page 118231F. International Society for Optics and Photonics, 2021.

J. Vernin, J. L. Caccia, G. Weigelt, and M. Mueller. Speckle lifetime and isoplanicity determinations: direct measurements and derivation from turbulence and wind profiles. A&A, 243(2):553–558, Mar. 1991.

S. Vievard, S. P. Bos, F. Cassaing, T. Currie, V. Deo, O. Guyon, N. Jovanovic, C. U. Keller, M. Lamb, C. Lopez, et al. Focal plane wavefront sensing on subaru/scexao. In *Adaptive Optics Systems VII*, volume 11448, page 114486D. International Society for Optics and Photonics, 2020.

A. Vigan, C. Moutou, M. Langlois, F. Allard, A. Boccaletti, M. Carbillet, D. Mouillet, and I. Smith. Photometric characterization of exoplanets using angular and spectral differential imaging. *Monthly Notices of the Royal Astronomical Society*, 407(1):71–82, 2010.

G. Villanueva, H. Hammel, S. Milam, S. Faggi, V. Kofman, L. Roth, K. Hand, L. Paganini, J. Stansberry, J. Spencer, et al. Endogenous co2 ice mixture on the surface of europa and no detection of plume activity. *Science*, 381(6664):1305–1308, 2023.

W. Voges, T. Boller, and R. Supper. Source population properties derived from ROSAT catalogues. In *26th International Cosmic Ray Conference (ICRC26), Volume 4*, volume 4 of *International Cosmic Ray Conference*, page 47, Aug. 1999.

F. Vogt, F. Martinache, O. Guyon, T. Yoshikawa, K. Yokochi, V. Garrel, and T. Matsuo. The subaru coronographic extreme ao (scexao) system: implementation and performances of the coronographic low order wavefront sensor. In *Adaptive Optics Systems II*, volume 7736, pages 407–414. SPIE, 2010.

A. Vorburger and P. Wurz. Modeling of possible plume mechanisms on europa. *Journal of Geophysical Research: Space Physics*, 126(9):e2021JA029690, 2021.

J. M. Vos, K. Allers, D. Apai, B. Biller, A. Burgasser, J. Faherty, J. Gagné, C. Helling, C. Morley, J. Radigan, A. Showman, X. Tan, and P. Tremblin. Astro2020 White Paper: The L/T Transition. *arXiv e-prints*, art. arXiv:1903.06691, Mar. 2019. doi: 10.48550/arXiv.1903.06691.

W. D. Vousden, W. M. Farr, and I. Mandel. Dynamic temperature selection for parallel tempering in Markov chain Monte Carlo simulations. MNRAS, 455(2):1919–1937, Jan. 2016. doi: 10.1093/mnras/stv2422.

J. H. Waite, C. R. Glein, R. S. Perryman, B. D. Teolis, B. A. Magee, G. Miller, J. Grimes, M. E. Perry, K. E. Miller, A. Bouquet, et al. Cassini finds molecular hydrogen in the enceladus plume: evidence for hydrothermal processes. *Science*, 356(6334):155–159, 2017.

A. Walter, B. B. Mazin, C. Bockstiegel, N. Fruitwala, P. Szypryt, I. Lipartito, S. Meeker, N. Zobrist, G. Collura, G. Coiffard, et al. Mec: the mkid exoplanet camera for high contrast astronomy at subaru (conference presentation). In *Ground-based and Airborne Instrumentation for Astronomy VII*, volume 10702, page 107020V. International Society for Optics and Photonics, 2018.

A. B. Walter, C. Bockstiegel, T. D. Brandt, and B. A. Mazin. Stochastic speckle discrimination with time-tagged photon lists: Digging below the speckle noise floor. *Publications of the Astronomical Society of the Pacific*, 131(1005):114506, 2019.

A. B. Walter, N. Fruitwala, S. Steiger, J. I. Bailey, N. Zobrist, N. Swimmer, I. Lipartito, J. P. Smith, S. R. Meeker, C. Bockstiegel, et al. The mkid exoplanet camera for subaru scexao. *Publications of the Astronomical Society of the Pacific*, 132(1018):125005, 2020.

J. J. Wang, A. Rajan, J. R. Graham, D. Savransky, P. J. Ingraham, K. Ward-Duong, J. Patience, R. J. De Rosa, J. Bulger, A. Sivaramakrishnan, et al. Gemini planet imager obser-

vational calibrations viii: characterization and role of satellite spots. In *Ground-based and Airborne Instrumentation for Astronomy V*, volume 9147, pages 1678–1692. SPIE, 2014.

J. J. Wang, J.-B. Ruffio, R. J. De Rosa, J. Aguilar, S. G. Wolff, and L. Pueyo. pyKLIP: PSF Subtraction for Exoplanets and Disks, June 2015.

J. J. Wang, J.-B. Ruffio, R. J. De Rosa, J. Aguilar, S. G. Wolff, and L. Pueyo. pyklip: Psf subtraction for exoplanets and disks. *Astrophysics Source Code Library*, pages ascl–1506, 2015.

J. J. Wang, J. R. Graham, L. Pueyo, P. Kalas, M. A. Millar-Blanchaer, J.-B. Ruffio, R. J. De Rosa, S. M. Ammons, P. Arriaga, V. P. Bailey, T. S. Barman, J. Bulger, A. S. Burrows, A. Cardwell, C. H. Chen, J. K. Chilcote, T. Cotten, M. P. Fitzgerald, K. B. Follette, R. Doyon, G. Duchêne, A. Z. Greenbaum, P. Hibon, L.-W. Hung, P. Ingraham, Q. M. Konopacky, J. E. Larkin, B. Macintosh, J. Maire, F. Marchis, M. S. Marley, C. Marois, S. Metchev, E. L. Nielsen, R. Oppenheimer, D. W. Palmer, R. Patel, J. Patience, M. D. Perrin, L. A. Poyneer, A. Rajan, J. Rameau, F. T. Rantakyrö, D. Savransky, A. Sivaramakrishnan, I. Song, R. Soummer, S. Thomas, G. Vasisht, D. Vega, J. K. Wallace, K. Ward-Duong, S. J. Wiktorowicz, and S. G. Wolff. The Orbit and Transit Prospects for β Pictoris b Constrained with One Milliarcsecond Astrometry. AJ, 152(4):97, Oct. 2016. doi: 10.3847/0004-6256/152/4/97.

J. J. Wang, M. D. Perrin, D. Savransky, P. Arriaga, J. K. Chilcote, R. J. De Rosa, M. A. Millar-Blanchaer, C. Marois, J. Rameau, S. G. Wolff, et al. The automated data processing architecture for the gpi exoplanet survey. In *Techniques and Instrumentation for Detection of Exoplanets VIII*, volume 10400, pages 614–633. SPIE, 2017.

J. J. Wang, M. D. Perrin, D. Savransky, P. Arriaga, J. K. Chilcote, R. J. De Rosa, M. A. Millar-Blanchaer, C. Marois, J. Rameau, S. G. Wolff, et al. Automated data processing architecture for the gemini planet imager exoplanet survey. *Journal of Astronomical Telescopes, Instruments, and Systems*, 4(1):018002–018002, 2018.

S. J. Wiktorowicz, M. Millar-Blanchaer, M. D. Perrin, J. R. Graham, M. P. Fitzgerald, J. Maire, P. Ingraham, D. Savransky, B. A. Macintosh, S. J. Thomas, et al. Gemini planet imager observational calibrations vii: on-sky polarimetric performance of the gemini planet imager. In *Ground-based and Airborne Instrumentation for Astronomy V*, volume 9147, pages 2574–2584. SPIE, 2014.

G. Witzel, A. Eckart, R. Buchholz, M. Zamaninasab, R. Lenzen, R. Schödel, C. Araujo, N. Sabha, M. Bremer, V. Karas, et al. The instrumental polarization of the nasmyth focus polarimetric differential imager naos/conica (naco) at the vlt-implications for time-resolved polarimetric measurements of sagittarius a. *Astronomy & Astrophysics*, 525:A130, 2011.

P. Wizinowich, J. Chin, C. Correia, J. Lu, T. Brown, K. Casey, S. Cetre, J.-R. Delorme, L. Gers, L. Hunter, S. Lilley, S. Ragland, A. Surendran, E. Wetherell, A. Ghez, T. Do, T. Jones, M. Liu, D. Mawet, C. Max, M. Morris, T. Treu, and S. Wright. Keck all sky precision adaptive optics. In L. Schreiber, D. Schmidt, and E. Vernet, editors, *Adaptive Optics Systems VII*, volume 11448, pages 49 – 63. International Society for Optics and Photonics, SPIE, 2020. doi: 10.1117/12.2560017. URL https://doi.org/10.1117/12.2560017.

A. Wolszczan and D. A. Frail. A planetary system around the millisecond pulsar psr1257+12. *Nature*, 355(6356):145–147, 1992.

E. L. Wright, P. R. Eisenhardt, A. K. Mainzer, M. E. Ressler, R. M. Cutri, T. Jarrett, J. D. Kirkpatrick, D. Padgett, R. S. McMillan, M. Skrutskie, et al. The wide-field infrared survey explorer (wise): mission description and initial on-orbit performance. *The Astronomical Journal*, 140(6):1868, 2010.

C. Wu, G. Gu, Q. Chen, W. He, W. Zhang, and H. Zhu. Design of a high-performance EMCCD imaging system. In *Society of Photo-Optical Instrumentation Engineers (SPIE)*

Conference Series, volume 11763 of *Society of Photo-Optical Instrumentation Engineers (SPIE) Conference Series*, page 117631J, Mar. 2021. doi: 10.1117/12.2586285.

Y. Wu, B. Lewis, and M. Fitzgerald. Modeling the spatial distributions of particle ejections. In *American Astronomical Society Meeting Abstracts*, volume 241 of *American Astronomical Society Meeting Abstracts*, page 104.10, Jan. 2023.

M. C. Wyatt. Evolution of debris disks. *Annu. Rev. Astron. Astrophys.*, 46:339–383, 2008.

W. J. Xuan, D. Mawet, H. Ngo, G. Ruane, V. P. Bailey, É. Choquet, O. Absil, C. Alvarez, M. Bryan, T. Cook, et al. Characterizing the performance of the nirc2 vortex coronagraph at wm keck observatory. *The Astronomical Journal*, 156(4):156, 2018.

S. K. Yeoh, T. A. Chapman, D. B. Goldstein, P. L. Varghese, and L. M. Trafton. On understanding the physics of the enceladus south polar plume via numerical simulation. *Icarus*, 253:205–222, 2015.

S. K. Yeoh, Z. Li, D. B. Goldstein, P. L. Varghese, D. A. Levin, and L. M. Trafton. Constraining the enceladus plume using numerical simulation and cassini data. *Icarus*, 281: 357–378, 2017.

M. Zhang, M. Millar-Blanchaer, B. Safonov, M. Lucas, L. Lilley, J. Ashcraft, B. Norris, J. Lozi, O. Guyon, and M. Bottom. Characterizing the instrumental polarization of scexao vampires. In *Techniques and Instrumentation for Detection of Exoplanets XI*, volume 12680, pages 261–282. SPIE, 2023.

M. V. Zombeck. *Handbook of space astronomy and astrophysics*. Cambridge University Press, 2006.